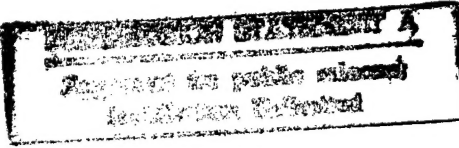
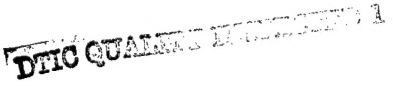


REPORT DOCUMENTATION PAGE			Form Approved OMB No. 0704-0188	
Public reporting burden for this collection of information is estimated to average 1 hour per response, including the time for reviewing instructions, searching existing data sources, gathering and maintaining the data needed, and completing and reviewing the collection of information. Send comments regarding this burden estimate or any other aspect of this collection of information, including suggestions for reducing this burden, to Washington Headquarters Services, Directorate for Information Operations and Reports, 1215 Jefferson Davis Highway, Suite 1204, Arlington, VA 22202-4302, and to the Office of Management and Budget, Paperwork Reduction Project (0704-0188), Washington, DC 20503.				
1. AGENCY USE ONLY (Leave blank)		2. REPORT DATE 11 September 1998		3. REPORT TYPE AND DATES COVERED
4. TITLE AND SUBTITLE MASS FIELD RETRIEVAL USING PROFILER DATA WITH APPLICATION TO LOW-LEVEL JET ANALYSIS				5. FUNDING NUMBERS
6. AUTHOR(S) DAN A. SHALTANIS				
7. PERFORMING ORGANIZATION NAME(S) AND ADDRESS(ES) NORTH CAROLINA STATE UNIVERSITY				8. PERFORMING ORGANIZATION REPORT NUMBER  98-066
9. SPONSORING/MONITORING AGENCY NAME(S) AND ADDRESS(ES) THE DEPARTMENT OF THE AIR FORCE AFIT/CIA, BLDG 125 2950 P STREET WPAFB OH 45433				10. SPONSORING/MONITORING AGENCY REPORT NUMBER
11. SUPPLEMENTARY NOTES				
12a. DISTRIBUTION AVAILABILITY STATEMENT Unlimited distribution In Accordance With 35-205/AFIT Sup 1				12b. DISTRIBUTION CODE
13. ABSTRACT (Maximum 200 words)				
 				
14. SUBJECT TERMS				15. NUMBER OF PAGES 157
				16. PRICE CODE
17. SECURITY CLASSIFICATION OF REPORT		18. SECURITY CLASSIFICATION OF THIS PAGE		19. SECURITY CLASSIFICATION OF ABSTRACT
				20. LIMITATION OF ABSTRACT

**MASS FIELD RETRIEVAL USING PROFILER DATA  
WITH APPLICATION TO LOW-LEVEL JET ANALYSIS**

by

**CAPTAIN DAN A. SHALTANIS**

**UNITED STATES AIR FORCE**

A thesis submitted to the Graduate Faculty of  
North Carolina State University  
in partial fulfillment of the  
requirements for the Degree of  
Master of Science

1998

157 pages

19980915 021

## ABSTRACT

SHALTANIS, DAN A. Mass Field Retrieval Using Profiler Data With Application To Low-Level Jet Analysis. (Under the direction of Yuh-Lang Lin)

A study into the method of reproducing the geopotential height and temperature fields using a higher resolution observational network is conducted. Wind profiler data is used with the addition of RAOB data to produce an accurate wind field on an hourly basis. From this higher resolution wind field, the divergence equation was employed to produce a new mass field. The method allows for a better analysis of atmospheric features. This technique allowed for a mesoscale study in two areas. The first component of the study involved three examples of a summer time low-level jet (LLJ) in the Great Plains of the United States. With the newly derived mass and wind field, it was determined the jet was formed by an inertial oscillation and low-level baroclinicity for two of the LLJs. A transverse ageostrophic circulation played a role for the third LLJ. The other component of this study concerned investigating the effects, if any, of the frictional stress term in the divergence equation and how it played on the retrieval of the new mass field. In past studies this term had been ignored. The lower atmosphere was analyzed and sensitivity studies were conducted to investigate the importance of the frictional stresses. It was determined for these two particular atmospheric case study days that the frictional force plays no significant role. These results were then compared to a mesoscale model to check the accuracy of the technique. The model output was generally in agreement with the retrieval technique analysis at the initial hour as well as at the forecasted hours.

## References

- Adams, M. E. 1996: Terrain-induced midtropospheric frontogenesis and jet streak development during STORM-FEST IOP-17, 8 & 9 March 1992. Ph. D. Thesis, North Carolina State University, 214pp.
- Anderson, J. R., E. E. Hardy, J. T. Roach, and R. E. Witmer, 1976: A land use and land cover classification system for use with remote sensor data. *U.S. Geological Survey Professional Paper 964*, U.S. Government Printing Office, Washington, 28pp.
- Arritt, R. W., T. D. Rink, M. Segal, D. P. Todey, and C. A. Clark, 1997: The Great Plains low-level jet during the warm season of 1993. *Mon. Wea. Rev.*, **125**, 2176-2192.
- Arya, S. P., 1988: *Introduction to Micrometeorology*. Academic Press, 303pp.
- Barnes, S. L., 1964: A technique for maximizing details in numerical weather map analysis. *J. Appl. Meteor.*, **3**, 396-409.
- Barnes, S. L., 1973: Mesoscale objective analysis using weighted time-series observations. *NOAA Tech. Memo.*, ERL NSSL-62, 60pp.
- Blackadar, A. K., 1957: Boundary layer wind maxima and their significance for the growth of nocturnal inversion. *Bull. Amer. Meteor. Soc.*, **38**, 283-290.
- Bluestein, H. B. and T. M. Crawford, 1997: Mesoscale dynamics of the near-dryline environment: analysis of data from COPS-91. *Mon. Wea. Rev.*, **125**, 2161-2175.
- Bolin, B., 1956: An improved barotropic model and some aspects of using the balance equation for three dimensional flow. *Tellus*, **8**, 67-75.
- Bonner, W. D., 1968: Climatology of the low-level jet. *Mon. Wea. Rev.*, **96**, 833-850.
- Bonner, W. D. and J. Paegle, 1970: Diurnal variations in boundary layer winds over the south-central United States in summer. *Mon. Wea. Rev.*, **98**, 735-744.
- Charney, J. G., 1955: The use of the primitive equation of motion in numerical weather prediction. *Tellus*, **7**, 22-26.
- Chen, T. C. and J. A. Kpaeyeh, 1993: The synoptic-scale environment associated with the low-level jet of the Great Plains. *Mon. Wea. Rev.*, **121**, 416-420.
- Cram, J. M., M. L. Kaplan, C. A. Mattocks, and J. W. Zack, 1991: The use and analysis of profiler winds to derive mesoscale height and temperature fields: simulation and real-data experiments. *Mon. Wea. Rev.*, **119**, 1040-1056.



- Daley, R., 1991: *Atmospheric Data Analysis*, Cambridge University Press, 457pp.
- Fast, J. D. and M. D. McCorcle, 1990: A two-dimensional numerical sensitivity study of the Great Plains low-level jet. *Mon. Wea. Rev.*, **118**, 151-163.
- Haltiner, G. J. and R. T. Williams, 1980: *Numerical Prediction and Dynamic Meteorology* John Wiley and Sons, Inc., 477pp.
- Kaplan, M. L. and P. A. Paine, 1977: The observational divergence of the horizontal velocity field and pressure gradient force at the mesoscale. Its implications for the parameterization of three dimensional momentum transport in synoptic-scale numerical models. *Beitr. Phys. Atmos.*, **50**, 321-330.
- Koch, S. E., M. DesJardins, and P. J. Kocin, 1983: An interactive Barnes objective map analysis scheme for use with satellite and conventional data. *J. Climate Appl. Meteor.*, **22**, 1487-1503.
- Kuo, Y. H. and R. A. Anthes, 1985: Calculation of geopotential and temperature fields from an array of nearly continuous wind observations. *J. Atmos. Oceanic Technol.*, **2**, 22-34.
- Kuo, Y. H., D. O. Gill, and L. Cheng, 1987: Retrieving temperature and geopotential fields from a network of wind profiler observations. *Mon. Wea. Rev.*, **115**, 3146-3165.
- Maddox, R. A., 1980: Mesoscale convective complexes. *Bull. Amer. Meteor. Soc.*, **61**, 1374-1387.
- Maddox, R. A., 1985: The relation of diurnal, low-level wind variations to summertime severe thunderstorms. Preprints, *14<sup>th</sup> Conf. On Severe Local Storms*, Indianapolis, IN, Amer. Meteor. Soc., 202-207.
- Marht, L. and H. Pan, 1984: A two-layer model of soil hydrology. *Boundary-Layer Meteorol.*, **29**, 1-20.
- McCorcle, M. D., 1988: Simulation of surface-moisture effects on the Great Plains low-level jet. *Mon. Wea. Rev.*, **116**, 1705-1720.
- McNider, R. T. and R. A. Pielke, 1981: Diurnal boundary-layer development over sloping terrain. *J. Atmos. Sci.*, **80**, 165-189.
- MESO, 1995: MASS Version 5.8 Reference Manual, MESO, Inc., Troy, NY, 119pp.
- Mitchell, M. J., R. W. Arritt, and K. Labas: A climatology of the warm season great plains low-level jet using wind profiler observations. *Wea. And For.*, **10**, 576-591.

- Mizzi, A. P. and R. A. Pielke, 1984: A numerical study of the mesoscale atmospheric circulation observed during a coastal upwelling event on 23 August 1972. I. Sensitivity studies. *Mon. Wea. Rev.*, **112**, 76-90.
- Noilhan, J. and S. Planton, 1989: A simple parameterization of land surface processes for meteorological models. *Mon. Wea. Rev.*, **117**, 536-549.
- O'Brien, J. J., 1970: Alternative solutions to the classical vertical velocity problem, *J. Appl. Meteor.*, **9**, 197-203.
- Ogura, Y., 1975: On the interaction between cumulus clouds and the larger-scale environment. *Pure Appl. Geophys.*, **113**, 869-889.
- Parish, T. R., A. R. Rodi, and R. D. Clark, 1988: A case study of the summertime great plains low-level jet. *Mon. Wea. Rev.*, **116**, 94-105.
- Pielke, R. A., R. A. Stocker, R. W. Arritt, and R. T. McNider, 1991: A procedure to estimate worst-case air quality in complex terrain. *Environ. Int.*, **17**, 559-594.
- Savijarvi, H., 1991: The United States Great Plains diurnal ABL variation and the nocturnal low-level jet. *Mon. Wea. Rev.*, **119**, 833-840.
- Stensrud, D. J., 1996: Importance of the low-level jet to climate: a review. *J. of Clim.*, **9**, 1698-1711.
- Strauch, R. G., 1981: Radar measurement of tropospheric wind profiles. Preprints, 20<sup>th</sup> Conference on Radar meteorology, Boston, MA, Amer. Meteor. Soc., 430-434.
- Stull, R. B., 1988: *An Introduction to Boundary Layer Meteorology*. Kluwer, 666pp.
- Uccellini, L. W., D. R. Johnson, 1979: The coupling of upper and lower tropospheric jet streaks and implications for the development of severe convective storms. *Mon. Wea. Rev.*, **107**, 682-703.
- Weber, B. L. and D. B. Wuertz, 1990: Comparison of rawinsonde and wind profiler radar measurements. *J. Atmos. Oceanic Technol.*, **7**, 157-174.
- Wexler, H., 1961: A boundary layer interpretation of the low-level jet. *Tellus*, **13**, 368-378.
- Whiteman, C. D., X. Bian, and S. Zhong, 1997: Low-level jet climatology from enhanced rawinsonde observations at a site in the southern great plains. *J. Appl. Meteor.*, **36**, 1363-1376.

Zack, J. W. and M. L. Kaplan, 1987: Numerical simulations of the subsynoptic features associated with the AVE-SESAME I case. Part I: the preconvective environment. *Mon. Wea. Rev.*, **115**, 2367-2382.

**MASS FIELD RETRIEVAL USING PROFILER DATA  
WITH APPLICATION TO LOW-LEVEL JET ANALYSIS**

by

**DAN A. SHALTANIS**

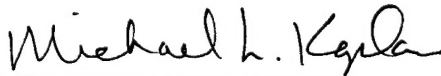
A thesis submitted to the Graduate Faculty of  
North Carolina State University  
in partial fulfillment of the  
requirements for the Degree of  
Master of Science

**DEPARTMENT OF MARINE, EARTH AND ATMOSPHERIC SCIENCES**

Raleigh

1998

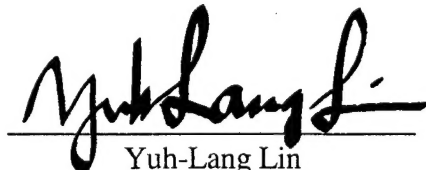
**APPROVED BY:**



Michael L. Kaplan



Sethu Raman



Yuh-Lang Lin  
Chair of Advisory Committee

## **PERSONAL BIOGRAPHY**

Captain Dan A. Shaltanis is an Officer in the United States Air Force. He was born in Ankeny, Iowa on November 3, 1970. His parents are Dennis Shaltanis, a secondary school administrator, and Judith, a private piano teacher. He has two brothers, Mark and Joel who are both in pastoral ministry. Captain Shaltanis received a Bachelor of Science degree in Meteorology from Iowa State University in 1993. Upon graduation, Captain Shaltanis was commissioned a Second Lieutenant through the Air Force Reserve Officer Training Corps program. His active military career began at I Corps, United States Army, Fort Lewis, Washington. In 1994, Captain Shaltanis was assigned to the 100<sup>th</sup> Air Refueling Wing, Royal Air Force Mildenhall, England. In 1996, he was selected by the Air Force Institute of Technology program to attend North Carolina State University to work towards his Masters of Science degree.

## TABLE OF CONTENTS

	Page
LIST OF TABLES .....	v
LIST OF FIGURES .....	vi
1. INTRODUCTION	
1.1 Objectives .....	1
1.2 Literature Review of Low-Level Jets and the Planetary Boundary Layer .....	3
1.3 Review of the Divergence Equation .....	17
2. DATA AND ANALYSIS METHODOLOGY	
2.1 Data .....	21
2.1.1 RAOB Data .....	23
2.1.2 Profiler Data .....	25
2.1.3 Surface Data .....	31
2.1.4 Model Data .....	33
2.2 Mass Retrieval .....	33
2.2.1 Retrieval Technique .....	33
2.2.2 Friction Parameterization .....	36
2.2.3 Errors Associated With the Retrieval Technique .....	38
2.3 Summary .....	40
3. RESULTS	
3.1 Synoptic Overview .....	43
3.1.1 Surface Analysis and Weather .....	43
3.1.2 Upper Air Analysis .....	51
3.2 Comparison of RAOB and Retrieved Mass Fields .....	60
3.3 Development of the Low-Level Jet as Diagnosed from Profiler Winds .....	70
3.4 The Effects of Friction .....	110
3.5 Model Comparison .....	123

	Page
4. CONCLUSION	
4.1 Summary of Work .....	150
4.2 Future Work .....	152
5. REFERENCES .....	154

## LIST OF TABLES

		Page
Table 1	Synoptic classification scheme shown in Mitchell <i>et al.</i> (1995) .....	15
Table 2	Stations included in the Wind Profiler Demonstration Network .....	27
Table 3	Technical information on the NOAA Wind Profilers .....	30
Table 4	Specification for MASS Model version 5.9 .....	34
Table 5	Root-mean-square error of retrieval technique .....	42
Table 6	Averages of terms for a nocturnal PBL with no frictional stresses .....	114
Table 7	Averages of terms for a nocturnal PBL using drag parameterization .....	117
Table 8	Averages of terms for a nocturnal PBL using Rayleigh friction .....	117
Table 9	Averages of terms for a mixed PBL with no frictional stresses .....	118
Table 10	Averages of terms for a mixed PBL using drag parameterization .....	122
Table 11	Averages of terms for a mixed PBL using Rayleigh friction .....	122



## LIST OF FIGURES

	Page
Figure 1.1    Regions where low-level jets are known or suspected to occur with some regularity .....	4
Figure 1.2    The number of low-level jet observations from Jan 1959-Dec 1960 at 1200 and 0000 GMT as observed in Bonner (1968) .....	5
Figure 1.3    Rotation of the wind direction about mean wind .....	5
Figure 1.4    (a) Model upslope winds and (b) model downslope winds .....	9
Figure 1.5    Baroclinically developed low-level jet from a model .....	9
Figure 1.6    Trade winds entering the United States .....	11
Figure 1.7    Schematic feature of a severe weather outbreak (from Newton 1967) .....	11
Figure 2.1    The grid used for computations .....	22
Figure 2.2    RAOB station locations .....	24
Figure 2.3    Locations of wind profilers comprising NOAA's Wind Profiler Network .....	26
Figure 2.4    The three beams of the NOAA Wind Profiler .....	28
Figure 2.5    Schematic of the 36 gates of a wind profiler .....	29
Figure 2.6    Surface station locations .....	32
Figure 3.1    Surface map for 0000Z 15 August 1995 .....	44
Figure 3.2    Surface map for 0400Z 15 August 1995 .....	46
Figure 3.3    Surface map for 1000Z 15 August 1995 .....	47
Figure 3.4    Surface map for 1400Z 15 August 1995 .....	48

	Page
Figure 3.5	Surface map for 1900Z 15 August 1995 .....49
Figure 3.6	Surface map for 0200Z 16 August 1995 .....50
Figure 3.7	Surface map for 1400Z 16 August 1995 .....52
Figure 3.8	Surface map for 2300Z 16 August 1995 .....53
Figure 3.9	850 mb RAOB heights and winds for 0000Z 15 August 1995 .....54
Figure 3.10	850 mb RAOB heights and winds for 1200Z 15 August 1995 .....56
Figure 3.11	850 mb RAOB heights and winds for 1200Z 16 August 1995 .....57
Figure 3.12	700 mb RAOB heights and winds for 0000Z 15 August 1995 .....58
Figure 3.13	700 mb RAOB heights and winds for 0000Z 17 August 1995 .....59
Figure 3.14	200 mb RAOB heights, winds, and isotachs for 0000Z 15 August 1995 .....61
Figure 3.15	200 mb RAOB heights, winds, and isotachs for 1200Z 16 August 1995 .....62
Figure 3.16	850 mb Retrieved heights, RAOB heights, and their differences for 0000Z 15 August 1995 .....63
Figure 3.17	850 mb Retrieved heights, RAOB heights, and their differences for 0300Z 15 August 1995 .....65
Figure 3.18	850 mb Retrieved heights, RAOB heights, and their differences for 1200Z 15 August 1995 .....66
Figure 3.19	700 mb Retrieved heights, RAOB heights, and their differences for 0000Z 15 August 1995 .....67
Figure 3.20	500 mb Retrieved heights, RAOB heights, and their differences for 0000Z 16 August 1995 .....68
Figure 3.21	850 mb Retrieved temperatures, RAOB temperatures, and their differences for 0000Z 15 August 1995 .....69

	Page
Figure 3.22 700 mb Retrieved temperatures, RAOB temperatures, and their differences for 0000Z 15 August 1995 .....	71
Figure 3.23 500 mb Retrieved temperatures, RAOB temperatures, and their differences for 0000Z 15 August 1995 .....	72
Figure 3.24 700 mb Retrieved heights and temperatures using a smoother for 0000Z 15 August 1995 .....	73
Figure 3.25 900 mb Profiler winds, speed, and maximum wind for 0000Z 15 August 1995 .....	74
Figure 3.26 850 mb Profiler winds, speed, maximum wind, and surface weather for 0200Z 15 August 1995 .....	76
Figure 3.27 900 mb Profiler winds, speed, and maximum wind for 0400Z 15 August 1995 .....	77
Figure 3.28 850 mb Profiler winds, speed, maximum wind, and surface weather for 0400Z 15 August 1995 .....	78
Figure 3.29 850 mb Profiler winds, speed, and maximum wind for 0800Z 15 August 1995 .....	79
Figure 3.30 900 mb Profiler winds, speed, and maximum wind for 1000Z 15 August 1995 .....	80
Figure 3.31 900 mb Profiler winds, speed, and maximum wind for 1400Z 15 August 1995 .....	81
Figure 3.32 900 mb Profiler winds, speed, maximum wind, and surface weather for 0000Z 16 August 1995 .....	83
Figure 3.33 700 mb Profiler winds, speed, and maximum wind for 0100Z 16 August 1995 .....	84
Figure 3.34 500 mb Retrieved heights, winds, speed, and locations of cross section points for 0300Z 16 August 1995 .....	85
Figure 3.35 Cross section between Scottsbluff, NE and Knoxville, TN for 1800Z 15 August 1995 .....	86

	Page
Figure 3.36 850 mb Isallobaric winds between 0200Z and 0300Z 16 August 1995 .....	87
Figure 3.37 900 mb Profiler winds, speed, and maximum wind for 0500Z 16 August 1995 .....	89
Figure 3.38 850 mb Profiler winds, speed, and maximum wind for 0500Z 16 August 1995 .....	90
Figure 3.39 900 mb Profiler winds, speed, maximum wind, surface weather, and locations of cross section points for 0700Z 16 August 1995 .....	91
Figure 3.40 850 mb Profiler winds, speed, and maximum wind for 0700Z 16 August 1995 .....	92
Figure 3.41 750 mb Profiler winds, speed, and maximum wind for 0700Z 16 August 1995 .....	93
Figure 3.42 Cross section between Garden City, KS and Ft Leonard Wood, MO for 0700Z 16 August 1995 .....	94
Figure 3.43 900 mb Profiler winds, speed, and divergence for 0700Z 16 August 1995 .....	95
Figure 3.44 850 mb RAOB winds, speed, and maximum wind for 0700Z 16 August 1995 .....	96
Figure 3.45 850 mb Geostrophic winds and speed difference for 0700Z 16 August 1995 .....	97
Figure 3.46 900 mb Ageostrophic winds and 200 mb isotachs for 0000Z 15 August 1995 .....	99
Figure 3.47 900 mb Ageostrophic winds and 200 mb isotachs for 2100Z 15 August 1995 .....	101
Figure 3.48 900 mb Ageostrophic winds and 200 mb isotachs for 1200Z 15 August 1995 .....	102
Figure 3.49 900 mb Ageostrophic winds and 200 mb isotachs for 1200Z 16 August 1995 .....	103

	Page
Figure 3.50 900 mb Model temperatures and 900 mb surface for 0000Z 16 August 1995 .....	104
Figure 3.51 900 mb Model temperatures and 900 mb surface for 1200Z 16 August 1995 .....	105
Figure 3.52 900 mb Wind direction at four locations from 0000Z 16 August to 0000Z 17 August 1995 .....	106
Figure 3.53 Time series of winds and speed at KPNC from 0000Z 16 August to 0100Z 17 August 1995 .....	107
Figure 3.54 900 mb Profiler winds, speed, and maximum wind for 1000Z 16 August 1995 .....	108
Figure 3.55 850 mb Profiler winds, speed, and maximum wind for 1000Z 16 August 1995 .....	109
Figure 3.56 900 mb Profiler winds, speed, and maximum wind for 1200Z 16 August 1995 .....	111
Figure 3.57 900 mb Profiler winds, speed, and maximum wind for 1800Z 16 August 1995 .....	112
Figure 3.58 900 mb Retrieved heights with friction, without friction, and their differences for 0800Z 15 August 1995 .....	113
Figure 3.59 900 mb Retrieved heights with friction, without friction, and their differences for 0600Z 16 August 1995 .....	115
Figure 3.60 900 mb Retrieved heights with friction, without friction, and their differences for 0700Z 16 August 1995 .....	116
Figure 3.61 900 mb Retrieved heights with friction, without friction, and their differences for 1900Z 15 August 1995 .....	119
Figure 3.62 850 mb Retrieved heights with friction, without friction, and their differences for 2100Z 16 August 1995 .....	120
Figure 3.63 700 mb Retrieved heights with friction, without friction, and their differences for 2100Z 16 August 1995 .....	121

	Page
Figure 3.64 850 mb Retrieved height and modeled heights for 0000Z 15 August 1995 .....	124
Figure 3.65 700 mb Retrieved height and modeled heights for 0000Z 15 August 1995 .....	125
Figure 3.66 850 mb Retrieved height and modeled heights for 0300Z 15 August 1995 .....	127
Figure 3.67 500 mb Retrieved height and modeled heights for 0600Z 15 August 1995 .....	128
Figure 3.68 850 mb Retrieved height and modeled heights for 1700Z 15 August 1995 .....	129
Figure 3.69 700 mb Retrieved height and modeled heights for 1700Z 15 August 1995 .....	130
Figure 3.70 500 mb Retrieved height and modeled heights for 1700Z 15 August 1995 .....	131
Figure 3.71 500 mb Retrieved height and modeled heights for 0000Z 16 August 1995 .....	132
Figure 3.72 850 mb Retrieved height and modeled heights for 0700Z 16 August 1995 .....	133
Figure 3.73 850 mb Retrieved height and modeled heights for 1200Z 16 August 1995 .....	134
Figure 3.74 500 mb Retrieved height and modeled heights for 1200Z 16 August 1995 .....	135
Figure 3.75 700 mb Retrieved temperatures and modeled temperatures for 0000Z 15 August 1995 .....	136
Figure 3.76 500 mb Retrieved temperatures and modeled temperatures for 0000Z 15 August 1995 .....	137
Figure 3.77 700 mb Retrieved temperatures and modeled temperatures for 0600Z 15 August 1995 .....	138

	Page
Figure 3.78 500 mb Retrieved temperatures and modeled temperatures for 0600Z 15 August 1995 .....	140
Figure 3.79 700 mb Profiler winds and modeled winds for 0000Z 15 August 1995 .....	141
Figure 3.80 500 mb Profiler winds and modeled winds for 0000Z 15 August 1995 .....	142
Figure 3.81 850 mb Profiler winds and modeled winds for 0400Z 15 August 1995 .....	143
Figure 3.82 850 mb Profiler winds and modeled winds for 0800Z 15 August 1995 .....	144
Figure 3.83 900 mb Profiler winds and modeled winds for 1400Z 15 August 1995 .....	145
Figure 3.84 900 mb Profiler winds and modeled winds for 0000Z 16 August 1995 .....	146
Figure 3.85 900 mb Profiler winds and modeled winds for 0500Z 16 August 1995 .....	147
Figure 3.86 900 mb Profiler winds and modeled winds for 0700Z 16 August 1995 .....	148
Figure 3.87 750 mb Profiler winds and modeled winds for 0700Z 16 August 1995 .....	149

## 1. INTRODUCTION

### 1.1 Objectives

This research will produce a mesoscale mass field, via the divergence equation with wind profiler and RAOB data, to characterize low-level jets (LLJ) and frictional stresses within the Planetary Boundary Layer (PBL). The divergence equation specifies the relationship between the dot product of the wind field and a measure of the pressure field. It can be used in atmospheric research to derive a mass field. A mass field is implicit in the combination of the pressure and temperature distribution of the atmosphere as specified by the equation of state. An understanding of the mass field is imperative in understanding the structure of weather systems that affect our lives. Currently the United States, and much of the world, rely on a coarsely-spaced network of upper air balloons to observe the existing mass field at 12 hour intervals. This technique has been in use for approximately fifty years. Recently, however, technology has provided improved ways to help observe the mass field of our complex atmosphere. The use of satellites and the placement of measuring devices in high altitude aircraft are current ways of sensing the observed mass field. Another way to better define the mass field is to use the divergence equation in conjunction with a higher resolution observed wind network to derive a mass field. Thus, with winds alone, a mass field can be retrieved given certain assumptions. As will be seen later, a more accurate mass field can be retrieved by a combination of upper air balloons and separate wind information. Up until now, the lack of higher frequently sensed winds was the missing link for a better mass field development using the divergence equation. The recent placement of the wind profiler now enhances the link. Wind profilers will be discussed in Section 2.1.

The technique to find the mass field, as discussed later, is not without its problems. Of major concern with the technique is the frictional force term found in the divergence equation. Frictional stresses, which compose this term, are found to be largest near the earth's surface (Stull 1988). This area is described as the PBL. Thus, errors in retrieving the mass field using the divergence equation can have errors in the PBL if friction is ignored.



Work needs to be done to see what, if any, impact PBL dynamics play with this retrieval technique.

The work that follows considers such concerns. Three examples of the PBL phenomena called the LLJ are used to highlight the dynamics within the PBL. The following section, Section 1.2, reviews PBL dynamics with an emphasis on the LLJ observed there. Then in Section 1.3 a discussion of the divergence equation will follow.

Chapter 2 deals with the process of retrieving the mass field using wind profilers and the divergence equation. First the data used will be reviewed. Next, Section 2.2 discusses the computations involved in finding the mass field. A summary will then follow in Section 2.3 to wrap up the basic fundamentals of what is needed to properly retrieve the mass field using this technique.

Chapter 3 is the focus of the work done. Here the results of the retrieval technique are shown. As with any good case study a look at the “big picture” is needed. Section 3.1 looks at just what is going on in the atmosphere. Here we can look at the coarse upper air mass field provided by rawinsonde data alone. With that in mind, Section 3.2 will reveal the newly retrieved mass field and show how, with the addition of wind profiler information, the mass field provides a more detailed structure than the previous analyses. Now with a clearer picture of the atmosphere, the development of the LLJ can be diagnosed. Section 3.3 looks into the dynamics of LLJs and explains its formative processes. Then the question of frictional stresses is addressed. The impact of frictional schemes in different stability regimes on the divergence equation will be reviewed in Section 3.4. For a conclusion of Chapter 3 a section on modeling is included. Here, a numerical weather prediction model is integrated in time and the resulting mass fields are compared with the retrieved mass field. Here, the model performance is compared against the retrieval technique and vice-versa.

Finally, Chapter 4 concludes the work performed. Section 4.1 summarizes what was done, how the process was accomplished, and evaluates how well it performed. Finally, Section 4.2 looks at what could be done with the technique in future studies.

## **1.2 Literature Review of Low-Level Jets and the Planetary Boundary Layer**

The “Low-Level Jet”, the “Nocturnal Low-Level Jet”, a “Southerly Wind Event”; among others have been used in literature to describe a supergeostrophic wind located in the lower troposphere. Authors have used each of the above terms to describe their definitions of the strong wind. A discussion of the wind, or jet, and the different characteristics that describe the jet follows. This will include several forcing mechanisms proposed to produce the LLJ. Also, recent research, including modeling of the LLJ, will be reviewed. An overview of the different forcing mechanisms and their synoptic situations will proceed next. To summarize the work on LLJs, unanswered questions and future work needed will be put forth. Finally, the characteristics of friction within the PBL will be reviewed.

The LLJ, as shown by Stensrud (1996), can be found throughout the world (Fig. 1.1). They have been related to Mesoscale Convective Complexes (Maddox 1980) and other severe thunderstorm events. This is because LLJs are efficient at transporting moisture to a storm. LLJs can produce strong vertical wind shear, which can be a significant hazard to jet aircraft on approach. A LLJ can contribute to the spreading of forest fires. Birds use the enhanced winds to aid in migration, and air quality can also be affected by the LLJ. This paper will focus on the Great Plains region of the United States of America. This location of the LLJ was first thoroughly reviewed by Bonner (1968) and then more recently by Mitchell, Arritt and Labas (1995).

Bonner (1968) developed a climatology of the LLJ using rawinsonde and a special pilot balloon (PIBAL) network from January 1959 to December 1960. He used data from 47 stations throughout the continental United States. A large number of LLJs occur in the Great Plains (Fig. 1.2). The maximum number exists in a region from Texas to Nebraska. More recent wind observations acquired via wind profilers, which give better temporal and spatial resolution (Mitchell et al. 1995), enhance Bonner’s results.

One problem with using wind profilers is the contamination of the wind signal by birds. For example, birds migrate preferentially at night. Also, they migrate usually on nights having strong LLJs. Confounding the problem is that bird migration paths are over

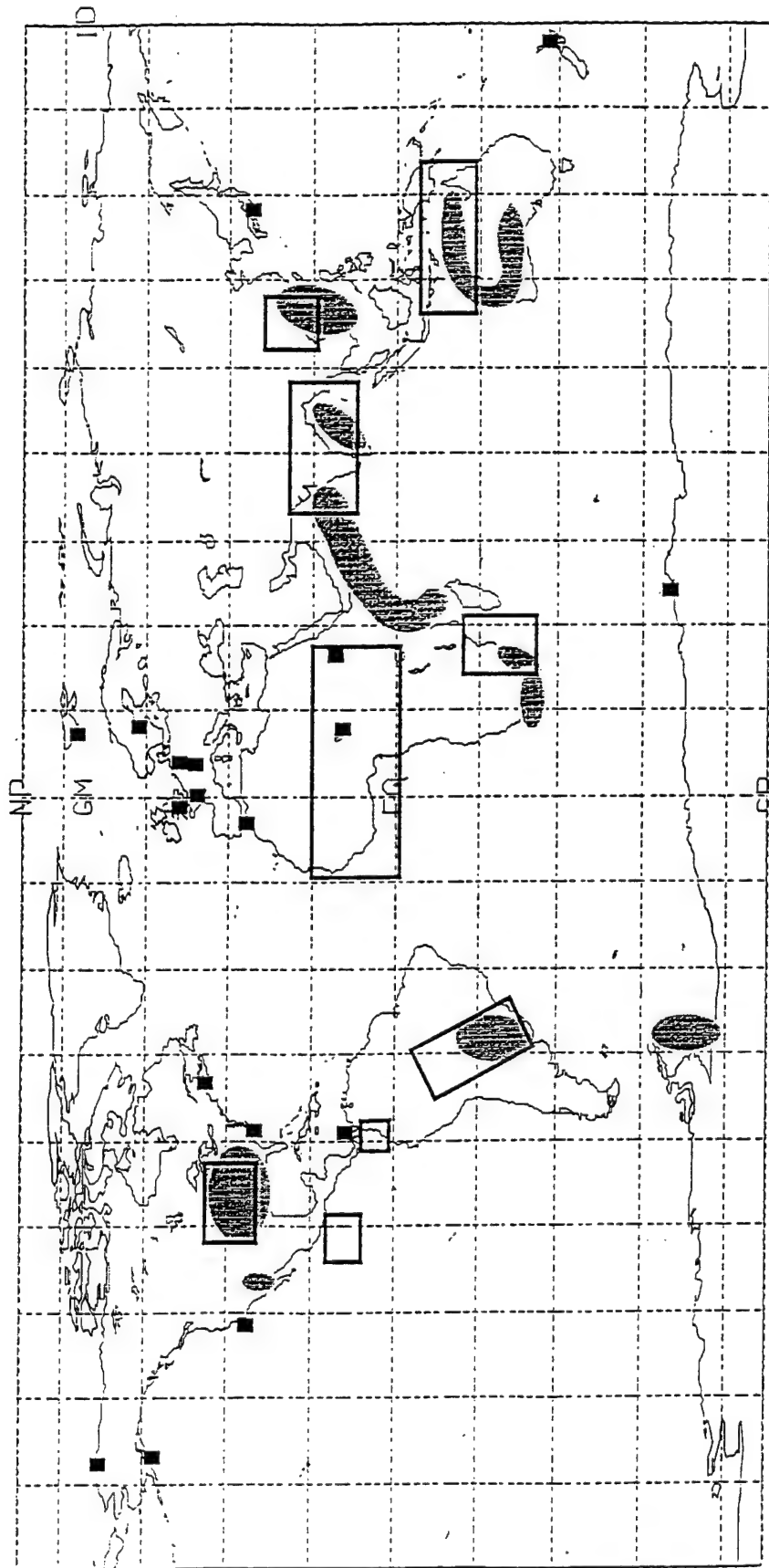


Figure 1.1. Regions where low-level jets are known to occur with some regularity (shaded and squares) and where mesoscale convective complexes occur (open boxes).

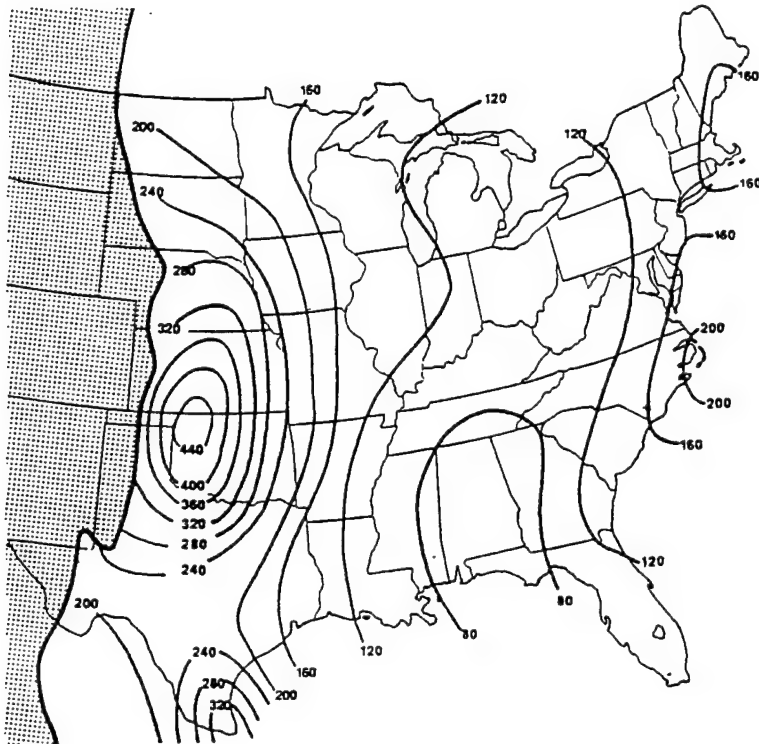


Figure 1.2. Number of low-level jets observations from Jan. 1959 to Dec 1960 (from Bonner, 1968).

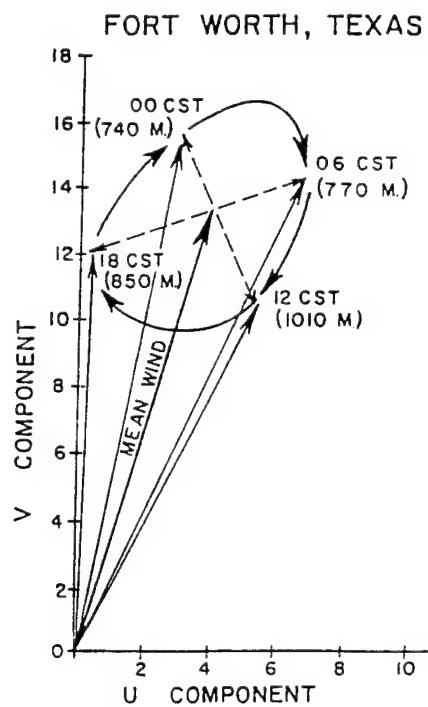


Figure 1.3. Vector mean winds for four daily observations. Wind maxima altitudes, in parentheses, are in meters AGL.

the Great Plains. Arritt *et al.* (1997) found a sharp reduction in the availability of good quality wind data after sunset, an increase after sunrise, and a significant reduction in usable data during the spring and the fall season, consistent with the signature of contamination by migratory birds.

The frequency of LLJs is highest in the summer months. A maximum in the months of August and September accounts for roughly one half of the jets. The reasons for this will be touched on later.

A diurnal response is also associated with the LLJ. This response is more pronounced during the warm season. The greater number of LLJs occur in the night; hence the name “nocturnal low-level jet.” This paper will further discuss these nighttime jets. The work of Mitchell *et al.* (1995) uses the wind profiler network to observe the diurnal frequency of the LLJ. Using hourly observations, they discovered the LLJ jet occurs the most often around 0100 to 0400 local time, with a noticeable decrease in number between 0400 and 0700 local time. Maddox (1985) found the LLJ evolved differently during the night in different air masses, with the LLJ attaining its maximum wind speed earlier within a dry air mass than within a moist air mass. These results indicate the conventional rawinsonde network is especially likely to miss the greater number of jets.

The duration of the Great Plains nocturnal LLJ, according to Mitchell *et al.* (1995), was about 4 hours. For stronger jets, whose criteria will be reviewed below, the duration decreased to about 2 hours. These stronger LLJs are found near the center of highest number of LLJs (see Fig. 1.2)

The elevation of the LLJ varies with each study in the literature. This variation is due, in part, to the requirements imposed (discussed below) on the jet before the average elevation is determined. The variation is also due in part to the observational system involved in the research. If the main requirement for the LLJ is to have a supergeostrophic wind, then the average elevation determined by Mitchell *et al.* is around 1000 m above ground level (AGL). Whiteman *et al.* (1997) using a specialized radiosonde for measuring at low levels (winds could be read at 60 m AGL) found LLJ elevations to be between the

300-600 m range. Jets occur as low as 200 m. These jets typically start at low elevations and increase in elevation as the night progresses, like the stable boundary layer height. These jets usually are above the nocturnal inversion. The lowest measurement height of the wind profilers used by Mitchell *et al.*, however, is 500 m AGL. Though the number of jets below 500 m and their influence on the average elevation is unknown, clearly an upper elevation of 2000 m can be imposed. The higher elevation jets can be attributed to large scale synoptic patterns, which will be discussed later.

The horizontal structure as discovered by Bonner (1968) and Mitchell *et al.* (1995) is described as roughly hundreds of meters wide by thousands of meters long. This corresponds to a sheet-like form, unlike the upper-level jet stream which maintain a more ribbon-like form. The thickness of the LLJ depends on the criterion given to the jet. For our purposes, however, we will set the thickness criterion at 100 m.

The speed criterion as given by Bonner (1968) establishes four different classes. Criterion 0 is defined as all wind maxima without regard to speed within the first 1500 m above the ground. Criterion 1 is the maximum wind speed exceeds  $12 \text{ m s}^{-1}$  and must decrease by at least  $6 \text{ m s}^{-1}$  to the next higher minimum or to the 3000 m level, whichever is lower. Criterion 2 is the maximum winds must exceed  $16 \text{ m s}^{-1}$  and must decrease by at least  $8 \text{ m s}^{-1}$  to the next higher minimum or to the 3000 m level, whichever is lower. Criterion 3 is the maximum winds must exceed  $20 \text{ m s}^{-1}$  and must decrease by at least  $10 \text{ m s}^{-1}$  to the next higher minimum or to the 3000 m level, whichever is lower. Criterion 3 winds are not uncommon during the summer months, as shown by Bonner.

According to Mitchell *et al.* (1995), weaker LLJs (criteria 0 and 1) were most common to the south of the area of maximum occurrence as found by Bonner (1968). For stronger jets (criteria 2 and 3) the maximum area extended farther north and east from the maximum center. This supports the hypothesis that strong LLJs develop because air parcels accelerate as they travel with the LLJ as opposed to strong LLJs being formed in situ.

The LLJs mean wind direction in the Great Plains is south to southwest. Mitchell *et al.* (1995) reported that about 25% of the summertime jets did occur from the north.

Northerly jets are usually associated with the passage of cold fronts. They will not be further considered here due to the lack of literature addressing this special LLJ. Throughout the literature, the wind direction has shown a rotation about the mean wind, as displayed by Bonner (1968), Fig. 1.3. This oscillation will be explained below.

It is important to investigate the forcing mechanisms for LLJs, so that the dynamics can be understood. A fundamental forcing mechanism was put forth by Blackadar (1957). He hypothesized a diurnal variance in eddy viscosity leads to LLJ formation. During the day, the mixed layer, and the associated friction, keep the boundary layer winds at subgeostrophic speeds. Once the evening begins, the friction decreases significantly, producing an imbalance between the pressure gradient and Coriolis forces. This starts an inertial oscillation of the wind in a clockwise direction (in the Northern Hemisphere) with a period of

$$P = \frac{2\pi}{f} = \frac{\pi}{\Omega \sin \phi}. \quad (1)$$

The period,  $P$  is a function of planetary angular rotation,  $\Omega$  and the latitude,  $\phi$ . At midlatitudes, this oscillation has a period of one-half pendulum day, nearly 17 hours, or about 8 hours after sunset. This corresponds well with the wind maximum observed as discussed previously.

Another forcing mechanism of LLJ formation is baroclinicity. Sharp horizontal differences in heating in the boundary layer can produce strong baroclinicity. This region can produce jets with strong mass forcing. Savijarvi (1991) shows the modeled initial motions of the upslope and downslope winds (Fig. 1.4) during baroclinicity events. In his study, Savijarvi applied realistic surface heating and had no geostrophic winds included. This way, the winds would be induced only by the thermal gradient along the slope of the terrain. McNider and Pielke (1981) show a similar model of a case where the geostrophic winds are included (Fig. 1.5). Notice now the winds do form a LLJ. These LLJs can occur at all times of the day (Mizzi and Pielke 1984). As observed over the Great Plains, the geostrophic wind can come from the south, and warmer temperatures exist to the west.

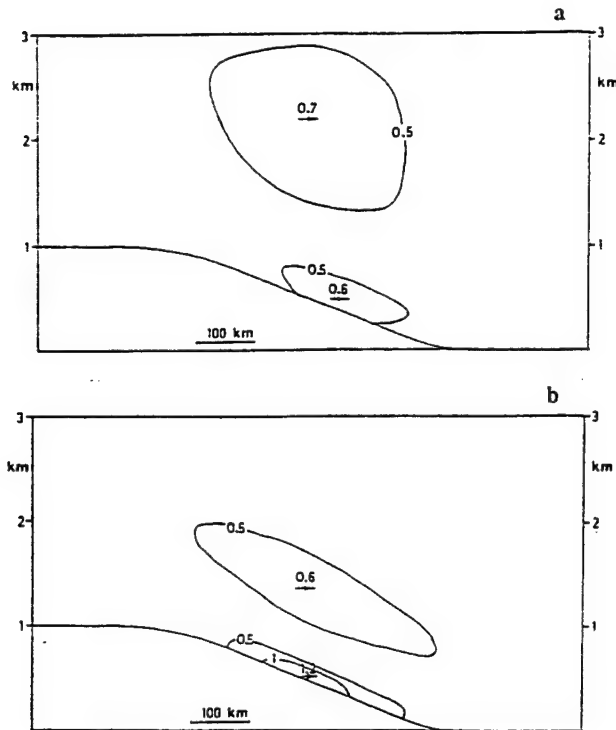


Figure 1.4. (a) Upslope wind (m/s) from model.  
(b) Downslope wind (m/s) from model (from Savijarvi, 1991).

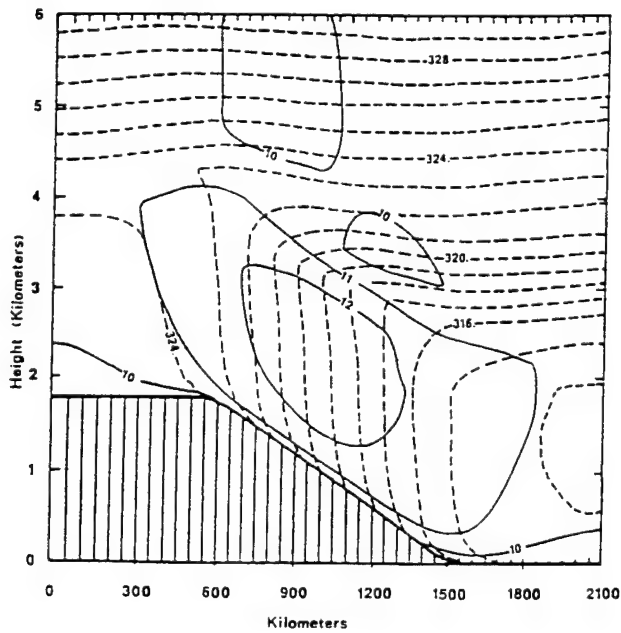


Figure 1.5. V-component (solid, m/s) and potential temperature (dashed, K) contours showing development of a low-level jet.



These conditions occur on a rising slope heading westward. McNider and Pielke (1981) found as the slope increases, the magnitude of the LLJ also increases. Fast and McCorcle (1990) showed a near linear response to slope and speed. For stronger LLJs, the growth of the nocturnal mesoscale pressure gradient is due to the heating of the sloping terrain during the day.

An early attempt to explain LLJ forcing was put forth by Wexler (1961). He described the terrain features that affect the LLJ. He showed how the Bermuda High and the Rocky Mountains together formed a favorable region for the LLJ (Fig 1.6). Through the conservation of potential vorticity, Wexler could explain the acceleration of parcels as they move northward. Though this mechanism shows a way for the LLJ to occur, it does not explain the observed nighttime maximum.

An important forcing mechanism is a transverse ageostrophic circulation associated with the exit region of an upper-level jet streak. This was discussed in the scientific literature starting in the late 1960's. The lower ageostrophic component (return branch circulation) accompanying this circulation can be labeled a LLJ. This characterization is a reason for a LLJ elevation of up to 2000 m, and for larger vertical thicknesses of the jet. This circulation is not due solely to boundary layer processes. Isallobaric forcing of the LLJ is due to the synoptic mass adjustments. When the exit region of the upper-level jet is over the Great Plains, the nocturnal LLJ will almost certainly occur at heights well above the stable boundary layer. Uccellini and Johnson (1979) document a case where a LLJ develops under this synoptic situation. Their work shows the upper-level jet could enhance an existing LLJ formed by boundary layer processes and vice-versa. Though these ageostrophic jets can occur at any time of the day, Uccellini and Johnson observed maximum winds in the morning. This morning phenomenon will be explored below.

The following reviews some recent work performed on LLJ research. Parish *et al.* (1988) performed a kinematic and dynamical evolution study of the LLJ. They used a Beechcraft Super King Air instrumented aircraft for their research. The aircraft flew over

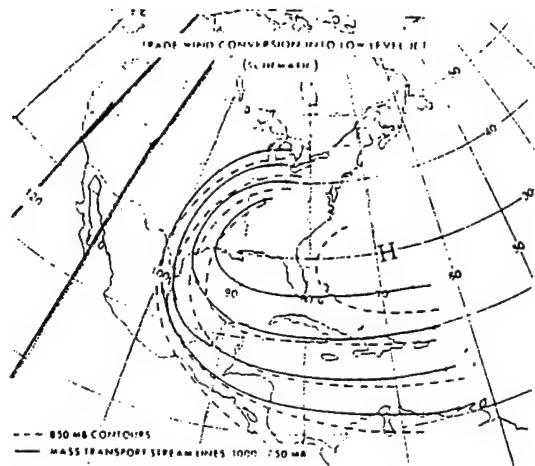


Figure 1.6. Schematic sketch of trade-winds entering the Caribbean Sea and the United States (from Wexler, 1967).

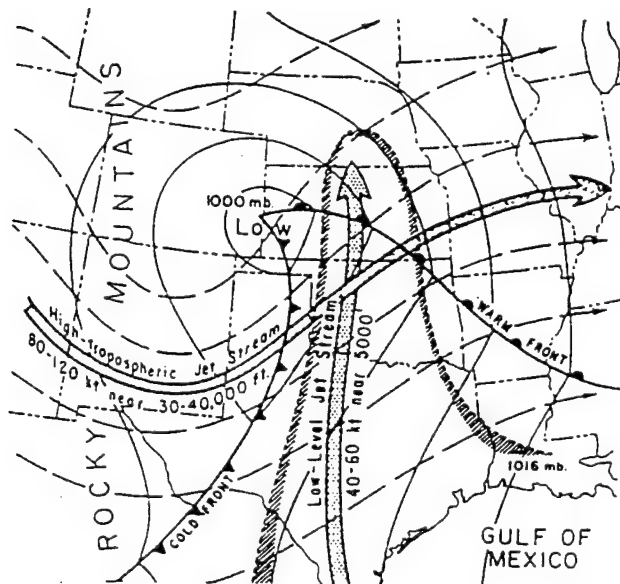


Figure 1.7. Schematic of severe weather outbreak with surface isobars (solid), streamlines of upper-level flow (dashed), and jets (arrows)(from Newton, 1967).

north central Oklahoma at approximately 300 m, 800 m, and 1500 m above ground level. The flights were carried out continuously throughout the night for the month of July 1983.

A case study of the night of 23-24 July was performed. The results of the study compared favorably to the mechanisms proposed by Blackadar (1957) and Wexler (1961). The authors presented the data showing  $u$ ,  $v$ , and  $\theta$  versus  $p$  in the lower atmosphere. A diurnal evolution of the stable boundary layer coincided with the strengthening of the LLJ. Also, the winds did veer while the night progressed, as theorized by Blackadar. The aircraft measured the eddy dissipation rate, which is indicative of frictional changes. This experiment revealed a strong relationship existing between the wind evolution and the changes in turbulent intensity levels. Parish *et al.* (1998) concluded that for this case, the isallobaric components of the wind were secondary to the frictional-decoupling inertial components in forcing the LLJ.

Another study on LLJs was done by Fast and McCorcle (1990). They developed a two-dimensional model which was linked with soil hydrology to determine the sensitivity of the LLJ to perturbations in thermal and frictional forces. The motions over sloped terrain used by the authors can be shown by two equations:

$$\begin{aligned}\frac{\partial u}{\partial t} - fv &= -\frac{1}{\rho_s} \frac{\partial p'}{\partial x} - \frac{gp'}{\rho_s} \frac{\partial Z_T}{\partial x} + \frac{\partial}{\partial z} \left( K_m \frac{\partial u}{\partial z} \right), \\ \frac{\partial v}{\partial t} + fu &= \frac{\partial}{\partial z} \left( K_m \frac{\partial v}{\partial z} \right).\end{aligned}\tag{2}$$

Advection is neglected,  $p'$  is the deviation of air pressure as a function of temperature, and  $K_m$  is the vertical eddy exchange coefficient.  $Z_T$  is the terrain height. The model used was both anelastic and hydrostatic. Turbulence was parameterized as a function of the turbulent kinetic energy,  $\alpha$ , according to

$$\begin{aligned}K_m &= 0.21l\alpha^{1/2}, \\ l &= \left( \frac{1}{l_0} + \frac{\phi(z/L)}{kz} \right)^{-1},\end{aligned}\tag{3}$$

where  $l$  is the mixing length scale,  $z$  the height,  $L$  the Monin-Obukov length, and  $k$  is the von Karman constant. The soil hydrology was also parameterized, according to McCorcle (1988).

Twenty-seven model simulations were shown in their study. The slope, soil moisture, soil type, and latitude were all varied. Their simulations showed the winds increased by  $9 \text{ m s}^{-1}$  from no slope to a slope of .001125 (the average slope of the Great Plains). The jet maximum wind also occurred 400 m higher with the slope. The addition of wet soil increases evaporation, which is important in the surface energy budget. When this is done, the horizontal surface temperature gradients are weakened, which decreases the ageostrophic upslope component. This decrease, in turn, reduces the strength of the LLJ. Fast and McCorcle (1990) found this to be true in their study. They also found the jet maximum to lower in height with the addition of a moist surface. Different soil types were used. They showed clay soils, which take more energy to evaporate water, produced higher LLJ speeds than sand-based soils which readily evaporate. They also found the structure of the jet core varied as the moisture varied along the model domain. Variations in the latitude were performed. The timing of the jet maximum occurred earlier for higher latitudes. This, however, cannot be verified due to the lack of observations of the LLJs variation with latitude.

Chen and Kpaeyeh (1993) reviewed the synoptic conditions when LLJs occur. They took 64 LLJ cases and made composites of the data to find an average. Charts of 200 mb and 850 mb streamfunctions, isotachs, water vapor transport, and divergence were shown. This is a simple way of locating the upper and lower maximum winds and the associated divergence or convergence. The authors concluded from the composites that, "the LLJ is formed during the developing stage of a short baroclinic wave over the lee side of the Rocky Mountains." This conclusion agrees with the work of Uccellini and Johnson (1979). The low-level streamfunction and water vapor transport work performed would also explain the importance of moisture transport during severe weather.

Mitchell *et al.* (1995) and Stensrud (1996) both have used recent technology advances to re-examine the LLJ. Mitchell *et al.* used the Wind Profiler Demonstration Network which consisted of 17 404-MHz radar wind profilers. The profiler network will be discussed further in Section 2.1.2. They viewed the entire Great Plains region for the summers of 1991 and 1992. The authors also included different synoptic situations indicative of LLJs, which will be covered below. Stensrud used a single 915-MHz profiler and incorporated two velocity azimuth displays produced by the WSR-88D. He studied a site in Oklahoma during June 1994. Both studies had their own purpose. Both advantages and disadvantages with the studies can be found. Stensrud argued the operational 404-MHz profiler with a minimum height reading of 500 m AGL is too high to consider all LLJ cases. Mitchell *et al.* addressed this issue by stating the average level of maximum wind was 785 m with a standard deviation of 127 m. The Stensrud case is lacking in temporal and spatial coverage. Overall, however, these recent studies have been very popular in LLJ research.

The following discusses the synoptic situations and their respective forcing mechanisms for LLJ conditions. The Great Plains has a wide variation of weather patterns. No day is ever the same, so putting synoptic situations into classes is a subjective exercise. Mitchell *et al.* (1995) considered five classes of weather shown in Table 1. They did a study of the LLJs found and discovered that Class 1 (see Fig. 1.7) situations were most conducive to LLJ formation. This situation relates closely to the studies of Uccellini and Johnson (1979) and Chen and Kpaeyeh (1993). These jets are not as affected by the boundary layer and can have jet maximum at 1200 m, much higher than the nocturnal inversion. Class 2 and 3 neither suppressed nor promoted the LLJ. The least likely situations were Class 4 and Class 5. The lower occurrences in Class 5 cases (subtropical high) contradict Wexler's (1961) theory. Mitchell *et al.* also studied the class relationship to the speed criteria set up by Bonner (1968). They showed Class 1 LLJs were stronger than the other classes. This suggests LLJ intensity is more of a function of the synoptic situation than the diurnal boundary layer conditions.

**Table 1 Synoptic classification scheme shown in Mitchell *et al.* (1995)**

Class 1	Class 2	Class 3	Class 4	Class 5
Warm sector of an extratropical cyclone.	Ahead of the warm front of an extratropical cyclone with cyclonic curvature of the isobars.	Behind the cold front of an extratropical cyclone, with cyclonic curvature of the isobars.	Under a polar high, with anticyclonic curvature of the isobars.	In the vicinity and west of a subtropical ridge.
Humid in both relative and absolute sense, with little temperature advection. Clear to partly cloudy skies.	Typically low dewpoints but high relative humidity. Cloudy or mostly cloudy skies.	Low dewpoints and cold advection at the surface. Clear to scattered or broken convective clouds.	Low dewpoints but relative humidity may be high. Usually clear, some-times with mid- or high-level clouds	Humid in both relative and absolute senses. Scattered fair weather cumulus during the day, mostly clear at night.

Class 5 LLJs still do occur though. The forcing mechanisms for these relate more closely to Blackadar's (1957), Wexler's (1961) and baroclinicity theory. These LLJs relate closely to the stable boundary layer height. It should be emphasized the forcing mechanisms are not in competition for the formation of LLJs, but they may collectively aid in the development of the LLJ. Bonner and Paegle (1970) showed a combination of the baroclinicity over sloping terrain plus a diurnally varying eddy viscosity yields the best reproduction of the observed wind variation associated with the LLJ over the southern plains of the United States. The synoptic situation should first be looked at to see if LLJ formation is feasible. After this has been determined, different mechanisms should be looked at to see how the LLJ will form, how intense the jet will be, and the elevation of the jet.

Much has been discovered about the low-level jet since the 1950's. A groundbreaking paper about observations of the LLJ was published by Bonner (1968). Mitchell *et al.* (1995) continued to enhance the understanding of the jet formation. Still, though, much can be done to better resolve the LLJ. An observing platform which can measure winds as low as 200 m over an area of the Great Plains with a spacing on the order of 200 km would be needed. A vertical resolution of 25 m would also be ideal. This platform, although not likely to happen any time soon, would better explain the LLJ phenomena. The timing of the

maximum wind, as it corresponds to latitude, is one benefit. Also, the irregular occurrence of the northerly LLJ could be fully explored with a better observing platform.

There is a large amount of literature dedicated to the non-dynamical aspects of the boundary layer and the LLJ. Moisture, land-use, and frictional effects all act to develop and modify the LLJ (Wu and Raman 1997). Parameterization of these effects has been employed, because no model can simply resolve these issues. Improved schemes and information on boundary layer interactions are needed to better model the LLJ. This task is made more difficult when one considers many synoptic situations have different effects on the LLJ. Stensrud (1996) theorized that if a model could simulate the correct timing, placing, and magnitude of the LLJ, then it is likely the boundary layer structure could also be simulated. This would include correct horizontal variation of daytime surface sensible and latent heat fluxes.

As mentioned above, friction plays a prominent role within the PBL and thus affects the LLJ. Arya (1988) defines the PBL *as the layer of a fluid (liquid or gas) in the immediate vicinity of a material surface in which significant exchange of momentum, heat, or mass takes place between the surface and the fluid*. Also, Stull (1988) defines *the boundary layer as that part of the troposphere that is directly influenced by the presence of the earth's surface, and responds to surface forcings with a timescale of about an hour or less*. The force which is due to the earth's surface is friction. For mesoscale flow, which the LLJ event falls under, friction can be divided into different categories. Following Bluestein and Crawford (1997), the frictional force is divided into two parts when the horizontal motion is considered. One is the acceleration due to turbulent horizontal mixing of horizontal momentum called  $\mathbf{F}_H$  in Eq. (4). The other is the acceleration due to turbulent vertical mixing of horizontal momentum called  $\mathbf{F}_Z$  in Eq. (5),

$$\mathbf{F}_H = - \left\{ \left[ \frac{\partial(\overline{u'^2})}{\partial x} + \frac{\partial(\overline{u'v'})}{\partial y} \right] \mathbf{i} + \left[ \frac{\partial(\overline{v'u'})}{\partial x} + \frac{\partial(\overline{v'^2})}{\partial y} \right] \mathbf{j} \right\}, \quad (4)$$

$$\mathbf{F}_z = -\left\{ \left[ \frac{\partial(\overline{u'w'})}{\partial z} \right] \mathbf{i} + \left[ \frac{\partial(\overline{v'w'})}{\partial z} \right] \mathbf{j} \right\}. \quad (5)$$

The primed terms represent eddy values; the overbarred terms represent mean values; and  $\mathbf{i}$  and  $\mathbf{j}$  are the unit vectors directed toward the east and north, respectively. Bell and Bosart (1988) further subdivided the vertical-mixing term into barotropic and baroclinic parts. The stress called surface drag ( $\mathbf{F}_D$ ) is a portion of the barotropic part in the vertical-mixing term. The remaining portion and the baroclinic part is represented by the stress associated with the vertical divergence of the vertical gradient of the horizontal velocity ( $\mathbf{F}_A$ ). Thus  $\mathbf{F}_z = \mathbf{F}_D + \mathbf{F}_A$ . These terms can be parameterized by:

$$\mathbf{F}_D = \frac{1}{Z_i} (-C_D \mathbf{v}^2), \quad (6)$$

$$\mathbf{F}_A = \frac{1}{Z_i} \left( -K \frac{\partial \mathbf{v}}{\partial z} \right). \quad (7)$$

Here,  $Z_i$  is the boundary layer depth.  $Z_i$  is typically given values of 300 m and 1500 m during nocturnal and mixed boundary layers, respectively (Stull 1988).  $C_d$  is the drag coefficient which is on the order of  $10^{-3}$  (Stull 1988).  $\mathbf{v}$  is the anemometer-level wind, and  $K$  is the eddy-transfer coefficient with a value on the order of  $1 \text{ m}^2 \text{ s}^{-1}$  (Stull 1988). If  $Z_i$  is 1500 m and  $\mathbf{v}$  is  $10 \text{ m s}^{-1}$ , then  $\mathbf{F}_D$  equals  $6.66 \times 10^{-5}$ . Also, if  $\partial \mathbf{v} / \partial z$  equals  $10 \text{ m s}^{-1} \div 1500 \text{ m}$ , then  $\mathbf{F}_A$  equals  $4.44 \times 10^{-6}$ . Using these typical values (as suggested above) it can be seen that  $\mathbf{F}_D$  is one order of magnitude larger than  $\mathbf{F}_A$ . For mesoscale flow,  $\mathbf{F}_H$  can be neglected as being too small. Thus, for typical conditions and mesoscale features, friction can be grossly estimated by Eq. (6) within the PBL.

### 1.3 Review of the Divergence Equation

The divergence equation is a powerful equation and contains many terms. Horizontal divergence, the horizontal dot product of the winds, can be qualitatively described as the spreading out of the winds. The opposite of divergence is convergence;



thus, the coming together of the winds. Surface convergence plays a strong role in convection, as does upper-level divergence.

From the horizontal equations of motion in pressure coordinates, the horizontal divergence equation can be obtained. Starting with the u-component:

$$\frac{\partial u}{\partial t} + u \frac{\partial u}{\partial x} + v \frac{\partial u}{\partial y} + \omega \frac{\partial u}{\partial p} - f v = -\frac{\partial \Phi}{\partial x} + F_u, \quad (8)$$

and then the v-component:

$$\frac{\partial v}{\partial t} + u \frac{\partial v}{\partial x} + v \frac{\partial v}{\partial y} + \omega \frac{\partial v}{\partial p} + f u = -\frac{\partial \Phi}{\partial y} + F_v, \quad (9)$$

where  $u$  and  $v$  are the horizontal wind components in the west-east and south-north directions respectively,  $\omega$  is the vertical velocity in pressure coordinates,  $f$  the Coriolis parameter,  $\Phi$  the geopotential, and  $F_u$  and  $F_v$  represent frictional and other subgrid-scale effects in  $x$  and  $y$  direction, respectively. Differentiating (8) with respect to  $x$  and (9) with respect to  $y$ , yields:

$$\begin{aligned} \frac{\partial(8)}{\partial x} &= \frac{\partial^2 u}{\partial x \partial t} + \frac{\partial^2 u}{\partial x^2} + u \frac{\partial^2 u}{\partial x^2} + \frac{\partial v}{\partial x} \frac{\partial u}{\partial y} + v \frac{\partial^2 u}{\partial x \partial y} + \frac{\partial \omega}{\partial x} \frac{\partial u}{\partial p} + \omega \frac{\partial^2 u}{\partial x \partial p} - \frac{\partial f}{\partial x} v - f \frac{\partial v}{\partial x} = -\frac{\partial^2 \Phi}{\partial x^2} + \frac{\partial F_u}{\partial x}, \\ \frac{\partial(9)}{\partial y} &= \frac{\partial^2 v}{\partial y \partial t} + \frac{\partial u}{\partial y} \frac{\partial v}{\partial x} + u \frac{\partial^2 v}{\partial x \partial y} + \frac{\partial^2 v}{\partial y^2} + v \frac{\partial^2 v}{\partial y^2} + \frac{\partial \omega}{\partial y} \frac{\partial v}{\partial p} + \omega \frac{\partial^2 v}{\partial y \partial p} + \frac{\partial f}{\partial y} u + f \frac{\partial u}{\partial y} = -\frac{\partial^2 \Phi}{\partial y^2} + \frac{\partial F_v}{\partial y}. \end{aligned}$$

When the above two equations are added together, the divergence equation is obtained.

Let  $D \equiv \nabla \cdot \mathbf{V}$ ,  $\zeta = \frac{\partial v}{\partial x} - \frac{\partial u}{\partial y}$ ,  $\gamma = \frac{\partial f}{\partial x}$ , and  $\beta = \frac{\partial f}{\partial y}$ , the equation can be reduced to :

$$\underbrace{\frac{\partial D}{\partial t}}_1 + \underbrace{\mathbf{V} \cdot \nabla D}_2 + \underbrace{D^2}_3 + \underbrace{\frac{\partial \omega}{\partial p} D}_4 + \underbrace{\omega \frac{\partial D}{\partial p}}_5 + \underbrace{J(u, v)}_6 - \underbrace{\gamma v}_7 + \underbrace{\beta u}_8 - \underbrace{f \zeta}_9 = -\underbrace{\nabla^2 \Phi}_{10} + \underbrace{\frac{\partial F_u}{\partial x} + \frac{\partial F_v}{\partial y}}_{11}, \quad (10)$$

where  $\nabla \equiv \frac{\partial}{\partial x} \mathbf{i} + \frac{\partial}{\partial y} \mathbf{j}$  and  $J(u, v) \equiv \frac{\partial u}{\partial x} \frac{\partial v}{\partial y} - \frac{\partial v}{\partial x} \frac{\partial u}{\partial y}$ .

Terms 1 and 2 in (10) collectively are the inertial terms, where the former is the tendency of the divergence and the latter is the wind advection of the divergence. Term 3 is the divergence squared term. Term 5 is the vertical advection of the divergence. Term 11 is

the divergence of the frictional stresses. Terms 6 through 10 collectively are called the Balance Equation. In the absence of large divergence tendencies, these terms alone resolve the temporal evolution of divergence (Charney 1955; Bolin 1956; Zack and Kaplan 1987). Term 6 is the Jacobian of the horizontal velocity. Term 7 (8) is the East-West (North-South) Coriolis force change times the North-South (East-West) velocity. Term 9 is the Coriolis force times the horizontal vorticity. Finally term 10 is the Laplacian of the geopotential height.

Surface forcings and upper-level jets result in the divergence usually being largest in the lower and upper troposphere. The largest contributors in the equation are the terms in the balance equation, especially the Laplacian of the geopotential height, during times of small divergence tendency (e.g., a high pressure region). At other times (e.g., a jet, a front, or convection) the full divergence equation must be used. The advection, tendency, and again the Laplacian of the geopotential height terms are often the main terms involved here (Kaplan and Paine 1977).

Using the divergence equation can help atmospheric scientists in many ways. If the incompressible continuity equation is used, the vertical motion can be found. The horizontal divergence is two of the three terms in the incompressible continuity equation. Once the divergence is known, the vertical motion can be solved. This process is known as the kinematic method of solving for the vertical motion.

Once the divergence terms are known, areas of convergence can be found within a mesoscale divergence field. These areas can be strong enough to cause convective precipitation and related stormy weather. This would be useful in short range weather forecasting (Ogura 1975)

With the finer resolution provided with the derivation of the divergence equation, another application would be to use this data in combination with numerical prediction models. The divergence field solved for in a model could be compared with what is calculated from observations and thus used to verify model accuracy. Also, the divergence calculated could be used to initialize the model with data of higher accuracy.

Using the various forms of the divergence equation (not shown) the temperature field can also be derived (Kuo *et al.* 1987). If, for example, the upper atmosphere could be resolved using wind profilers, the temperature could be determined from the divergence equation. This could result in a cheaper (than temperature profilers) and denser network of temperature information. Alternate methods would include vertical temperature sounders (expensive and inaccurate) or the existing RAOB network (too coarse a scale for mesoscale resolution). Another method of producing the temperature field is discussed next.

One very powerful and exciting use of the divergence equation comes to light when the equation is solved for the pressure distribution. If only the component winds and frictional effects are known, Eq. (10) can be used to find the geopotential height field. With this technique, a height field could be determined on a higher spatial and temporal resolution if winds from a wind profiler network were used with the existing RAOB network (Kuo and Anthes 1985; Cram *et al.* 1991). From this newly-retrieved height field, a temperature field could be calculated using the hypsometric equation. This technique will comprise the majority of this study. Its use is important because it will allow a better analysis of the LLJ and a look at modifying techniques for the effects of friction. The following chapter will discuss this application.

## 2. DATA AND ANALYSIS METHODOLOGY

### 2.1 Data

A case study was performed starting at 0000Z on August 15 and ending at 0000Z on 17 August, 1995. This 48 hour period was selected because at least one known low-level jet (LLJ) formed during this period and because it was of interest during the NASA AVOSS experiment. Data was selected over an area covering the entire LLJ and encompassing the entire wind profiler network.

Three types of data are used in order to retrieve the mass field in and above the planetary boundary layer (PBL). They are RAOB, wind profiler, and surface data. All of the data came from the National Center for Atmospheric Research (NCAR) archives. Model data was used for comparison against the derived mass fields. This data was produced by the Mesoscale Modeling Group at North Carolina State University.

In order to take irregularly-spaced wind observations and then solve equations, a standard grid superimposed on a polar stereographic projection must be used. In this way, finite differences can then be solved in a convenient and logical manner. One way to do this is through a simple Barnes (1964) analysis technique. A two-pass Barnes (1973) analysis scheme (Koch *et al.* 1983) was used to take observations and analyze them onto a grid.

The grid consisted of 50 by 45 points in the horizontal (Fig. 2.1) and 17 levels in the vertical. The grid spacing was 58 km in the horizontal. This spacing was picked for three reasons. First, the weaker August jet streaks require more resolution and sensitivity than the stronger features which Cram *et al.* (1991) and Adams (1996) previously studied in similar retrieval techniques. Second, it is twice the resolution interval, and hence an even multiple of the coarsest mesh of the model simulations to be shown later, therefore it will be numerically more compatible with initialization, assimilation, or verification experiments. Third, the PBL features which are germane to this project are very narrow LLJs which are only 100-200 km across, therefore at least five points are necessary to properly resolve the

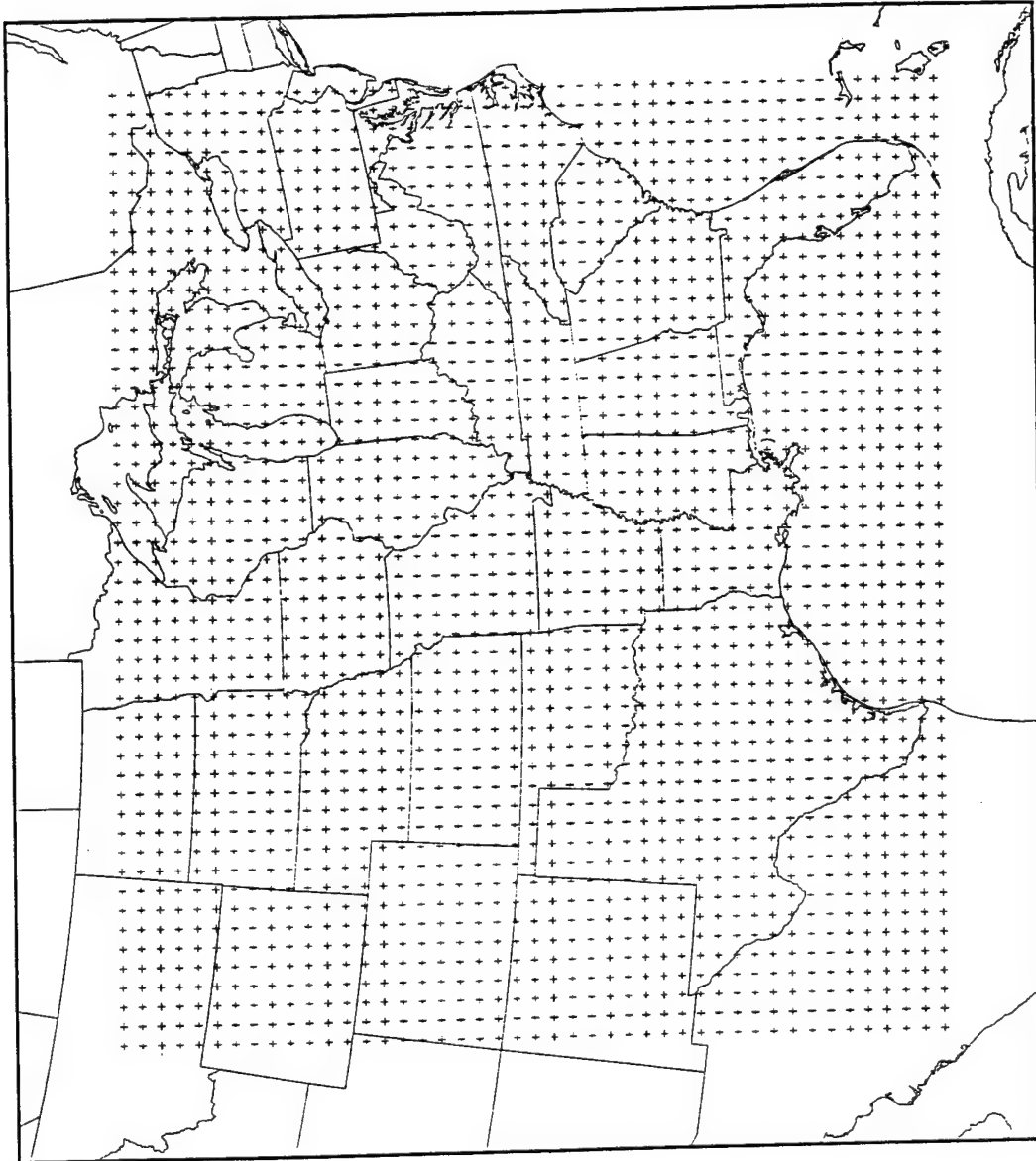


Figure 2.1. The grid used for computations.

wind maximum and minimum. The grid was based on a Polar Stereographic projection true at Tulsa, Oklahoma (36.20° N, 95.90° W).

### **2.1.1 RAOB Data**

The first of three types of data include RAOB observations operated by the National Weather Service. Figure 2.2 shows the location of the stations used for this study. The average grid spacing for the RAOB network is 345 km in this study. Approximately 70 soundings were included within and near the grid domain at each hour. RAOB soundings outside of the domain were used for better data resolution during the Barnes analysis. The vertical levels chosen for the analysis were 850, 800, 750, 700, 650, 600, 550, 500, 450, 400, 350, 300, 250, 200, 150, and 100 mb (sixteen levels). RAOB observations are normally taken every twelve hours. In order to match the temporal resolution of normal wind profiler data, the RAOB data was linearly interpolated to the asynoptic time of every hour.

The RAOB pressure/height and wind information was used for the retrieval of the derived height field. The wind data was used for two purposes. First, the additional set of wind observations will enhance the wind profiler network and thus the spatial resolution. Second, the RAOB wind data could be used as a first guess in the Barnes analysis of the wind profiler wind data. The height data was also used for two purposes. The height information from the RAOBs was used as a first guess in the over-relaxation method in the retrieval of the height field (the final step of the retrieval process will be discussed in Section 2.2.1). The second use of RAOB height data was to aid in the conversion of the profiler data from its discrete height above ground level to pressure levels. That is, the profiler data is available in height above ground level; whereas, the retrieval process solves for the Laplacian of the geopotential height using pressure coordinates. A bilinear interpolation from the four surrounding grid point height values at a given pressure level provided consistent height estimates for each profiler site.

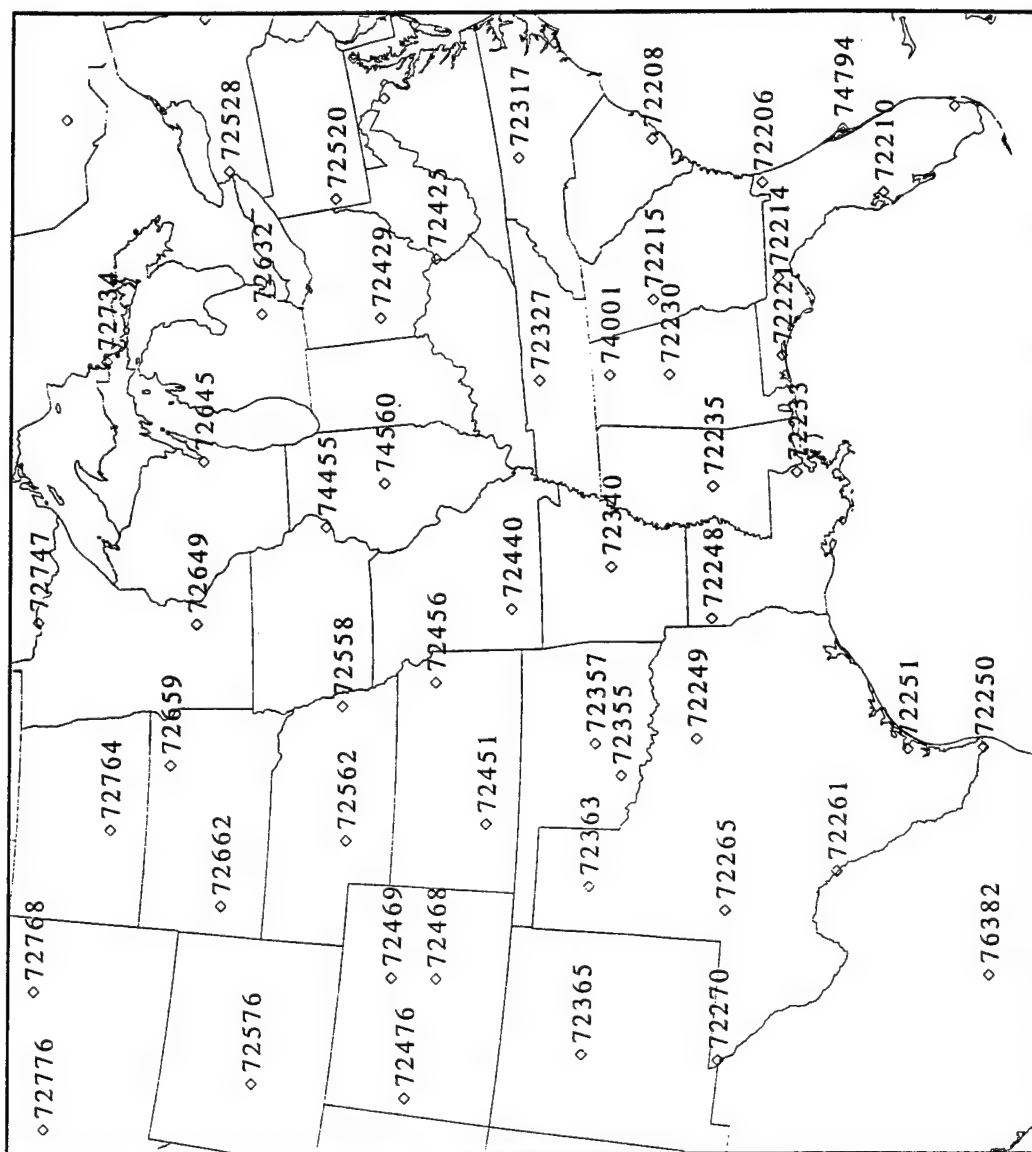


Figure 2.2. RAOB station locations.

### 2.1.2 Profiler Data

The second set of data used is wind profiler data from the National Oceanic and Atmospheric Administration (NOAA) Wind Profiler Network. Figure 2.3 shows the location of the profiler stations. The average grid spacing for the profiler network is 185 km for this study. Table 2 lists the stations and provides information for each station. If the station is used in the retrieval process, then it is indicated in the table. Stations not used were either well outside the grid domain or were not reporting winds during this time.

A wind profiler is basically a Doppler radar with three radial beams pointing in the vertical. The radar detects inhomogeneities of the atmosphere, e.g., aerosols, hydrometeors, cloud droplet, and refractive index gradients. The profiler assumes these fluctuations are advected by the mean wind, thus giving a wind speed. The three radial beams are aligned as shown in Figure 2.4. One is directed toward the vertical, the other two are  $16.3^\circ$  off-vertical to the north and east.

The NOAA profilers have a wavelength of 404MHz and operate in a “low” and “high” mode. Each mode contains 36 gates of which to measure the wind speed (see Fig. 2.5). Note, the two modes overlap each other between 7.5 km and 9.25 km. The wavelength determines the elevations at which the profiler can accurately measure the winds. The vertical resolution of an operational wind profiler is much greater than the operational RAOB. Horizontal wind data is recorded from 500 m to 16.25 km at every 250 m (see Fig. 2.5). Even though the wind profiler data can be read at every six minutes, only every hour is used for the retrieval process. The upper limit is approximate because there might not be enough scattering information for the wind profiler to accurately read the winds at the upper levels. A study by Strauch *et al.* (1987) shows the accuracy of the horizontal wind components measured by these profilers to be within  $\pm 1 \text{ m s}^{-1}$ . Weber and Wuertz (1990) did a similar study. They found the accuracy to be  $\pm 1.3 \text{ m s}^{-1}$  in clear air and  $\pm 2\text{-}4 \text{ m s}^{-1}$  in precipitation. Sources of error occur for three reasons. First, the horizontal homogeneity of the wind field across all beams is assumed even though the three beams do separate further



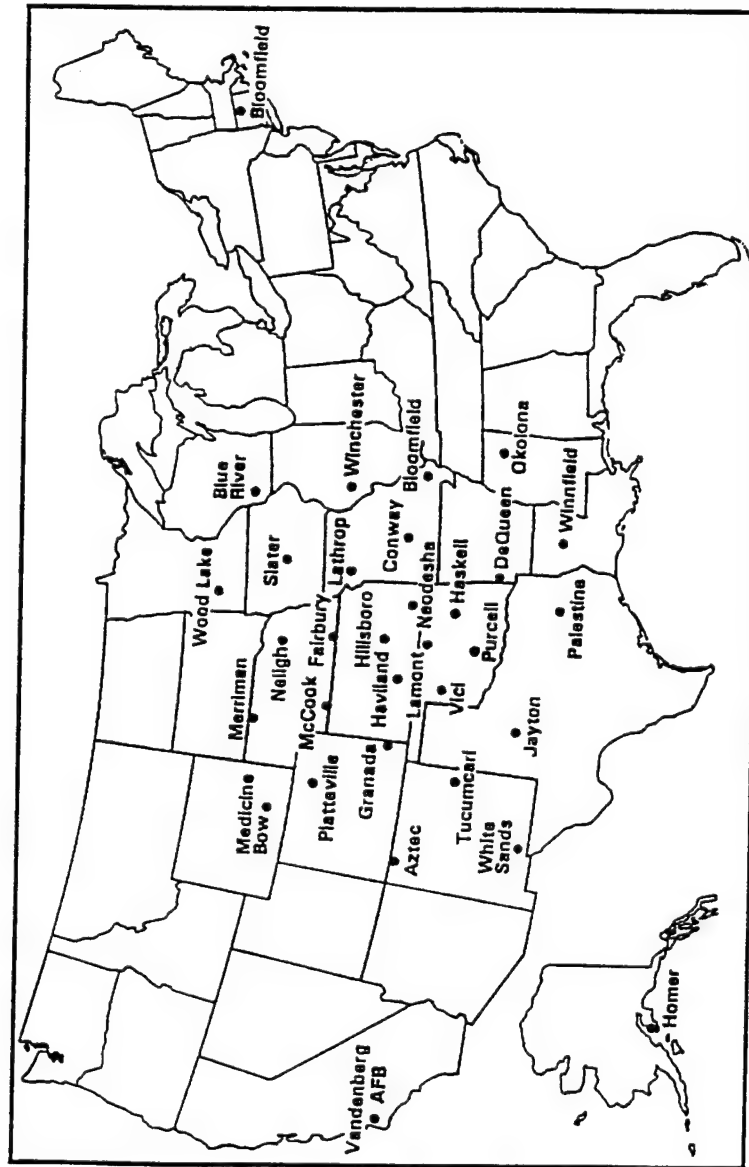


Figure 2.3. Locations of Doppler wind profilers comprising NOAA's Wind Profiler Network.

**Table 2 Stations included in the Wind Profiler Demonstration Network**

Identifier	WMO	Location	Lat(°)	Lon(°)	Elev(m)	Used
AZCN	74630	Aztec, NM	36.84	-107.90	1902	Yes
BLMM	74662	Bloomfield, MO	36.88	-89.97	130	Yes
BLRW	74357	Blue River, WI	43.22	-90.53	226	No
CNWM	74550	Conway, MO	37.52	-92.70	390	Yes
DQUA	74752	DeQueen, AK	34.11	-94.29	195	Yes
FBYN	74440	Fairbury, NE	40.09	-97.34	433	No
GDAC	74530	Granada, CO	37.77	-102.17	1155	Yes
HBRK	74546	Hillsboro, KS	38.30	-97.29	447	Yes
HKLO	74648	Haskell, OK	35.80	-95.78	212	Yes
HMRA	70341	Homer, AK	59.76	-151.17	298	No
HVLK	74541	Haviland, KS	37.65	-99.09	648	Yes
JTNT	74735	Jayton, TX	33.01	-100.98	707	Yes
LMNO	74647	Lamont, OK	36.69	-97.48	306	Yes
LTHM	74551	Lathrop, MO	39.57	-94.18	297	Yes
MBWW	74431	Medicine Bow, WY	41.90	-106.18	1997	Yes
MRRN	74437	Merrion, NE	42.90	-101.69	991	No
NDSK	74542	Neodesha, KS	37.37	-95.63	255	Yes
NLGN	74445	Neligh, NE	42.20	-97.79	524	Yes
OKOM	74769	Okolona, MS	34.08	-88.86	125	Yes
PATT	74750	Paleshine, TX	31.77	-95.71	119	Yes
PLTC	74533	Platteville, CO	40.18	-104.71	1524	Yes
PRCO	74649	Purcell, OK	34.97	-97.51	331	Yes
RWDN	74433	McCook, NE	40.08	-100.65	800	Yes
SLAI	74449	Slater, IA	41.90	-93.74	315	No
TCUN	74731	Tucumcari, NM	35.08	-103.65	1241	No
VBGC	74604	Vandenberg AFB, CA	34.76	-120.53	149	No
VCIO	74640	Vici, OK	36.07	-99.21	648	Yes
WDLM	74341	Wood Lake, MN	44.67	-95.44	319	Yes
WNCL	74556	Winchester, IL	39.65	-90.48	170	No
WNFL	74753	Winnfield, LA	31.89	-92.78	93	Yes
WSMN	74629	White Sands, NM	32.40	-106.34	1224	Yes

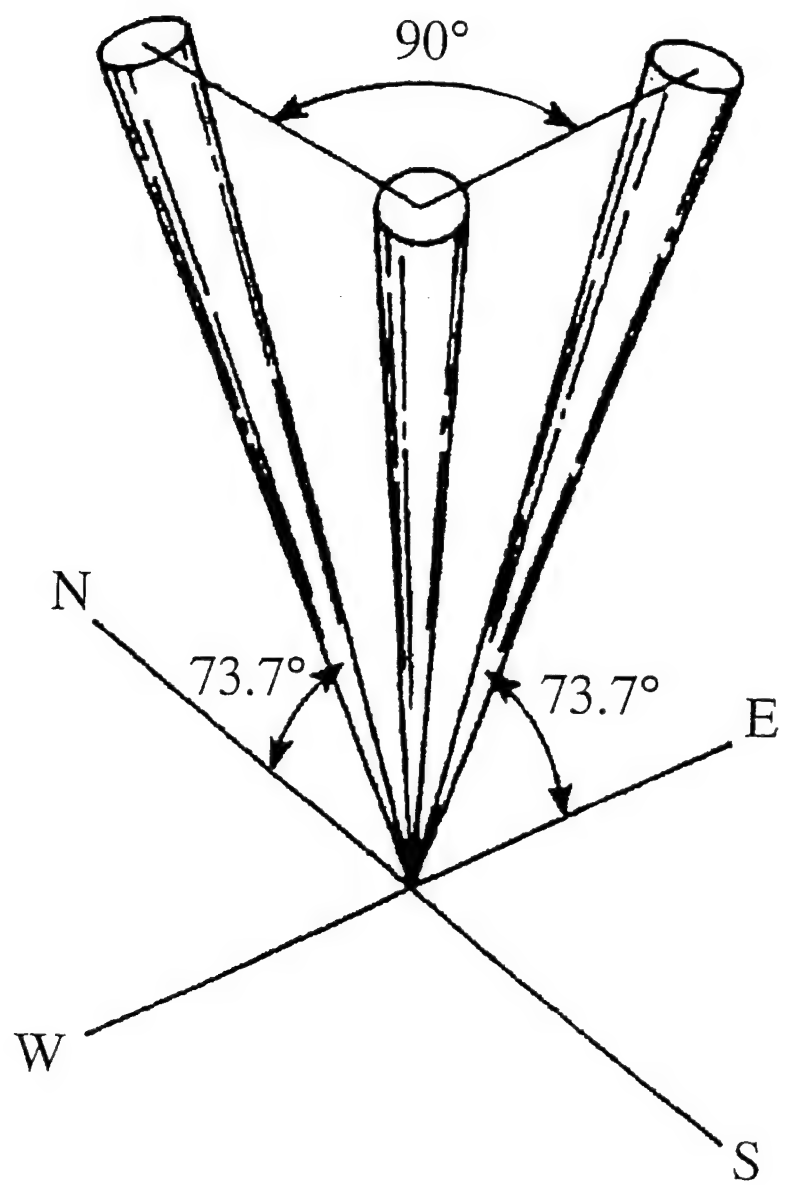


Figure 2.4. Schematic depicting the three beams of a NOAA wind profiler.

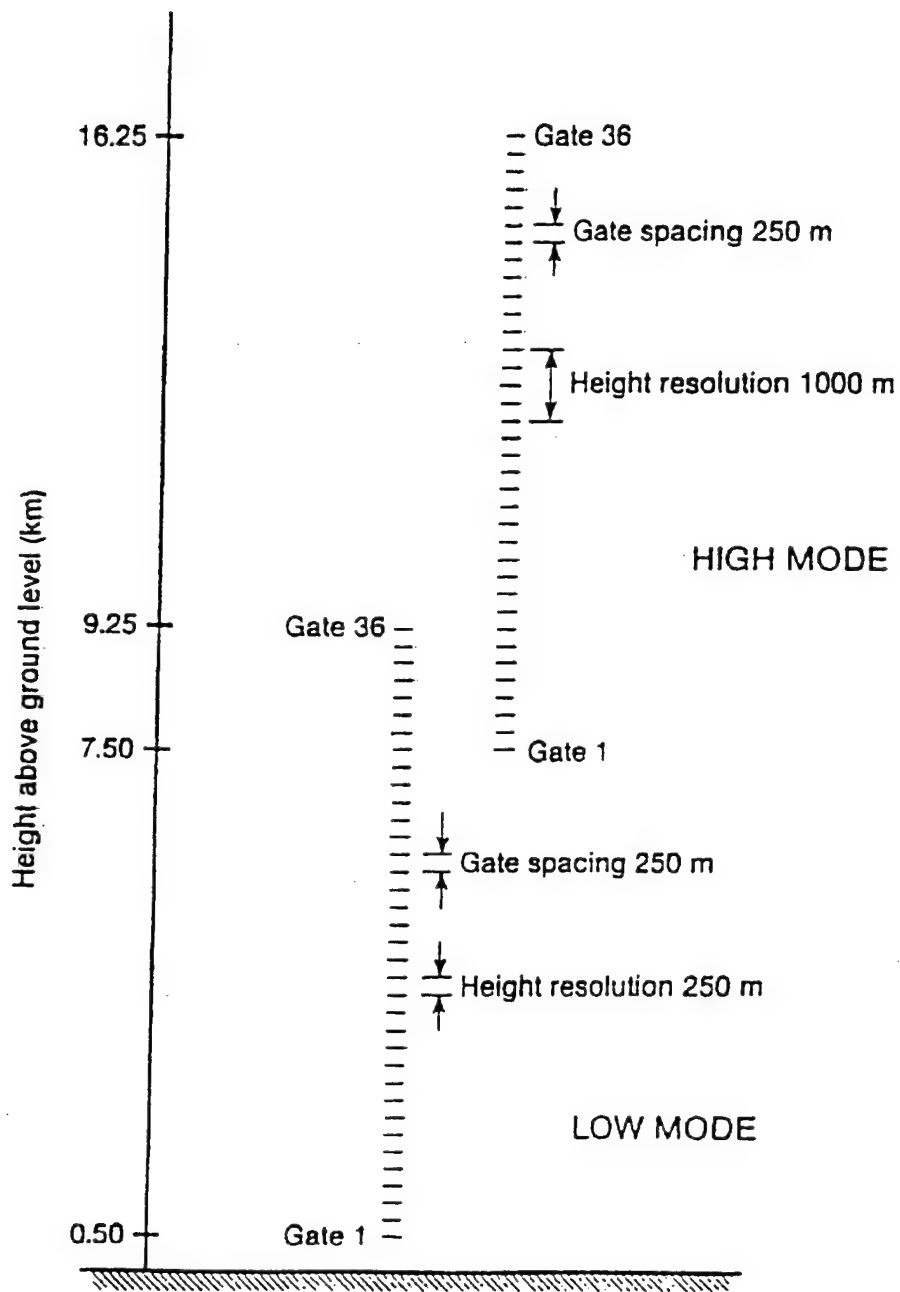


Figure 2.5. Schematic of the 36 gates in both low and high mode. Note the overlap of coverage from 7.5 to 9.25 km AGL.

apart away from the ground. Second, the inhomogeneities are assumed to advect with the mean wind. Third, as seen above, precipitation can decrease the accuracy of the measurement. The first two reasons are not a big concern here because the 6 minute winds are averaged for one hour. Table 3 lists the technical attributes of the NOAA Doppler wind profilers.

**Table 3 Technical information on the NOAA Wind Profilers**

Operating Frequency		404.37 MHz
Wavelength		74 cm
Peak Power		1500 W
Nyquist Velocities:	Low mode vertical beam	$\pm 12.6 \text{ m s}^{-1}$
	High mode vertical beam	$\pm 12.5 \text{ m s}^{-1}$
	Low mode oblique beams	$\pm 15.6 \text{ m s}^{-1}$
	High mode oblique beams	$\pm 23.3 \text{ m s}^{-1}$
Low Mode Height Range		0.5 - 9.25 km
High Mode Height Range		7.5 - 16.25 km
Gate Spacing		250 m
Range Resolutions:	Low mode	350 m
	High mode	1000 m
Pulse repetition Periods:	Low mode	100 $\mu\text{s}$
	High mode	150 $\mu\text{s}$
Complete Volume Scan Period		6 min

Only the horizontal winds produced by the wind profilers are used. Thus, the tainting of the vertical wind speed component during precipitation is not a factor. As discussed above, the wind profiler data must first be converted from a height above ground level to pressure level information. Then, a vertical linear interpolation of the wind data was performed to extract the appropriate horizontal wind components for the given pressure level. Then the data is analyzed to the grid using the RAOB wind data as a first guess in the Barnes scheme. The final gridded profiler wind data is used for many processes in the retrieval technique. They will be discussed in Section 2.2.1.

### 2.1.3 Surface Data

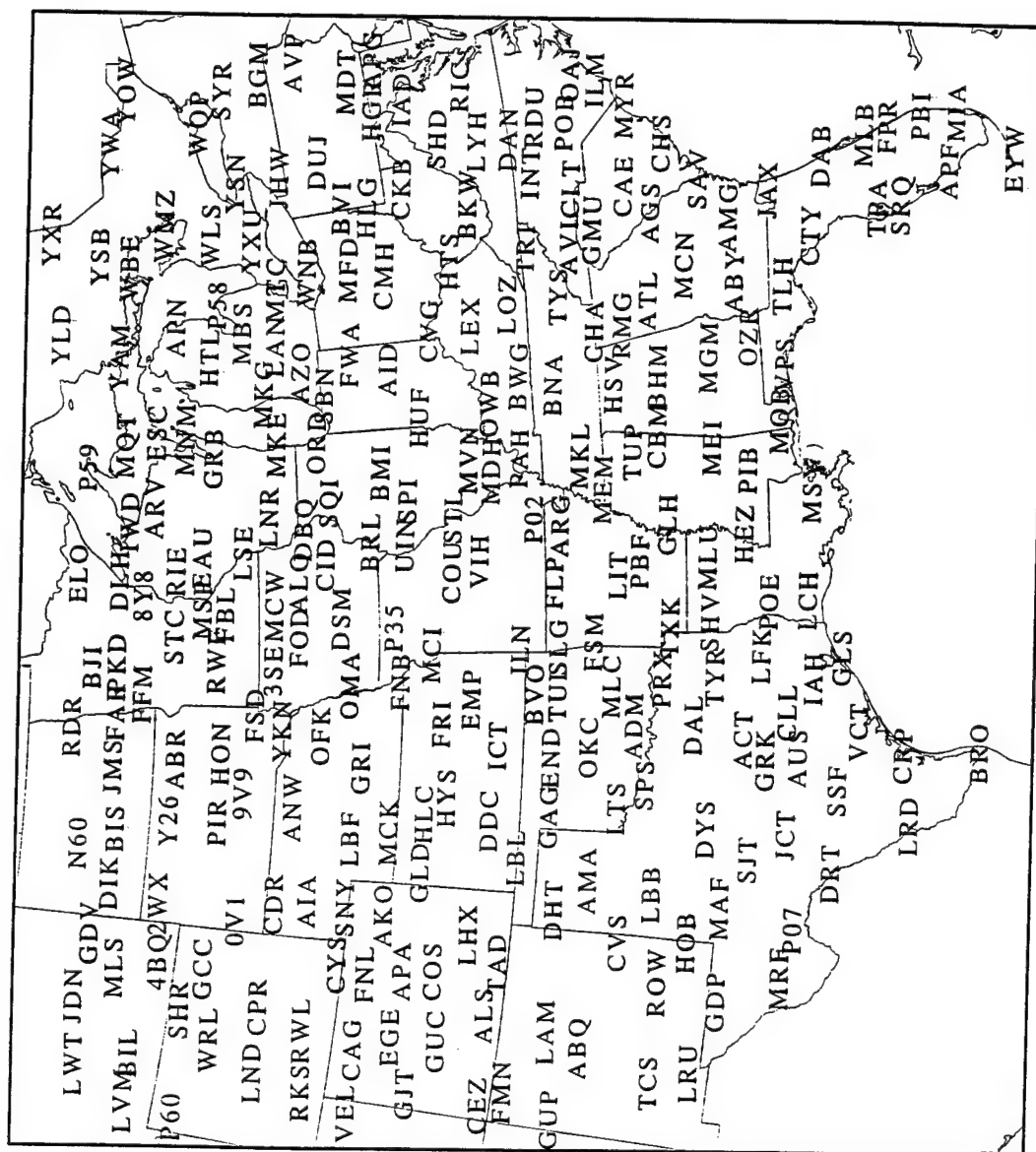
The third and final set of observational data used in the retrieval process is surface data. Approximately 500 observations were included within the grid domain each hour. Figure 2.6 shows the location of most of the stations used for this study. Hourly surface winds and pressures were utilized to derive a 900 mb wind level, the seventeenth level. Since 900 mb is not a mandatory reporting level in normal operational RAOB data, the wind level had to be created.

The reason for this is for frictional concerns. Often the planetary boundary layer, and thus enhanced friction, is located within the 900 mb region. This is particularly true in the Great Plains region. Here, the surface elevation above sea level can be found to be around 400 m. The 900 mb average height (MSL) can be found to be around 1000 m. The difference (1000 m-400 m) is 600 m (MSL) which is an acceptable depth of the PBL during the day. The western part of the grid (Fig. 2.1) contains surface elevations which will even contain nocturnal boundary layers at the 900 mb level. Since friction is a term in the divergence equation, the retrieval process includes this level to study the effects of friction upon the equation.

The 900 mb wind level created uses the hourly surface data and the generated wind profiler data at 850 mb. The winds are logarithmically interpolated between the surface and 850 mb using the following weighted equation:

$$V_{900} = \left( \frac{\log 900 - \log 850}{\log P_s - \log 850} \right) V_s + \left( \frac{\log P_s - \log 900}{\log P_s - \log 850} \right) V_{850}, \quad (11)$$

where  $V_{900}$  is the velocity at 900 mb,  $P_s$  the surface pressure,  $V_s$  the velocity at the surface, and  $V_{850}$  the velocity at 850 mb. This is done for both the  $u$  and  $v$  horizontal wind components. If the surface pressure is within 1 mb of 900 mb, the surface wind is used for the newly derived 900 mb wind level. After this, the raw profiler data at 900 mb is analyzed into the 900 mb level using the Barnes analysis. Approximately a third of the profilers (Fig.2.3) could not provide wind information at 900 mb. This is because those profiler stations has surface elevations plus their 500 m first gate above 900 mb (roughly, 1000 m).



Of course, these profilers are located in the northern and western parts of the profiler network where the Great Plains meets the elevations of the Rocky Mountains. On the extreme edge of the profiler network stations like Aztec (AZCN), Platteville (PLTC), and Medicine Bow (MBWW) does not report wind data until 800 mb.

#### **2.1.4 Model Data**

As mentioned above, in order to compare and verify the mass retrieval technique, a numerical model was employed. The modeling experiments were run using the Mesoscale Atmospheric Simulation System (MASS) model version 5.9 (MESO 1995). The model was initialized at 0000Z 15 August, 1995 and run for 24 h. The model was again initialized at 0000Z 16 August, 1995 and run for 12 h. The horizontal grid consisted of 120 by 100 points with a grid spacing of 29 km. The vertical resolution consisted of 50  $\sigma$  surfaces with approximately  $\frac{1}{2}$  of the model's  $\sigma$  levels located between the surface and 850 mb. A summary of the MASS model is found in Table 4.

### **2.2 Mass Retrieval**

#### **2.2.1 Retrieval Technique**

The data processing has created  $u$  and  $v$  horizontal wind components for 17 levels within the grid. This will allow for the calculation of divergence, vorticity, and omega for each level. The divergence, used in terms 1 through 5 of Eq. (10) is calculated first. Then the vorticity, used in term 9, is derived. Finally omega, used in terms 4 and 5, is solved by applying the kinematic method as described in Section 1.3. Omega was assumed to be zero for the lowest and highest levels. The method for finding omega to minimize the calculated error was O'Brien's (1970) adjustment technique. This method minimizes the accumulation of errors as divergence is vertically integrated to the top of the domain (i.e., 100 mb).

Calculation of the Coriolis force uses latitude information within the grid. The Coriolis force is used in terms 7, 8, and 9. The first two terms involve the horizontal change



**Table 4 Specification for MASS Model version 5.9**

Numerics

- Hydrostatic primitive equation model
- 3-D primitive equations for  $u$ ,  $v$ ,  $T$ ,  $q$ , and  $p$
- Vertical resolution consists of 50 sigma levels
- 29 km grid spacing with 120 by 100 grid points
- Rigid lid upper domain
- Terrain following sigma-p coordinate system
- Fourth-order accurate horizontal spatial differencing
- 15 sec. short time step gravity wave mode
  - Forward-backward scheme
- 30 sec. long time step slow advective mode
  - Split-explicit time marching integration employing Adams-Bashforth scheme

Initialization Scheme

- First Guess provided by NMC/NCAR Reanalysis gridded data set
  - $2.5^\circ \times 2.5^\circ$  lat/lon global grid
  - 17 vertical pressure levels
- Reanalysis using 3-D OI scheme (Daley 1991)
- High resolution average terrain using one pass 9-point smoother
- Enhanced moisture analysis through synthetic RH retrieval scheme
- Weekly average  $1^\circ \times 1^\circ$  lat/lon SST data
- Anderson Level II land use classification scheme (Anderson *et al.* 1976)
- Climatological subsoil moisture database
- Normalized Difference Vegetation Index (NDVI)

PBL Specification

- TKE high resolution PBL scheme
- Surface energy budget based upon Noilhan and Planton scheme (1989)
- Soil hydrology based upon Marht and Pan scheme (1984)

Moisture Physics

- Grid scale prognostic equations for cloud water and ice, rain water, and snow
- Sub-grid scale Kuo-MESO convective parameterization scheme

in the Coriolis force times the horizontal velocity. The last term, term 9, is the product of the relative vorticity and the Coriolis force. The mesoscale domain of the grid is large enough to include a significant variation of the Coriolis force terms. If neglected, a proper balance could not be obtained. That is, the retrieved height would have considerable error.

All of the terms in Eq. (10) involve differentials in their calculations. The horizontal, vertical, and time differentials all included first-order central differencing schemes in their calculations. Since this retrieval technique is a diagnostic tool rather than a prognostic one, central differencing is done on the time differential. The time difference is one hour or 3,600 seconds. This amount of time coincides with the rate of smoothed wind profiler data availability. The vertical space difference is 50 mb to coincide with the vertical spacing of the wind levels discussed above. The horizontal space difference of 58 km was set to the grid spacing predetermined when the data was put into a grid using a Barnes analysis, as mentioned above.

Two other factors must be considered before the terms are solved for term 10. One, a map factor is included in Eq. (10) (not shown). The map scale factor is included in all horizontal space differentials. This is done because all calculations are done assuming a flat grid, not a realistic curved one. Two, friction must be considered, especially within the PBL. Frictional parameterizations are discussed in the next section.

Finally the Laplacian of the geopotential height is solved. Again, the map factor is included in this calculation. In order to solve this Laplacian, a relaxation method was used in the retrieval process. For this retrieval process, a Liebmann over-relaxation method (Haltiner and Williams 1980) was adopted. The over-relaxation method requires a minimum threshold of error in order to call the Laplacian "relaxed". A threshold of 1 m was determined to be an acceptable error. Additional information, a boundary condition, is needed for the relaxation method. A Dirichlet type boundary condition, which requires an independent height specification along the lateral boundary, is utilized. The independent height information is taken from the hourly interpolated RAOB height data.

With the retrieved geopotential height field now solved for, the temperature field can be solved by the hypsometric equation which assumes a hydrostatic balance,

$$\Phi(z_u) - \Phi(z_l) = R \int_{P_u}^{P_l} T d \ln P = R \bar{T}_v \ln \frac{P_l}{P_u}, \quad (12)$$

with the subscripts  $u$  and  $l$  representing the upper and lower boundaries, respectively,  $R$  the dry air gas constant, and  $\bar{T}_v$  the mean virtual temperature within the layer.

### 2.2.2 Friction Parameterization

Section 1.3 discussed how friction plays a role in the PBL. Eq. (10) has a frictional divergence term which must be considered when solving the equation within the PBL. This section looks at how the term is computed. Two methods were employed for finding the frictional stresses. They are the use of Rayleigh friction and the use of the drag coefficient.

Rayleigh friction is a simple way of computing the viscous drag on a fluid. It is based on the speed of the fluid. That is, if the fluid is moving faster, the drag is higher. The drag in the horizontal can be expressed as  $F_u = -v u$  and  $F_v = -v v$ . Where  $v$  is a coefficient describing the viscosity of the fluid. The negative sign states the friction is opposing the velocity. The PBL structure is such that  $v$  varies inside the layer. It is strongest at the surface and reaches a value close to zero at the top of the PBL. To account for this, a Gaussian relationship is used to describe the variation in  $v$ . The relationship can be described as,

$$v = v_0 \exp \left\{ - \left( \frac{z - z_0}{H} \right)^2 \right\}, \quad (13)$$

where  $v_0$  is the initial value of  $v$ .  $H$  is the height of the PBL.  $Z_0$  is the height of the surface, and  $Z$  is the geopotential height computed for in the divergence equation. On the ground (i.e.,  $Z = Z_0$ ),  $v = v_0$ .

The value used for  $v_0$  was  $1 \times 10^{-5}$ . The value of  $H$  was varied for mixed and nocturnal PBLs. The daytime case used a value of  $H=1000$  m. The nocturnal case used  $H=600$  m. The times used to determine if the PBL was mixed or stable was based on the MASS model output. This model was discussed in Section 2.1.4. A coarse mesh simulation was performed to determine the height and characteristics of the PBL. The value of  $Z_0$  was also varied. For the first 20 grid points (out of 50) in the East-West direction, the value was  $Z_0=1000$  m. For the remainder of the grid points, the eastern portion, the value was  $Z_0=0$  m.

Once the value of  $v$  is determined, it is then multiplied by the wind speed at that layer (e.g., 900 mb). This gives us values of  $F_u$  and  $F_v$  at all of the grid points. Finally, to compute Term 11 of Eq. (10), the divergence of these values is taken.

This method affords some benefits. For one, the computation is quite simple. Only programming the PBL height differences and the variation of the surface height could pose problems. Though these approximations are not the most accurate, the results are not hindered as will be seen later. Another benefit has to do with the PBL height. On the western edge of the grid, PBL heights will be located within higher layers of the retrieval technique. That is, the 800 mb layer, for example, might contain the nocturnal PBL in the western part of the grid, but definitely not in the eastern part of the grid where the surface elevations are much lower. The Gaussian relationship helps account for this variation in a smooth manner.

The other method employed to compute the frictional stresses within the PBL was done by parameterizing the frictional drag within the PBL. This drag coefficient method was touched on at the end of Section 1.2. Here, Eq. (6) is used to compute the amount of friction involved in the divergence equation. A brief look at the Rayleigh friction method shows the two methods are closely related. Here, however, the drag coefficient,  $C_d$ , will vary according to the theory discussed in Stull (1988).  $C_d$  was given a value of  $1.3 \times 10^{-3}$  for the nocturnal PBL period and values ranging from  $1.8 \times 10^{-3}$  to  $10 \times 10^{-3}$  during the mixed PBL times. The mixed PBL value of  $C_d$  was varied to see how much of an effect, if any, there would be on the retrieval process. The values of  $Z_i$ , the boundary layer depth, were 300 m

for the nocturnal times and ranged from 750 m to 1500 m during the mixed layer periods. The value of  $Z_i$  was also varied to see how much of an effect there would be on the retrieval process.

As with the last method, the PBL depth was determined by the MASS model output as a first guess. The drag coefficient method discreetly determined the layers involved in the PBL. The prior method divided the ground elevations into two sections. This method divided the grid into three parts. The western part included higher levels (700 mb during the day - 850 mb during the night) where friction would be a concern. The middle part included fewer layers of concern (750 mb during the day - 900 mb during the night). The eastern part of the grid only included mixed layer frictional processes (up to 800 mb) due to its lower surface elevations. Thus, the layers mentioned above all had the drag coefficient calculated for using Eq. (6). The wind velocity here is the surface wind speed. This frictional stress was calculated for the horizontal wind velocity components (i.e.,  $u$  and  $v$ ). Once this was done the divergence of the drag terms was computed just like in the Rayleigh friction method.

The drag coefficient method offers an advantage. Fundamentally, it is more theoretically sound. The theory, as discussed in Section 1.2, was applied in this second method. When variations to the constants are made (e.g.,  $C_d$  or  $Z_i$ ) the reasons why these changes are made can be understood. An increase in  $C_d$  means a rougher surface which the grid might contain. Also, during a strong convective situation,  $Z_i$  might be much larger. These situations can then be studied more accurately.

### **2.2.3 Errors Associated With the Retrieval Technique**

As with any finite difference calculation, there are errors affiliated with the process discussed above. The foremost concern of note are frictional stress effects. The question is, "just how accurate are the frictional parameterizations, and are they important?" Though a good first step towards this question was taken, many assumptions were still incorporated

into the friction term. The crude first approximation involved in finding the PBL evolution based on model data is also a source of error for this term. Given the available data used, no other practical parameterization of the frictional stresses could be derived. Thus with the data on hand the parameterization used was the best available. Unfortunately, other sources of error in this technique do occur and need to be discussed.

The type of weather can also influence the outcome of the retrieved height field. As discussed in Kuo et. al. (1987) the synoptic situation can vary the retrieval error. They found for weak summer (high pressure) cases the error was smallest. Higher errors were found in winter frontal situations. Other errors can be found when the grid spacing is too large to accurately depict the correct mass field. These subgrid scale effects are usually very small and are not much of a factor for most grid spacings.

Since a Barnes analysis is performed, errors arise due to observed data being at irregularly spaced points. The computation is performed at the grid point, not the original point of the source of data. This error is also small, but should be mentioned. Another source of error occurs when an original source of data has measurement error. For example, the winds read by the RAOB might not be completely flawless. This can be called initial data errors. The retrieval process was performed on a computer. Thus, small computational truncation errors can also alter the retrieved height field.

Other calculation errors include boundary conditions assumptions and iterative relaxation procedure errors. During the Barnes analysis of the profiler derived winds, a first guess (a boundary condition) is given via the RAOB winds. This initial condition, while close, is not the true reading. Thus errors result. During the calculation of the retrieved height, the Laplacian is solved with the Liebmann over-relaxation method. As the computer solves this Laplacian, iterations produce small errors. Finally the relaxation method can only solve the equation within a certain error value.

As stated above, the kinematic method of finding the vertical velocity was employed. The kinematic method assumes an incompressible atmosphere which is not entirely true. Areas of strong convection can violate assumptions in the incompressible continuity

equation, thus making the solution for  $\omega$  unattainable. Also, when a scale analysis is performed on the incompressible continuity equation, it is found  $\omega$  is much smaller in magnitude than the horizontal velocity. As a result, if there are even inconsequential errors in the horizontal velocity, significant errors can occur in the vertical velocity because of errors in the velocity divergence. The question of, "why does not one just use the vertical wind velocity produced by the wind profilers for  $\omega$ ?" may arise. The answer involves one of the weaknesses of wind profiler technology. During times of precipitation, the wind profiler will measure the vertical velocity of the precipitation, not of the wind. Wind profilers, however, can still measure the horizontal velocity during precipitation episodes and thus a vertical velocity can be produced which is necessary for the divergence equation. Avoiding wind profiler vertical velocities allows the divergence equation solution to be solved during wet and dry conditions.

### **2.3 Summary**

The combination of wind profiler data with the divergence equation offers a new branch of meteorological research. Now instead of twelve hourly upper air analysis on an operational basis, an hourly analysis can be achieved. This analysis will also be more beneficial than RAOBs alone because now the station spacing will be about half of the RAOB station spacing. That is, the profiler/RAOB network is twice as dense as the existing RAOB only network. These new spatial and temporal resolutions can benefit the meteorological community. This would include a higher resolution analysis of the mass field adjustment resulting in a low-level jet event. Such a case will be presented in the next chapter.

Once all of the data is collected and processed the retrieved mass field can be produced. The retrieval technique is computationally efficient. This procedure, as adopted here, took under an hour to complete on a Dec Alpha 3000 workstation for each hour of analysis. The only delays are data reception and quality control. This entails receiving the

data from a source provider and also waiting until the next hour's data was available in order to calculate the time derivative of divergence tendency. Thus, a 1200Z mass analysis field could be produced easily by 1345Z. The majority of the quality control performed on the data was automated in the programming. Some, though, was done by subjective analysis of the individual fields of data. A more rigorous automated quality control technique could be incorporated for a fully automated retrieval process.

All of the data used in the retrieval technique was from operational data sets. No intensive observation periods or special measuring equipment was used. This process could be used operationally for the real-time forecaster. All it takes is surface, RAOB, and profiler data and a computer to handle the calculations and present the results.

The only question then is how to handle the PBL parameterization. Since the LLJ usually is a PBL phenomenon, friction is important in the case study that follows. Two schemes as discussed earlier, were employed for representing the frictional stresses. The results of these schemes will be shown in Section 3.4.

The errors associated with this technique are quite small given the power that the divergence equation yields. A good review of the errors associated with the divergence equation can be found in Modica (1987) and, for this exact technique, in Adams (1996). A root-mean-square error calculation, Eq. (14), was done at selected vertical levels,

$$\text{RMSE} = \left[ \sum_{i=1}^N (F_i - O_i)^2 / N \right]^{1/2}, \quad (14)$$

where RMSE is the root-mean-square error,  $N$  is the number of observations,  $F$  is the forecasted scalar (i.e., geopotential height or temperature), and  $O$  is the observed scalar (i.e., the actual RAOB value). Table 5 shows the results of the RMSE for this case study. Modica (1987) stated stronger low-level divergences result in larger temperature errors. This can be seen in Table 5 where the 850 mb temperature errors are larger than any other level. Also, the profiler observations are prone to error, as mentioned above. These small errors are magnified once the divergence of these errors are calculated. This will result is a



noisy retrieval of the mass field. The examples of the mass field shown in the next section are un-smoothed fields.

**Table 5 Root-mean-square error of retrieval technique**

<b>Geopotential height RMSE values (m)</b>					
<b>Hour:</b>	<b>15 Aug 00Z</b>	<b>15 Aug 12Z</b>	<b>16 Aug 00Z</b>	<b>16 Aug 12Z</b>	<b>17 Aug 00Z</b>
<b>850 mb</b>	10.66	8.58	11.76	13.18	14.13
<b>700 mb</b>	8.54	8.98	9.90	10.81	13.18
<b>500 mb</b>	12.99	10.49	12.84	11.58	19.78
<b>400 mb</b>	14.43	10.56	15.79	18.09	23.62
<b>250 mb</b>	20.26	12.03	17.10	21.15	30.75
<b>Temperature RMSE values (°C)</b>					
<b>Hour:</b>	<b>15 Aug 00Z</b>	<b>15 Aug 12Z</b>	<b>16 Aug 00Z</b>	<b>16 Aug 12Z</b>	<b>17 Aug 00Z</b>
<b>850 mb</b>	9.23	7.95	9.52	10.23	10.18
<b>700 mb</b>	2.62	2.20	2.04	2.18	4.75
<b>500 mb</b>	1.59	1.58	2.63	1.37	1.92
<b>400 mb</b>	1.20	1.06	1.56	1.21	2.73
<b>250 mb</b>	1.83	1.16	1.30	1.80	7.12

### **3. RESULTS**

#### **3.1 Synoptic Overview**

It is important to understand the synoptic weather situation in order to understand the benefits of the mass retrieval technique discussed in Chapter 2. Here, the synoptic situation, or large scale weather picture, is analyzed. First, the surface data is presented and then the upper air data is discussed. Surface data characteristics were discussed in Section 2.1.3. The upper air data employed, which consisted of RAOB observations only, was discussed in Section 2.1.1.

##### **3.1.1 Surface Analysis and Weather**

The beginning of the 48 hour event studied was at 0000Z on 15 August, 1995. The surface analysis can be seen in Figure 3.1. Here, temperature, dew point, pressure and winds are shown. In the Southern Plains, 0000Z corresponds to roughly 1900 local time, or close to sunset. Figure 3.1 shows a line of thunderstorms and rain showers along a line extending from eastern New Mexico through Texas, Oklahoma, and Kansas and ending in southern Iowa. This rain band is roughly aligned with the 21°C isodrosotherm. The isobaric analysis shows two main features. First, the inverted trough just east of the rain band. Second, the high pressure region located in the southeast corner of Figure 3.1. This high pressure is a predominant feature throughout the entire 48 hour period. This is a typical synoptic situation where the high pressure is located in the Southeast. The pressure gradient is weak and there is not much large-scale forcing (e.g., a front or jet stream). The pressure pattern is such that the "Gulf is opened up." That is, moisture from the Gulf of Mexico flows into the Great Plains region due to the position of the high pressure center. This situation was used in Wexler's (1961) interpretation of the low-level jet (LLJ). According to the synoptic classes defined in Table 1, this would be a Class 5 synoptic situation.

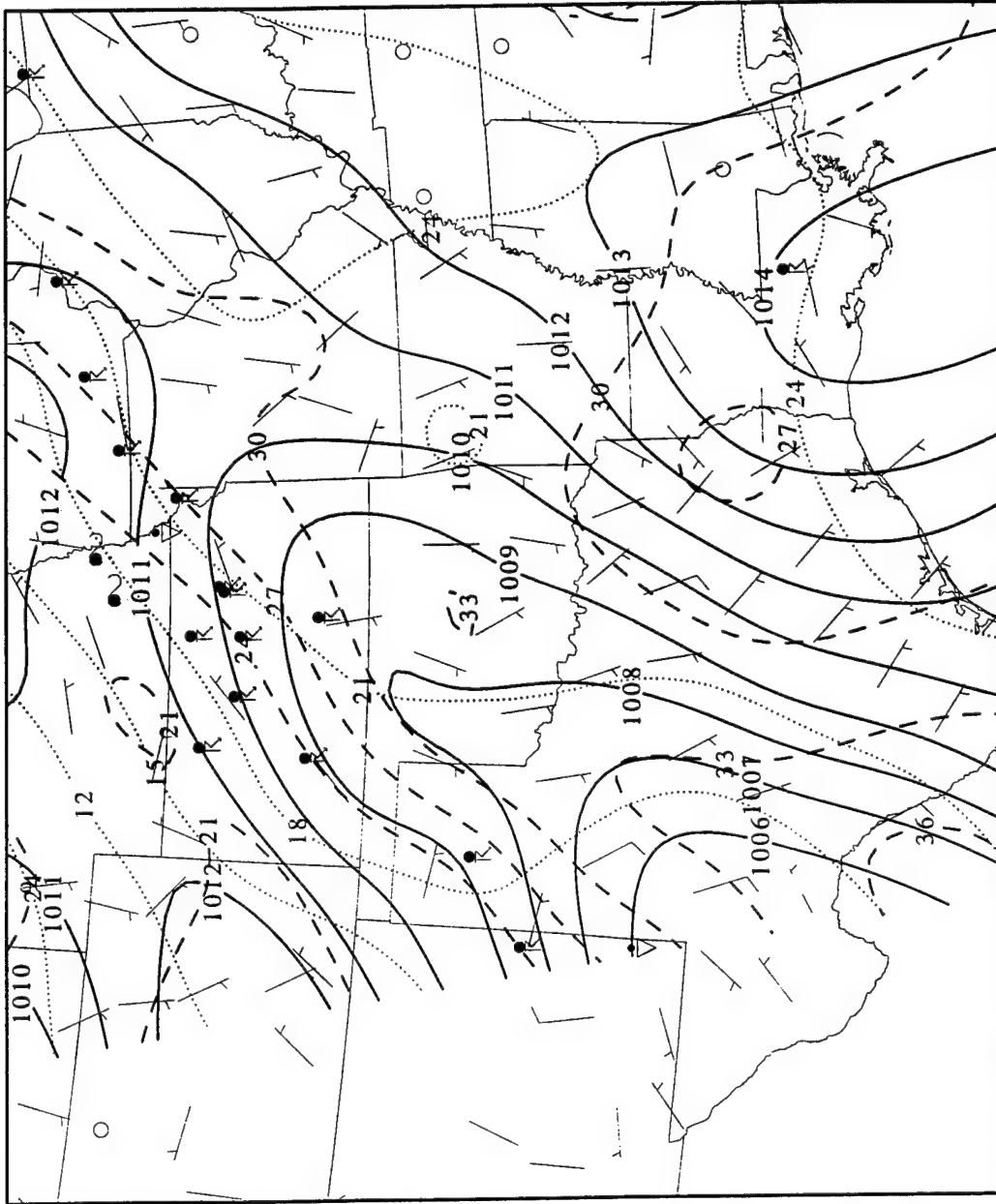


Figure 3.1. 950815/0000 Surface temp.(dashed, C),  
dewpt.(dotted, C), PMSL(solid, mb), wind(m/s), and WX.

The surface winds here are generally light (under  $7 \text{ m s}^{-1}$ ) and are from the southeast in eastern Texas and turn to generally the south in Oklahoma and Kansas. The winds behind the rain band are also weak. This keeps the rain band from moving quickly. The temperatures in the region are roughly in the  $21\text{--}33^\circ\text{C}$  range. Warmer temperatures are located in the southeast and cooler temperatures are in the northwest part of Figure 3.1. This is consistent for a typical weak high pressure region during the late summer months in the Great Plains.

Four hours later in Figure 3.2, the sun has gone down for some time. The rain band begins to weaken. Again the rain band is located near the  $21^\circ\text{C}$  isodrosotherm. The temperature has dropped in the region. The maximum temperature is now around  $27^\circ\text{C}$ . The pressure gradient as well as the winds have weakened also while maintaining a similar pattern.

By 1000Z (roughly 0500 local time) the convective line of showers is nearly dissipated (Fig. 3.3). The trough, though still apparent, has mostly filled as well. The winds remain weak and the temperatures are routinely getting lower. The Gulf remains open also. The winds in the eastern part of the figure are now near calm.

At 1400Z the sun has now risen and convection regenerates this day as well. Two main areas of convection are depicted in Figure 3.4. The first is located in western Texas, the other is centered over northern Missouri. The pressure field no longer shows a trough, allowing the weak high pressure to become the only pressure feature for the day. Over the course of the daytime the convection continues and does not move much from its location. The winds remain below  $7 \text{ m s}^{-1}$  with little change in direction, and the  $21^\circ\text{C}$  isodrosotherm has not moved much at all (see Fig. 3.5).

Shortly after sunset on 15 August (roughly 0200Z, 16 August) the convection in Missouri has developed into a mesoscale convective system, and the temperatures have cooled. The winds have still remained out of the south or southeast (see Fig. 3.6). By 0600Z, though, the convection from the previous day has nearly gone. The winds are also at there weakest with many stations reporting calm conditions again.

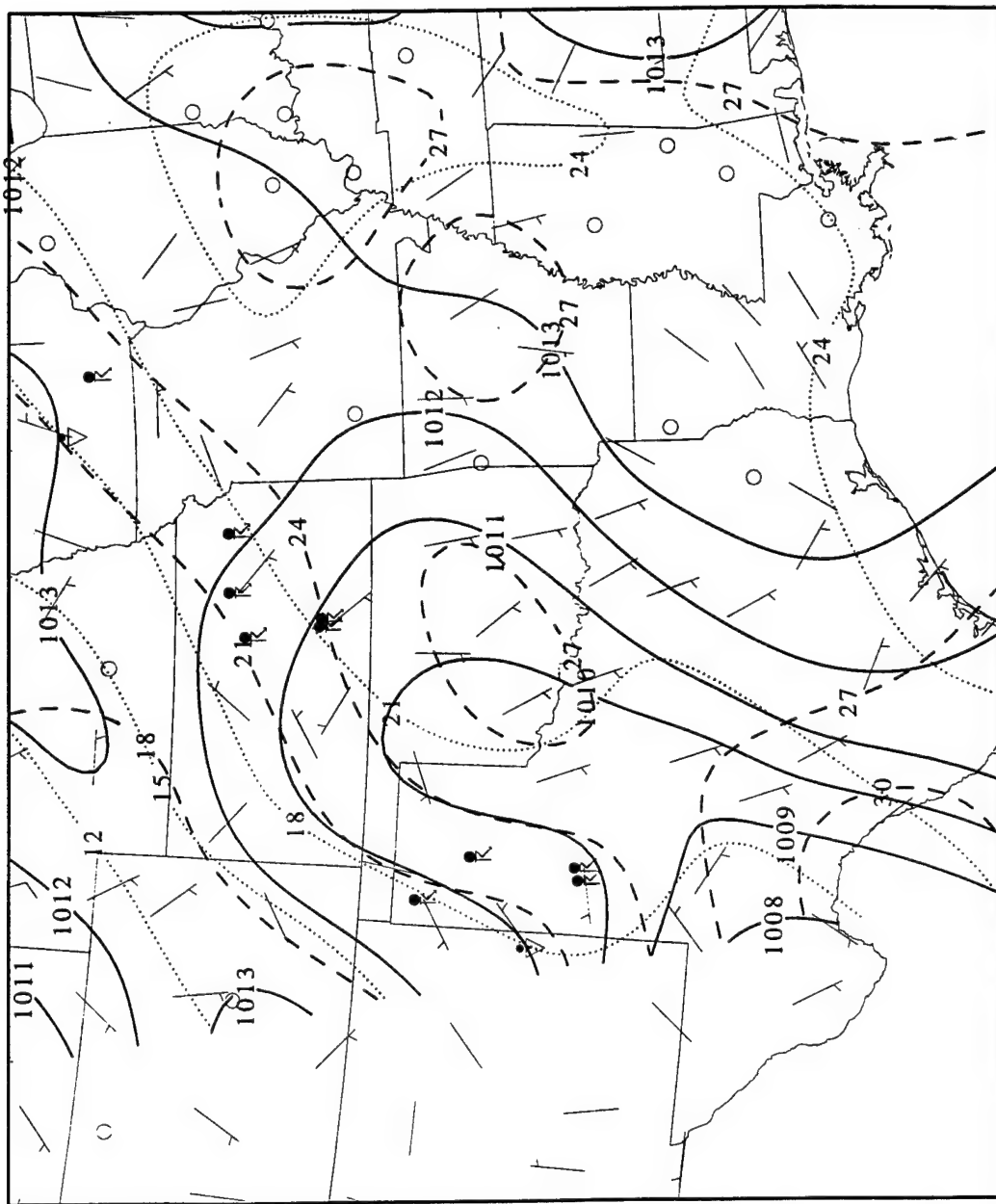


Figure 3.2. 950815/0400 Surface temp.(dashed, C), dewpt.(dotted, C), PMSL(solid, mb), wind(m/s), and WX.

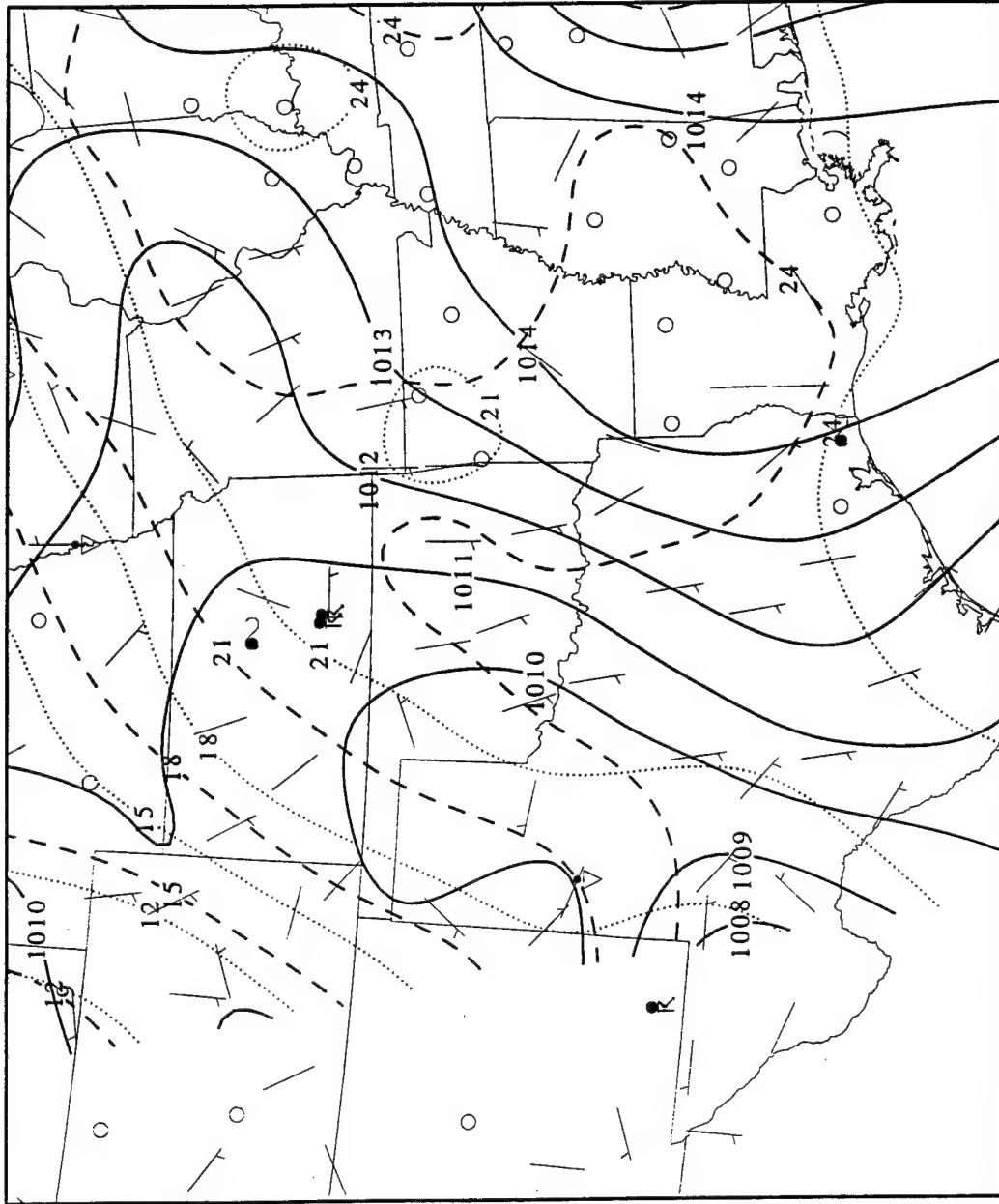


Figure 3.3. 950815/1000 Surface temp.(dashed, C), dewpt.(dotted, C), PMSL(solid, mb), wind(m/s), and WX.

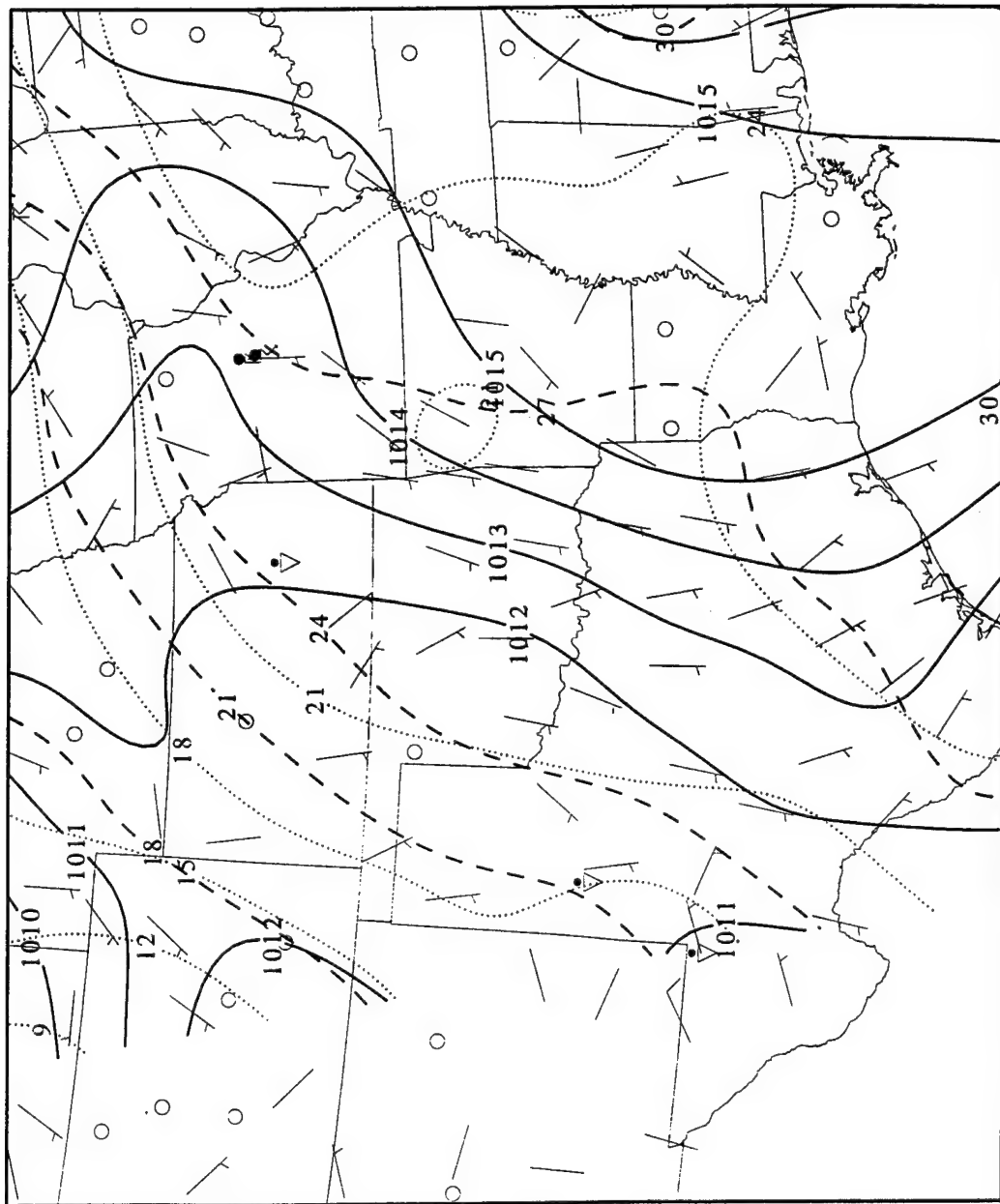


Figure 3.4. 950815/1400 Surface temp.(dashed, C),  
dewpt.(dotted, C), PMSL(solid, mb), wind(m/s), and WX.

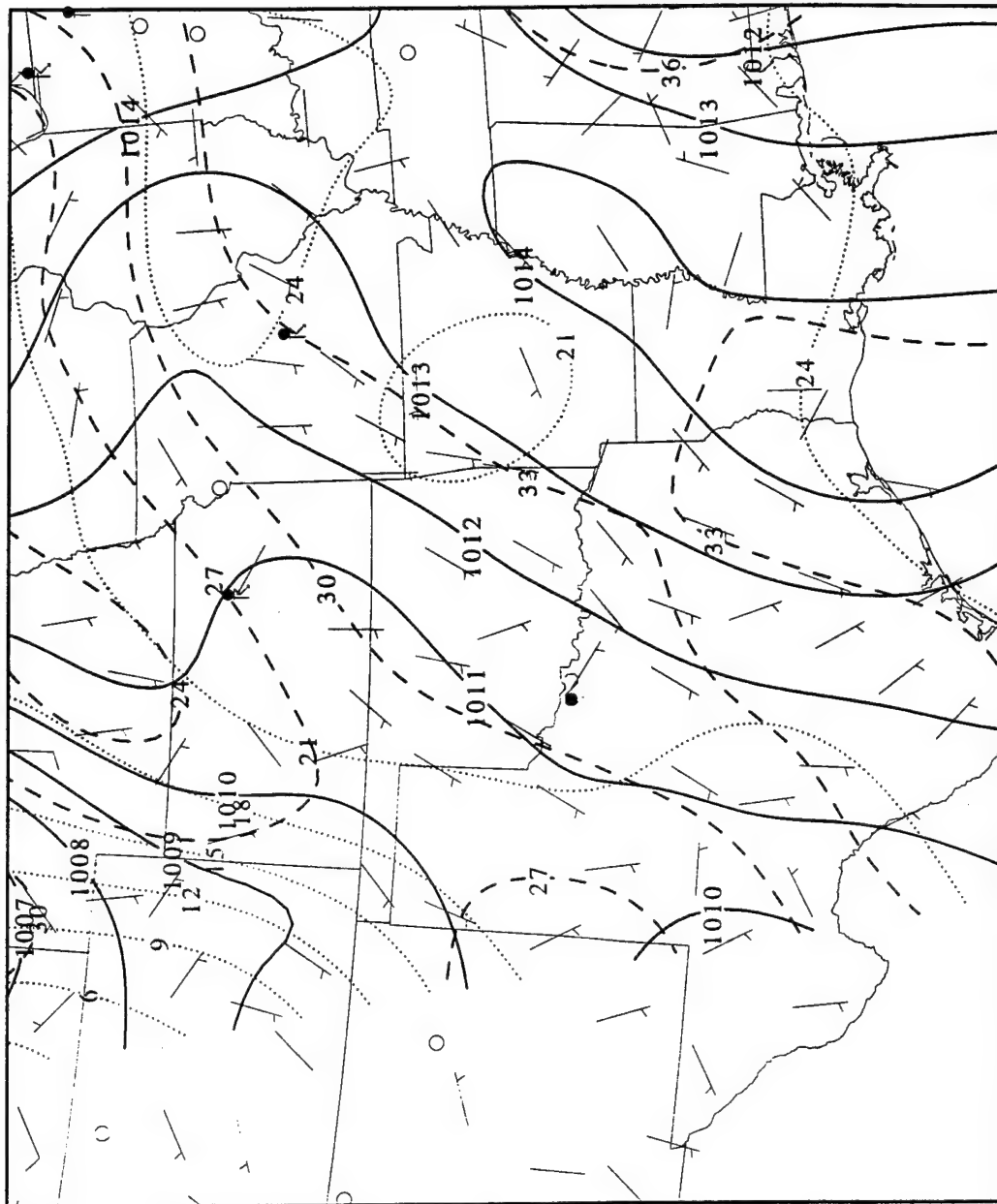


Figure 3.5. 950815/1900 Surface temp.(dashed, C), dewpt.(dotted, C), PMSL(solid, mb), wind(m/s), and WX.



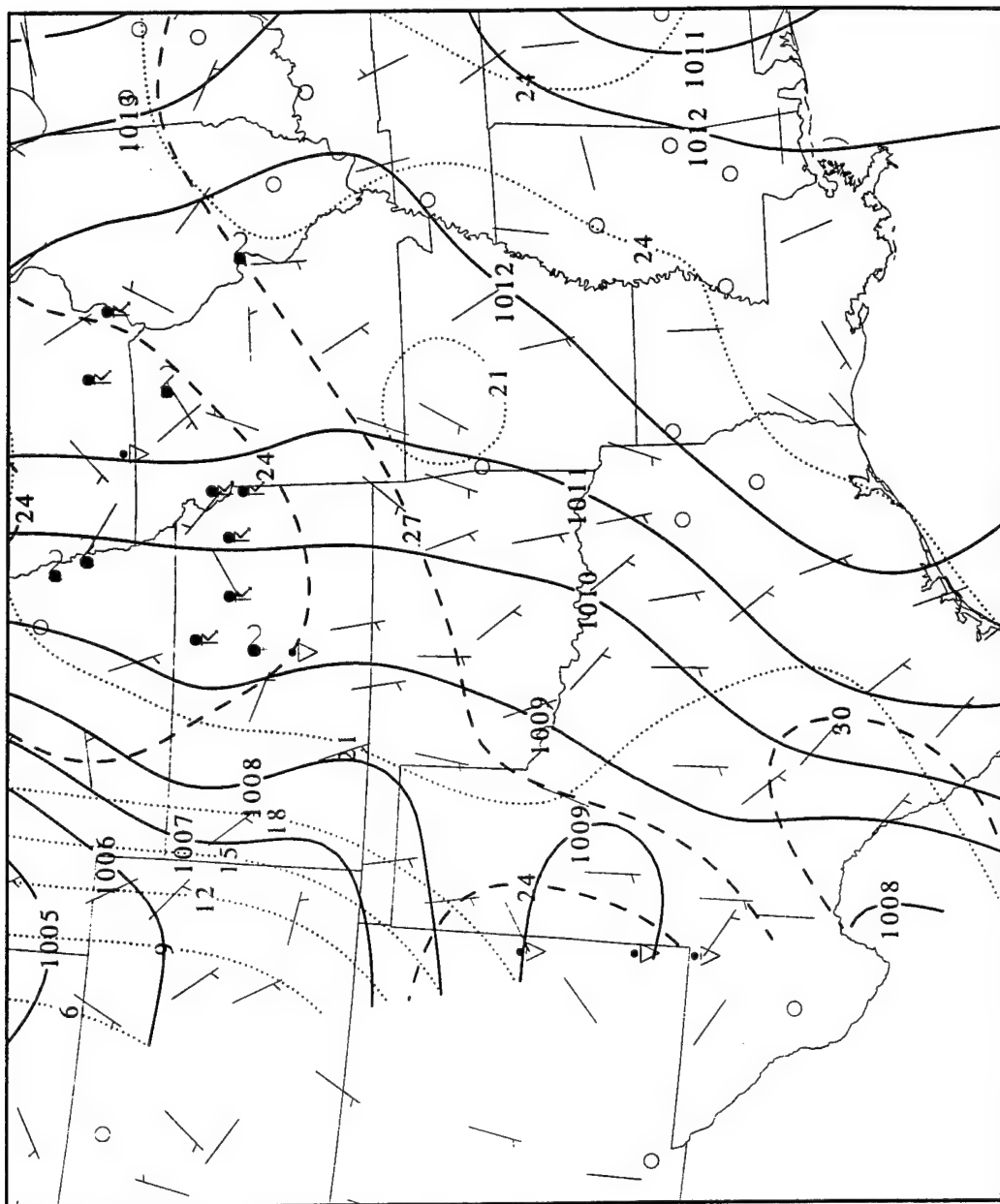


Figure 3.6. 950816/0200 Surface temp.(dashed, C), dewpt.(dotted, C), PMSL(solid, mb), wind(m/s), and WX.

The beginning of day time on 16 August welcomes the almost typical occurrence of convection in the Great Plains states one more time. This time the location is northern Missouri and southeastern Iowa. Yesterday's weak showers in New Mexico will intensify and a larger region of showers and thunderstorms will develop there (see Fig. 3.7). Winds during the day on 16 August are now a little stronger and maintain the same general direction. Temperatures are warmer with the entire region having maximums up to 35°C.

The end of the 48 hour period shows only minor differences from the beginning within the grid domain. The 1012 mb isobar has not moved its position much, and the pressure gradient has not changed much either. The 21°C isodrosotherm has rotated only slightly to a more north-south axis. The winds have also maintained a southeasterly direction in eastern Texas and southerly direction in Oklahoma and Kansas and speeds generally remain under 10 m s<sup>-1</sup> (see Fig. 3.8). The differences were that the nighttime convection remained longer and covered a larger area on 15 August and the daytime temperatures were a little warmer for 16 August.

Even though the differences were minor, the convection timing and location played a strong role in the development of a LLJ. Section 3.3 will discuss this issue. For now, however, it is important to note the timing of the dissipation of convection during the times of 0200Z through 0600Z on both days.

### **3.1.2 Upper Air Analysis**

As discussed in Section 2.1.1, the RAOB data was used at 16 levels. For the purpose of review, though, a discussion of only four mandatory levels will be shown here. The levels include the 850 mb (the lowest RAOB level), 700 mb, 500 mb, and 200 mb (the level of maximum winds).

At the beginning of the period, the 850 mb level shows a pressure pattern similar to Wexler's diagram (see Fig. 3.9). Here, high pressure dominates the region. The Gulf is indeed opened up with flow over the southern Great Plains from the south and southeast.

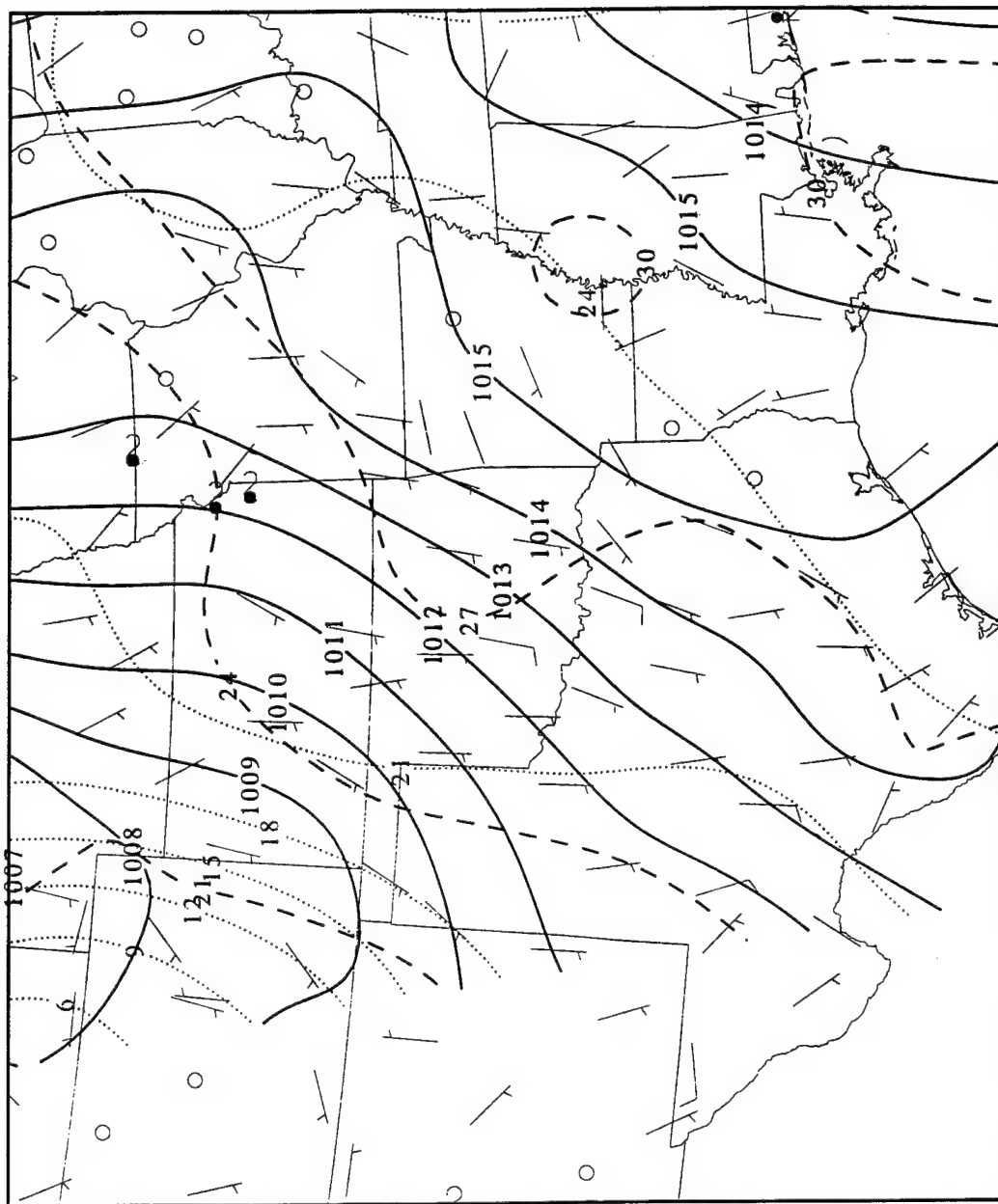


Figure 3.7. 950816/1400 Surface temp.(dashed, C), dewpt.(dotted, C), PMSL(solid, mb), wind(m/s), and WX.

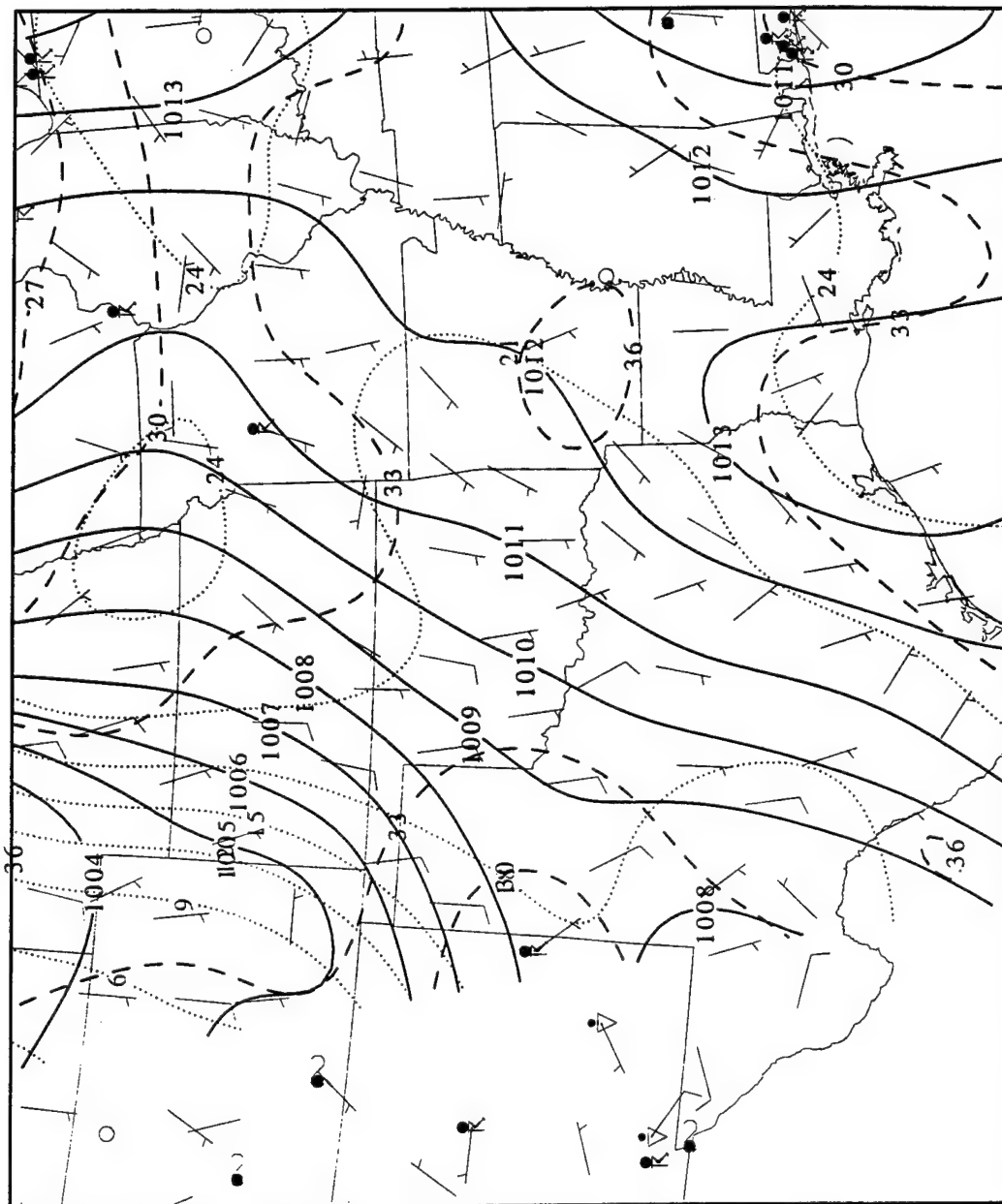


Figure 3.8. 950816/2300 Surface temp.(dashed, C), dewpt.(dotted, C), PMSL(solid, mb), wind(m/s), and WX.

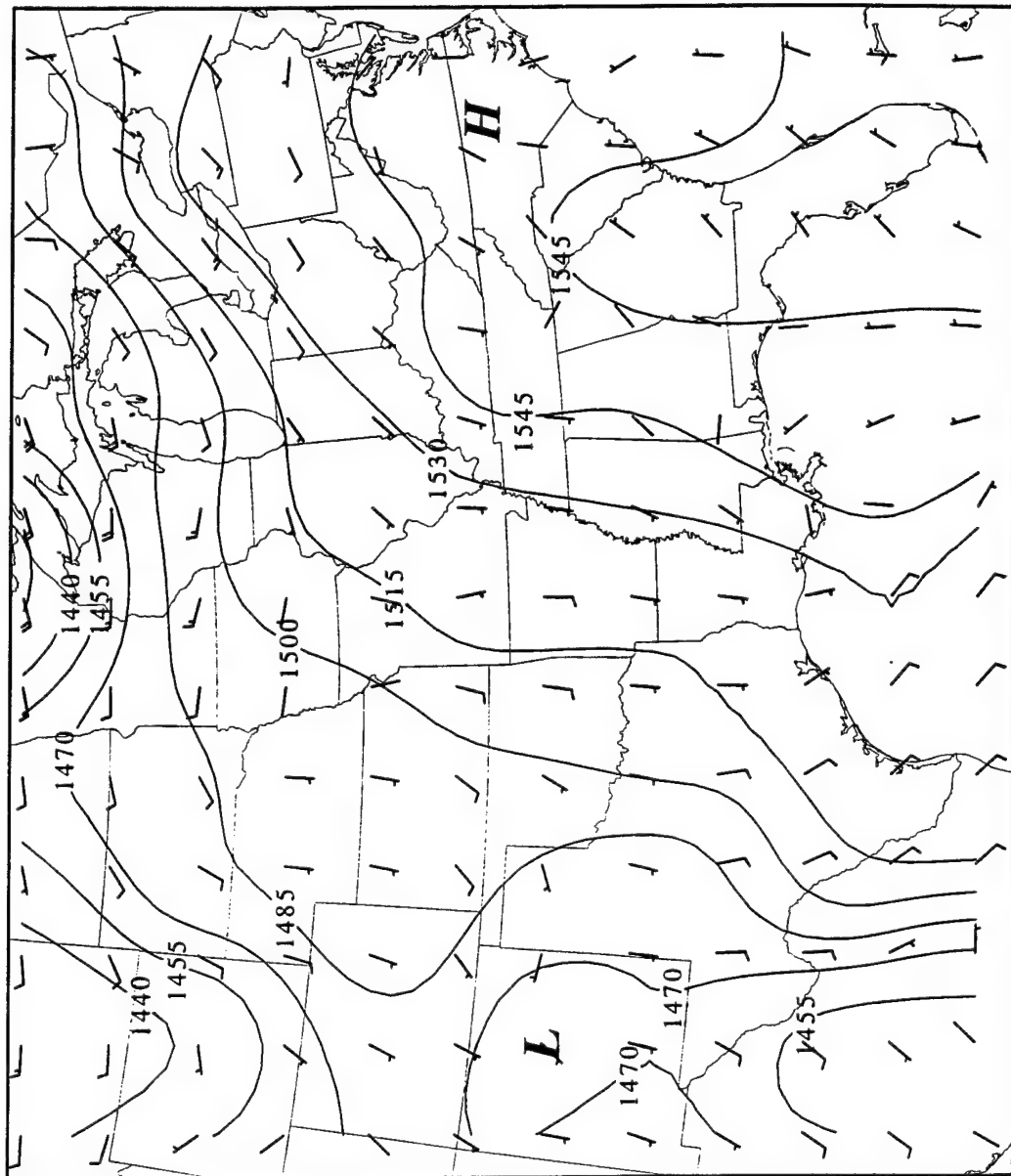


Figure 3.9. 950815/0000 850mb RAOB heights(solid, m) and wind(m/s).

Wind speeds are generally below  $12 \text{ m s}^{-1}$ . The exception to this is just ahead of a short-wave trough which is in the northwest corner of Figure 3.9. Here the winds exceed  $20 \text{ m s}^{-1}$ . Twelve hours later (Fig. 3.10), at 1200Z on 15 August, the short-wave trough has filled somewhat and the region of stronger 850 mb winds has propagated east-northeast to almost outside the grid domain. Again the region of high pressure dominates. The winds have generally turned clockwise over the Great Plains states.

The RAOB observations 24 hours later at 850 mb shows a similar pattern from the previous 24 hours. The winds have the similar speed and direction as before. By 1200Z on 16 August (Fig. 3.11) a new trough appears in the eastern Montana area. Also, the pressure gradient in the central Great Plains has increased from east to west. Winds are as they were before with one exception. Over the Texas panhandle, winds exceed  $13 \text{ m s}^{-1}$ . This area of the grid is located near the Rocky Mountains. The 850 mb level is very close to the surface here. The pressure gradient does not support these stronger winds. That is, the winds here are supergeostrophic. Thus, these winds are indicative of a mature LLJ wherein inertial-advective effects dominate. From all of the available RAOB observations, Figure 3.11 shows the only area where a classic inertially-driven LLJ might exist.

At 700 mb (Fig. 3.12), the pressure pattern again shows the structure indicative of LLJ formation as described by Wexler (1961). Anticyclonic patterns dominate. The short-wave trough, apparent at 850 mb, cannot be seen here. The flow here is zonal in nature. The 700 mb level does not show much change in the Great Plains throughout the 48 hour period. By 0000Z 17 August the pressure gradient remains the same in the Texas - Oklahoma area (see Fig. 3.13). This is a clear indication of weak forcing during this summertime weather event.

The 500 mb level (not shown) provides little additional synoptic information. Here the pressure pattern can be broken into two parts. First, the anticyclonic pattern located over the Southeast, and second the zonal flow across the northern tier of the grid. By 0000Z 16 August the 500 mb geopotential heights reveal a short-wave trough in the Nebraska area (not shown). More on this will be discussed in Section 3.3.

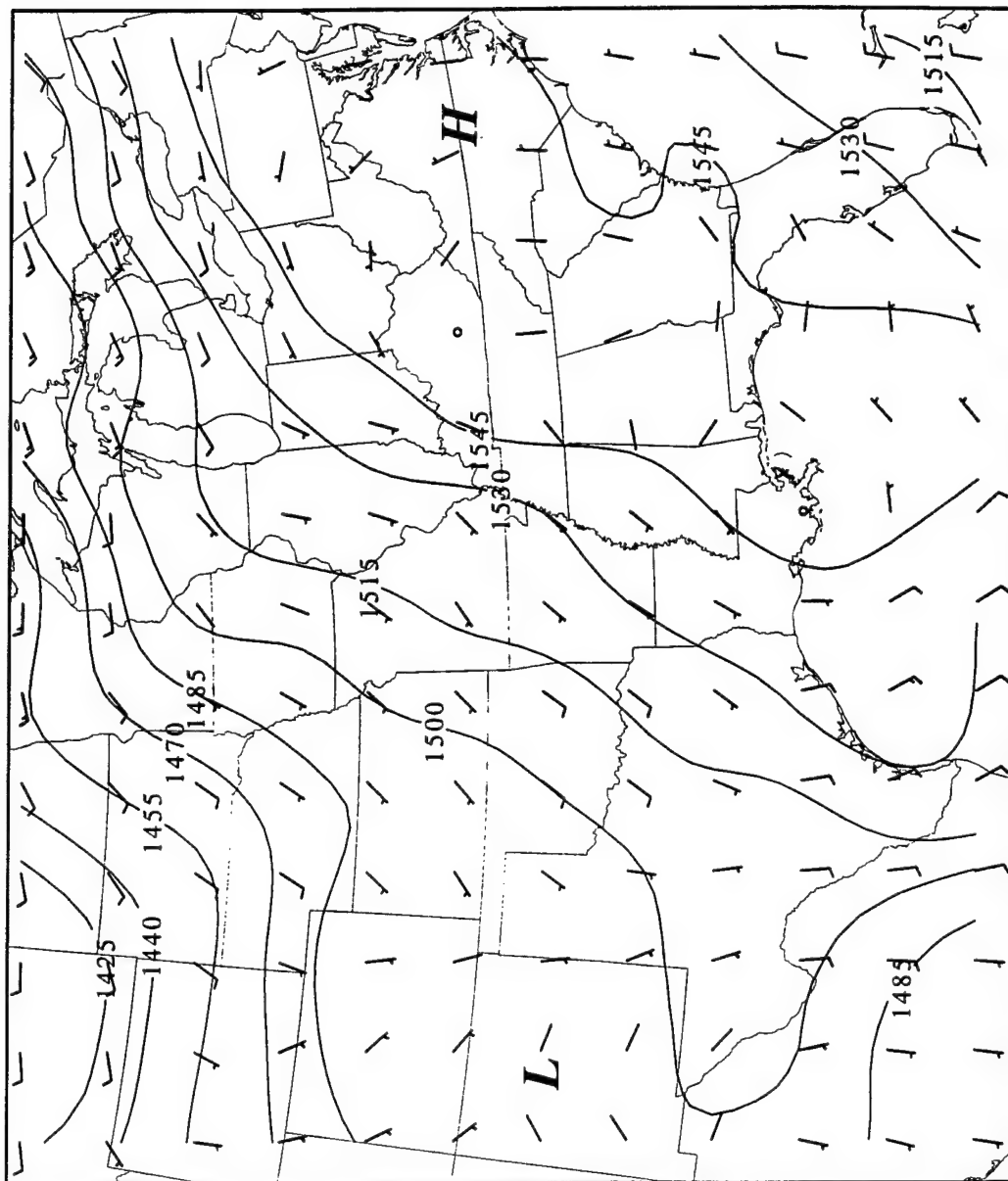


Figure 3.10. 950815/1200 850mb RAOB heights(solid, m) and wind(m/s).

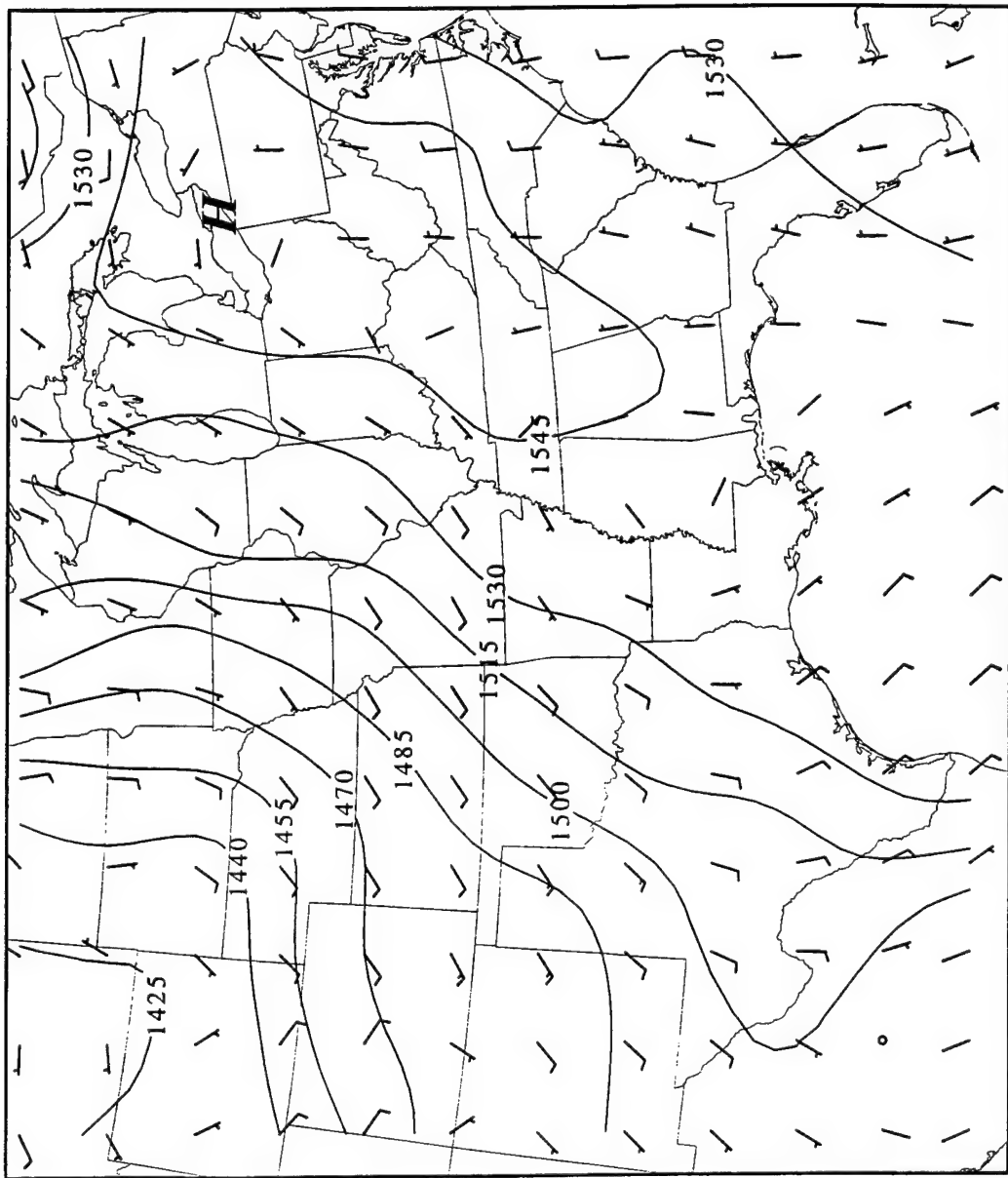


Figure 3.11. 950816/1200 850mb RAOB heights(solid, m) and wind(m/s).



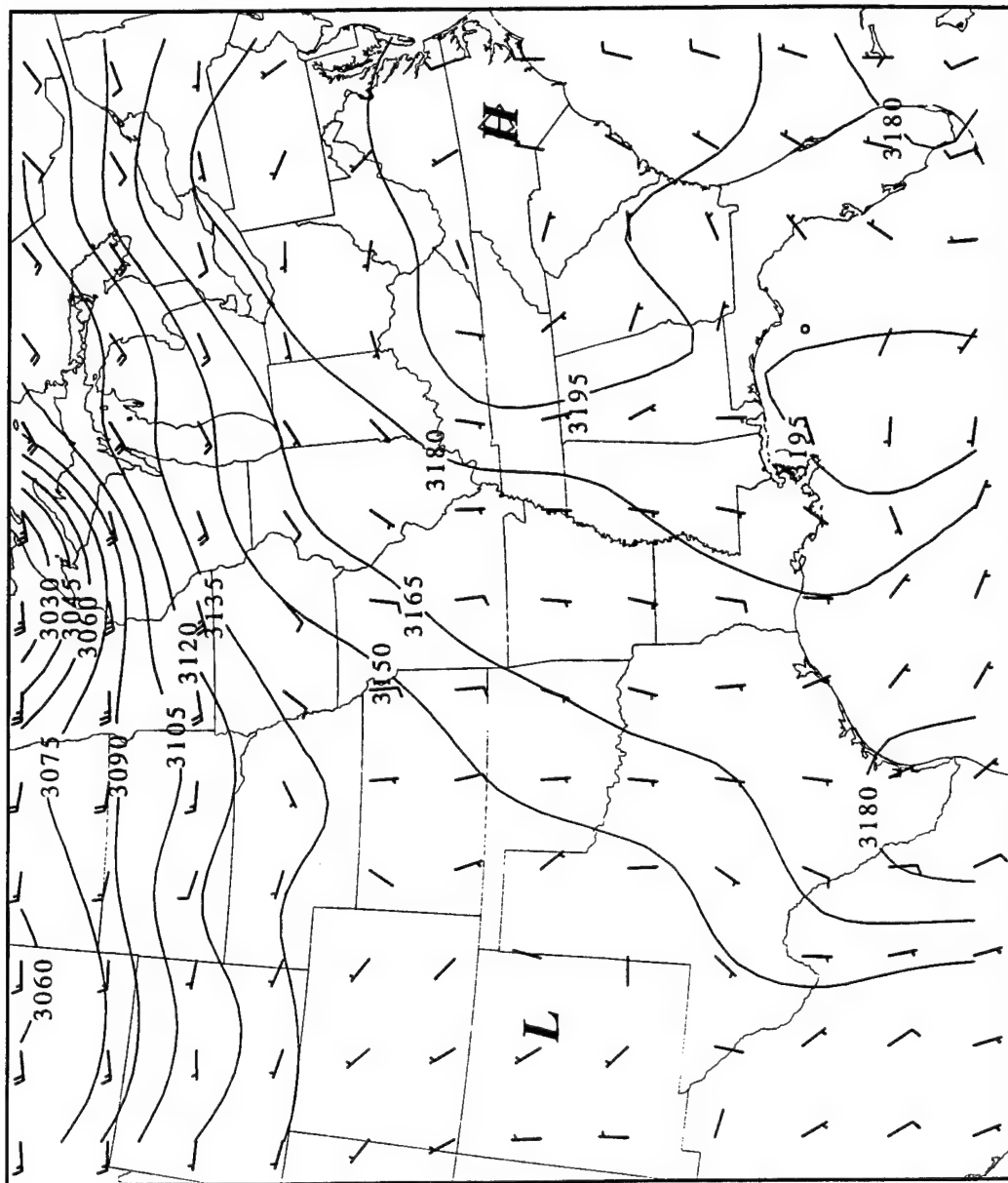


Figure 3.12. 950815/0000 700mb RAOB heights(solid, m) and wind(m/s).

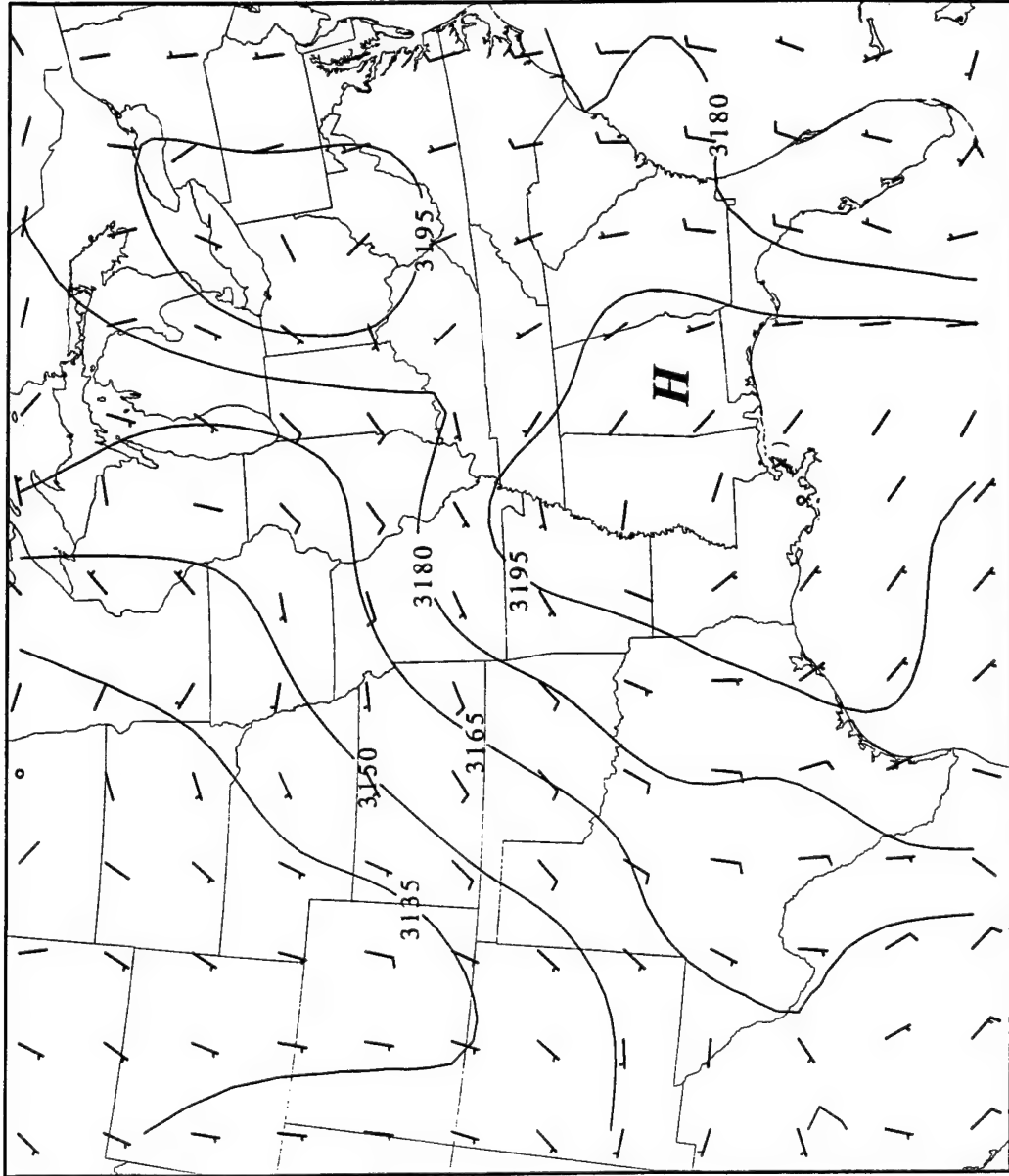


Figure 3.13. 950817/0000 700mb RAOB heights(solid, m) and wind(m/s).

Along with the pressure and wind fields shown, the 200 mb level isotachs are also depicted in order to show the location of the tropospheric jet. Figure 3.14 shows a similar height pattern on the 500 mb charts. The region is again divided into two parts: anticyclonic to the southeast, and zonal to the north. The jet, while weaker than winter time jets, still maintains jet characteristics. To the south of the entrance region, is where the line of convection was found. The vertical ascent in this region triggers and prolongs the convection here. Twelve hours later (Fig 3.15), the jet entrance region has moved to Iowa. By 1200Z on 16 August, the tropospheric jet has moved to the edge of the grid and no longer plays a role in the convection. Again, the grid domain is separated into two wind regimes.

The upper air analysis can be summarized in the following manner. Weak high pressure is located over the Southeast throughout the period. Shallow troughs moving zonally across the northern tier of the grid. There is only a small hint of a weak LLJ at one observation. The upper-level jet, which provides a sustaining mechanism for the convection, moves outside of the Great Plains by the end of the 48 hour period.

### **3.2 Comparison of RAOB and Retrieved Mass Fields**

In this section, a comparison of the RAOB mass field and the retrieved mass field at multiple levels are shown. The retrieved mass field computed here does not include any of the previously mentioned friction or smoothing schemes. Friction is assumed to be zero. Section 3.4 will include a discussion of the effects of friction. Figure 3.16 shows the newly retrieved geopotential height field at 0000Z 15 August using the technique described in Section 2.2.1. The solid isopleths denote the heights. The dashed isopleths indicate the RAOB-measured height field as seen in Section 3.1.2 (Fig. 3.9). The differences in the height are also shown. By looking at Figure 3.16, it can be seen the retrieval process has obviously made some modifications to the height field. The most dominant and persistent (as will be seen) difference is the strengthening of the anticyclone in the Southeast. Geopotential heights are now 20 m higher in some locations. Also, the isopleths which are

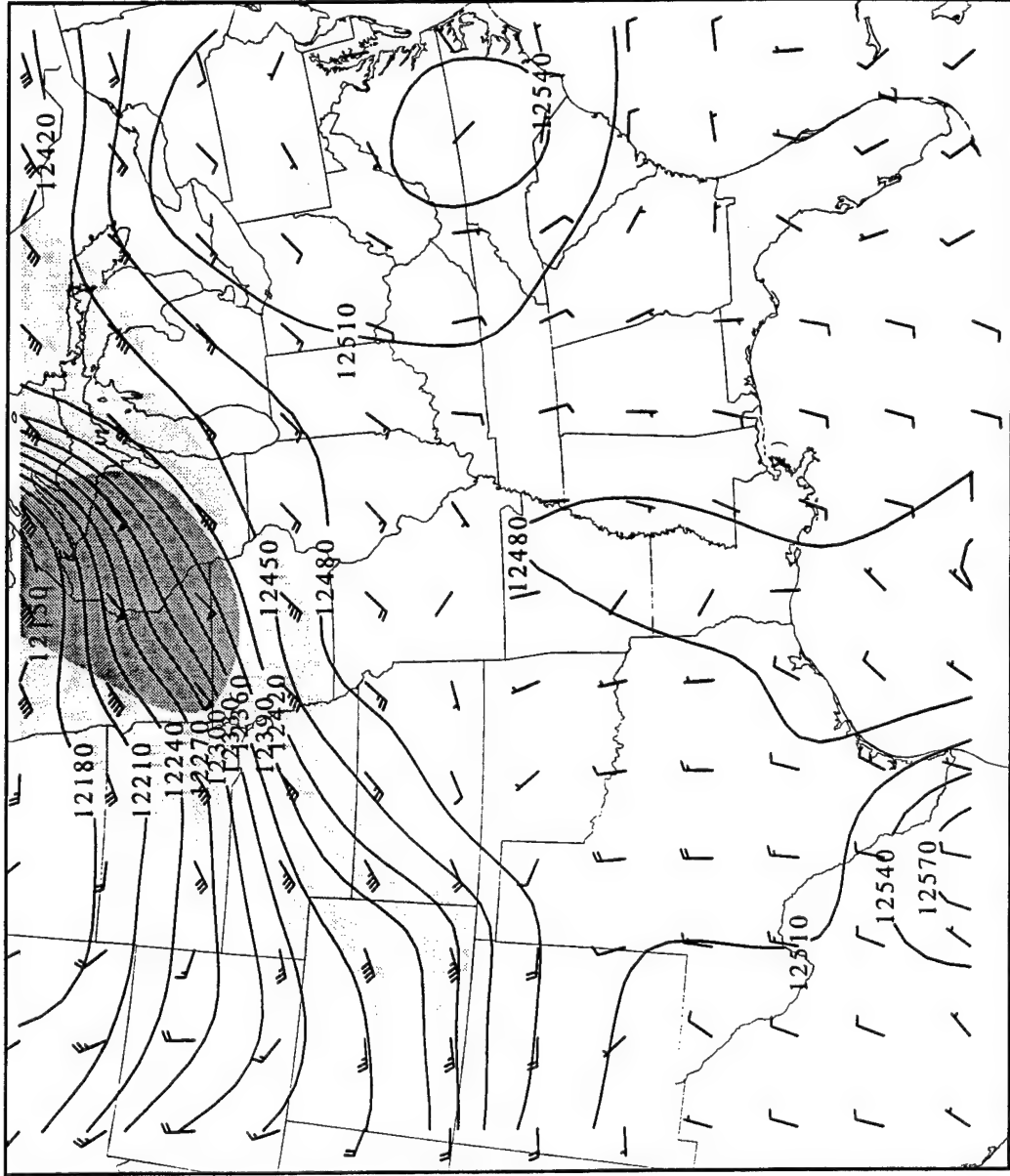


Figure 3.14. 950815/0000 200mb RAOB heights (solid, m), wind (m/s), and isotachs (shaded, >30m/s, >45m/s).

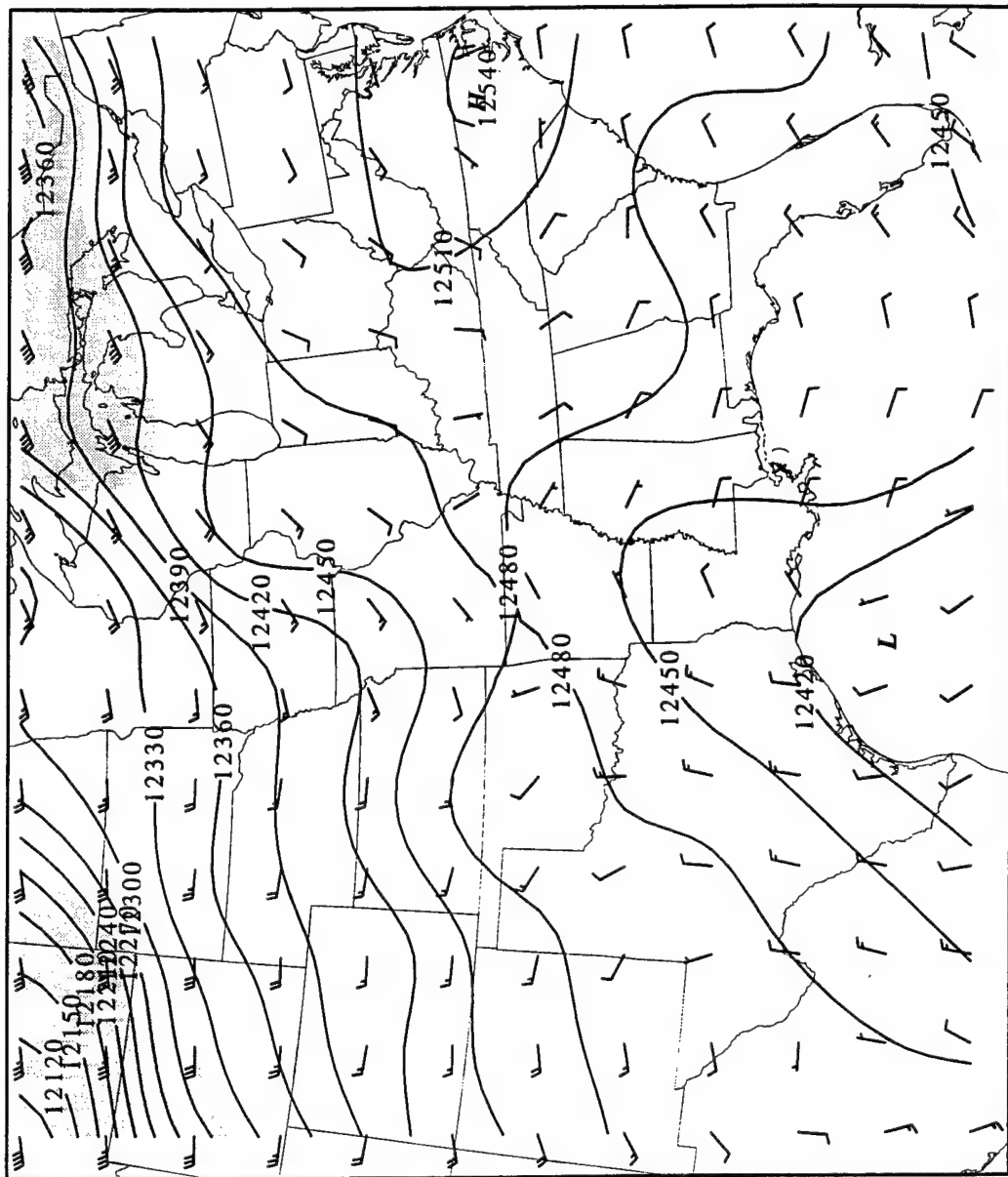


Figure 3.15. 950816/1200 200mb RAOB heights(solid, m), wind(m/s), and isotachs (shaded, >30m/s, >45m/s).

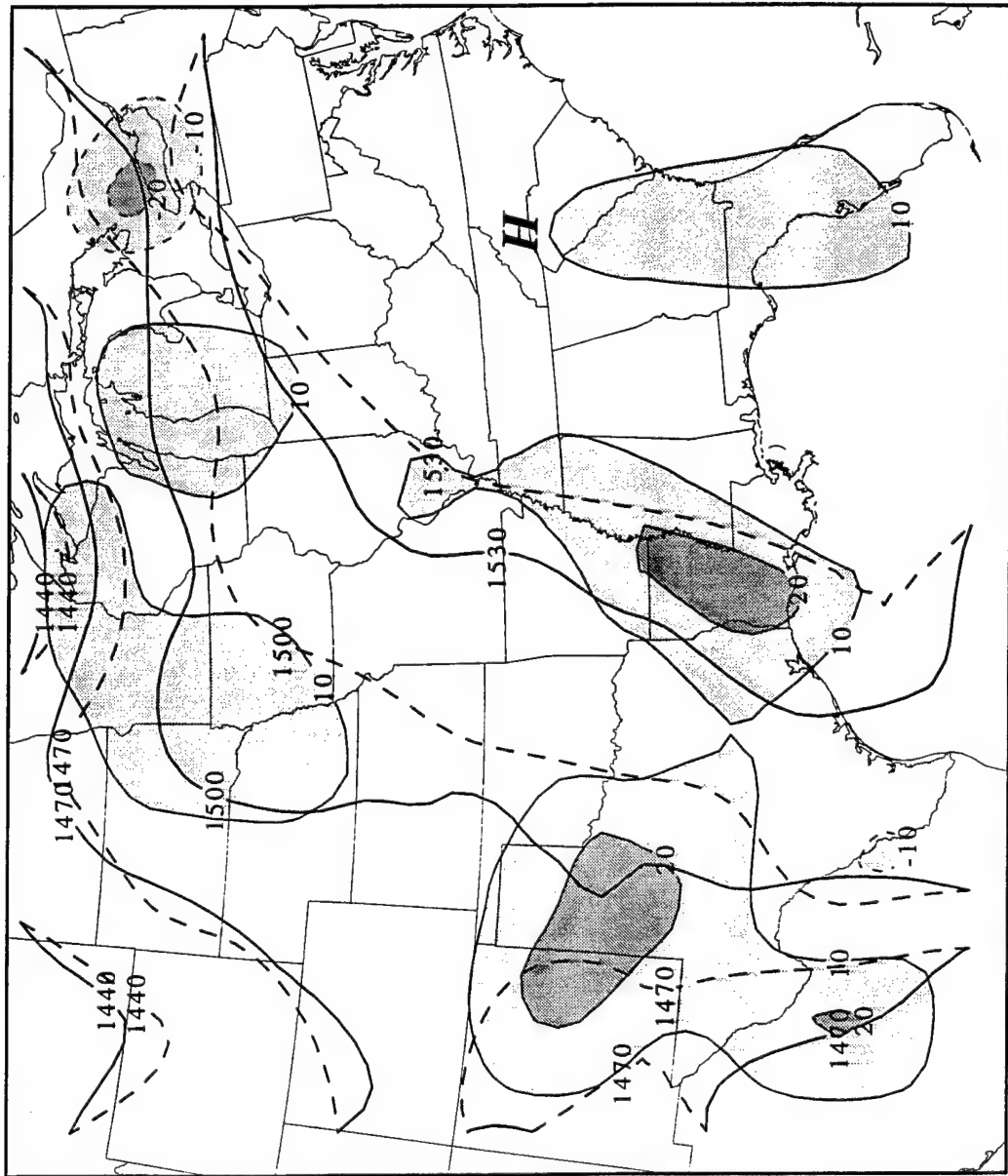


Figure 3.16. 950815/0000 850mb Retrieved heights(solid, m), RAOB heights(dashed, m), and difference(shaded, m).

shown exhibit shorter wavelengths. This is due to a higher resolution network of observations (i.e., the wind profilers). One such wave is found in the panhandles of Texas and Oklahoma in Figure 3.16. In the Northern Plains, the effects of the stronger high pressure are also found. Here, the ridging of the isopleths are more well defined.

Three hours later, in Fig. 3.17, the retrieved height field shows some interesting characteristics. For one, a meso-high has developed in the panhandle of Texas. Why did this occur? Upon taking a closer look, the surface charts (e.g., Fig 3.2) show a line of showers in this very area. Also note the wind profiler station location of Vici, Oklahoma (VCIO), see Figure 2.3. The rainband has obviously biased the winds at VCIO to produce strong divergence in this area resulting in the meso-high. A similar, but opposite, effect can be found in northeastern Kansas.

By 1200Z (Fig. 3.18) the meso-high at 850 mb still remains but has weakened. Mesoscale waves still persist throughout the domain, but overall the height field still only increases the intensity of the synoptic high pressure in the Southeast. After this time, the 850 mb charts show no significant difference throughout the rest of the period. The height differences remain below 30 m.

Figure 3.19 shows the 700 mb chart at 0000Z on 15 August. Again, the two pressure fields can be seen. The anticyclone in the Southeast is ever-present and its height has strengthened in the new retrieved field. The zonal flow in the northern tier also shows no surprises. The largest differences occur in northwest Iowa where the boundary of the two flow regimes meet. Here, the retrieved field maintains higher heights for the profiler winds, and their resulting divergence produces this outcome. The dual pattern fields are also apparent at 500 mb (see Fig. 3.20). Again, the height differences are no larger than 30 m.

Largely, the temperature fields are in agreement and show no significant features. Figure 3.21 shows the 850 mb temperature field at 0000Z 15 August. Again, the RAOB isotherms are dashed and the retrieved isotherms are solid. The differences between the two are shown with shading. The differences are rarely above 4°C. The large continuous isotherm shown in Figure 3.21 indicates a rather uniform temperature field across the entire

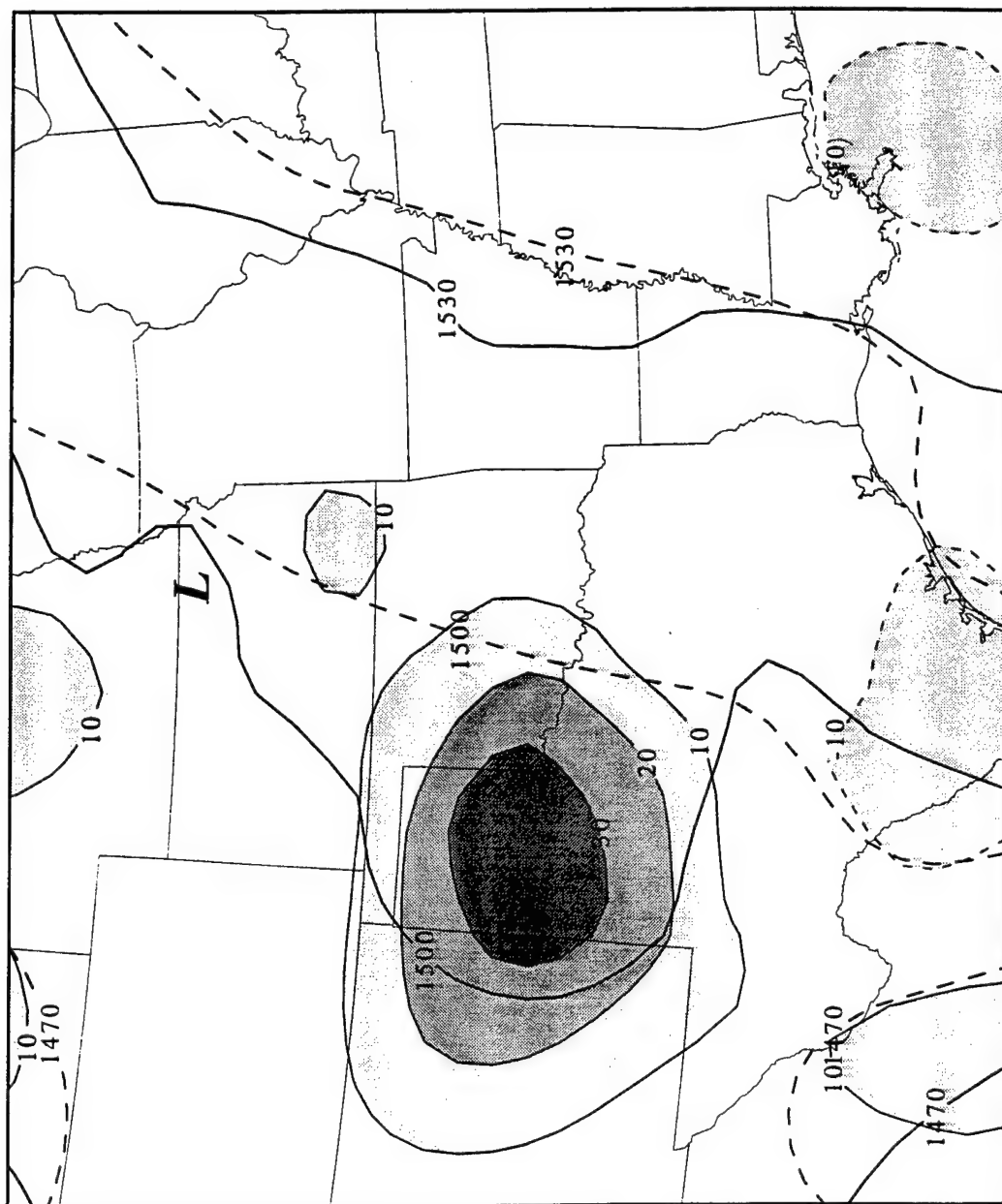


Figure 3.17. 950815/0300 850mb Retrieved heights(solid, m),  
RAOB heights(dashed, m), and difference(shaded, m).



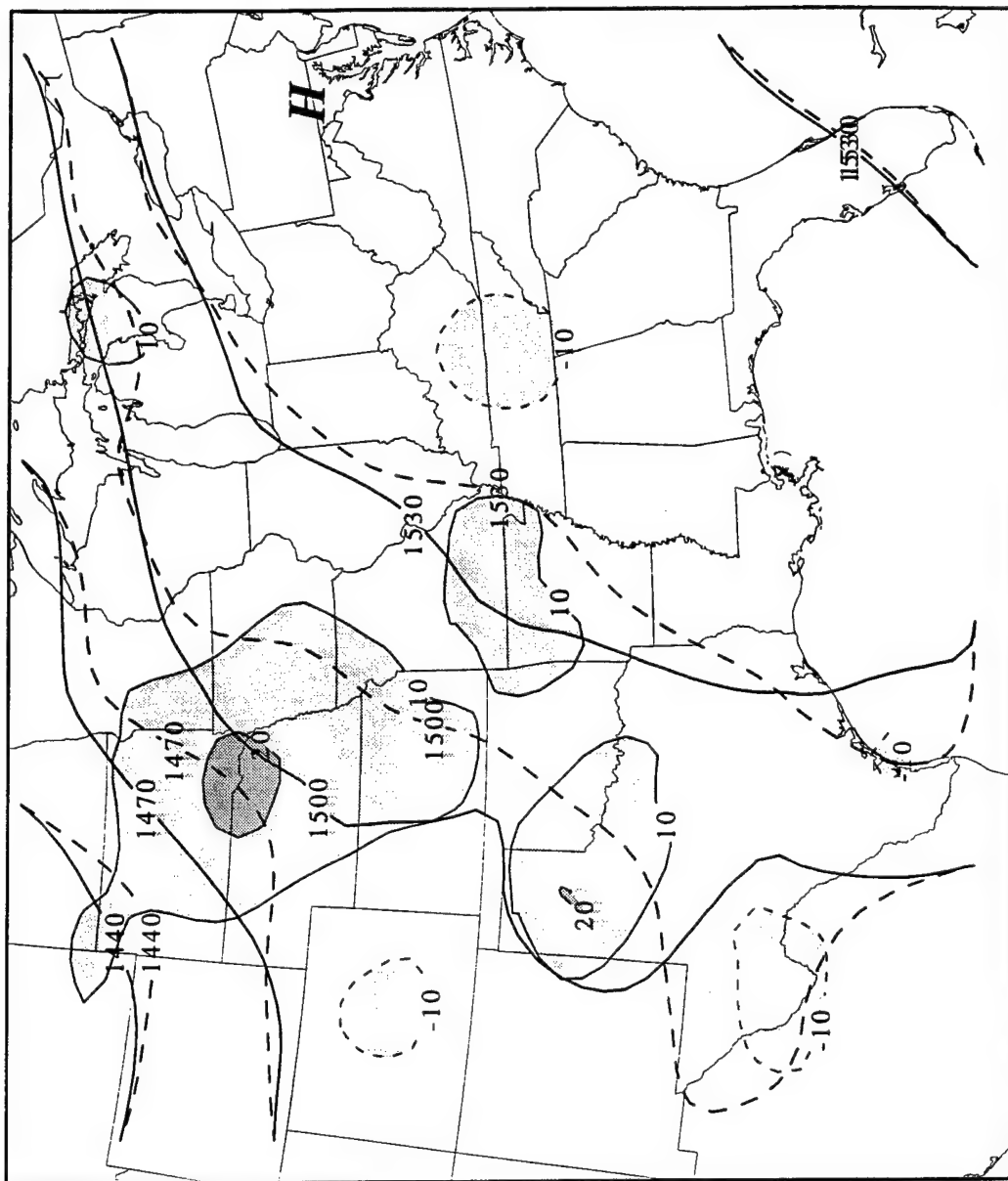


Figure 3.18. 950815/1200 850mb Retrieved heights(solid, m),  
RAOB heights(dashed, m), and difference(shaded, m).

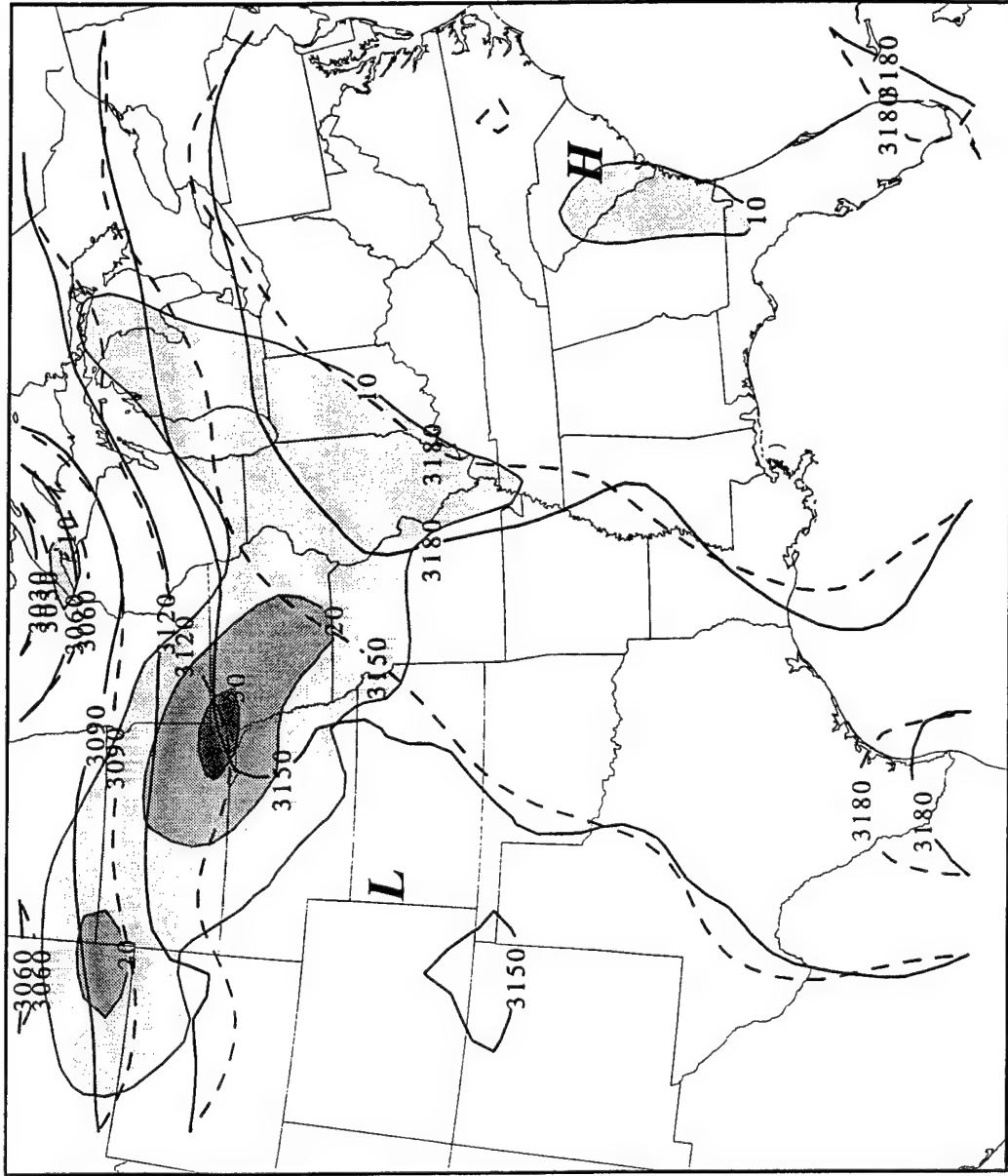


Figure 3.19. 950815/0000 700mb Retrieved heights(solid, m),  
RAOB heights(dashed, m), and difference(shaded, m).

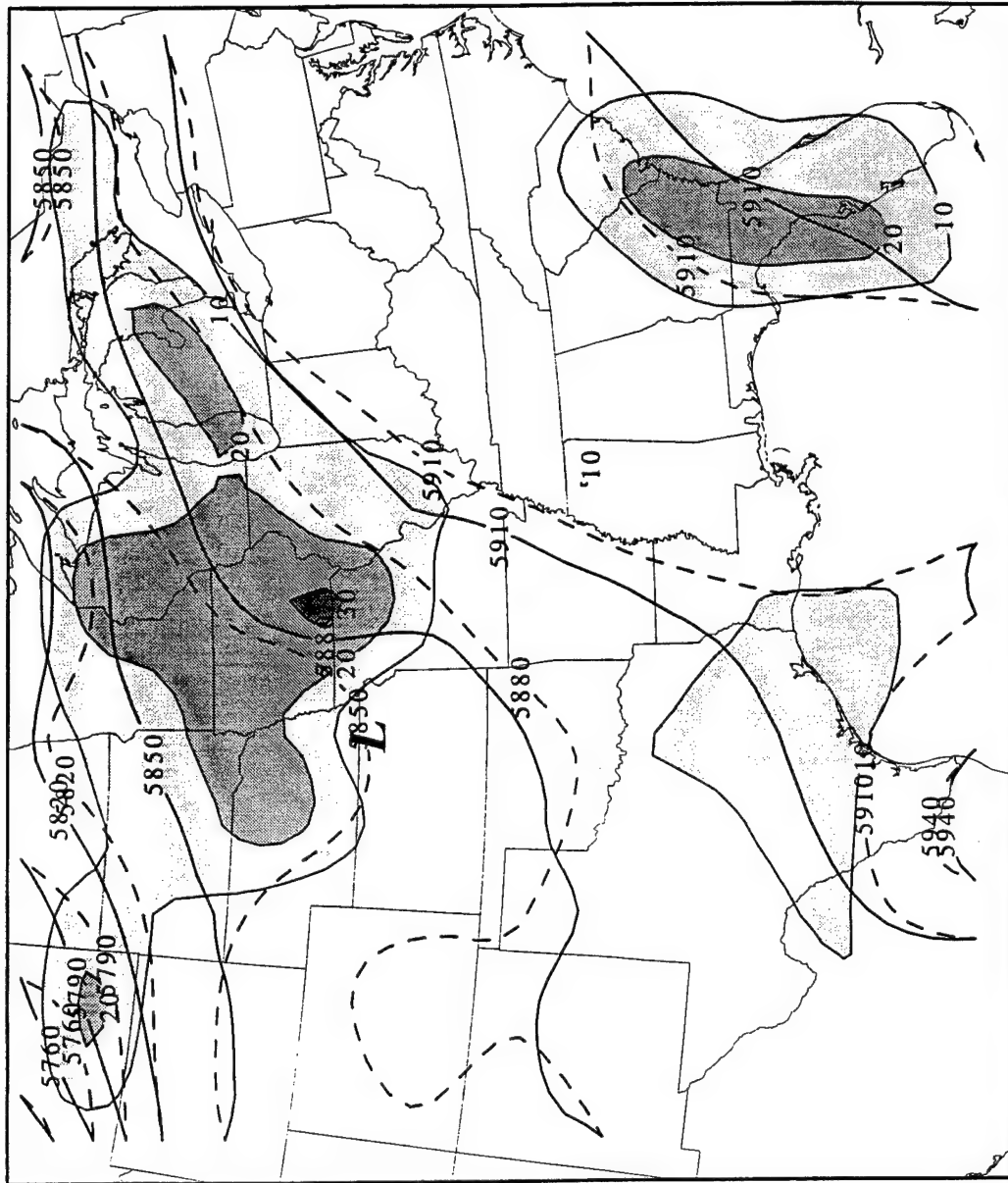
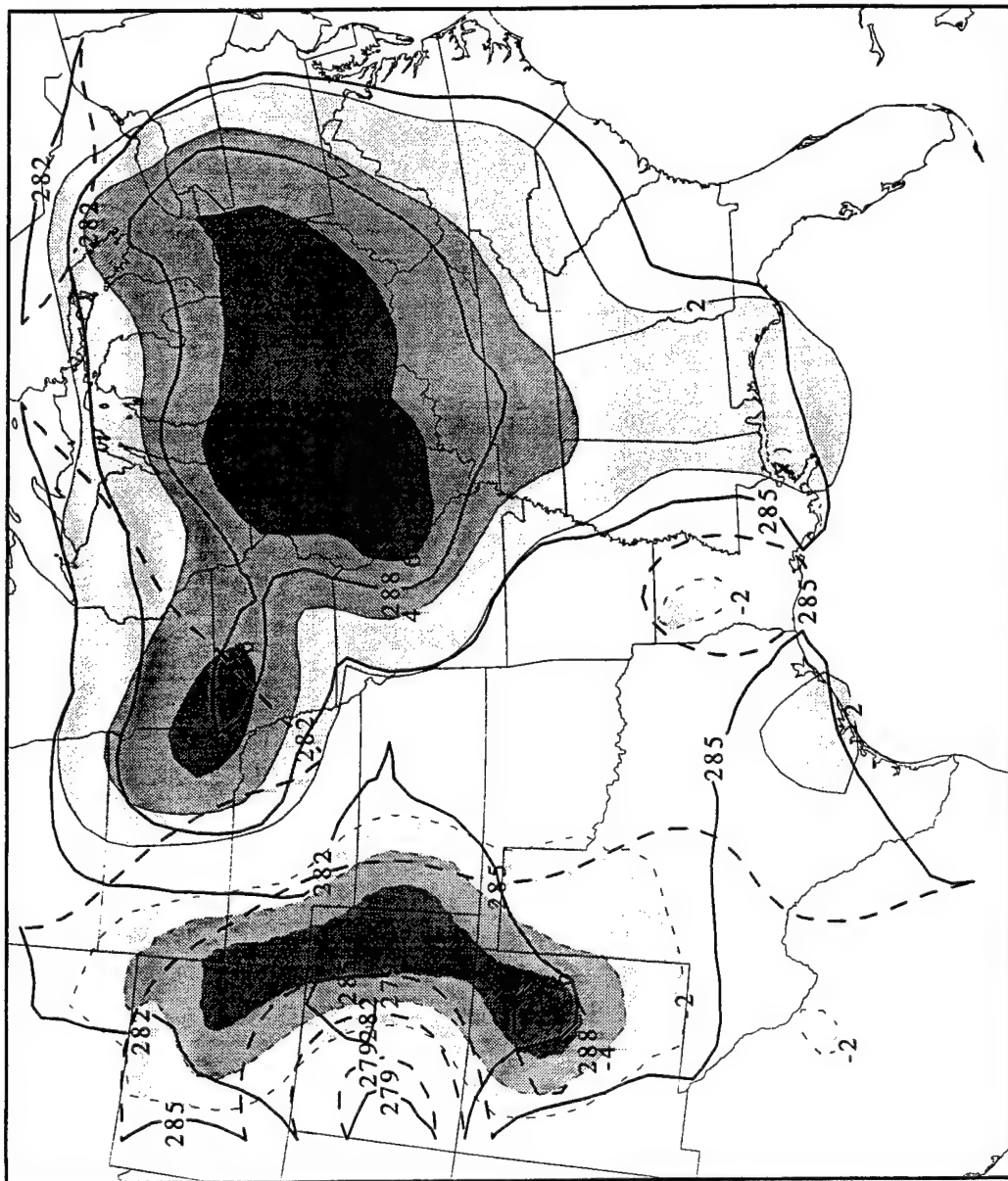


Figure 3.20. 950816/0000 500mb Retrieved heights(solid, m),  
RAOB heights(dashed, m), and difference(shaded, m).



grid. This field shows up throughout the period and appears at all levels. With no strong fronts within the grid, this is no surprise. The stronger temperature gradients and larger differences along the western boundary are indicative of problems of resolving the temperature field within the mountains where profilers are sparse and the lowest measuring level is too high. Throughout the 48 hour period the 850 mb temperature changes little, thus no other figures of temperature are shown.

Some 700 mb and 500 mb temperature charts for the period are shown in Figures 3.22 and 3.23. Little temperature gradient exists and the differences are again small. Note the effect of the mountains can still be seen at 700 mb but disappear at 500 mb.

In summary, the results of the retrieval process are encouraging. The retrieved mass fields, while modified, generally agree with the RAOB mass fields. The finer spatial and temporal resolution shows many new mesoscale features not normally seen from ambient observational equipment. Finally in Figure 3.24, a smoothed mass field was produced to show the effects of smoothing. A 9-point smoother was employed. The un-smoothed equivalent of these fields can be found in Figures 3.19 and 3.22.

### **3.3 Development of the Low-Level Jet as Diagnosed from Profiler Winds**

This section examines the formation of LLJs during the 48 hour period and the forcing mechanisms behind the development employing the profiler wind fields. Figure 3.25 shows the 900 mb analysis of the profiler-induced winds in the southern Great Plains at 0000Z on 15 August. The winds here are generally below  $10 \text{ m s}^{-1}$  with a small maximum located over the Red River Valley of Texas and Oklahoma. This region is near a large rise in the surface elevation. The mountain surfaces are acting as a baroclinic mechanism, thus increasing the winds. This shows a hint of the situation required for LLJ development as described by Wexler (1967). Recalling from Section 1.2, Wexler described a synoptic pattern conducive for LLJ development but did not mention any baroclinic forcing mechanisms for LLJ acceleration. Figure 3.25 shows the Wexler pattern of Bermuda High

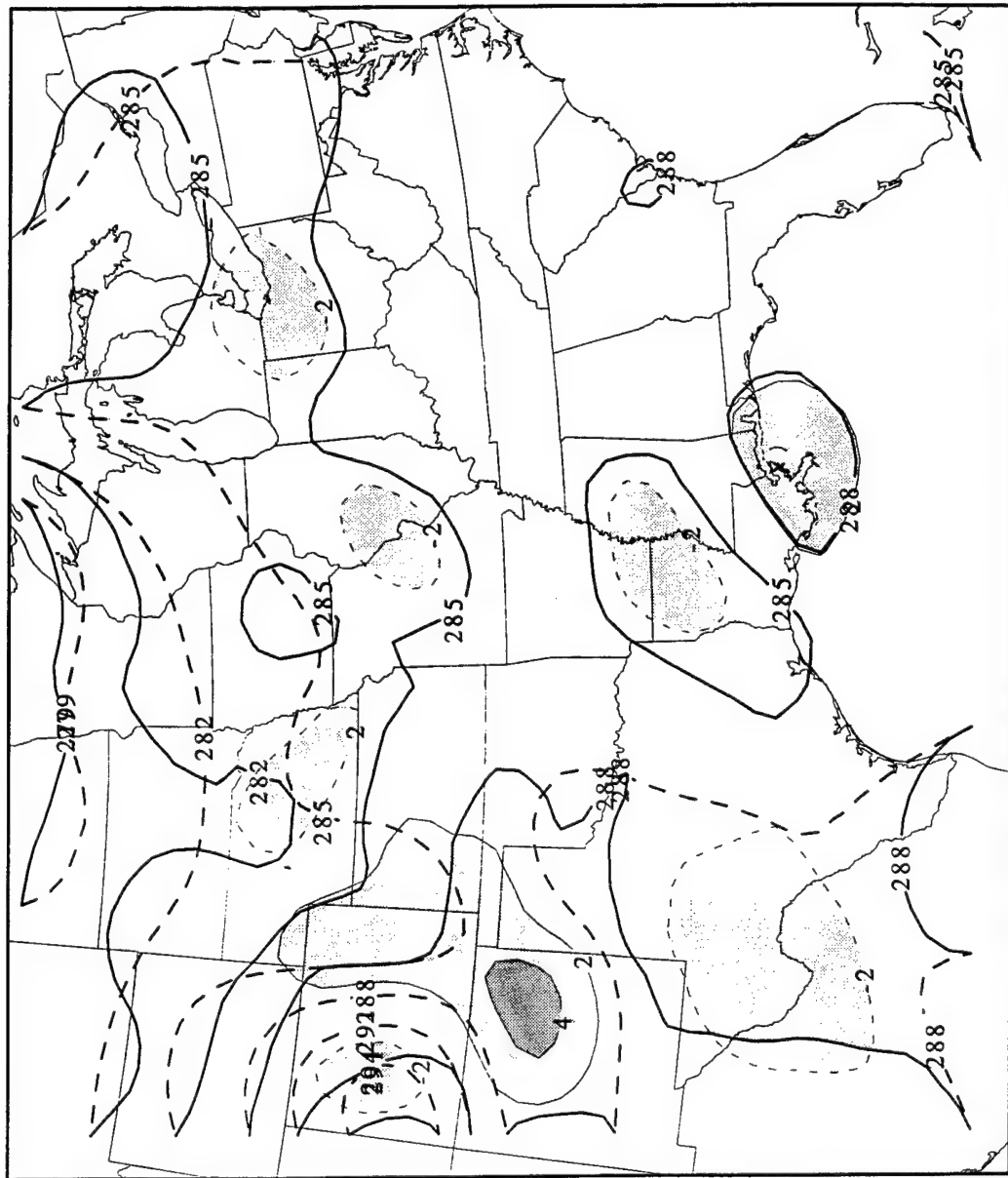


Figure 3.22. 950815/0000 700mb Retrieved temps.(solid, K),  
RAOB temps.(dashed, K), and difference(shaded, K).

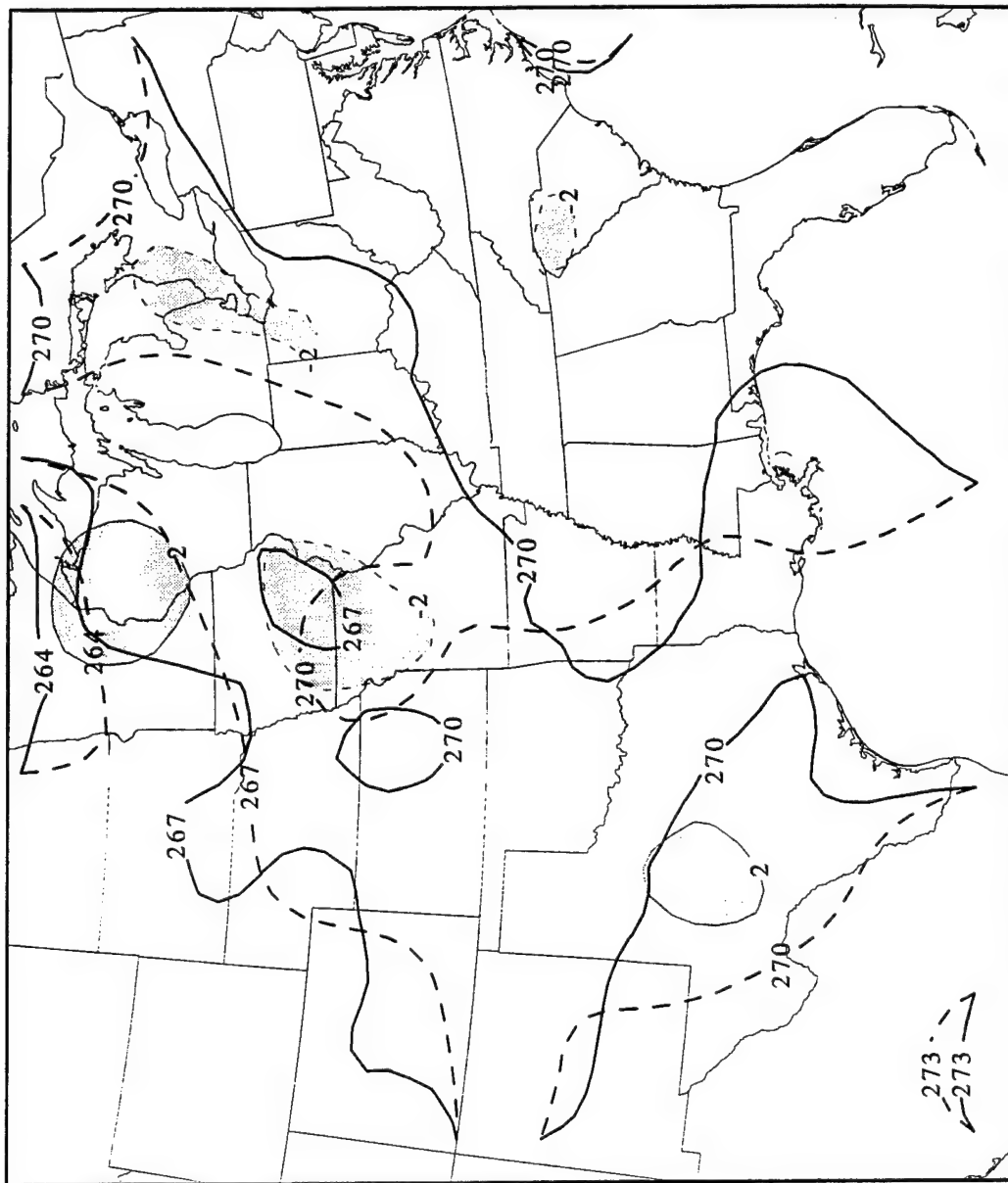


Figure 3.23. 950815/0000 500mb Retrieved temps.(solid, K),  
RAOB temps.(dashed, K), and difference(shaded, K).

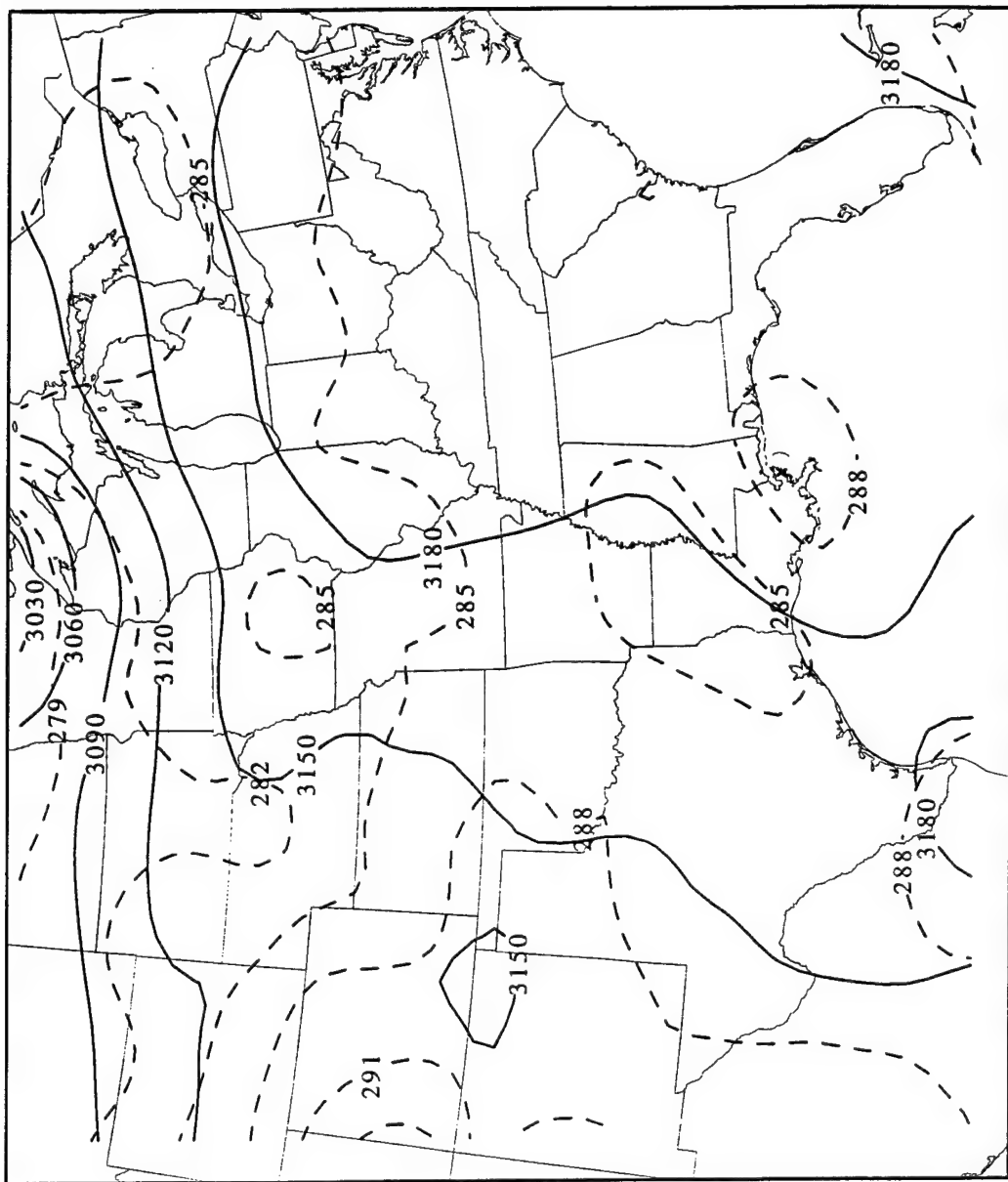


Figure 3.24. 950815/0000 700mb Retrieved heights(solid, m) and tmps.(dashed, K) using a smoother.



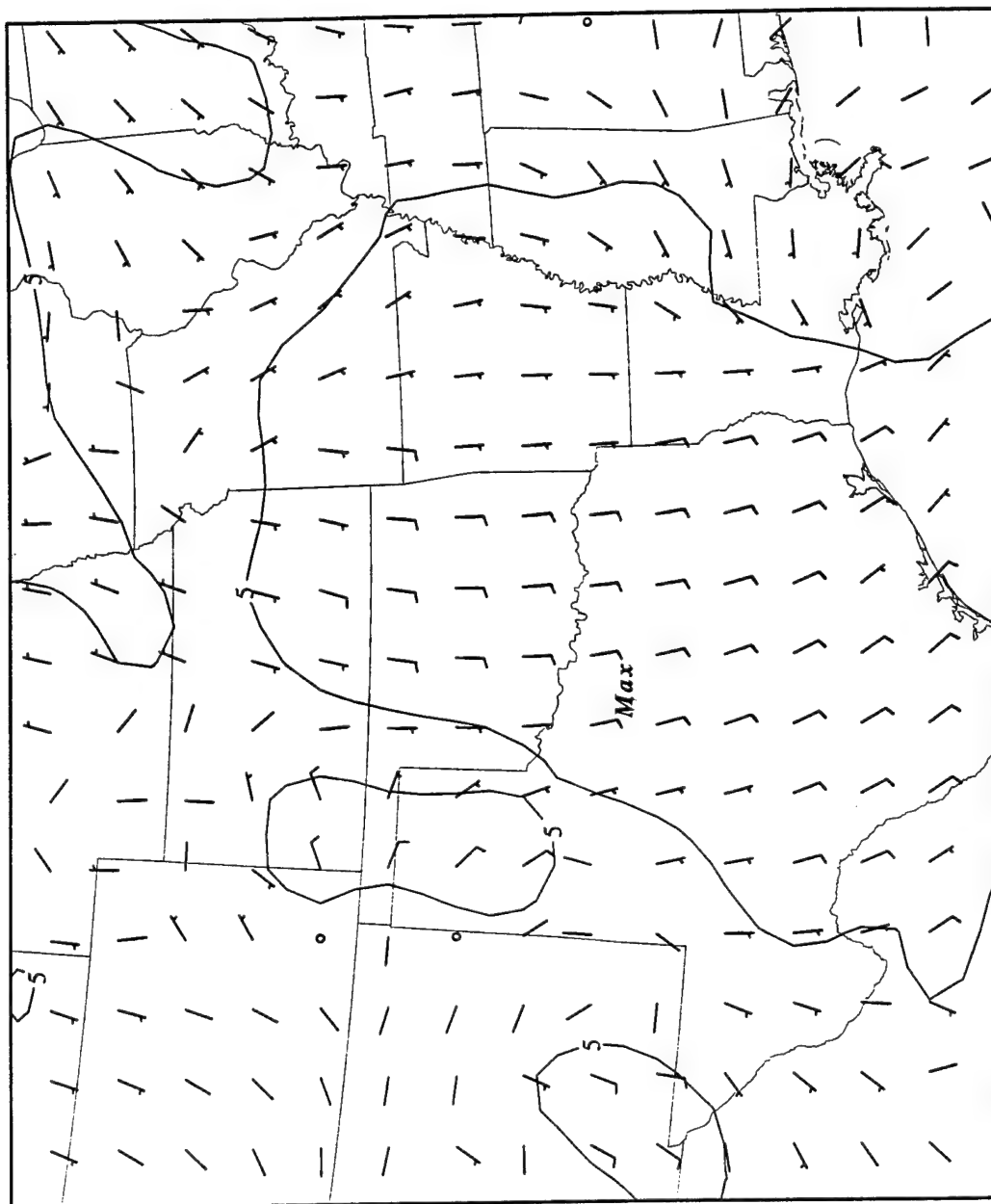


Figure 3.25. 950815/0000 900mb Profiler winds(m/s), isotachs(solid, m/s), and maximum wind location.

winds and curvature near the eastern slopes of the Rocky Mountains. The 850 mb analysis at 0200Z, shown in Figure 3.26, also shows a Wexler formation regime. Here, the winds do have speeds reaching  $15 \text{ m s}^{-1}$  which are very near thunderstorms in Texas. These stronger winds are converging into the convective line of showers located here.

Four hours later, at 0400Z, the 900 mb winds show a small increase in speed in central Oklahoma and eastern Texas (see Fig. 3.27). These winds would be classified as a Criterion 0 LLJ by Bonner (1968). The line of showers remains to the west of the large speed gradient which is the signal of a weak LLJ. At 850 mb, the  $15 \text{ m s}^{-1}$  maximum is still present at 0300Z, but has decreased in its aerial extent. By 0400Z (Fig 3.28) the wind maximum has gone and a new phenomenon has started to form in the same region of the maximum. This was discussed in the previous section. The cold air outflow of the thunderstorms in the area have influenced the wind field and have thus caused a meso-high to form. The thunderstorm outflow region can be seen as anticyclonic flow vectors over the Texas panhandle in Figure 3.28. Also, note the  $5 \text{ m s}^{-1}$  isotach in the 900 mb chart. Here the outflow represents an area of weaker wind speeds. In fact by 0500Z, the area of maximum winds has decreased in aerial extent in this region. The line of thunderstorms has inhibited the growth of the LLJ.

As the night progresses, weakened LLJs never reach Criterion 1. The 850 mb surface at 0800Z in Figure 3.29 shows only weak areas of a LLJ signal in northeastern Missouri. Even when the storm activity has died down at 1000Z, the 900 mb chart only has a weak Criterion 0 LLJ (Fig. 3.30). By this time, the night has progressed too far for any further LLJ enhancement. Mitchell et al. (1995) discussed this very result when they stated: *the acceleration of the LLJ can be viewed in a Lagrangian sense; that is, strong LLJs develop because air parcels accelerate as they travel along in the LLJ rather than strong LLJs being formed in situ.* After the storms have inhibited LLJ growth due to the terrain baroclinic effects as well as inertial-advective effects, no time exists for the acceleration of the LLJ during the stable PBL before the daytime mixing produces a convective PBL. Figure 3.31 affirms the destruction of the weak LLJ signals. Here, only a Criterion 0 signal can be found

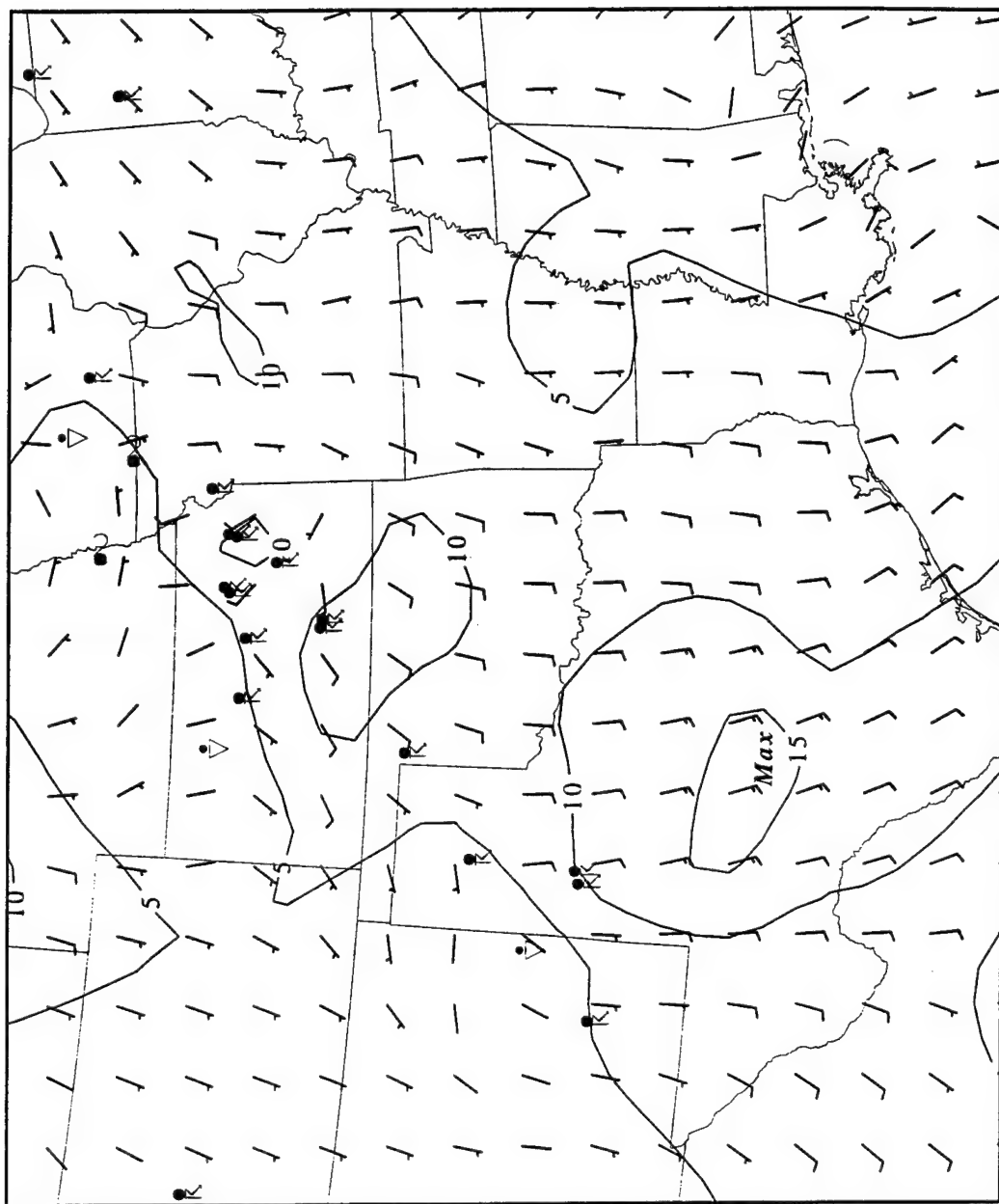


Figure 3.26. 950815/0200 850mb Profiler winds(m/s), isotachs(solid, m/s), WX, and maximum wind location.

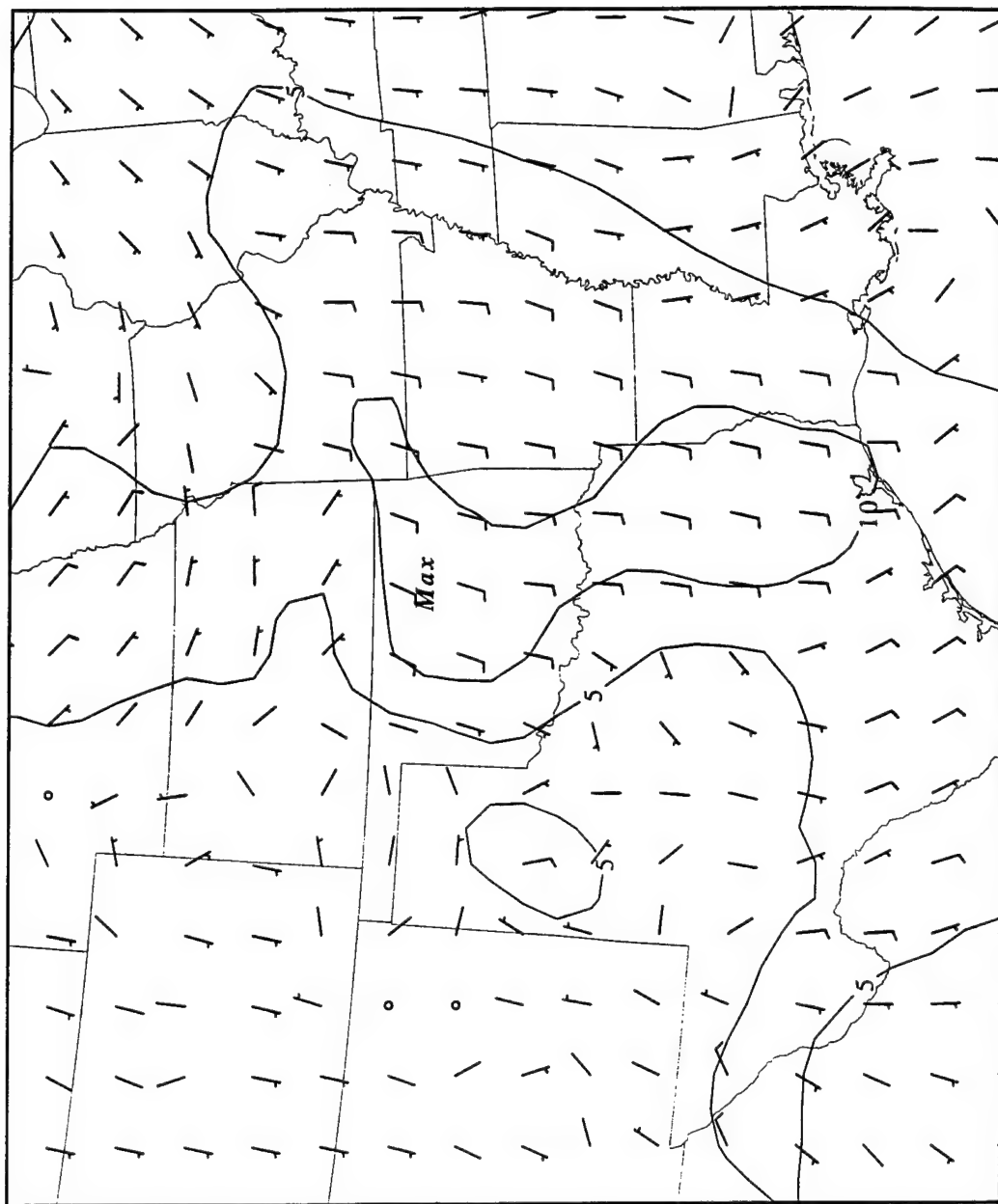


Figure 3.27. 950815/0400 900mb Profiler winds(m/s), isotachs(solid, m/s), and maximum wind location.

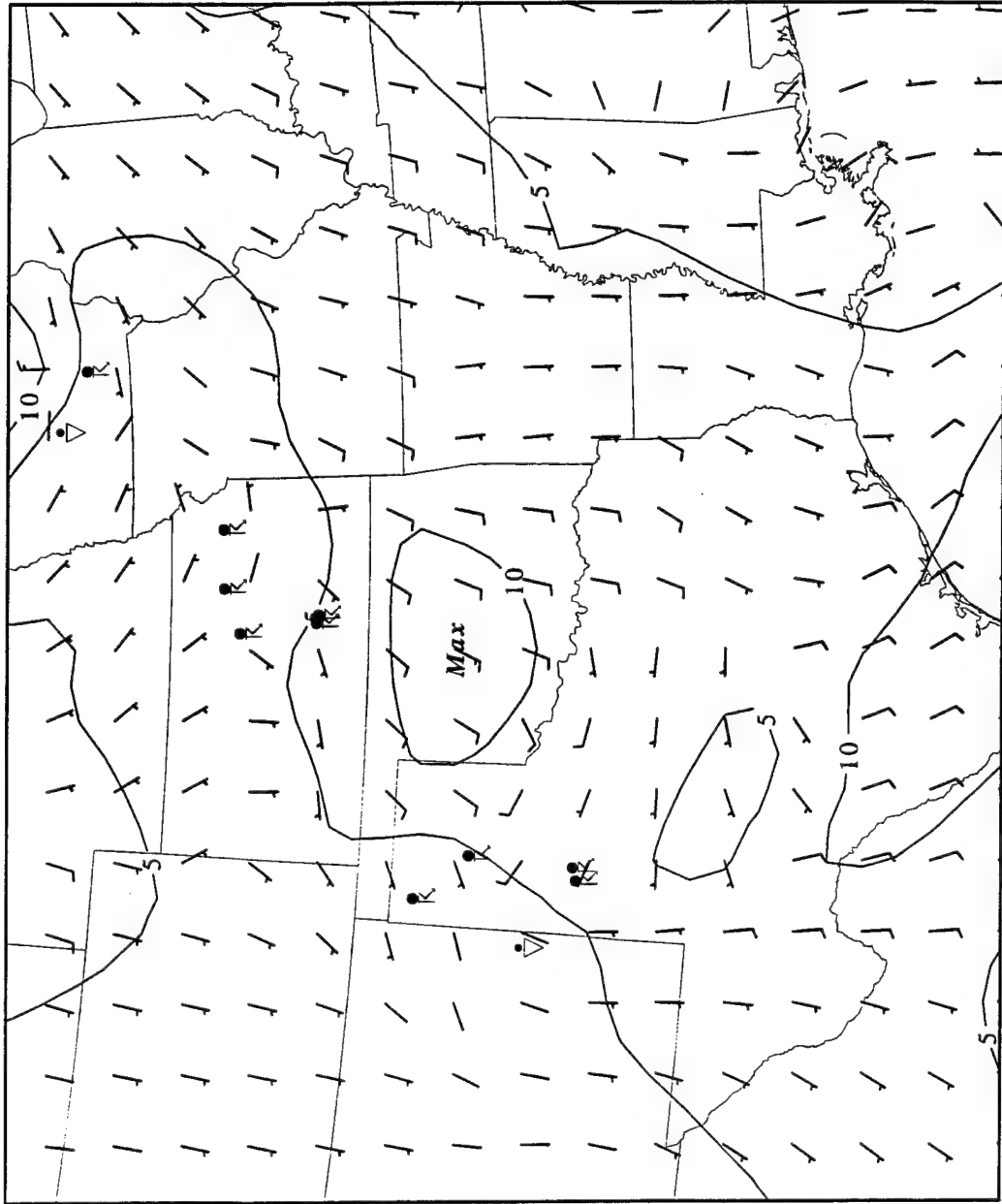


Figure 3.28. 950815/0400 850mb Profiler winds(m/s), isotachs(solid, m/s), WX, and maximum wind location.

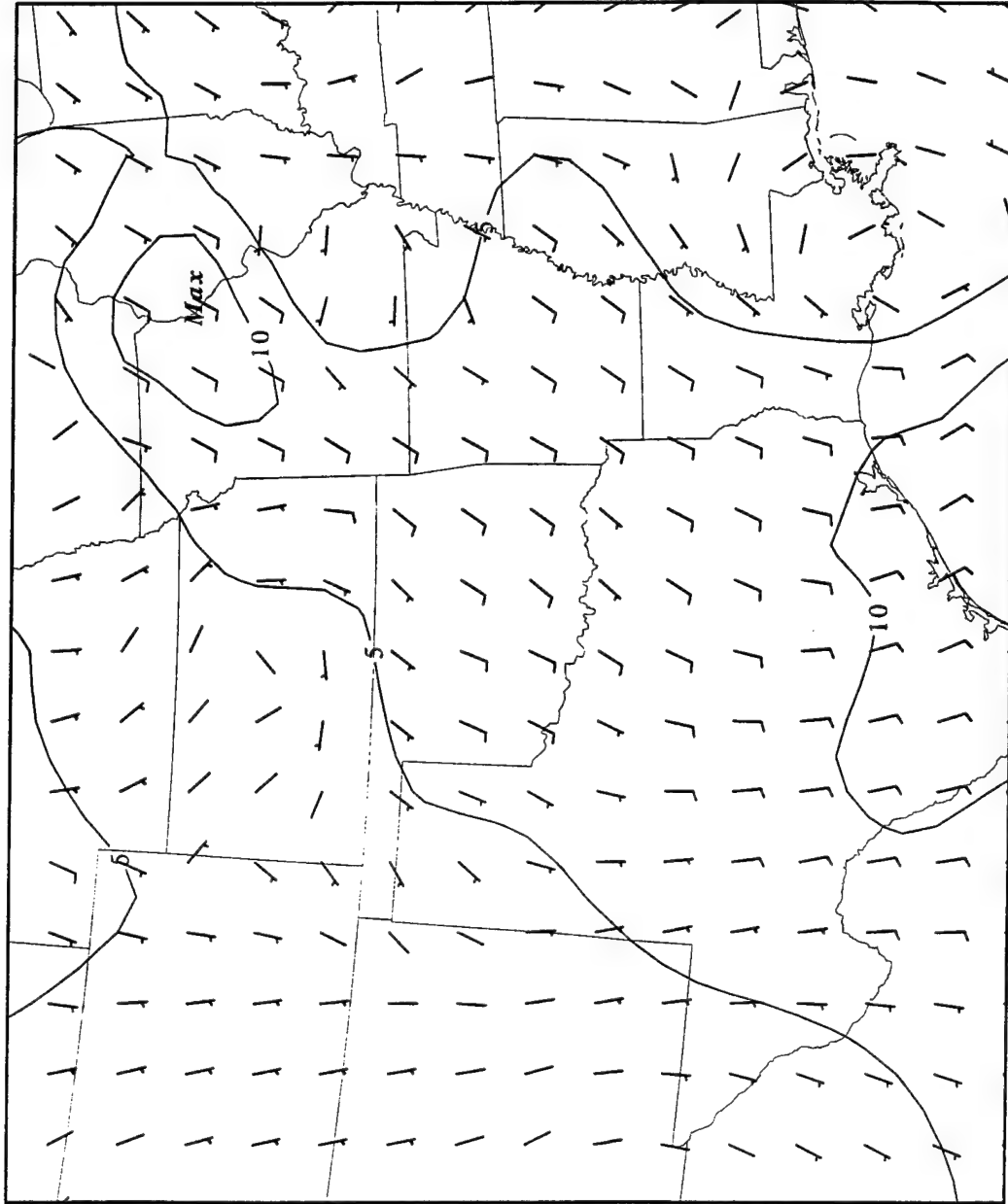


Figure 3.29. 950815/0800 850mb Profiler winds(m/s), isotachs(solid, m/s), and maximum wind location.

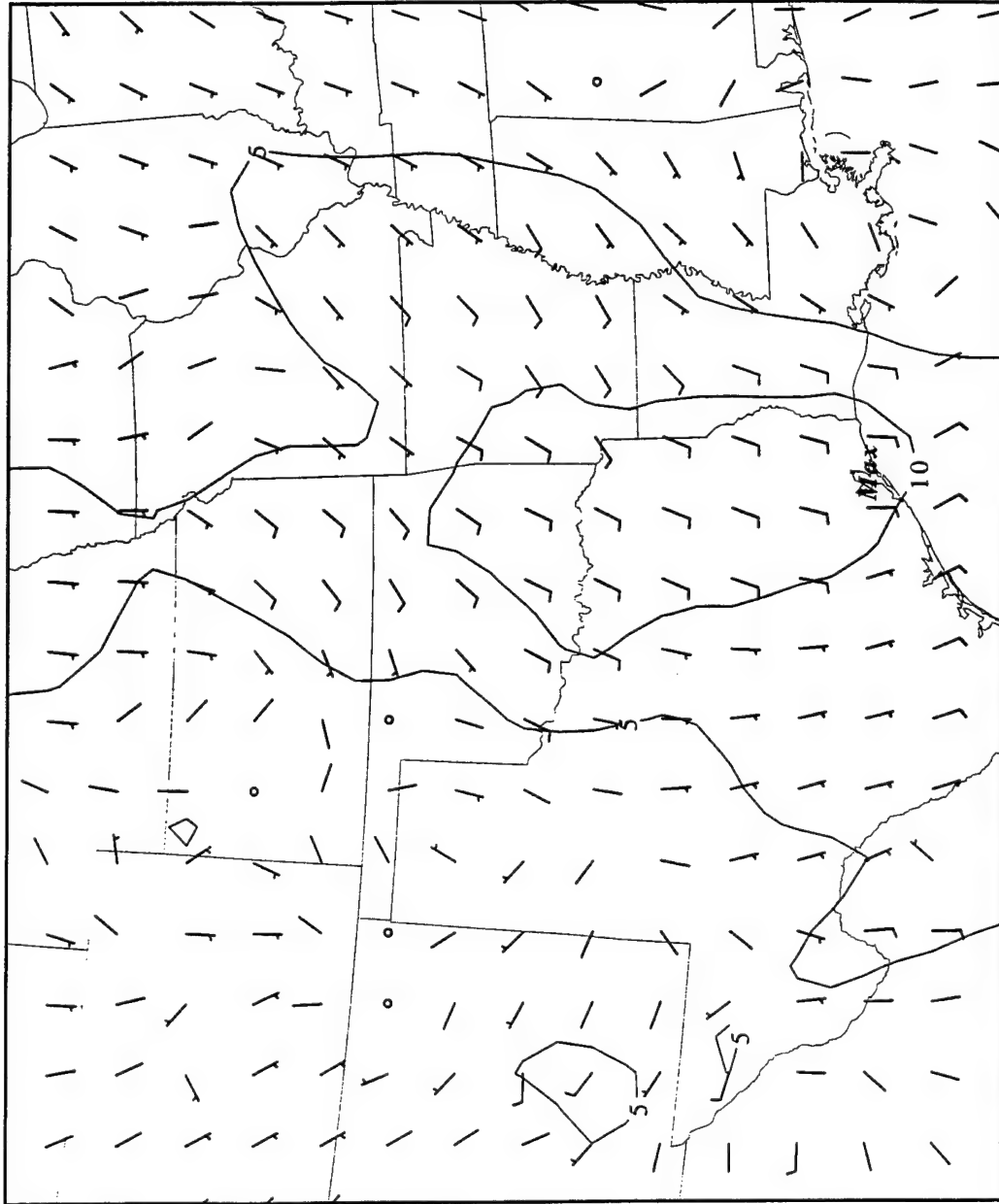


Figure 3.30. 950815/1000 900mb Profiler winds(m/s), isotachs(solid, m/s), and maximum wind location.

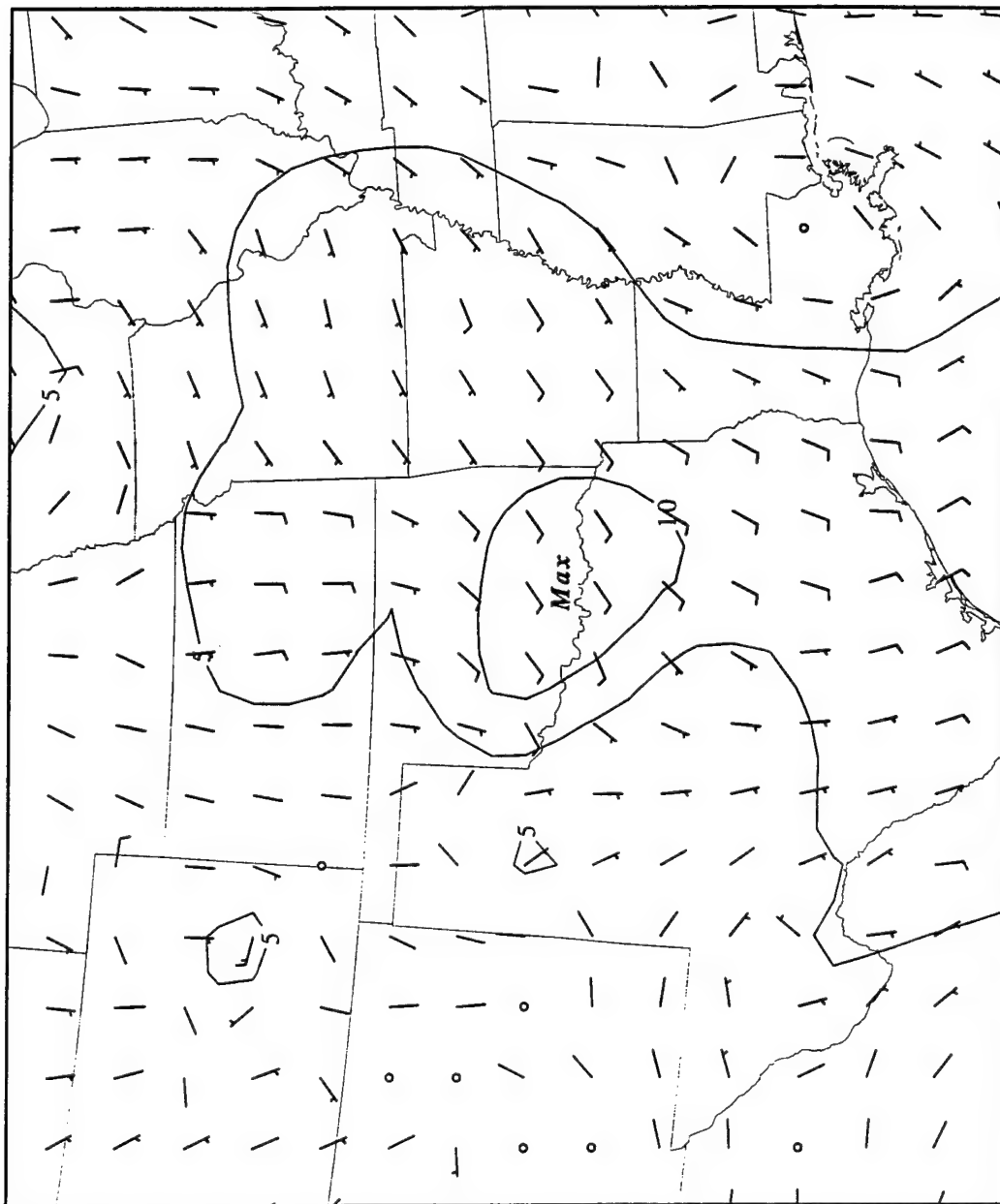


Figure 3.31. 950815/1400 900mb Profiler winds(m/s), isotachs(solid, m/s), and maximum wind location.



in the Red River Valley as the wind speeds have diminished from the earlier morning's speeds.

Throughout the course of the daylight hours of 15 August, the wind speeds remain weak. The Criterion 0 signal in northeastern Oklahoma remains weak and does not intensify. By 0000Z on 16 August the synoptic situation is more favorable for LLJ formation due to the fact that the convection is weaker and is located further north than the night before (Fig. 3.32). Again, the winds at 900 mb are showing a pattern similar to what Wexler (1967) discussed. At 700 mb, the winds also show a max in the Oklahoma-Kansas area at 0100Z on 16 August (Fig. 3.33). What is causing this early-evening maximum in wind speeds with larger vertical extent (900 mb to 700 mb) to occur? Looking at the retrieved heights and winds during this period reveal a short-wave trough in the Kansas, Nebraska, and Missouri area at 500 mb (Fig. 3.34). Here, the winds show a small jet appearance just ahead of the trough. *This leads to the belief that a transverse-ageostrophic circulation may be the cause of this weaker LLJ.*

A cross section taken from Scottsbluff, Nebraska (BFF) to Knoxville, Tennessee (TYS) at 1800Z on 15 August is done to show the structure of the 500 mb jet and the associated ageostrophic motions (Fig. 3.35). The city locations are indicated in Figure 3.34. Notice that the 330 K isentrope slopes downward from western Nebraska to eastern Kansas. This indicates cold air to the northwest of the jet entrance region and warm air to the southeast. The ageostrophic wind vectors generally indicate ascent and a northwestward orientation around the middle of the cross section. This is where the circulation contour (dotted in Figure 3.35) is located just below 500 mb over Kansas City. This indicates ascent within the right rearward quadrant of the midtropospheric jet streak oriented from Illinois to Arkansas as seen in Figure 3.34. This ascent is generally centered around Kansas City and the wind fields beneath this feature indicate a relative maximum entering into the ascent zone from 700 mb through 500 mb. Underneath the ascent, an area of pressure falls exist (see the isallobaric winds in Fig. 3.36) resulting in deep LLJ feeding into the right entrance region of the streak located just to the southeast of the circulation center. This 500 mb

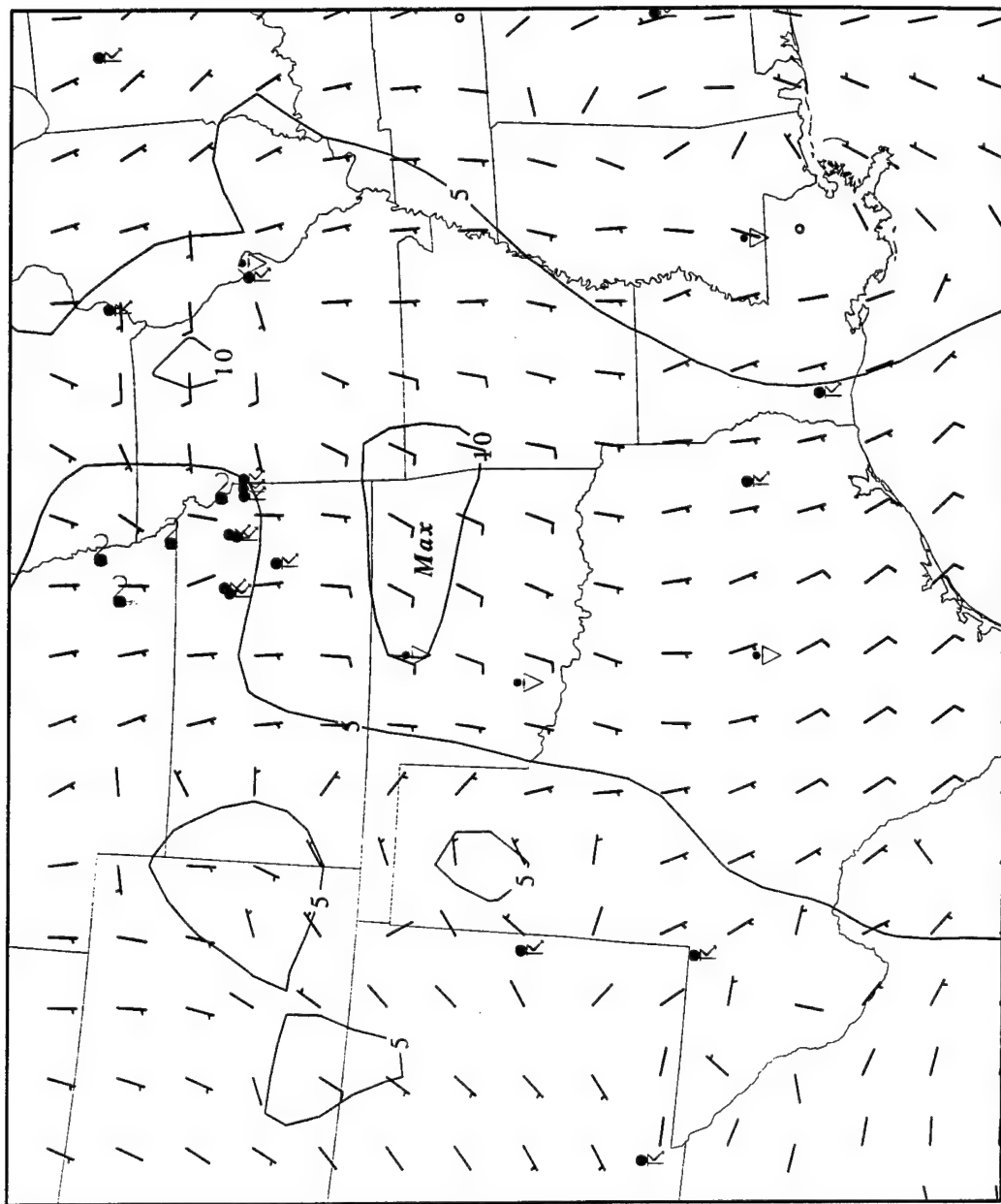


Figure 3.32. 950816/0000 900mb Profiler winds(m/s), isotachs(solid, m/s), WX, and maximum wind location.

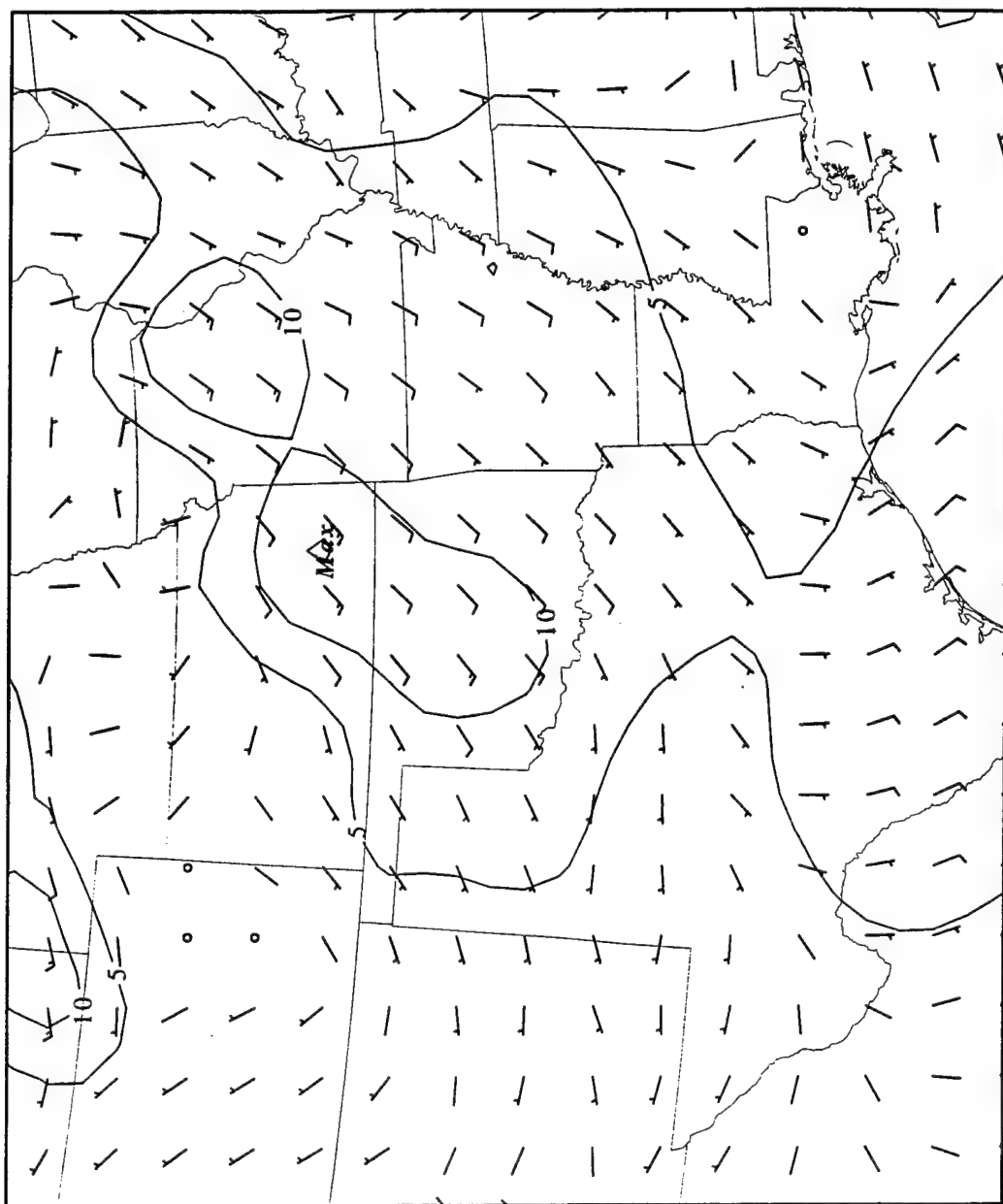


Figure 3.33. 950816/0000 700mb Profiler winds(m/s), isotachs(solid, m/s), WX, and maximum wind location.

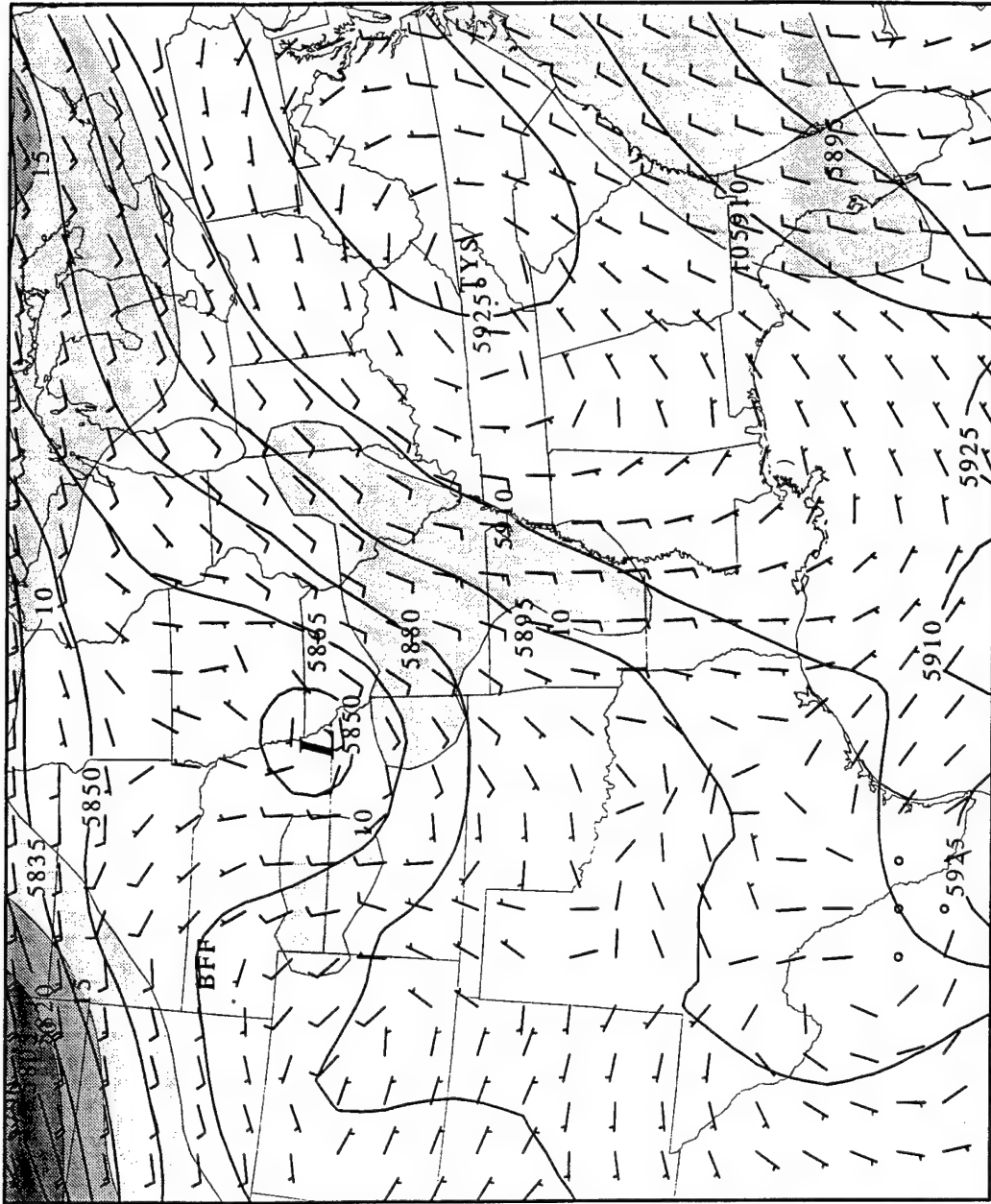


Figure 3.34. 950816/0300 500mb Retrieved heights(solid, m), winds, speed(shaded, >10m/s), and station locations.

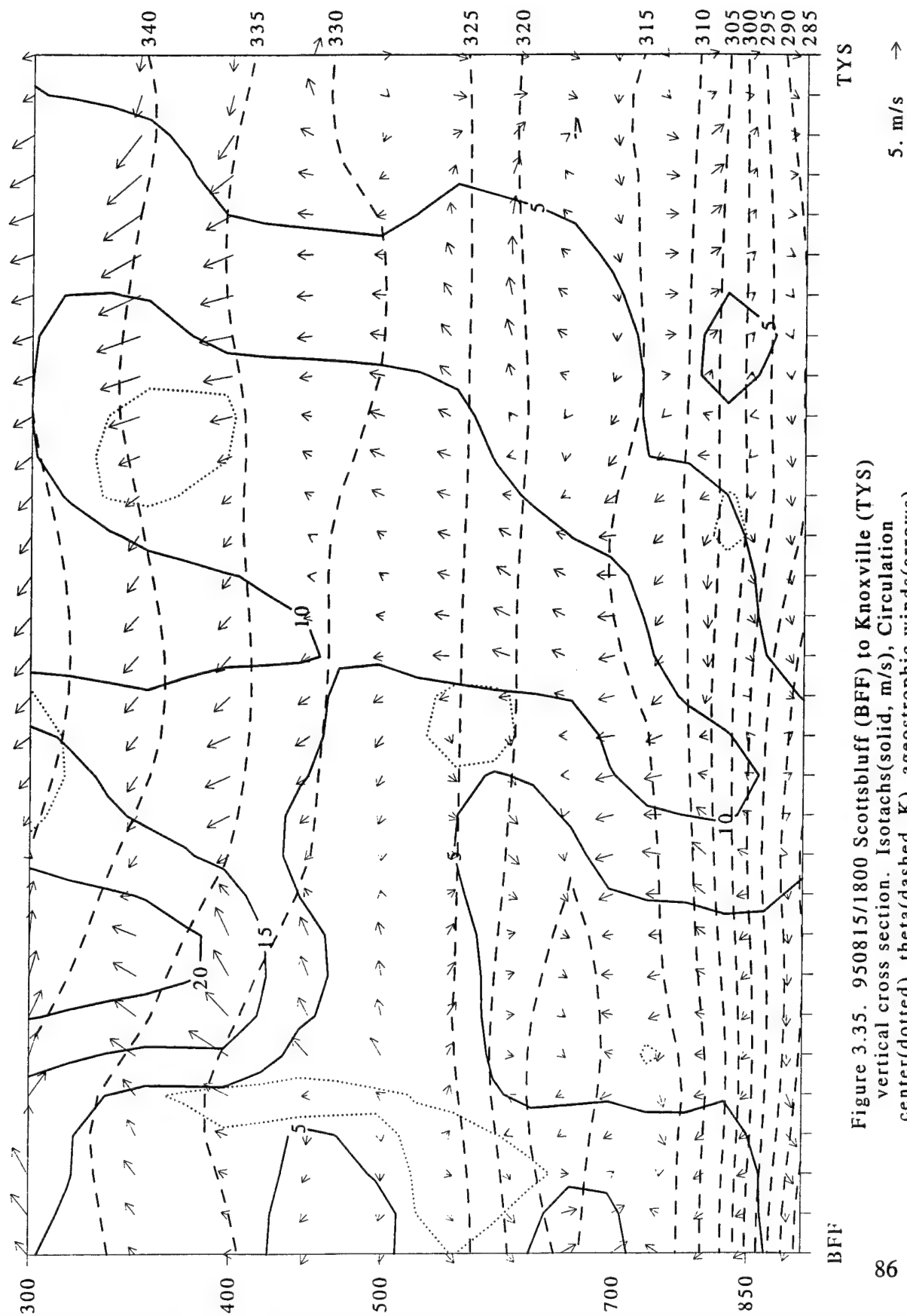


Figure 3.35. 950815/1800 Scottsbluff (BFF) to Knoxville (TYS) vertical cross section. Isotherms(solid, m/s), Circulation center(dotted), theta(dashed, K), ageostrophic winds(arrows).

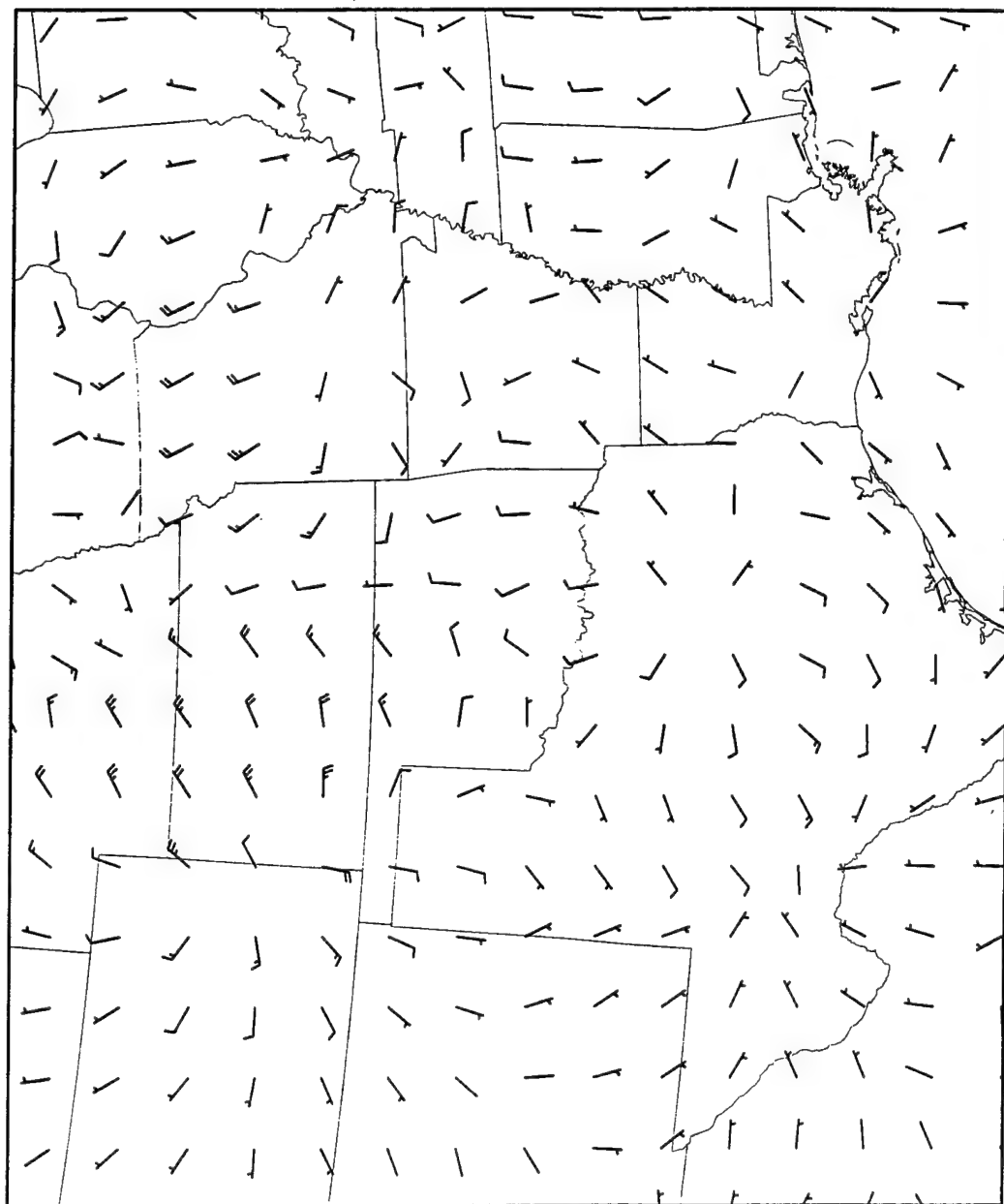


Figure 3.36. 950816/0200 : 950816/0300 850mb Isallobaric winds(m/s).

trough and its associated transverse ageostrophic LLJ continue to exist until 0300Z on 16 August.

By 0400Z the 900 mb chart (not shown) reveals a promising extension of the  $10 \text{ m s}^{-1}$  isotach in the Red River Valley. There is also a lack of convective activity in the area. By 0500Z, the  $15 \text{ m s}^{-1}$  isotach has formed over central Oklahoma at both 900 mb and 850 mb (see Figs. 3.37 and 3.38). The  $10 \text{ m s}^{-1}$  region has also pushed further north and now extends from Texas to Iowa enlarging the coverage of the main LLJ signal for 16 August.

At 0700Z on 16 August, the LLJ has reached its maximum speed of  $19 \text{ m s}^{-1}$ . This makes the main LLJ a Criterion 2 (nearly Criterion 3) by the Bonner (1968) scale. Figure 3.39 shows the extent of the LLJ at 900 mb. Here, the convection is quite weak. Notice the strong speed gradient along the western boundary of the LLJ as it reaches the upslope region east of the Rockies. Also, the simplistic description of a sheet-like form for the LLJ is apparent. The surface winds below the LLJ core are at or below  $5 \text{ m s}^{-1}$ . At 850 mb the speeds are above  $15 \text{ m s}^{-1}$  in the 900 mb core region (see Fig. 3.40). In Figure 3.41, the 750 mb winds in the vicinity of the LLJ are around  $10 \text{ m s}^{-1}$  showing a definite decrease in the wind speed in the vertical.

By looking at a vertical cross sectional slice through the LLJ, a different perspective of the LLJ can be seen. In Figure 3.42 the slice starts at Garden City, Kansas (GCK) and finishes at Fort Leonard Wood, Missouri (TBN). The city locations are indicated in Figure 3.39. The Criterion 2 LLJ is located in the middle of the cross section. Notice the jet core appearance of the isotachs similar to that of a deep tropospheric jet. Another scalar which has similar patterns is the velocity divergence. Figure 3.43 shows the divergence around the 900 mb LLJ. The entrance region of the classic LLJ shows strong convergence (opposite of divergence) and the exit region shows strong divergence.

So what causes this Criterion 2 LLJ to form? Is it any stronger than the ambient geostrophic winds? Figure 3.44 shows the linearly-interpolated RAOB observed winds at 0700Z at 850 mb. These winds are obviously much weaker than the profiler-enhanced wind field. In Figure 3.45 the geopotential heights are used to calculate the geostrophic winds.

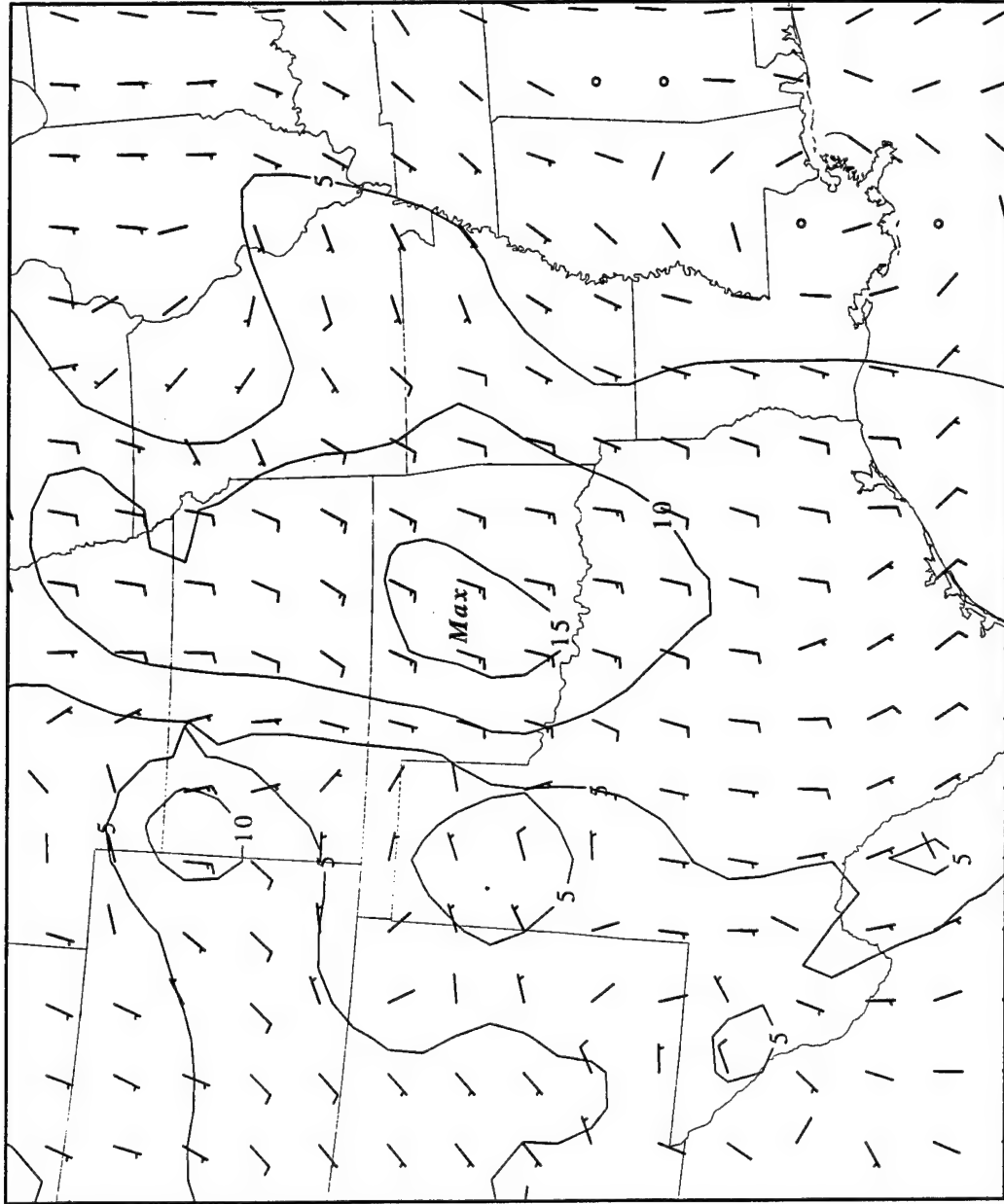


Figure 3.37. 950816/0500 900mb Profiler winds(m/s), isotachs(solid, m/s), and maximum wind location.



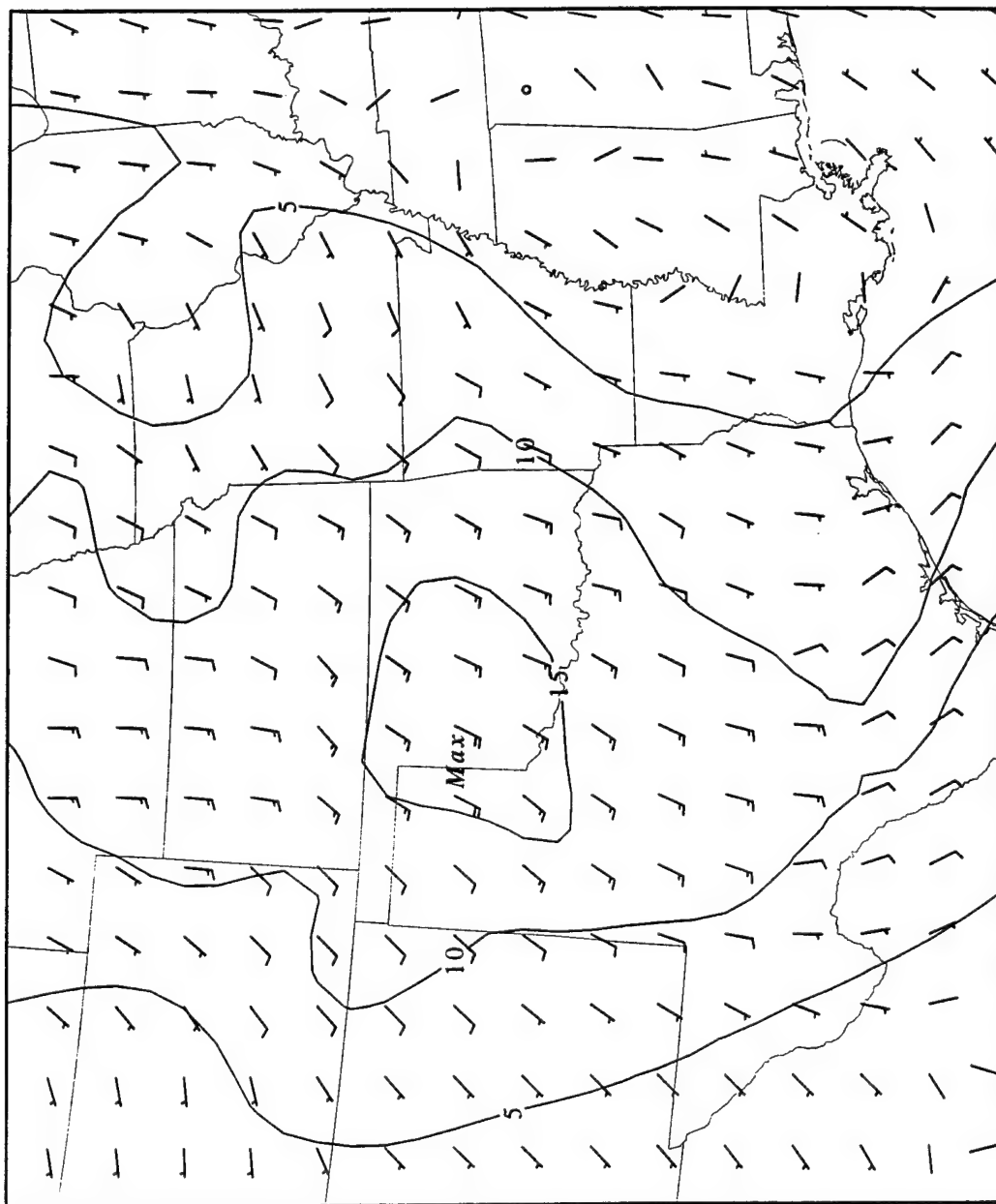


Figure 3.38. 950816/0500 850mb Profiler winds(m/s), isotachs(solid, m/s), and maximum wind location.

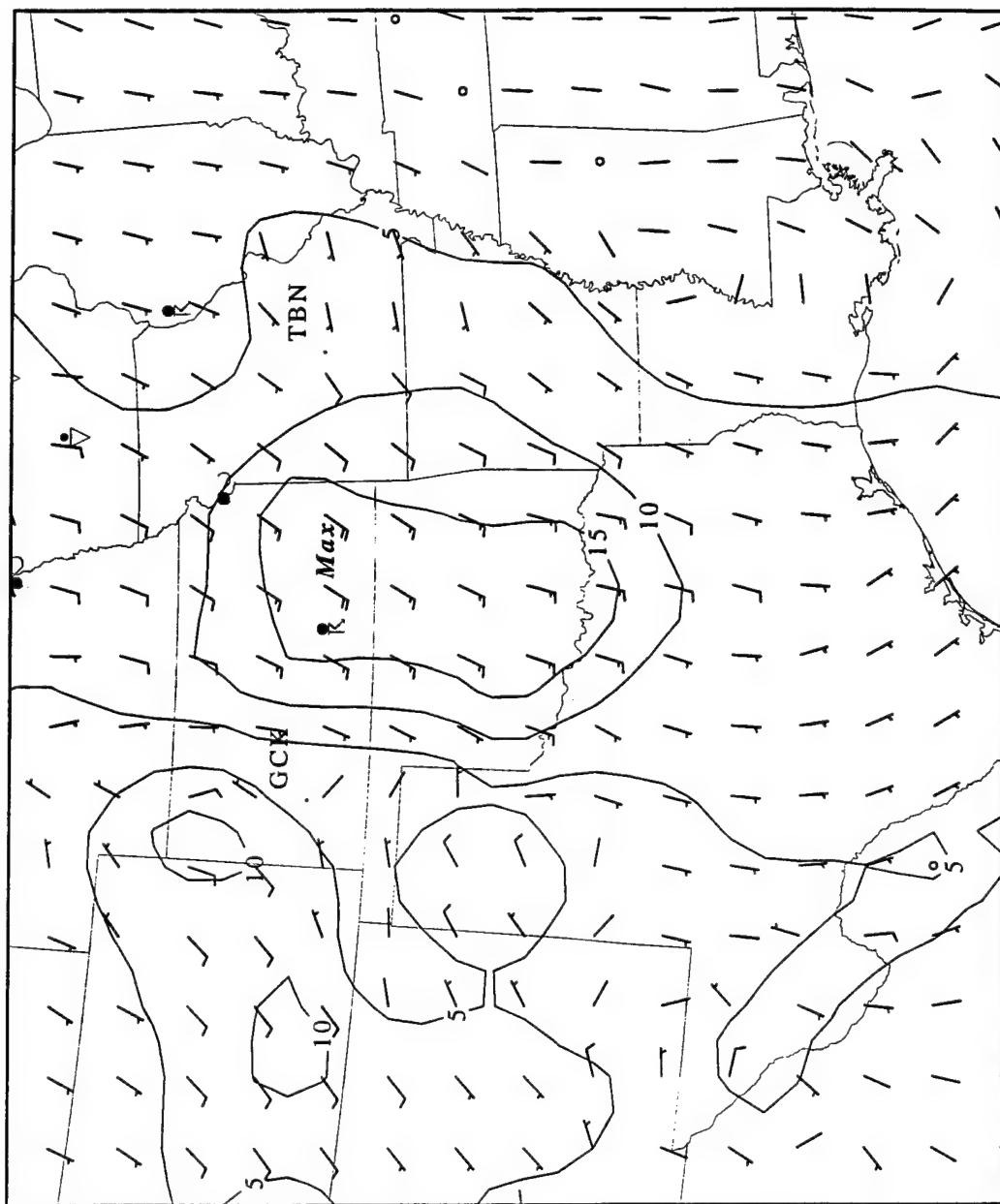


Figure 3.39. 950816/0700 900mb Profiler winds(m/s), isotachs (solid, m/s), station locations, WX, and maximum wind location.

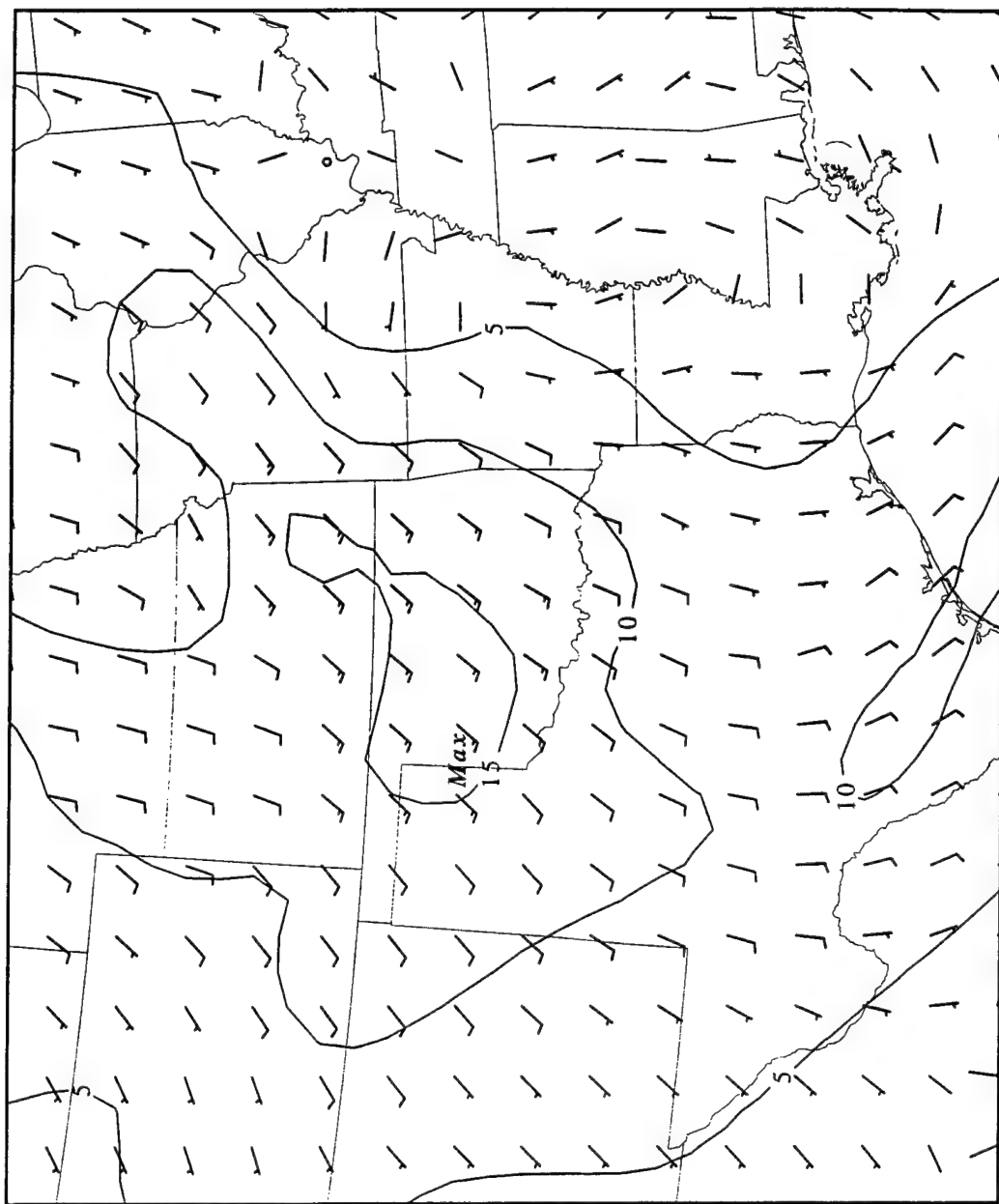


Figure 3.40. 950816/0700 850mb Profiler winds(m/s), isotachs(solid, m/s), and maximum wind location.

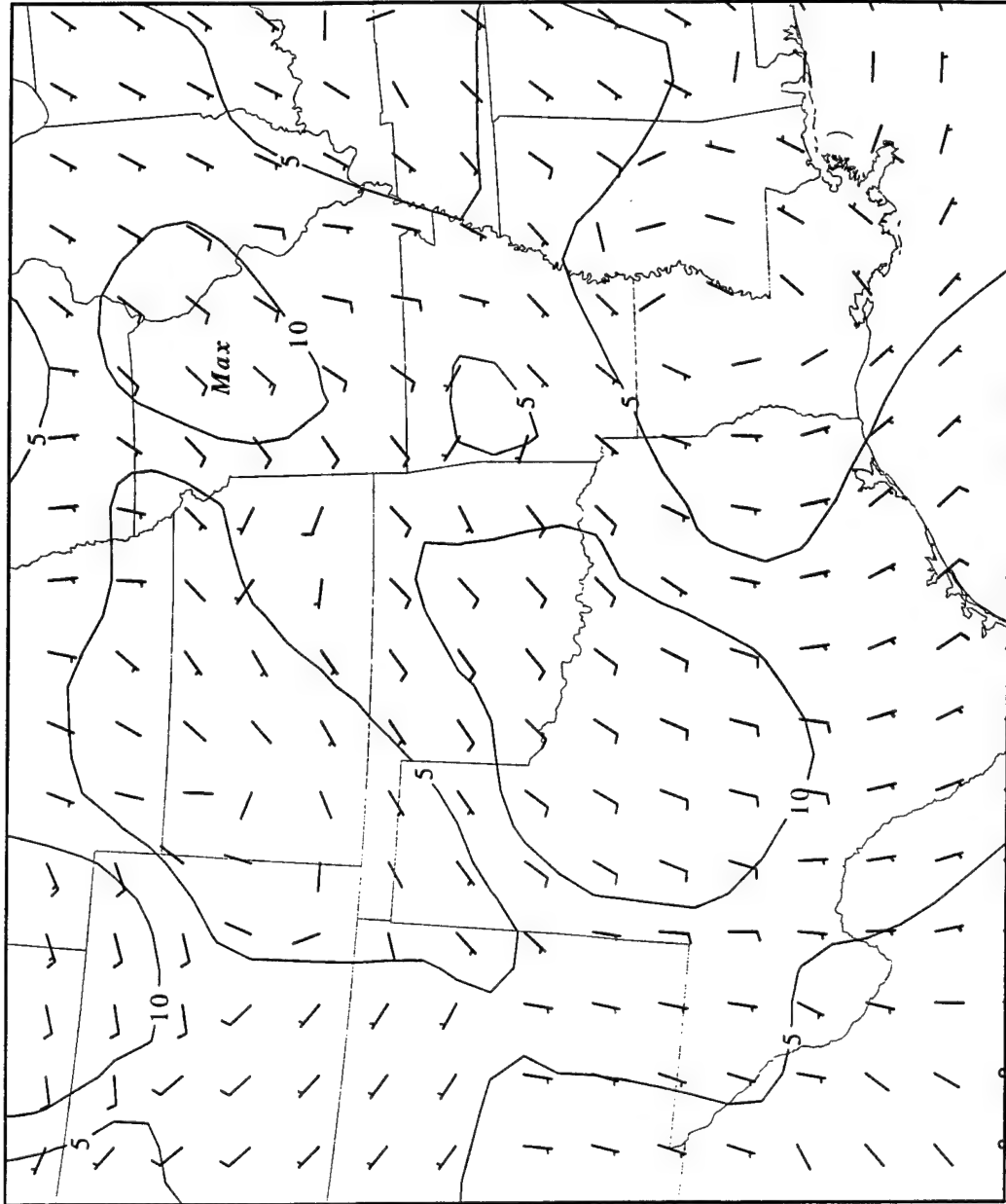


Figure 3.41. 950816/0700 750mb Profiler winds(m/s), isotachs(solid, m/s), and maximum wind location.

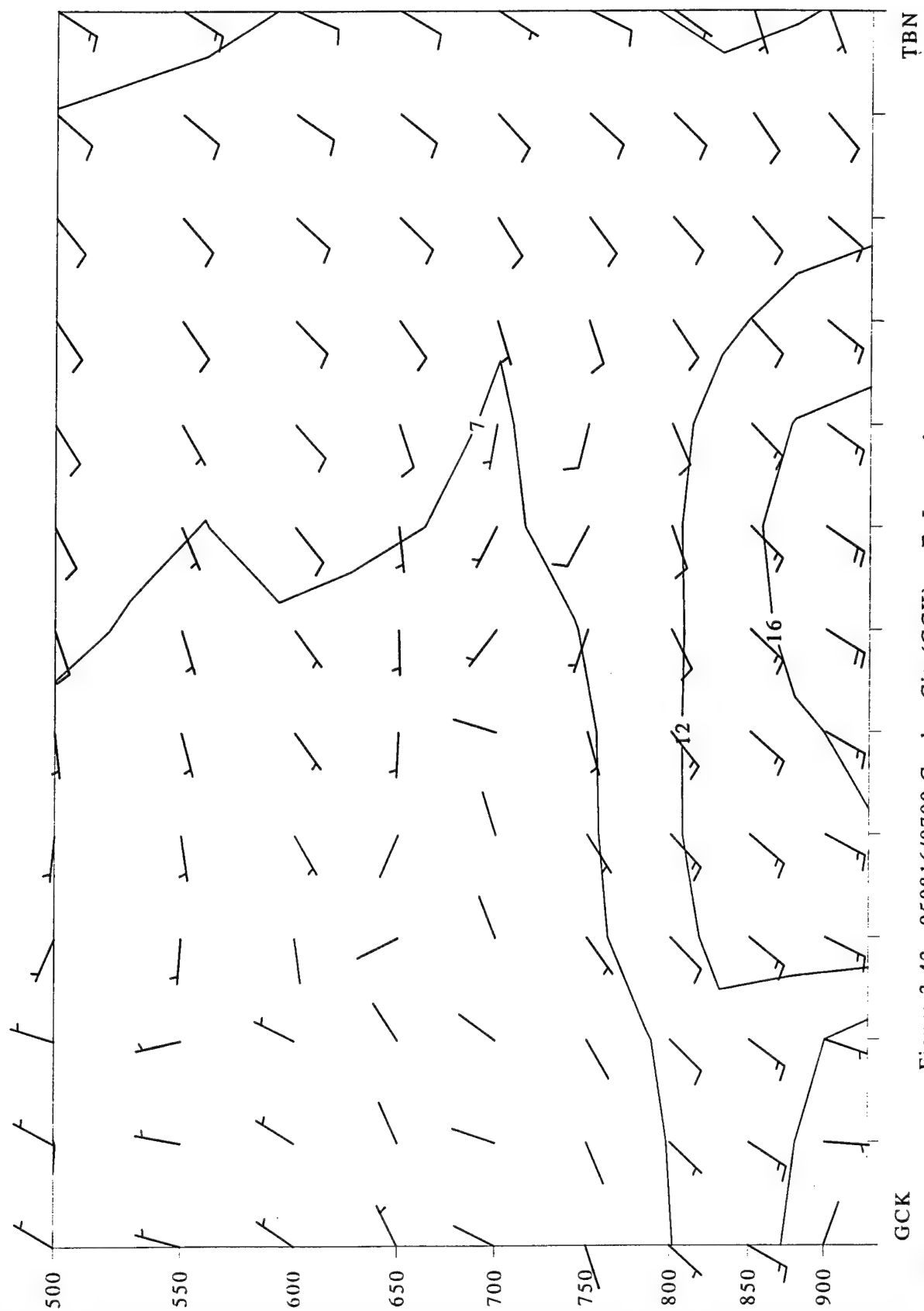


Figure 3.42. 950816/0700 Garden City(GCK) to Ft Leonard Wood(TBN) vertical cross section, isotachs(solid, m/s).

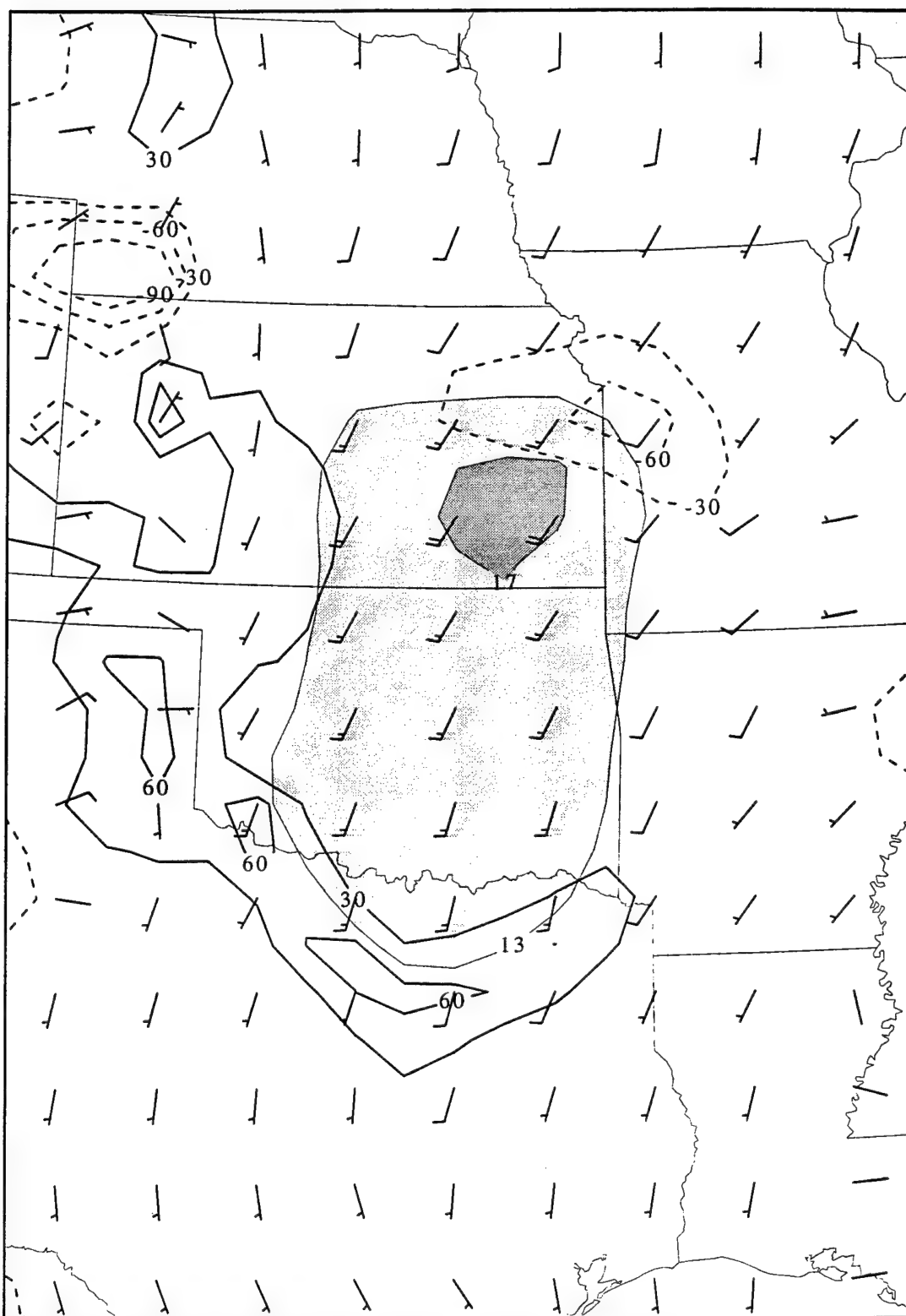


Figure 3.43. 950816/0700 900mb Profiler winds(m/s), speed (shaded, >13m/s, >17m/s), divergence(solid,  $\times 10^{+6}/s^{+2}$ ), and convergence(dashed,  $\times 10^{+6}/s^{+2}$ ).

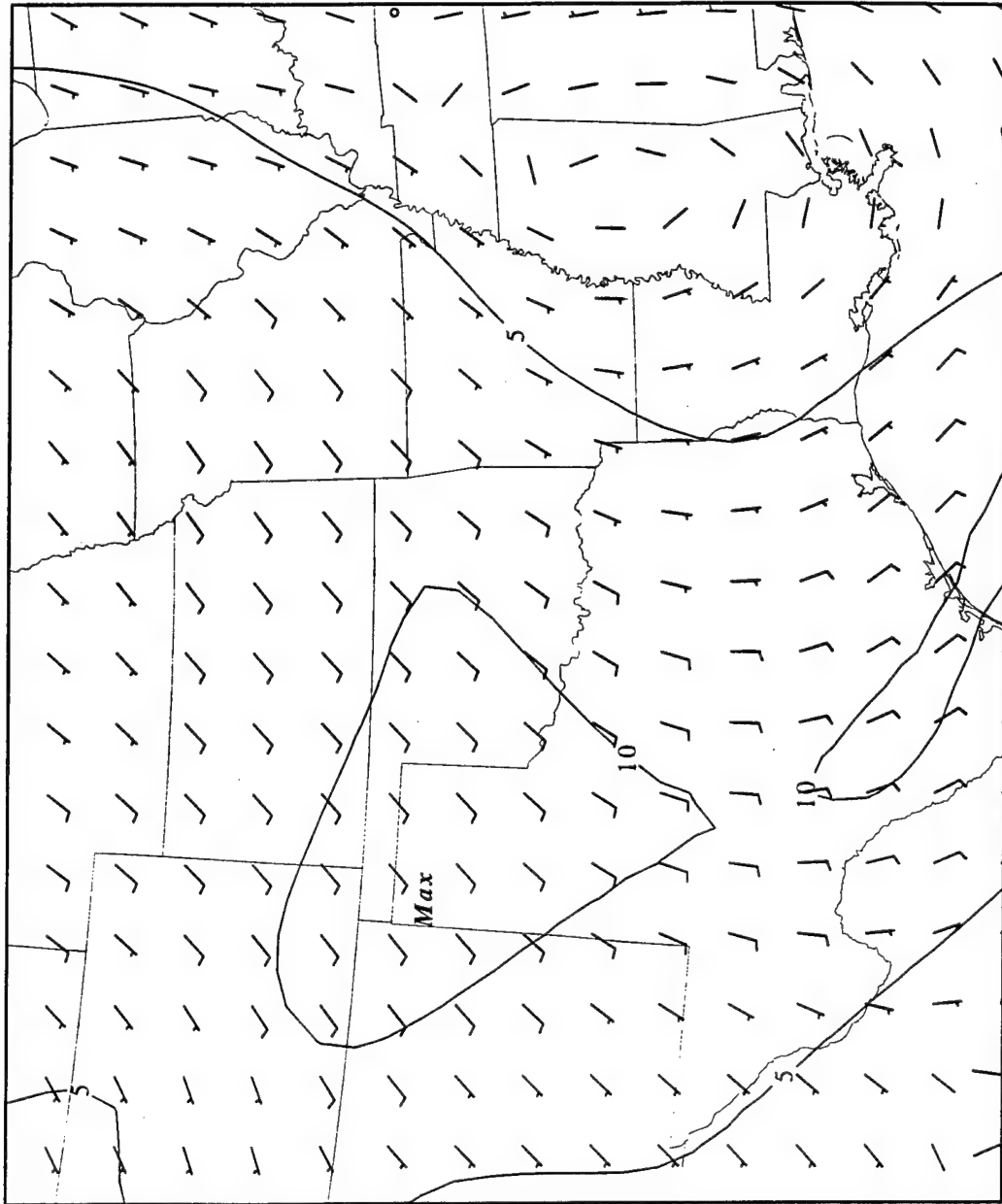


Figure 3.44. 950816/0700 850mb ROAB winds(m/s), isotachs(solid, m/s), and maximum wind location.

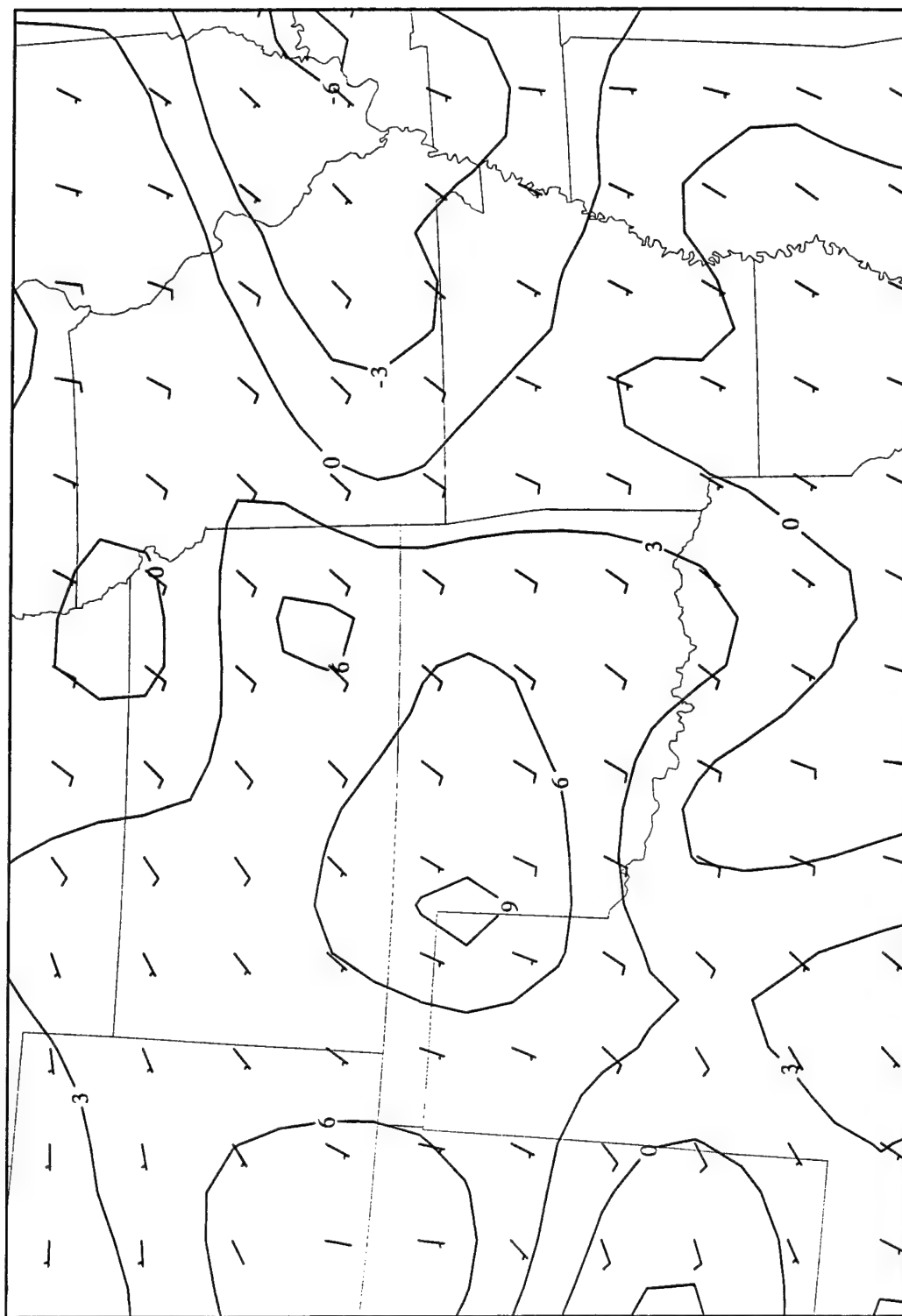


Figure 3.45. 950816/0700 850mb RAOB geostrophic winds(m/s), and speed difference from profiler winds(solid, m/s).



This shows just what the speed should be under typical quasi-geostrophic flow usually found in the middle troposphere. In the vicinity of the LLJ, the winds do not exceed  $12 \text{ m s}^{-1}$ . The isopleths shown are the differences calculated by subtracting the profiler wind speeds from the geostrophic wind speeds. There is obviously quite a difference in the speeds around the classic LLJ in western Oklahoma. What are the forcing mechanisms which cause this speed enhancement?

In order to see some of the mechanisms at work, a look back at the beginning of the review period, 0000Z on 15 August, is needed. Figure 3.46 shows two parameters. The contour is the 200 mb isotach at  $30 \text{ m s}^{-1}$  intervals. This shows the location of the upper-level jet. It is shown here that the jet entrance region lies over eastern Wyoming. Figure 3.46 also displays the ageostrophic wind at 900 mb defined as:

$$\mathbf{V}_{\text{age}} = \mathbf{V} - \mathbf{V}_{\text{geo}}. \quad (15)$$

Near the entrance region, there is a transverse ageostrophic circulation signal in the wind field as described by theory (e.g., Uccellini and Johnson 1979) (see Fig. 3.46). This northwesterly wind (low-level return branch circulation) in southeastern Wyoming is obviously in opposition to any LLJ formation. In Section 1.2 the forcing mechanism related to LLJ formation discusses the *exit* region of the upper-level jet. As just shown in Section 3.1.2, the jet moves outside of the grid as the time progresses. No jet exit region exists over the LLJ area. *Thus, the classical transverse ageostrophic circulation as described by Uccellini and Johnson is not the cause of the LLJ formation in the Texas-Oklahoma-Kansas area on the morning of 16 August.*

The ageostrophic winds are still beneficial to this case study, however. Fast and McCorcle (1990) describe it best: *During the day, an ageostrophic upslope component is induced producing easterly winds near the surface due to differential heating across the slope; the magnitude of this upslope wind depends on the slope of the terrain. Near sunset, the upslope wind decreases as the temperature difference is reduced across the slope. The Coriolis force acts to turn the ageostrophic component to the right, producing southerly winds some time during the night. In addition, the higher slopes cool faster at night, forcing*

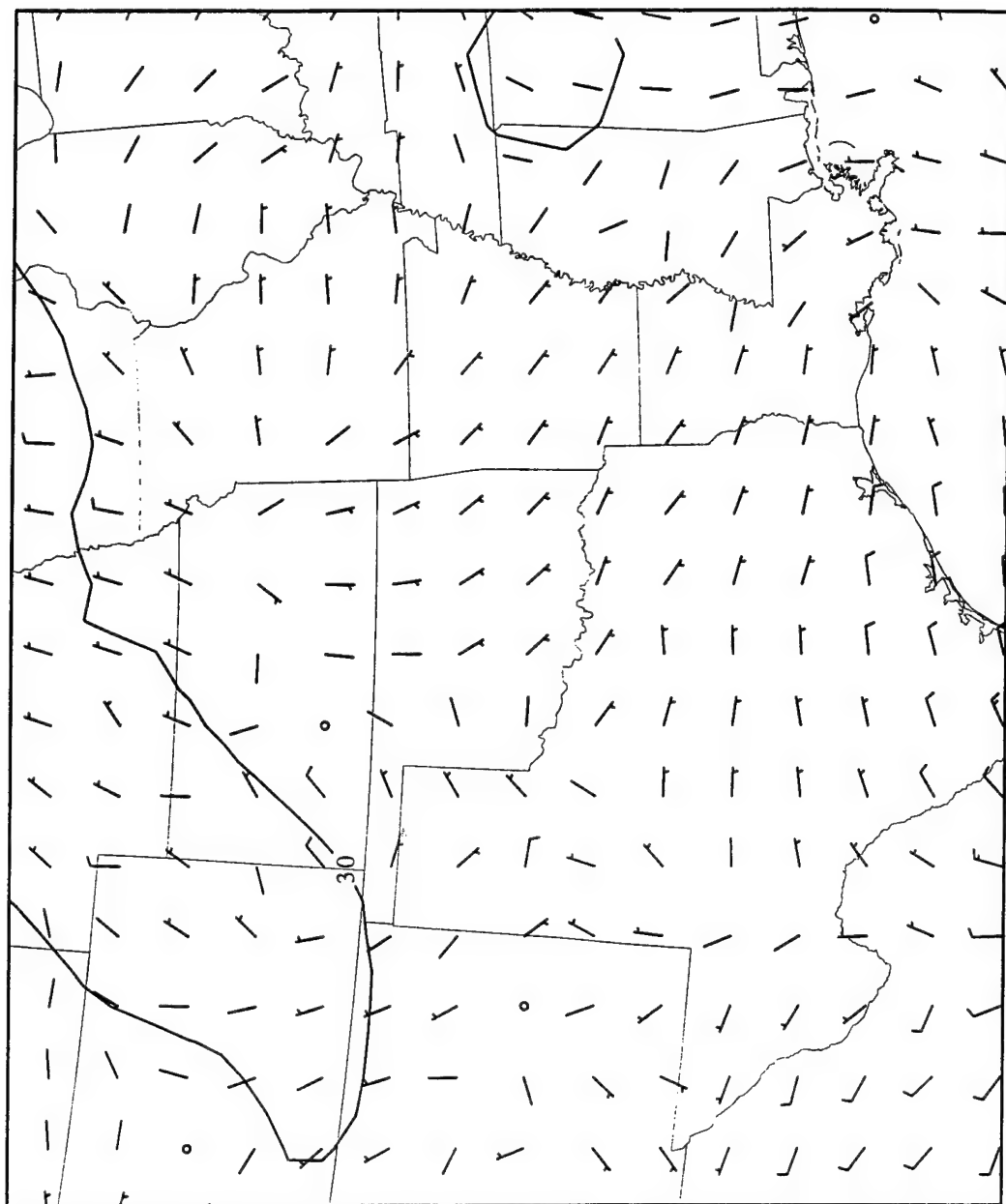


Figure 3.46. 950815/0000 900mb Ageostrophic winds(m/s),  
and 200mb isotachs(solid, m/s).

*a downslope ageostrophic component that increases during the night. This can affect the magnitude and rate of rotation of the supergeostrophic wind if the slope of the terrain is significant.* In Figure 3.46, the 0000Z 15 August sunset ageostrophic winds in central Texas are definitely showing an upslope component. This can also be seen in Figure 3.47 during the day in the area where there will be strong LLJ development. The opposite effect of downslope winds can also be observed during this period (Figs. 3.48 and 3.49) in the central Oklahoma area.

As mentioned above, the ageostrophic winds are indicative of a temperature gradient near and just above the surface on sloped terrain. Figures 3.50 and 3.51 show MASS model simulated output of the temperature at 0000Z (daytime) and 1200Z (nighttime) on 16 August, respectively at 900 mb. A weak, but opposite, temperature gradient can be found in these figures. This is representative of the baroclinicity effects discussed in Section 1.2. In that section, the dynamical concept of an inertial oscillation was also reviewed. Blackadar (1957) described a rotating wind in the clockwise direction for the beginning of LLJ formation. Figure 3.52 depicts this feature by showing the change in the wind direction at four stations in and around the classic nocturnal LLJ. This sort of chart could not have been produced with any accuracy if only RAOB winds were used. The addition of wind profilers is very crucial for the study of LLJs. The station PNC, located in northern Oklahoma, also shows the oscillation effect for a single station (Fig. 3.53). By observing the isotachs and the wind barbs at the 900 mb and 850 mb levels, the rotation of the winds is seen.

The combined effects of the inertial oscillation and baroclinicity are both forcing functions acting in the development and continuation of the classic Criterion 2 LLJ. The theories of both can be observed in the figures provided here. Wexler's theory, while beneficial because it lays out a favorable synoptic situation, cannot fully explain the diurnal period of the LLJ. With differential heating of a sloped terrain (an obviously diurnal effect) the forces are put into motion for the development of a classic LLJ.

By 1000Z on 16 August, the LLJ is still apparent, although it is slightly weaker (Figs. 3.54 and 3.55). The jet has also moved gradually to the north and east as is generally

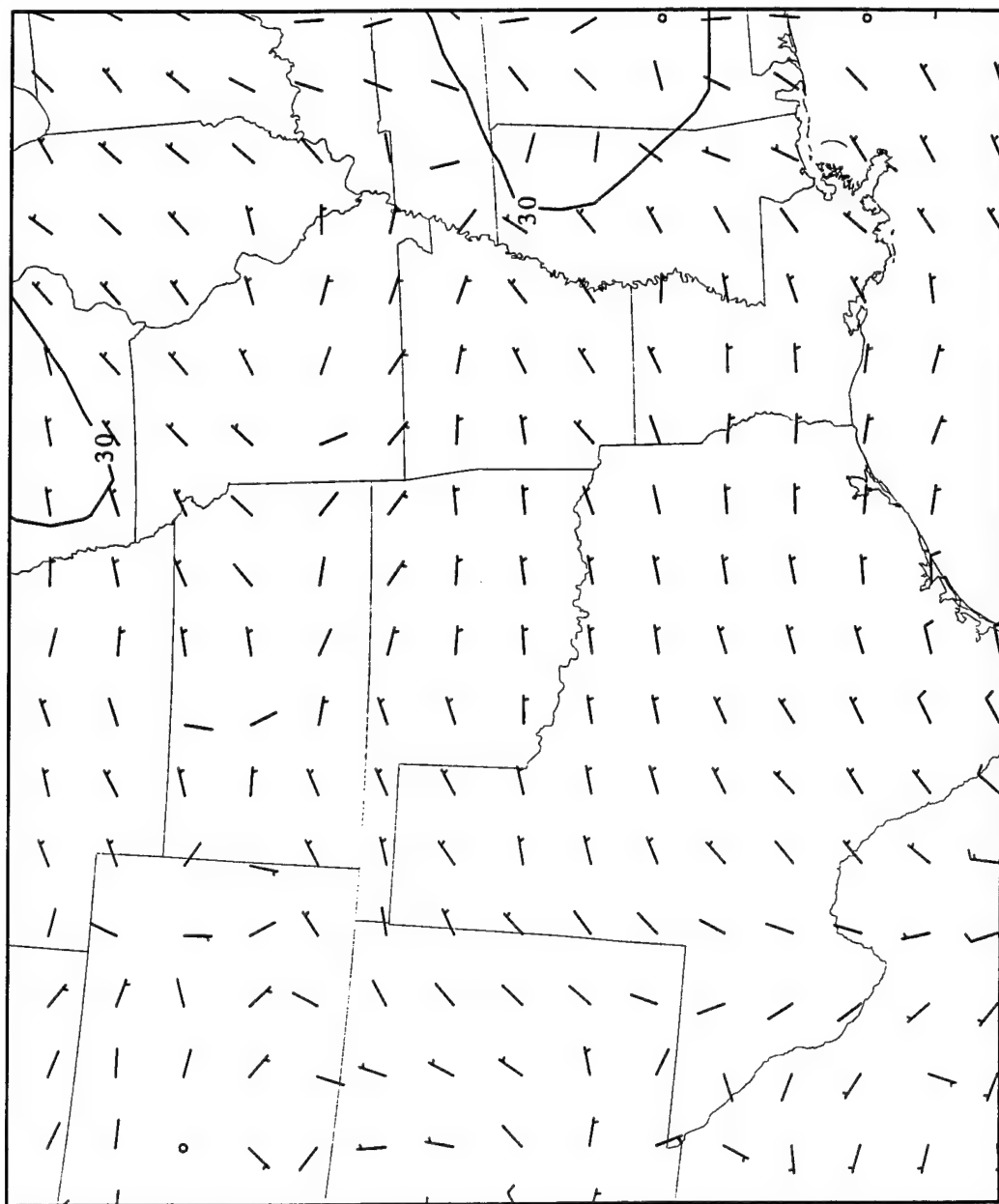


Figure 3.47. 950815/2100 900mb Ageostrophic winds(m/s),  
and 200mb isotachs(solid, m/s).

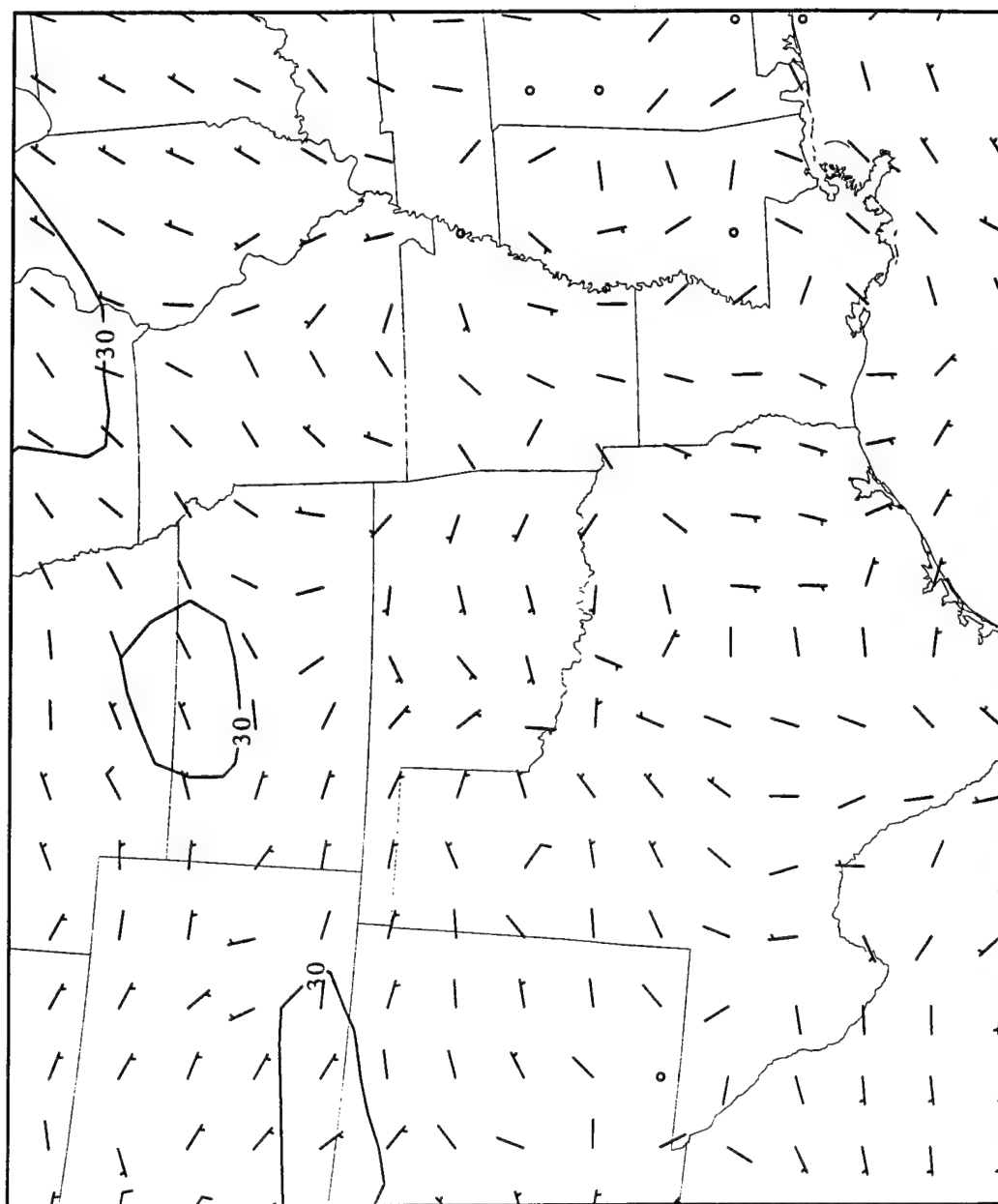


Figure 3.48. 950815/1200 900mb Ageostrophic winds(m/s),  
and 200mb isotachs(solid, m/s).

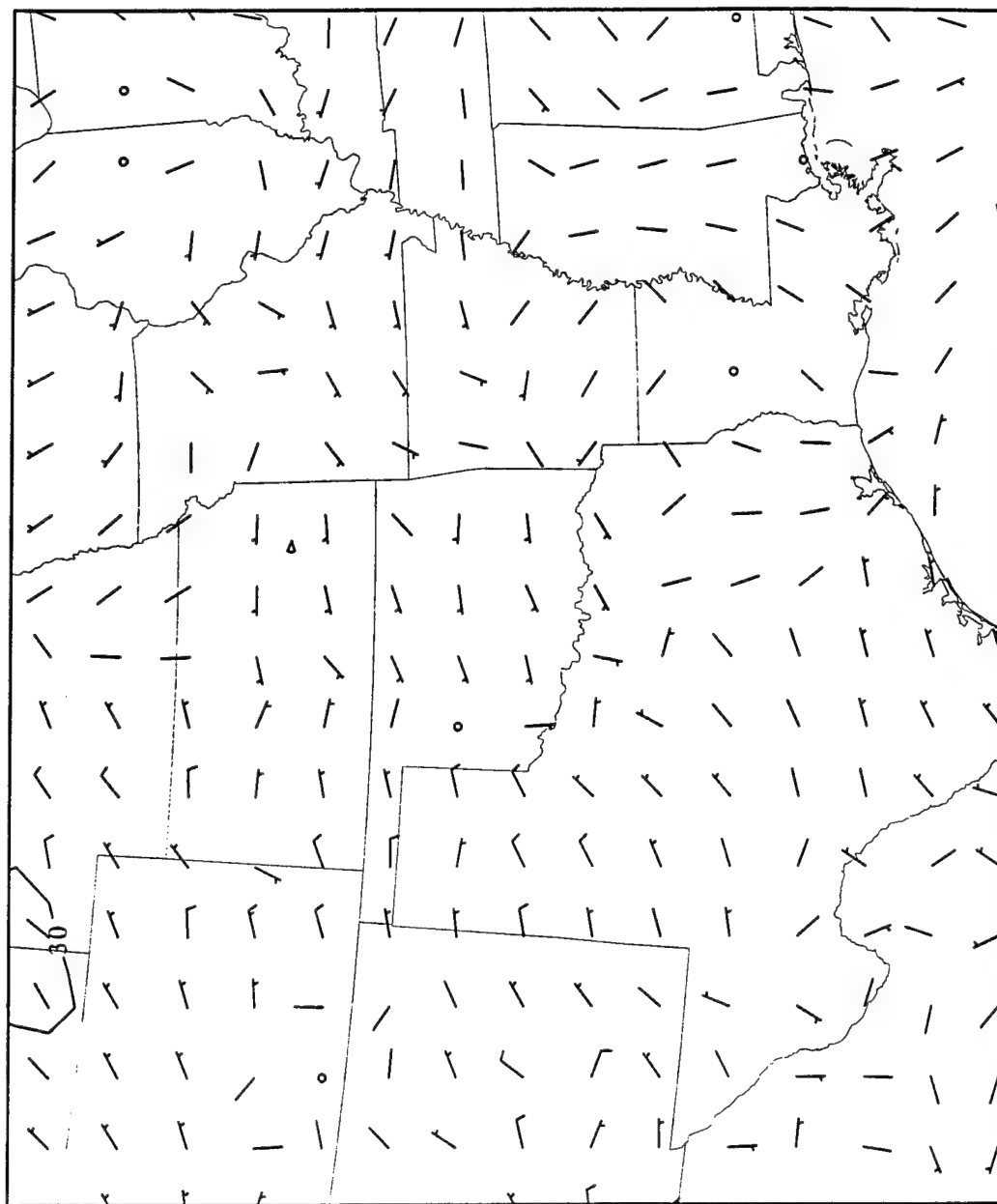


Figure 3.49. 950816/1200 900mb Ageostrophic winds(m/s), and 200mb isotachs(solid, m/s).

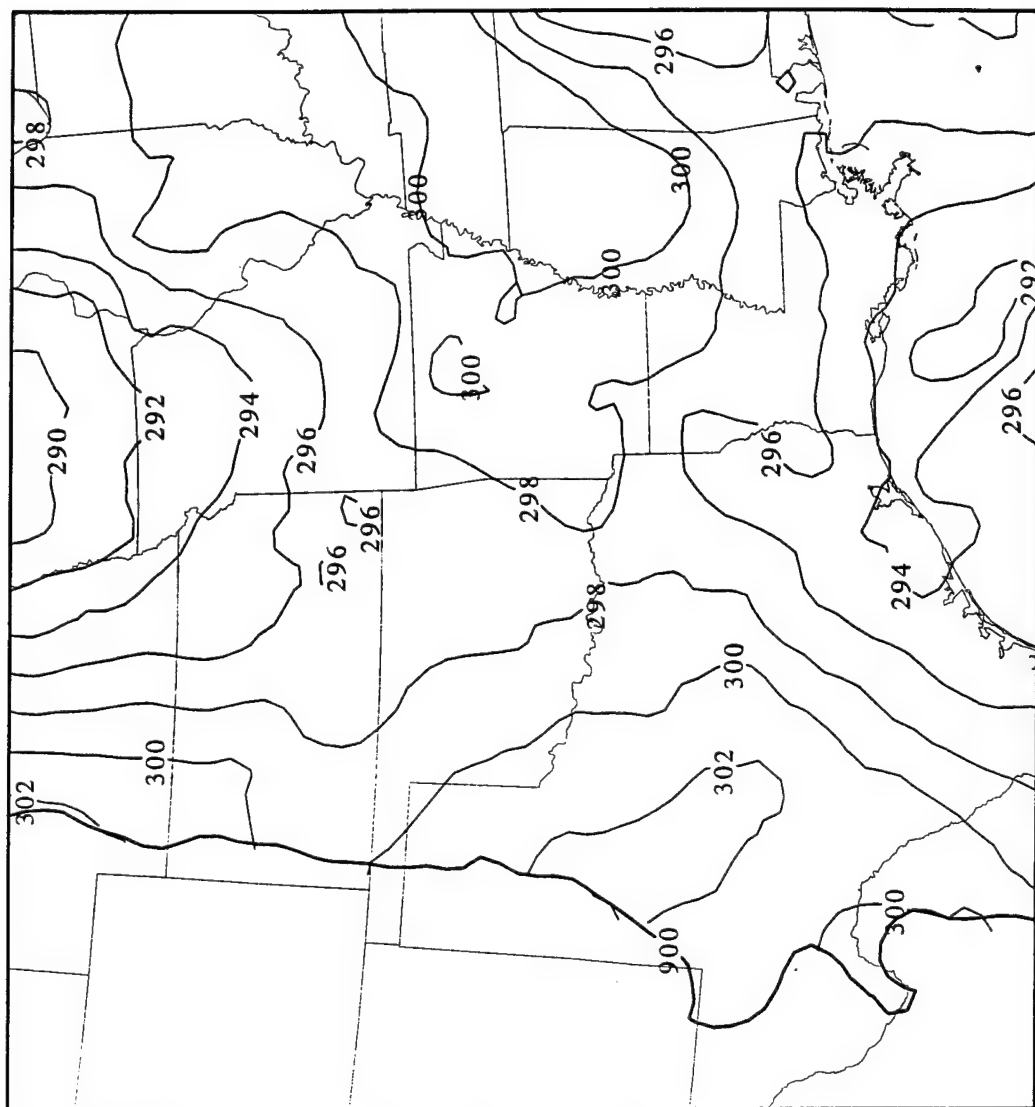


Figure 3.50. 950816/0000F000 900mb Surface(thick solid) and temperature(solid, K).

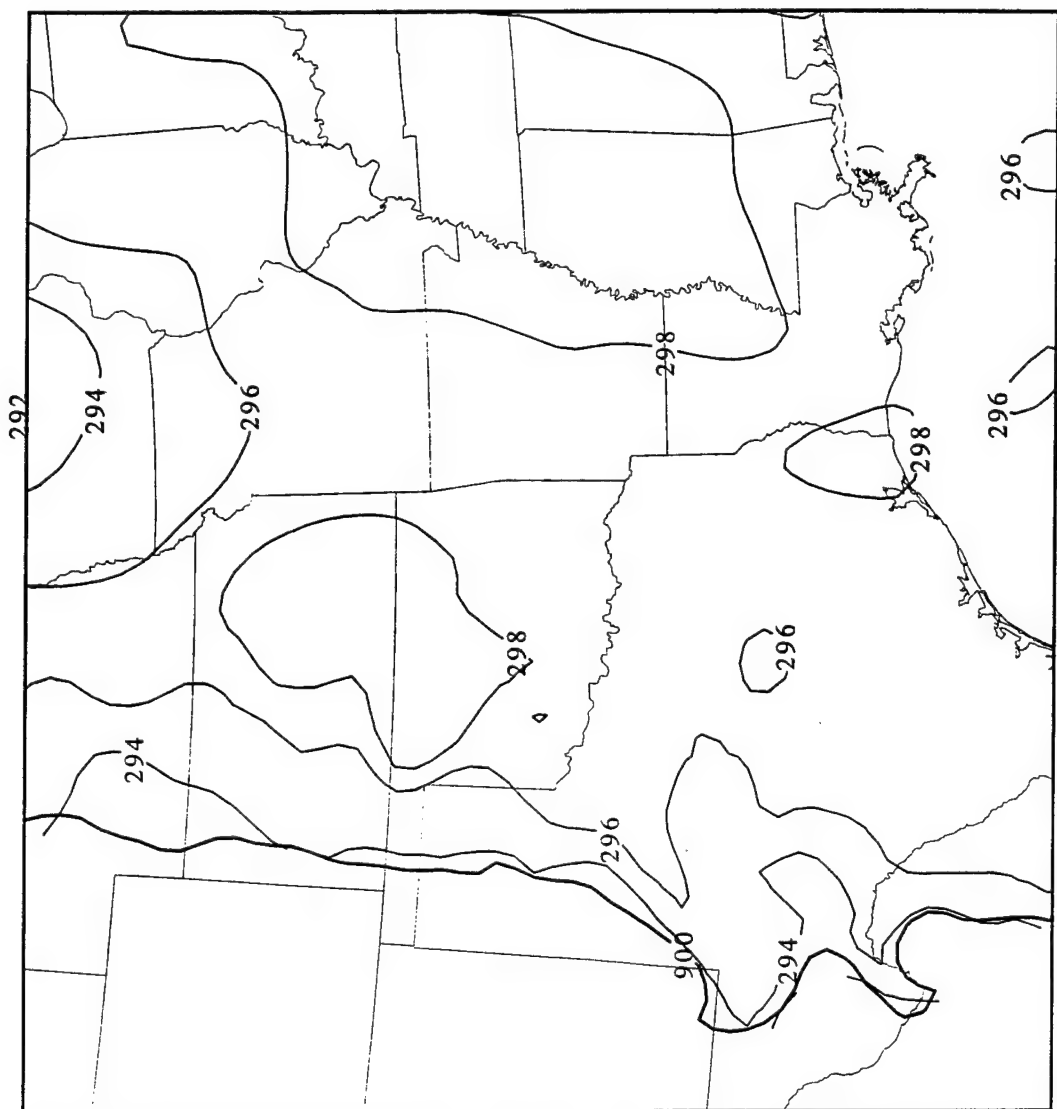


Figure 3.51. 950816/0000F012 900mb Surface(thick solid) and temperature(solid, K).



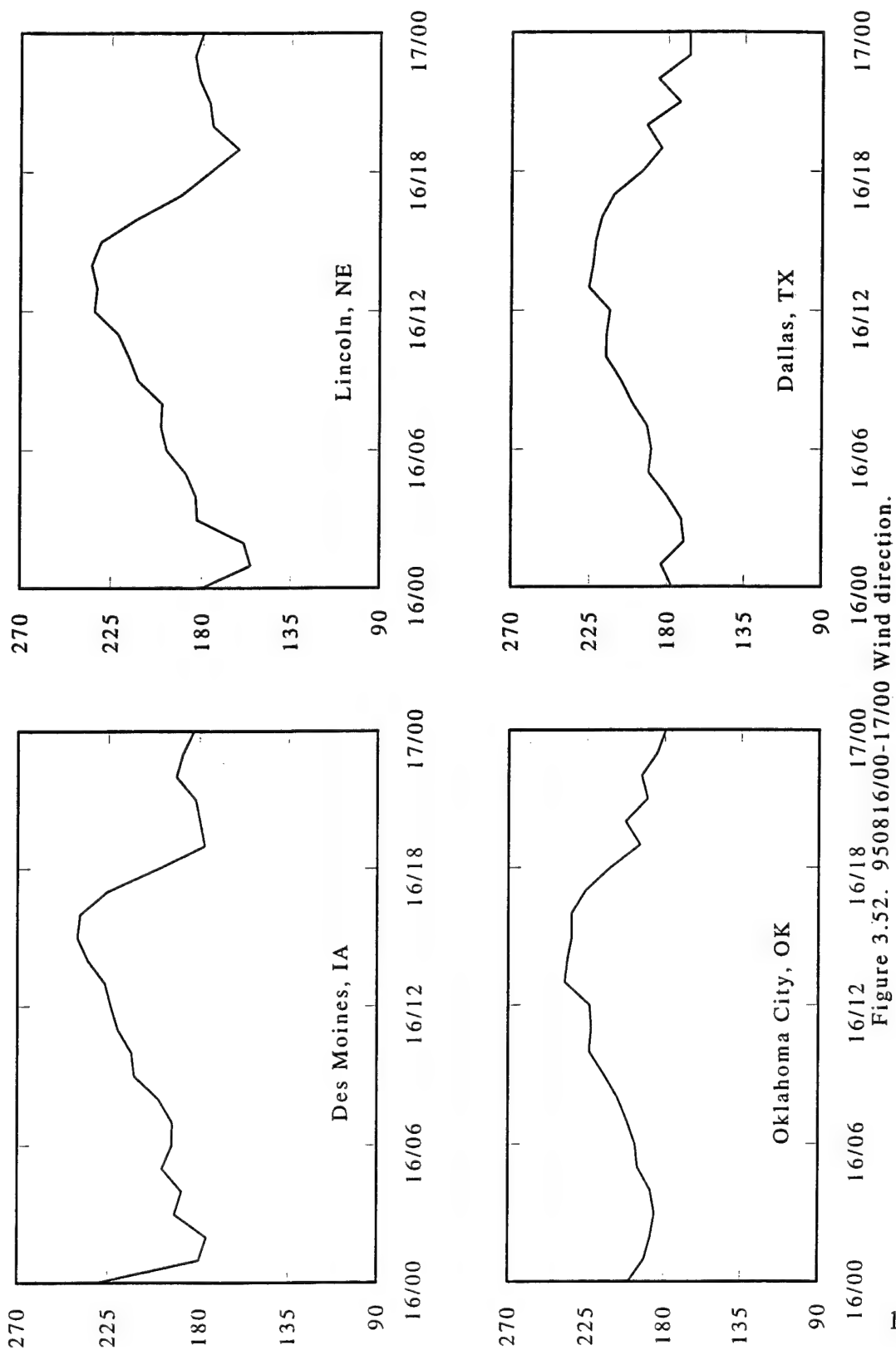


Figure 3.52. 950816/00-17/00 Wind direction.

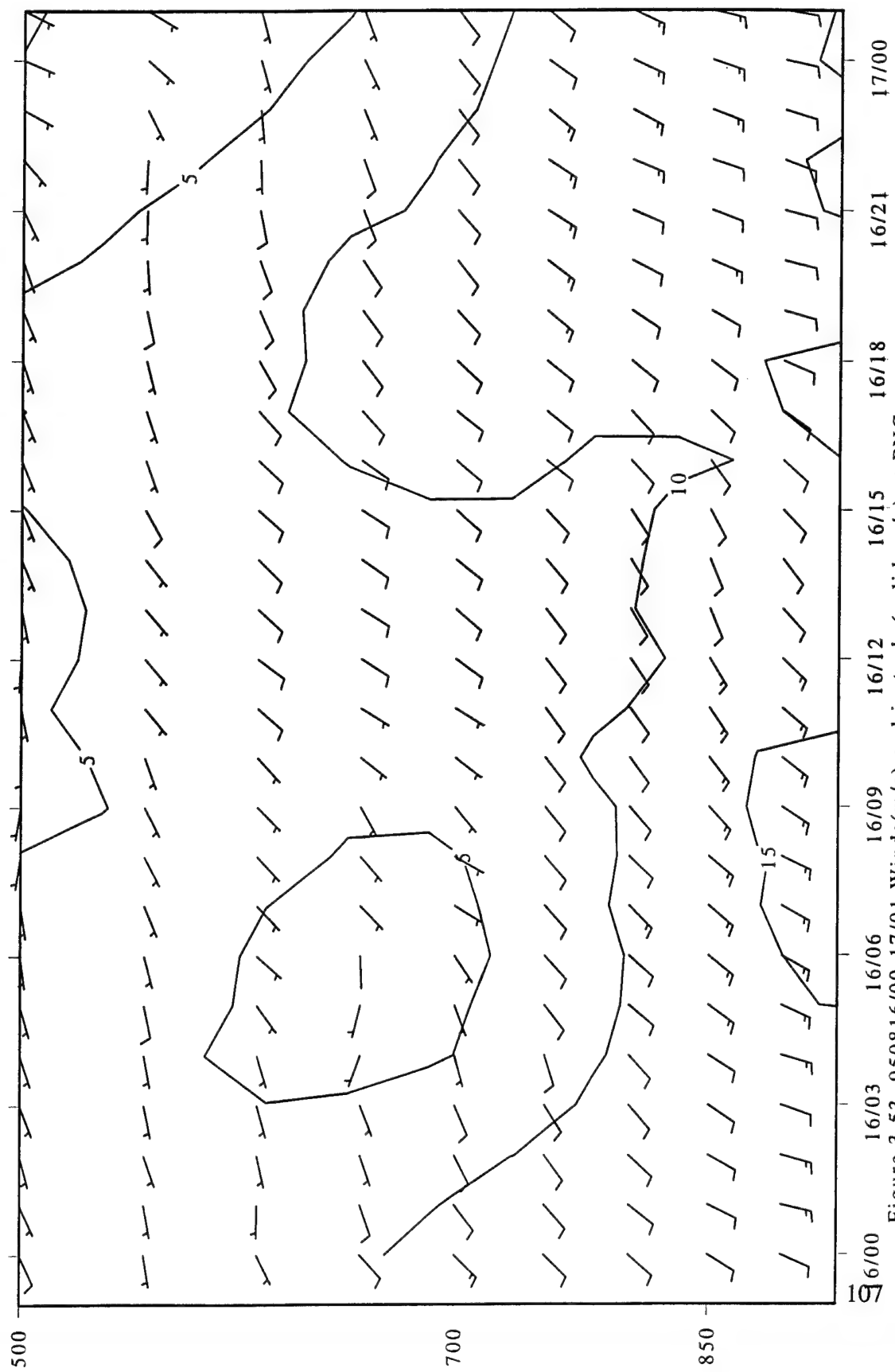


Figure 3.53. 950816/00-17/01 Winds(m/s) and isotachs(solid, m/s) at PNC.

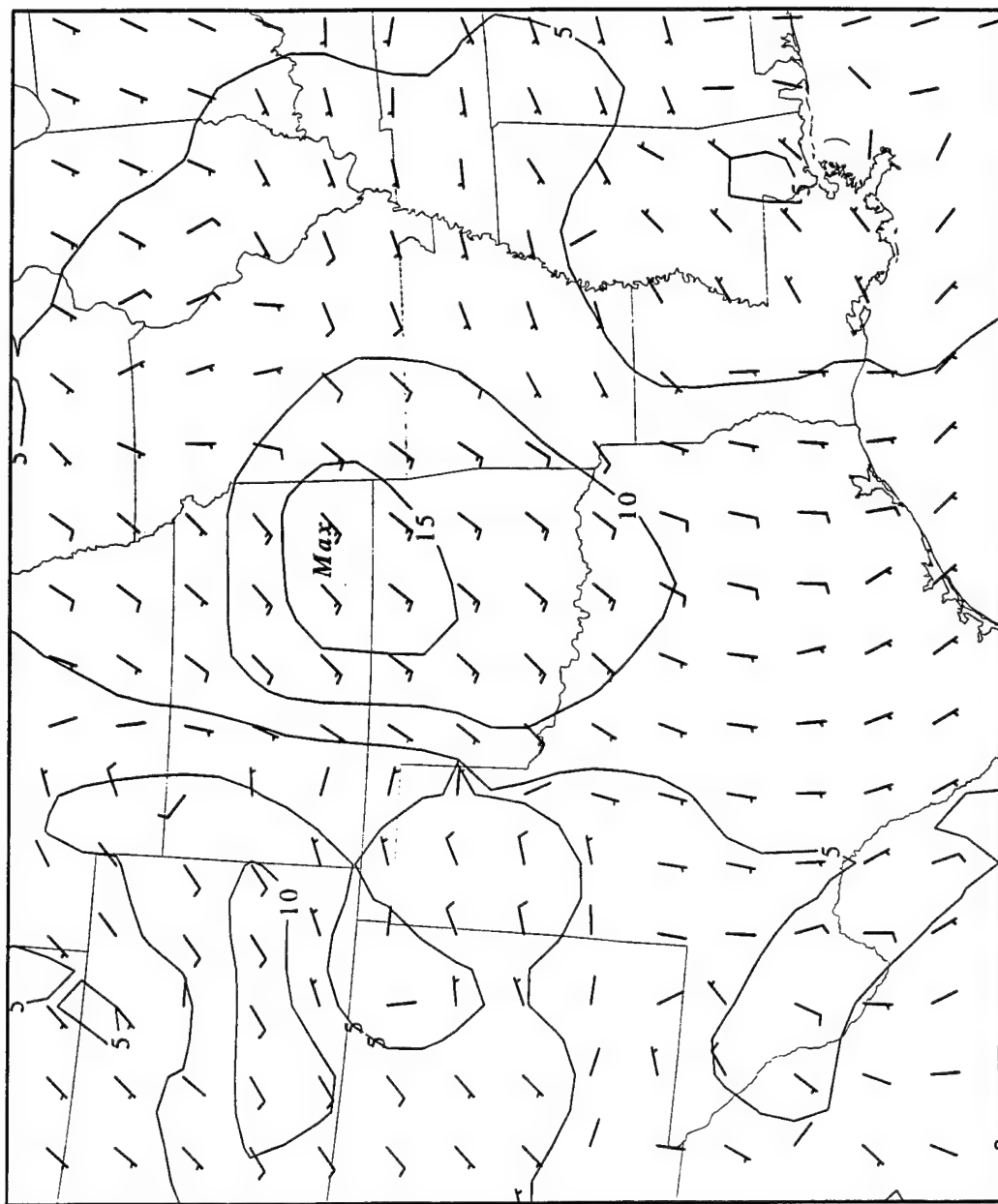


Figure 3.54. 950816/1000 900mb Profiler winds(m/s), isotachs(solid, m/s), and maximum wind location.

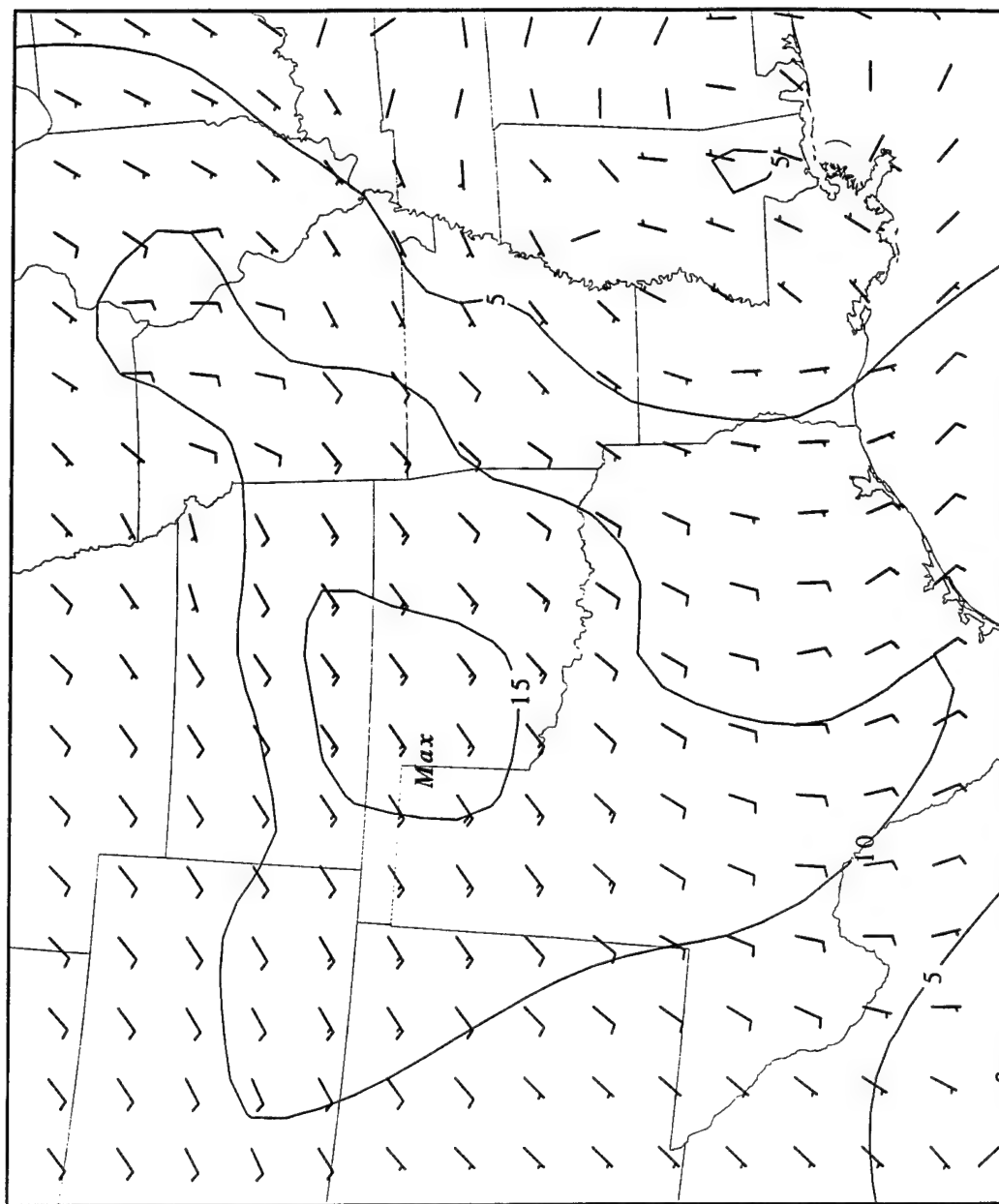


Figure 3.55. 950816/1000 850mb Profiler winds(m/s), isotachs(solid, m/s), and maximum wind location.

observed (Mitchell et al. 1995). At 1200Z, the 900 mb wind chart shows the LLJ weakening and spreading out (Fig. 3.56). This is the time the RAOB network observed a hint of a LLJ (see Fig. 3.11). Notice the difference in the extent of the LLJ and the speed gradients provided by the profiler network over the RAOB network. Shortly afterwards, the LLJ diminishes in a similar fashion to the previous day (Fig. 3.57).

### 3.4 The Effects of Friction

Frictional stresses which were added to the divergence equation did not produce significant changes to the mass field for this experiment. When Term 11 was added to Eq. (10), the height differences between friction and no-friction cases was no more than 4 m. In fact, the average difference was closer to  $< 1$  m. For example, Figure 3.58 shows the height field and its friction-added height field at 0800Z on 15 August at 900 mb. The difference is calculated and is shown by the dotted lines. For this time, the Rayleigh friction scheme was used for a nighttime PBL case (see Section 2.2.2).

Other times showed similar results. Before these are shown, though, a scale analysis of the individual terms is conducted to see explicitly the impact of Term 11. This was done by taking the average of the absolute value of each term for a specific area within the grid. The area used is the same as used for the LLJ analysis (see Fig. 3.39). This area consisted of 644 grid points for each vertical level. Table 6 shows the average values for two nocturnal PBL times at four levels. These two cases were calculated assuming no friction (i.e., Term 11=0). Each value has been multiplied by the grid spacing squared and divided by the gravity or,

$$\text{Term shown} = \text{Actual value} \left[ \frac{(\Delta x)^2}{g} \right].$$

Note that Terms 1, 4, and 5 are zero at the lowest level. This is because these terms include  $\omega$  which has been assumed to be zero at the vertical boundaries (i.e., 900 mb and 100

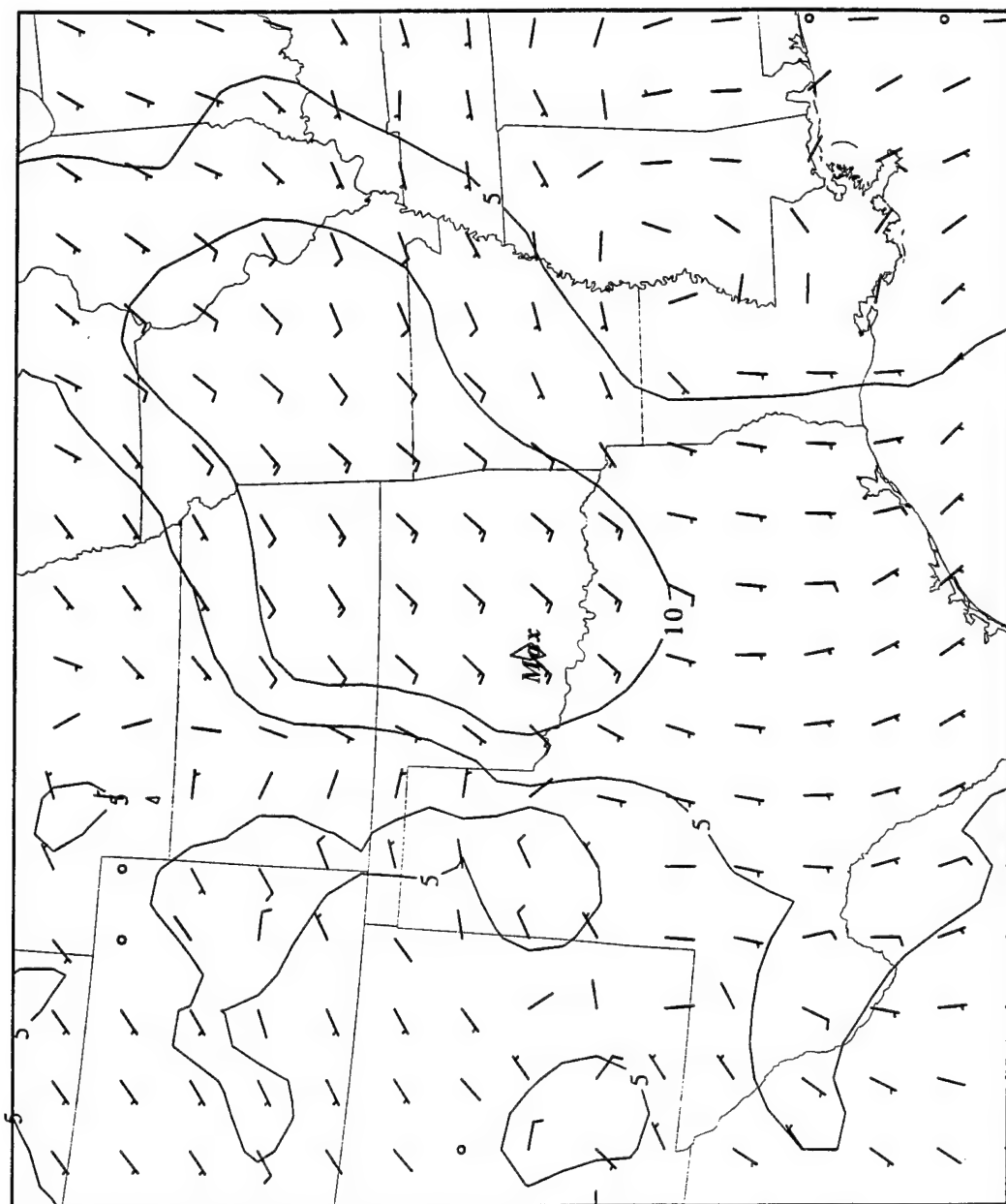


Figure 3.56. 950816/1200 900mb Profiler winds(m/s), isotachs(solid, m/s), and maximum wind location.

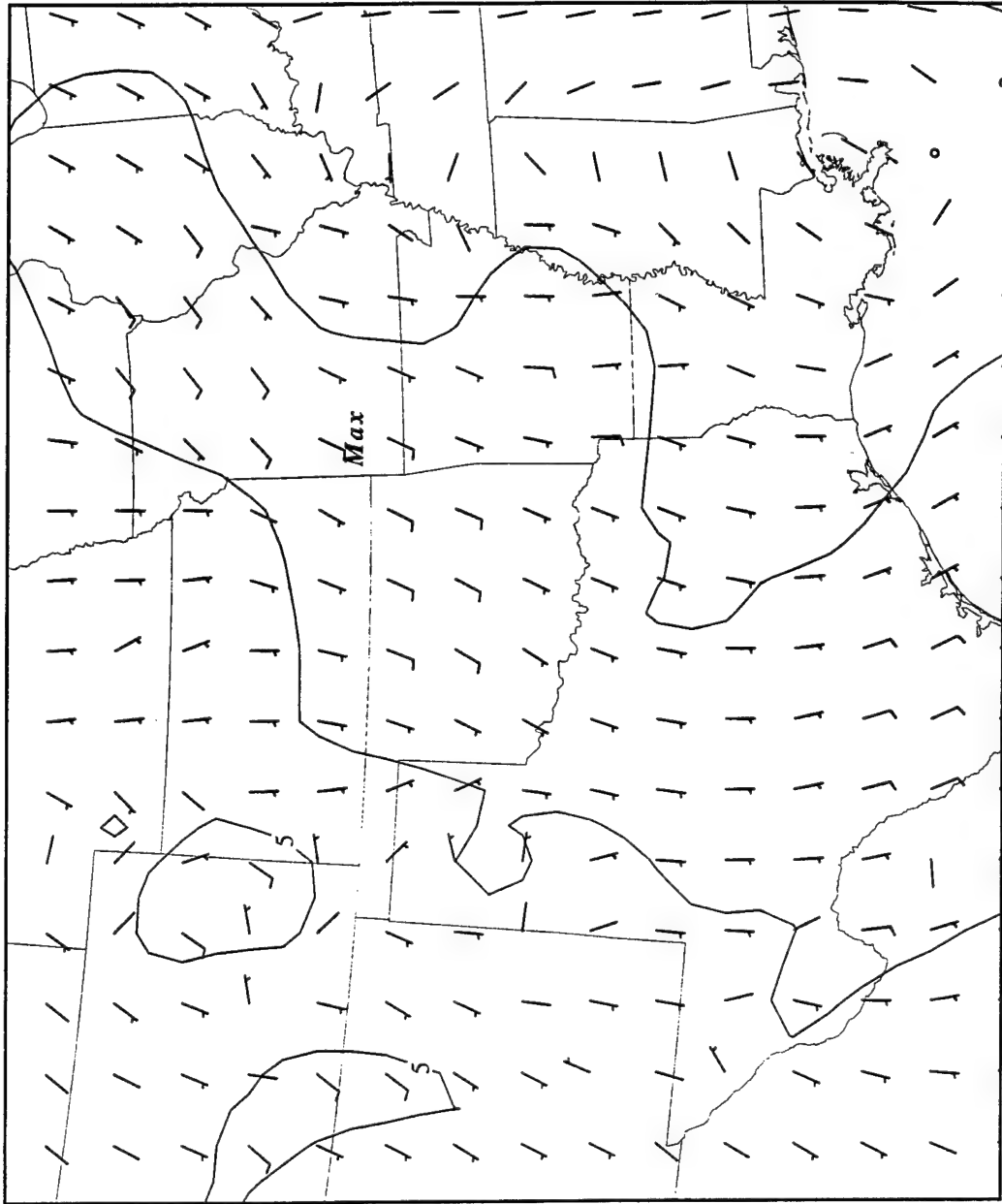


Figure 3.57. 950mb/1800 900mb Profiler winds(m/s), isotachs(solid, m/s), and maximum wind location.

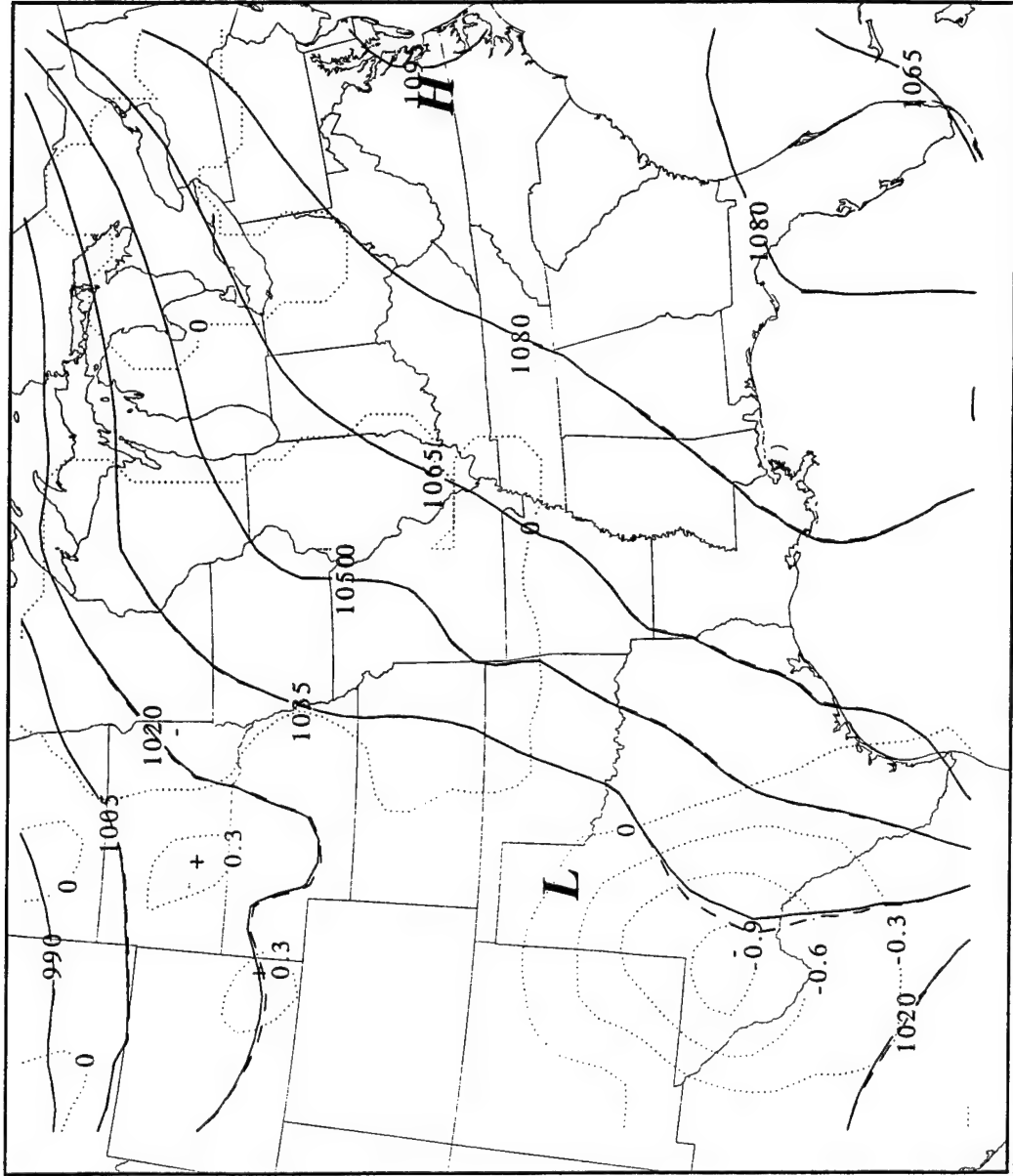


Figure 3.58. 950815/0800 900mb No friction heights(solid, m), with friction(dashed, m), and difference(dotted, m),  $\text{Mu}=.00001$ .



mb). Term 11 is, of course, zero for no-friction cases. It can be clearly seen Terms 1, 2, 9, and 10 are the dominant terms here.

**Table 6 Averages of terms for a nocturnal PBL with no frictional stresses**

Term	1	2	3	4	5	6	7	8	9	10	11
15 August, 1995 0900Z											
900 mb	.000	.410	.251	.000	.000	.171	.001	.013	.493	.677	.000
850 mb	.545	.392	.162	.068	.012	.132	.001	.016	.450	.774	.000
700 mb	.489	.434	.287	.272	.075	.189	.002	.013	.644	1.090	.000
500 mb	.323	.282	.073	.227	.056	.116	.002	.014	.457	.650	.000
16 August, 1995 0700Z											
900 mb	.000	.577	.302	.000	.000	.197	.001	.015	.600	.857	.000
850 mb	.425	.391	.117	.054	.011	.122	.002	.021	.486	.733	.000
700 mb	.460	.488	.327	.258	.073	.190	.001	.014	.561	.979	.000
500 mb	.337	.312	.098	.249	.067	.156	.001	.017	.542	.671	.000

Table 7 now includes the effects of frictional stresses in the divergence calculations. Here, the drag coefficient scheme is used with  $C_d = 1.3 \times 10^{-3}$  and  $Z_i = 300$  m. All of the terms with the exception of 10 and 11 remain the same. The value of Term 11 is at least two orders of magnitude smaller than the dominant terms in the divergence equation. Thus, its effect is rather small.

On a similar note, Table 8 shows the values of the terms one hour earlier. Here, the Rayleigh friction scheme is used to calculate the frictional stresses. The terms are of similar relative magnitude. Friction again is much smaller than the rest of the terms in this case.

With these small values for Term 11, what will the impact be on the retrieved height field? Figure 3.58 already showed one example. Figure 3.59 shows an example using the Rayleigh friction scheme at 0600Z on 16 August at 900 mb. Notice the largest differences in the height field are in the vicinity of the LLJ (see the previous section). This makes sense, for where the wind speeds are greater, the value of Term 11 will be larger. Using the other friction parameterization, the drag coefficient, produces different results as seen in Figure 3.60. Here the height differences are more widespread over the grid domain with the largest being in the mid-Texas area.

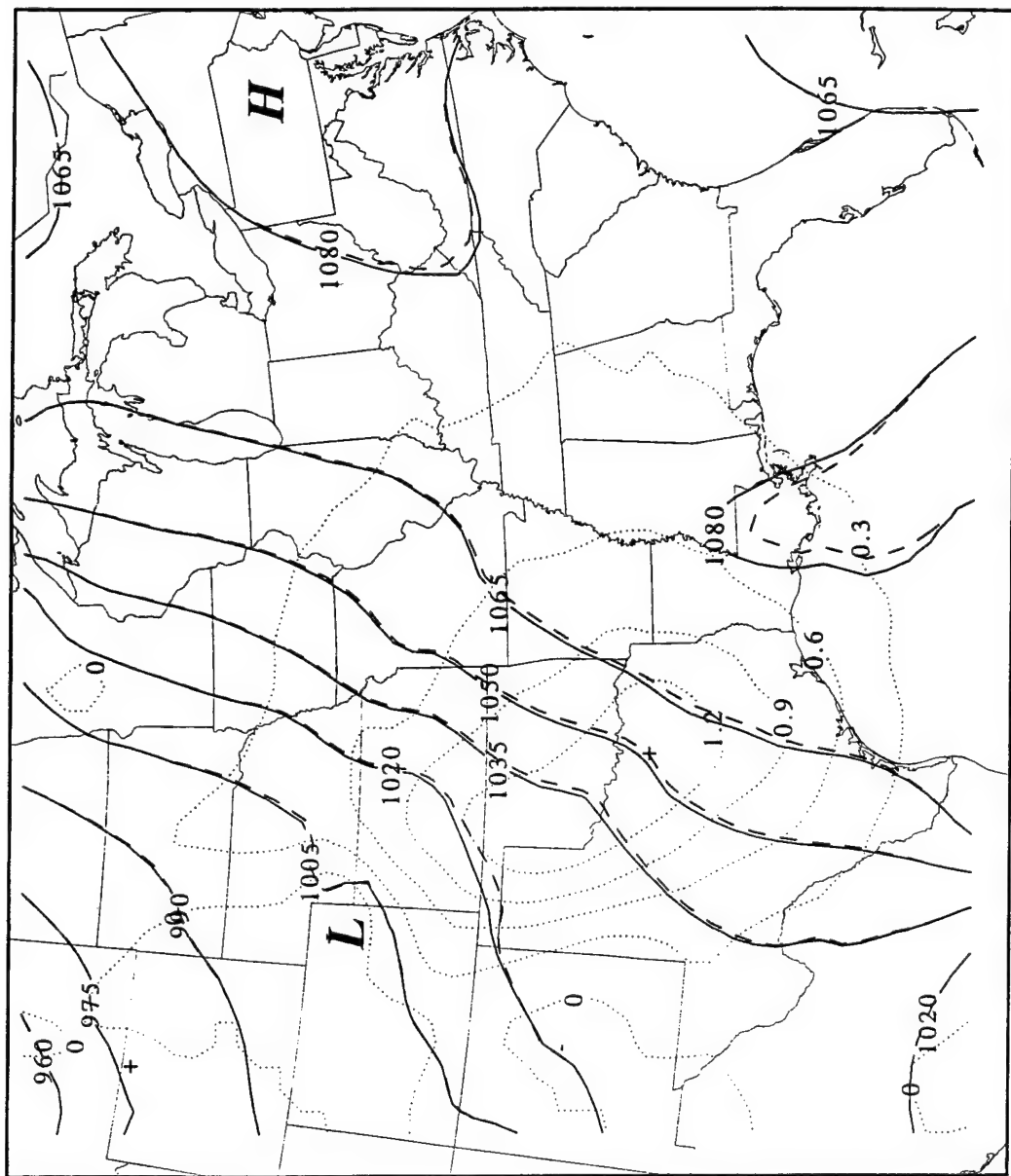


Figure 3.59. 950816/0600 900mb No friction heights(solid, m), with friction(dashed, m), and difference(dotted, m),  $\mu = .00001$ .

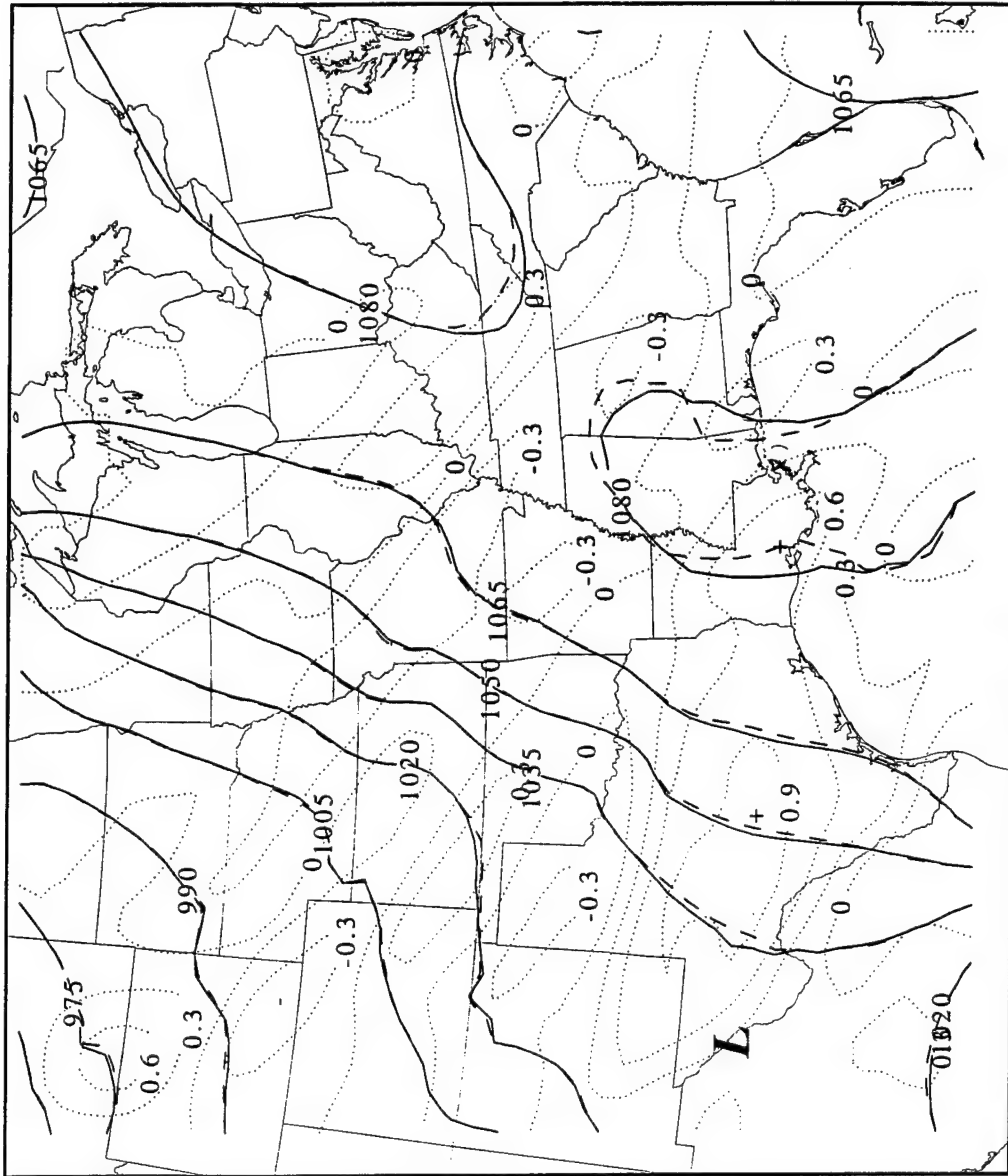


Figure 3.60. 950816/0700 900mb No friction heights(solid, m),  
with friction(dashed, m), and difference(dotted, m),  
Cd=.0013 and Zi=300m.

**Table 7 Averages of terms for a nocturnal PBL using drag parameterization**

Term	1	2	3	4	5	6	7	8	9	10	11
15 August, 1995 0900Z											
900 mb	.000	.410	.251	.000	.000	.171	.001	.013	.493	.676	.004
850 mb	.545	.392	.162	.068	.012	.132	.001	.016	.450	.774	.000
700 mb	.489	.434	.287	.272	.075	.189	.002	.013	.644	1.089	.000
500 mb	.323	.282	.073	.227	.056	.116	.002	.014	.457	.650	.000
16 August, 1995 0700Z											
900 mb	.000	.577	.302	.000	.000	.197	.001	.015	.600	.856	.005
850 mb	.425	.391	.117	.054	.011	.122	.002	.021	.486	.733	.000
700 mb	.460	.488	.327	.258	.073	.190	.001	.014	.561	.979	.000
500 mb	.337	.312	.098	.249	.067	.156	.001	.017	.542	.671	.000

**Table 8 Averages of terms for a nocturnal PBL using Rayleigh friction**

Term	1	2	3	4	5	6	7	8	9	10	11
15 August, 1995 0800Z											
900 mb	.000	.355	.192	.000	.000	.142	.001	.011	.480	.615	.023
850 mb	.466	.301	.131	.062	.013	.114	.002	.014	.436	.719	.008
700 mb	.453	.473	.288	.281	.076	.217	.002	.013	.699	1.159	.000
500 mb	.293	.253	.086	.283	.054	.128	.002	.014	.487	.669	.000
16 August, 1995 0600Z											
900 mb	.000	.508	.258	.000	.000	.231	.001	.014	.614	.859	.031
850 mb	.401	.390	.115	.052	.010	.113	.002	.020	.448	.690	.009
700 mb	.377	.488	.325	.262	.056	.161	.001	.014	.559	.937	.000
500 mb	.297	.306	.093	.320	.109	.145	.001	.016	.563	.767	.000

All of the previous examples and tables have been for the nocturnal PBL. The original goal of this study was to analyze the effects of friction in the divergence equation for a LLJ scenario. It can now be seen that this effect is minimal. The inclusion of the daylight hours was done to enhance the detail in this study. What effect does a mixed PBL have?

As with the nocturnal PBL, a scale analysis was performed to see the effects of the individual terms in the divergence equation. Table 9 shows similar data as that of Table 6 but for two mixed layer PBLs. The terms here are again of the same relative magnitudes and showing zero values at the same places.

**Table 9 Averages of terms for a mixed PBL with no frictional stresses**

Term	1	2	3	4	5	6	7	8	9	10	11
15 August, 1995 1900Z											
900 mb	.000	.206	.108	.000	.000	.099	.001	.008	.379	.456	.000
850 mb	.367	.215	.064	.028	.007	.063	.002	.012	.330	.570	.000
700 mb	.271	.383	.147	.218	.058	.106	.002	.018	.486	.690	.000
500 mb	.319	.280	.116	.353	.108	.119	.001	.020	.442	.753	.000
16 August, 1995 2100Z											
900 mb	.000	.329	.207	.000	.000	.125	.002	.008	.385	.529	.000
850 mb	.415	.360	.171	.049	.011	.088	.002	.014	.442	.781	.000
700 mb	.280	.291	.116	.173	.062	.106	.002	.020	.437	.638	.000
500 mb	.271	.244	.074	.219	.066	.112	.001	.018	.0462	.571	.000

Table 10 is similar to Table 7 except this is for a daytime PBL. Table 11 and Table 8 are also similar in this respect. During the daytime (i.e., Tables 10 and 11), the values of friction have been increased. This, of course, goes along with theory and observations. With short-wave radiational heating of the earth's surface comes an increase in the turbulent kinetic energy. This energy is the foundation of the frictional stresses discussed here. The friction averages for the daytime using the drag coefficient have the largest values. That is, they affect the retrieval process the most. Figures 3.61 and 3.62 show these largest achievable height differences. The latter, 2100Z on 16 August, shows that friction weakens both the high pressure in Texas and the trough in the Nebraska, South Dakota area. The highest obtainable difference here is less than 2 m. When the parameterization is grossly increased above theoretical values by halving the boundary layer height, the maximum height difference obtained is still no more than 4 m. Table 10 shows some minor influence of the friction at the 700 mb level. This is because the mixed layer reaches this level in the higher elevations in the western part of the grid. Figure 3.63 shows the impact to the height field at 2100Z 16 August at 700 mb.

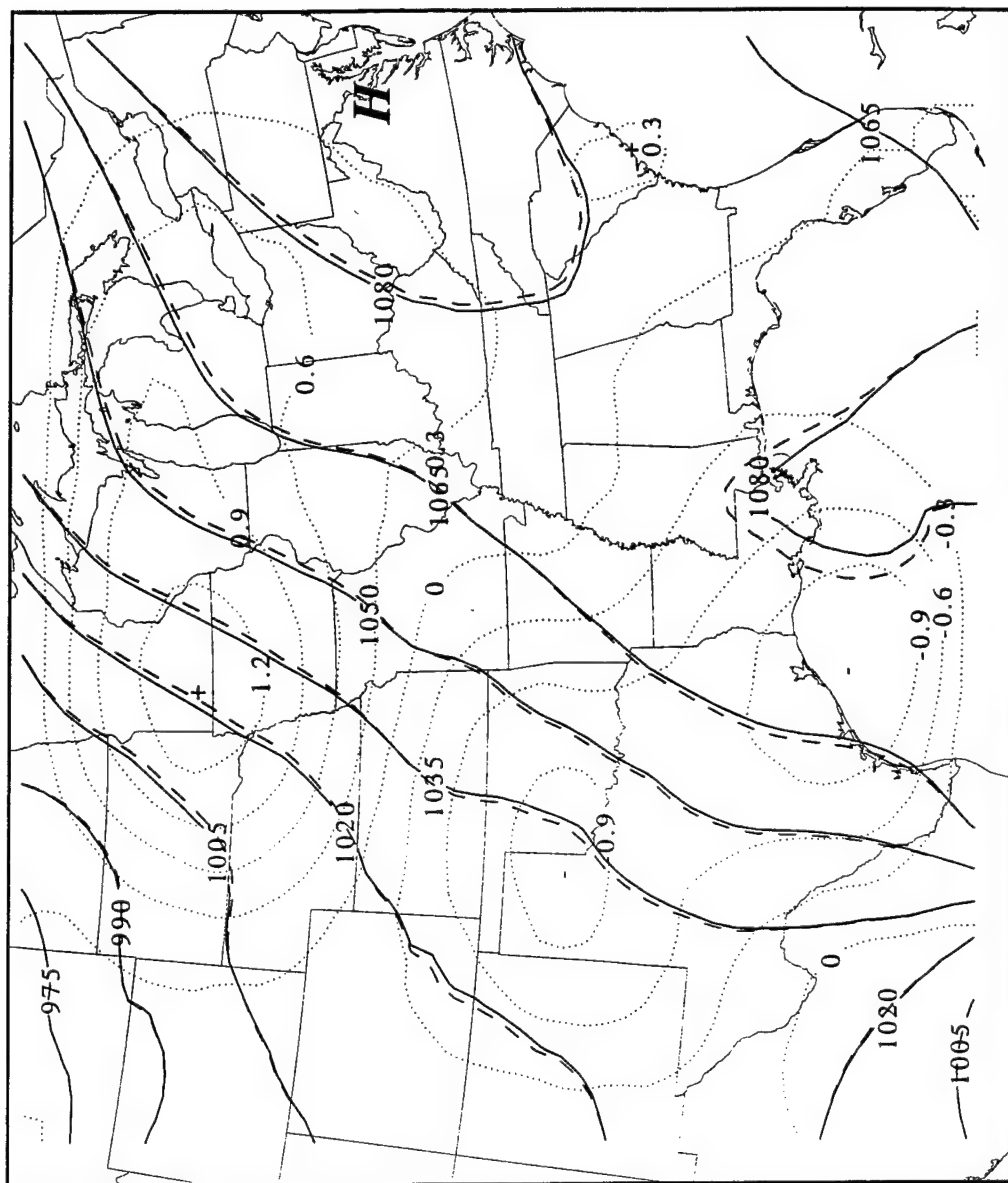


Figure 3.61. 950815/1900 900mb No friction heights(solid, m),  
with friction(dashed, m), and difference(dotted, m),  
 $C_d=.01$  and  $Z_i=1500m$ .

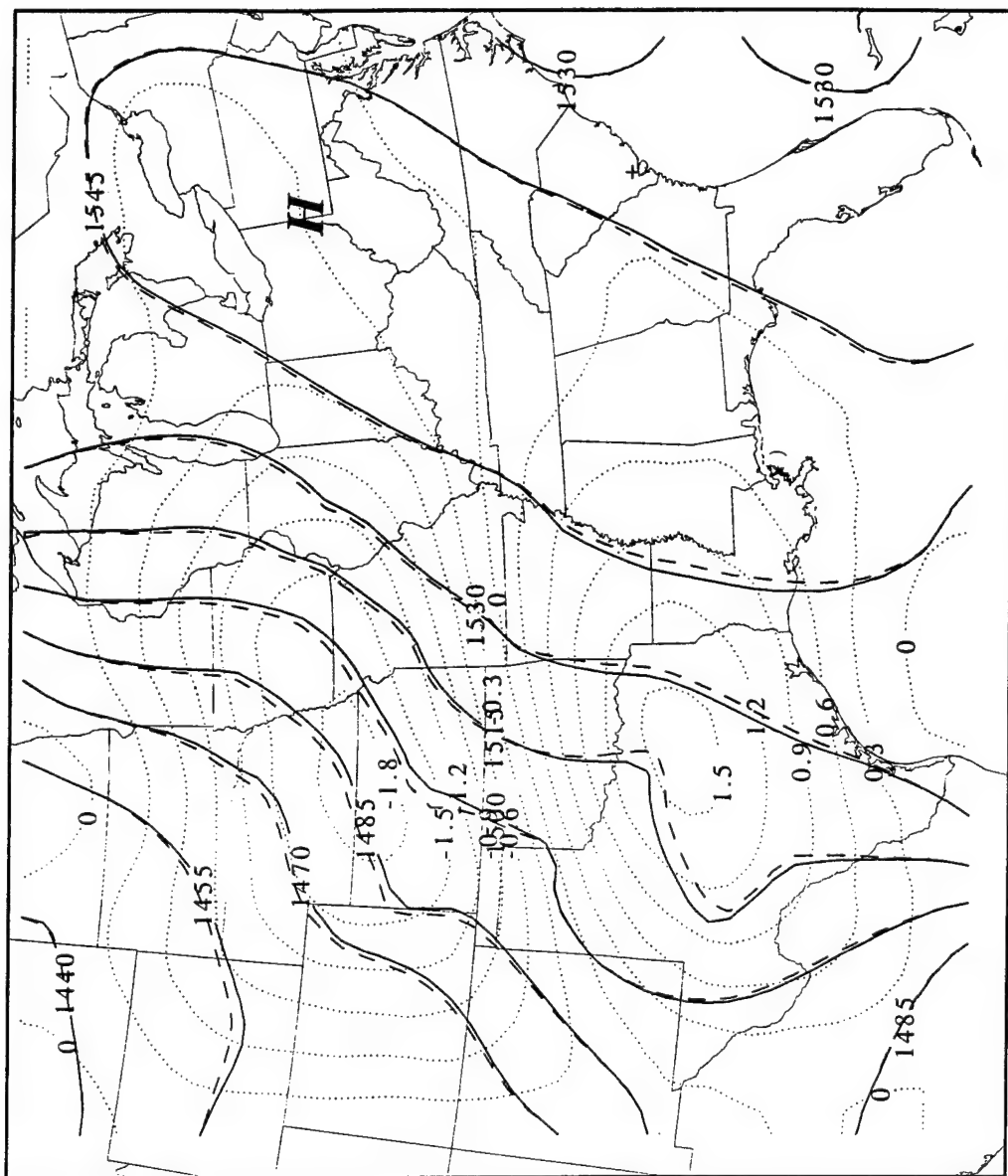


Figure 3.62. 950mb/2100 850mb No friction heights(solid, m),  
with friction(dashed, m), and difference(dotted, m),  
Cd=.01 and Zi=1500m.

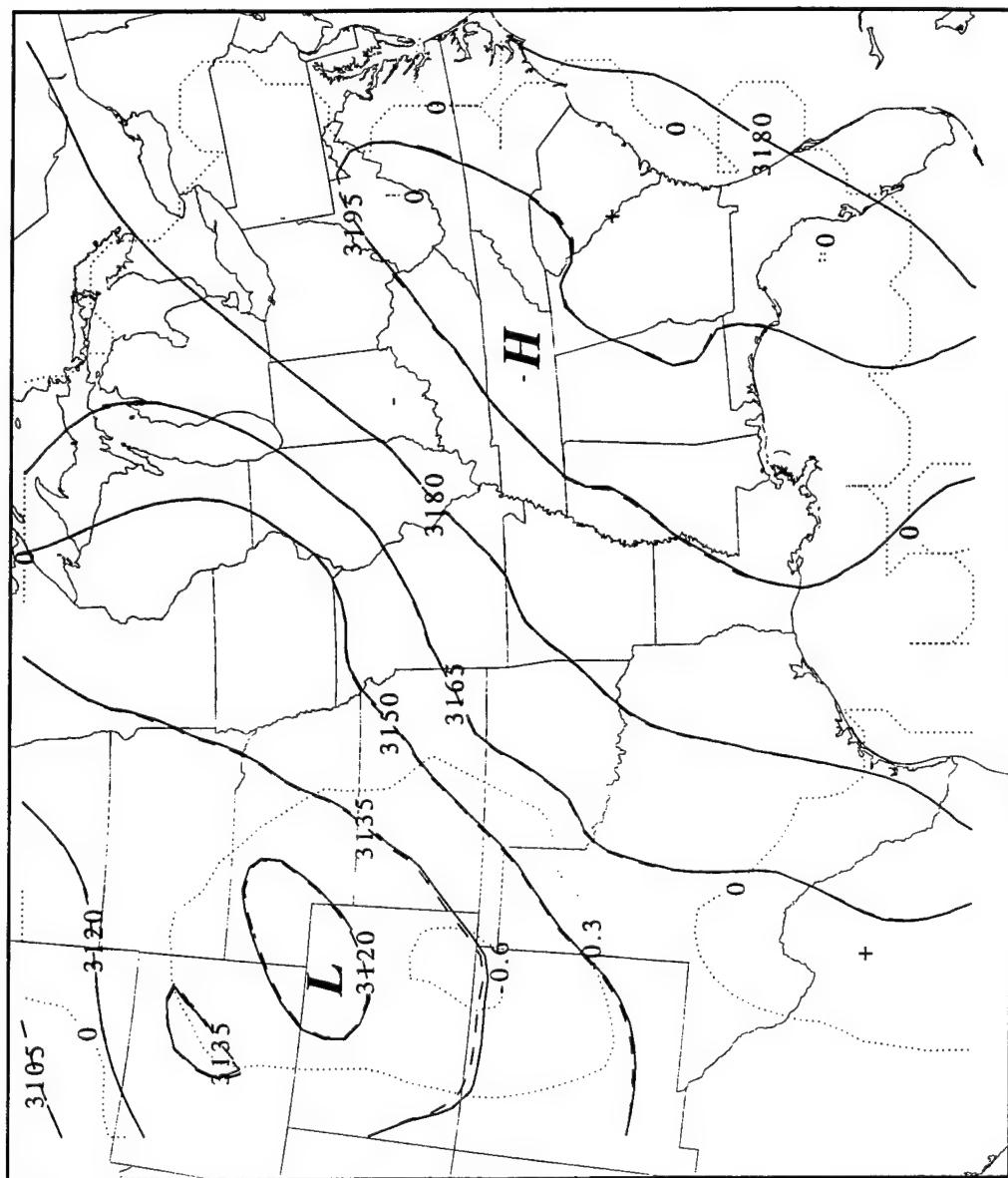


Figure 3.63. 950816/2100 700mb No friction heights(solid, m),  
with friction(dashed, m), and difference(dotted, m),  
 $C_d=.01$  and  $Z_i=1500m$ .



**Table 10 Averages of terms for a mixed PBL using drag parameterization**

Term	1	2	3	4	5	6	7	8	9	10	11
15 August, 1995 1900Z											
900 mb	.000	.206	.108	.000	.000	.099	.001	.008	.379	.459	.020
850 mb	.367	.215	.064	.028	.007	.063	.002	.012	.330	.571	.020
700 mb	.271	.383	.147	.218	.058	.106	.002	.018	.486	.690	.001
500 mb	.319	.280	.116	.353	.108	.119	.001	.020	.442	.753	.000
16 August, 1995 2100Z											
900 mb	.000	.329	.207	.000	.000	.125	.002	.008	.385	.517	.040
850 mb	.415	.360	.171	.049	.011	.088	.002	.014	.442	.770	.040
700 mb	.280	.291	.116	.173	.062	.106	.002	.020	.437	.638	.002
500 mb	.271	.244	.074	.219	.066	.112	.001	.018	.0462	.571	.000

**Table 11 Averages of terms for a mixed PBL using Rayleigh friction**

Term	1	2	3	4	5	6	7	8	9	10	11
15 August, 1995 1800Z											
900 mb	.000	.207	.109	.000	.000	.101	.001	.009	.386	.440	.021
850 mb	.313	.223	.088	.028	.008	.075	.002	.014	.076	.576	.014
700 mb	.263	.384	.171	.183	.056	.113	.002	.014	.471	.718	.000
500 mb	.293	.314	.126	.285	.073	.131	.001	.020	.457	.771	.000
16 August, 1995 2000Z											
900 mb	.000	.330	.185	.000	.000	.119	.001	.011	.418	.592	.031
850 mb	.332	.424	.218	.053	.011	.101	.002	.016	.480	.748	.023
700 mb	.283	.300	.082	.193	.069	.095	.002	.020	.450	.696	.000
500 mb	.290	.255	.069	.339	.096	.107	.001	.020	.449	.691	.000

As stated in the beginning of this section, the frictional stresses did not play a major role in the accuracy of the retrieval process. Term 11 is too small to have an impact. This is explained by several reasons. For one, the term is not only the friction involved, but the *divergence* of the friction. This means the difference of friction between grid points is used *instead of* the friction itself. Thus the differences along the grid may be very small and show little contribution to the divergence equation.

Also, this case study contained weak flow throughout the domain. This is good for the retrieval process in general (see Kuo *et al.* 1987), but friction will not play much of a role here. Bluestein and Crawford (1997) spoke of conditions, however, where the simple

parameterizations used in Section 1.2 will not be sufficient to describe the true frictional stresses place upon the environment. They noted that in the vicinity of a deep convective layer with vigorous mixing, the stress associated with the vertical divergence of the vertical gradient of the horizontal velocity can be large. This stress was ignored for it was too small for this case.

Finally, there were areas of strong convection as seen on the surface maps. The scale size of 58 km, though, was too large to detect most of these signals. Thus the grid size was too coarse to adequately depict the smaller frictional stresses that might be involved in this case study. In order to better see this convection, though, a higher resolution network is needed. Decreasing the grid size would not help, though, unless the data was there to help support it. Also, more vertical resolution of wind data within the PBL is necessary to define the effects of vertical wind shear on the mass field. The wind profilers used could not read the winds below 500 m AGL where frictional stresses are larger.

### **3.5 Model Comparison**

After the retrieval process was complete, the results were compared to the model results. The MASS model specifics can be found in Section 2.1.4. In general, the results of the two height fields showed desirable agreement. The differences between the two fields usually was below 30 m. At the initialization period of the model, 0000Z on 15 and 16 August, the results were understandably better. Figure 3.64 shows the 0000Z 15 August 850 mb height field. The fields are in general agreement with each other. At 700 mb, the two fields again agree well (Fig. 3.65) except in the southern Texas area. Here, the model shows a meso-high, this is probably due to a bad RAOB reading in that area. The 500 mb chart (not shown) also shows the two pattern flow of the zonal winds in the north and the high pressure in the southeastern part of the grid. The model initialization does show a stronger high pressure with heights in the vicinity of 15 m greater than the retrieved heights.

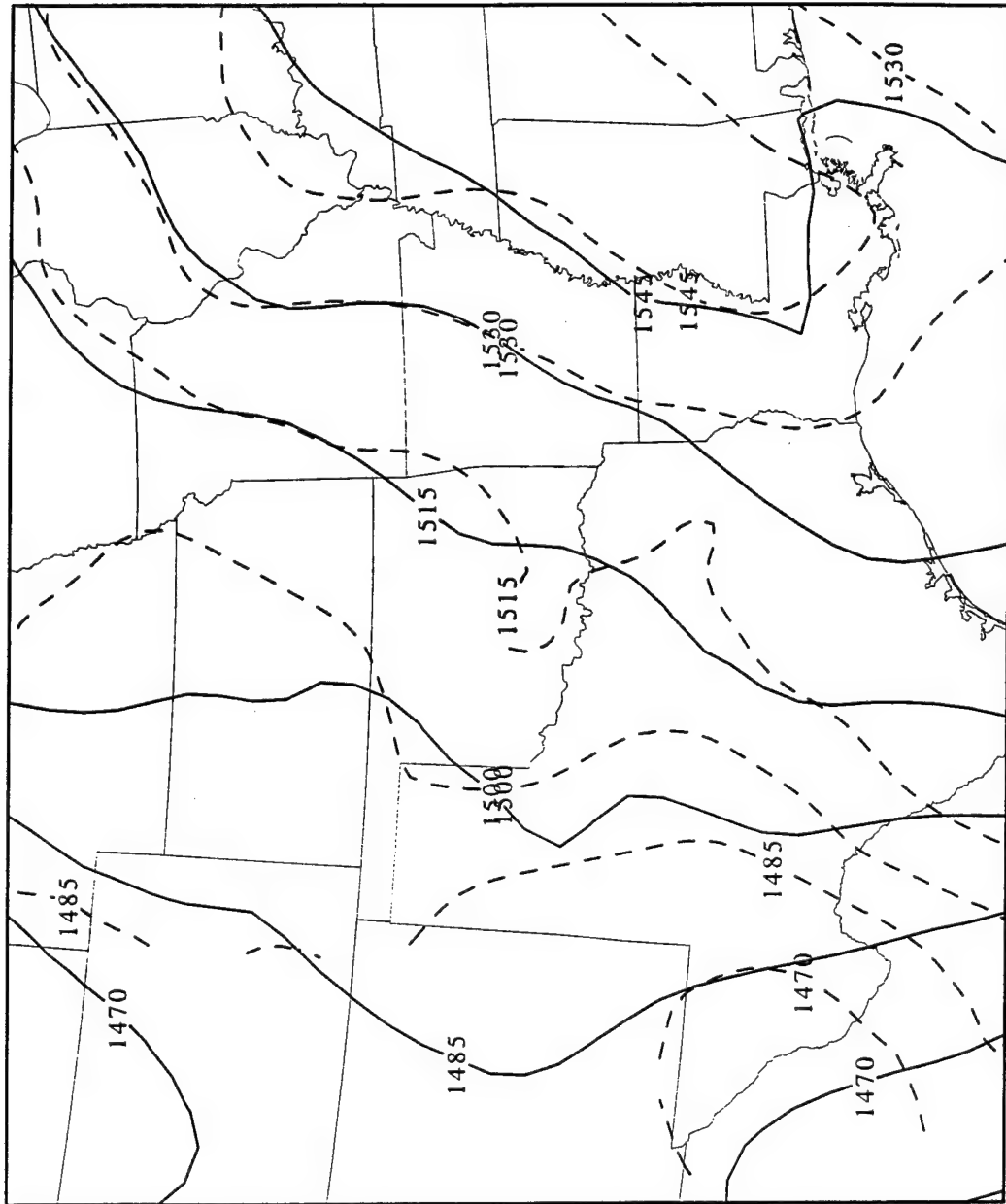


Figure 3.64. 950815/0000 850mb Retrieved heights (solid, m) and model heights(dashed, m).

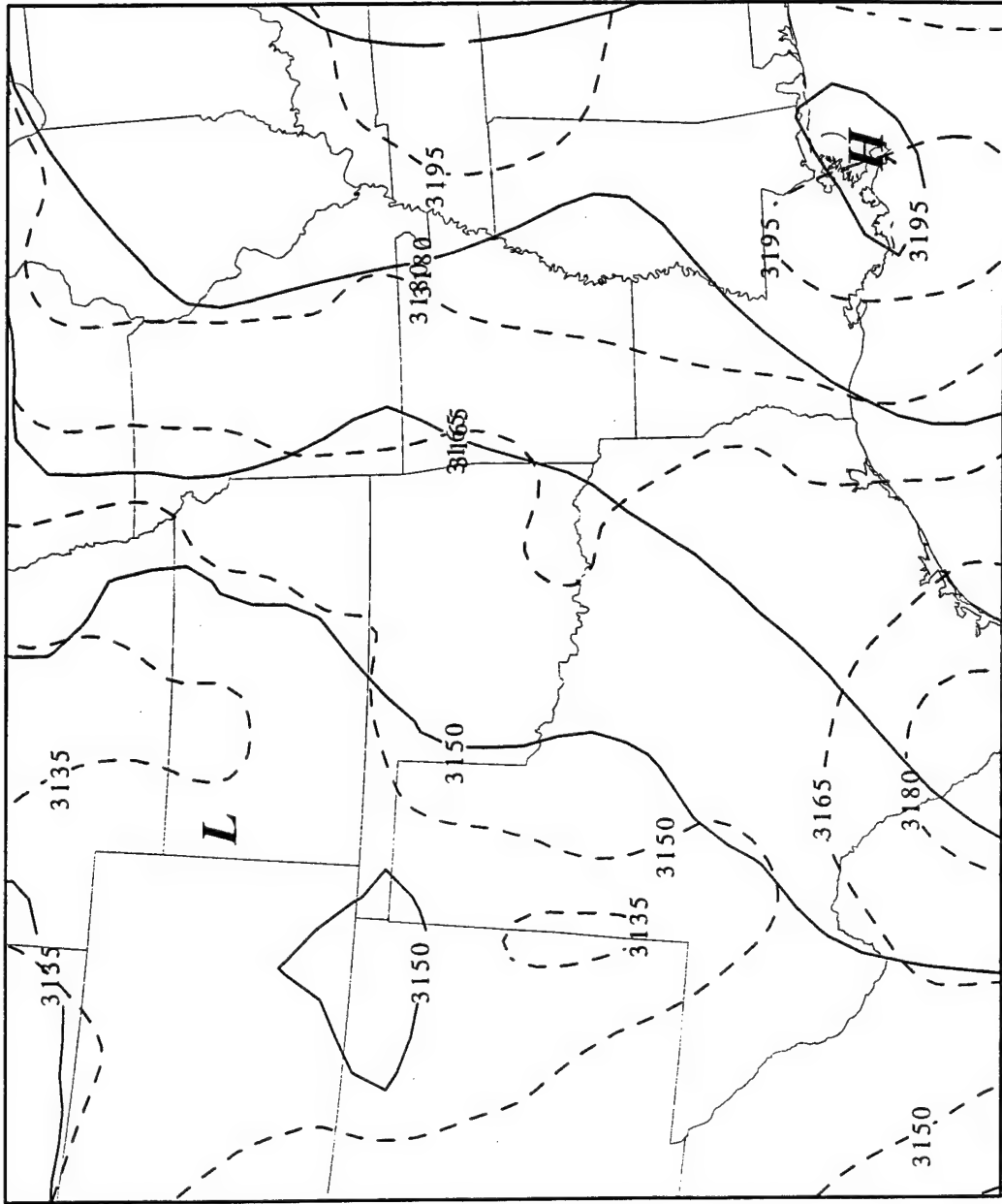


Figure 3.65. 950815/0000 700mb Retrieved heights (solid, m) and model heights(dashed, m).

Once the model integration begins, the differences between the model and retrieved heights increase. In the area of the thunderstorm outflow region discussed earlier, the two fields show considerable disparity. Figure 3.66 shows the 0300Z fields at 850 mb. The retrieved field shows the meso-high produced by the thunderstorm outflow. The model, however, does not. Here, the model would seem to be a more useful field for the general conditions in the area. The retrieval process is taking one isolated meso-gamma scale circulation (i.e., the outflow) and rearranging the height field too much. With the exception of this area, the rest of the field looks good. Six hours after the initialization, the 500 mb chart still shows favorable agreement with the model's high pressure which remains roughly 15 m greater (Fig. 3.67). The trough in the northwest part of the figure is also in agreement.

By 1700Z on 15 August, the 850 mb chart still shows good general agreement with each other (Fig. 3.68). The model, though, still shows higher pressure in the southeastern part of the grid, and now the model's height gradient in the Southern Plains is stronger. Looking at the 700 mb chart (Fig. 3.69) shows the model's trough is larger and slower moving than the retrieval's trough. This can also be seen at the 500 mb level (Fig. 3.70). At 0000Z on 16 August, the 500 mb chart, now reinitialized, shows the trough properly located as would be expected (Fig. 3.71). The remainder of the second model run shows minor differences at multiple levels (see Figs. 3.72, 3.73, and 3.74). In general, better correspondence exists between the model and the second day as convection is less important on August 15 than August 16.

The temperature field showed good agreement between the model and retrieval process. Figure 3.75 shows a typical initialization temperature field at 700 mb. The differences are no larger than 6 K with the model showing warmer tendencies. At 500 mb (Figure 3.76) the temperatures are similar. After six hours of the model run, the temperature field shows comparable results. Note that at 700 mb the model shows small areas of larger temperature gradients in the Wyoming area (Fig. 3.77). This area is at or near the ground and thus radiational cooling is strong and the hypsometrically derived temperatures will not produce this. Diabatic heating during the day can also be seen in these areas. Above this

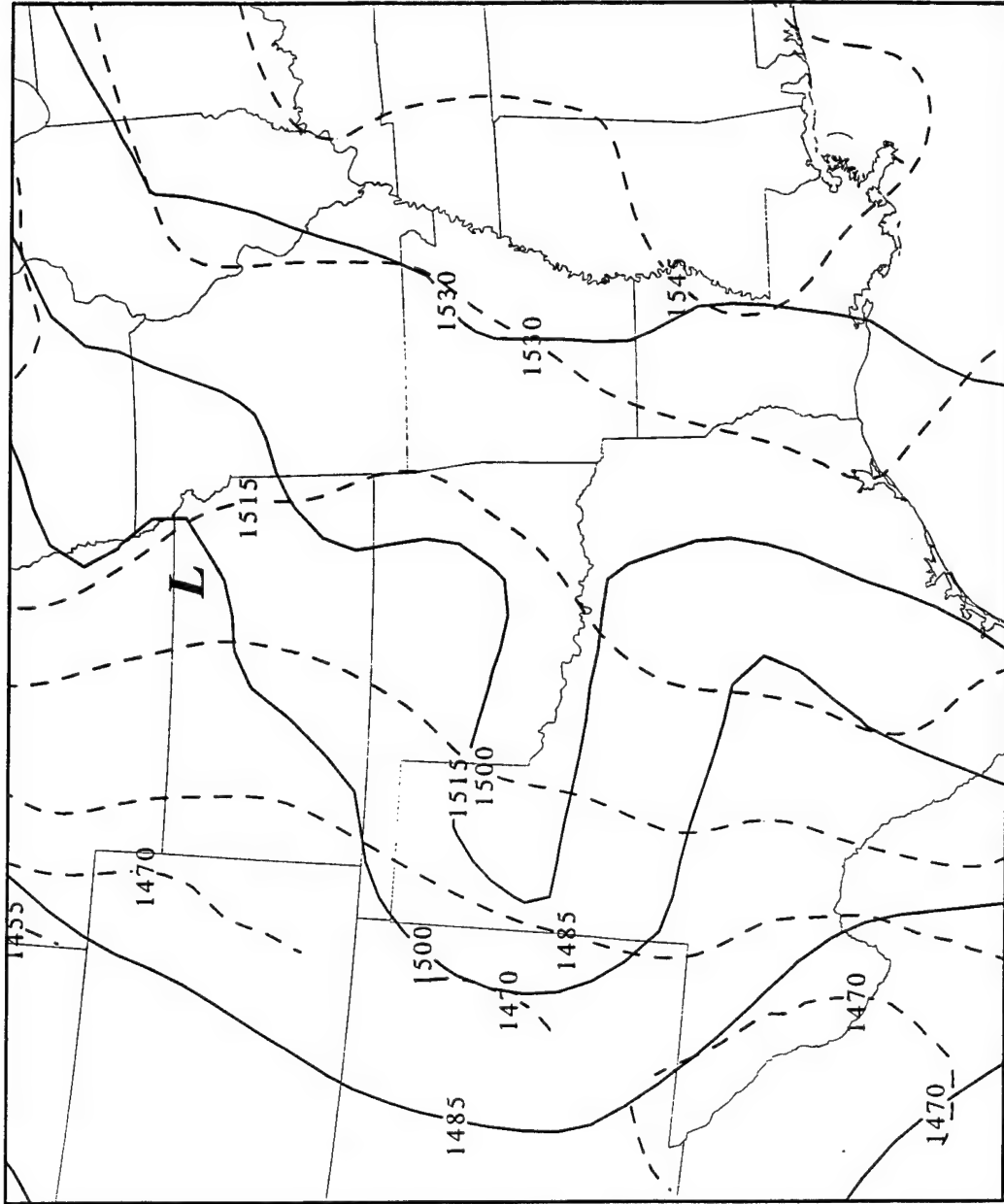


Figure 3.66. 950815/0300 850mb Retrieved heights (solid, m) and model heights(dashed, m).

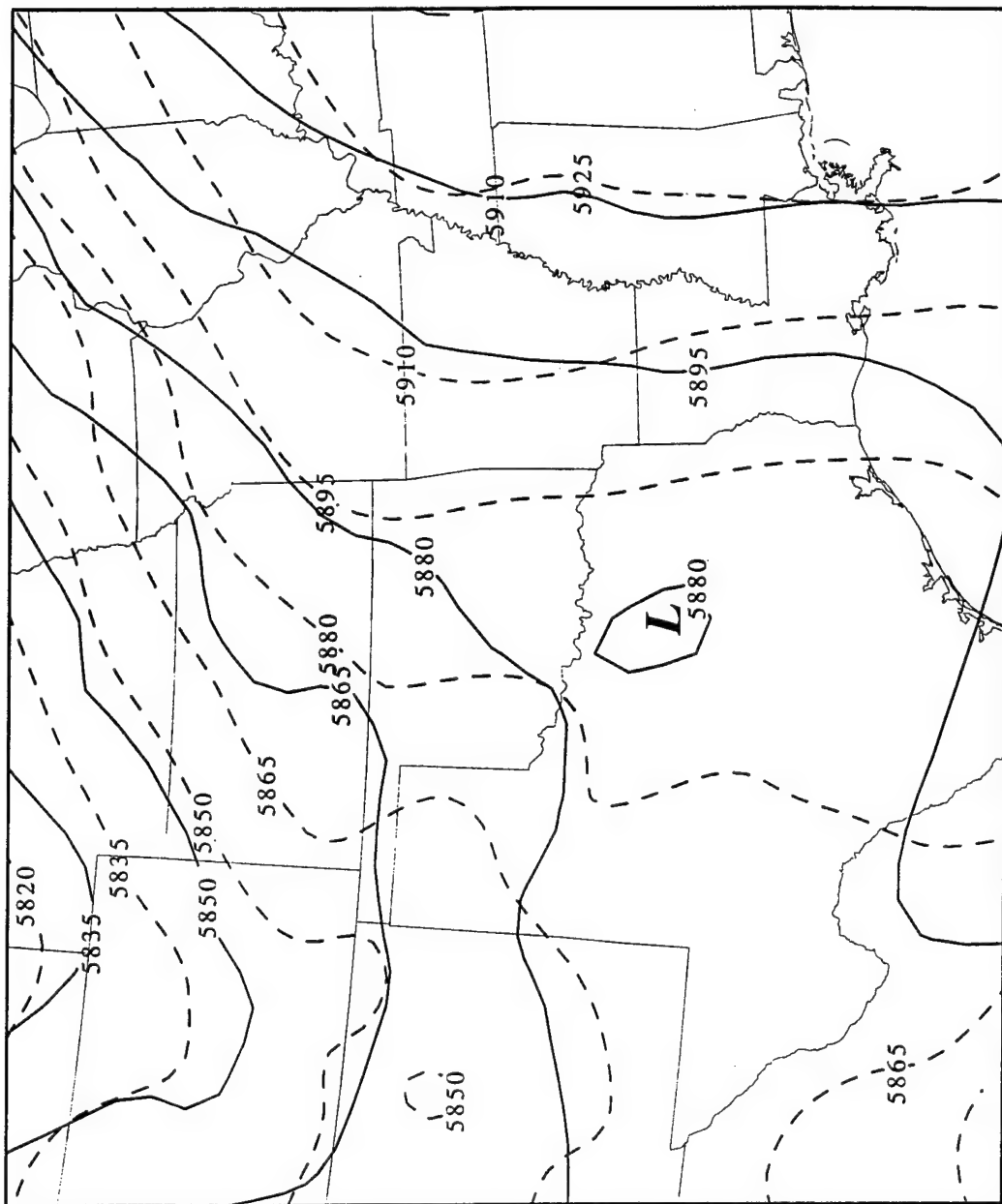


Figure 3.67. 950815/0600 500mb Retrieved heights (solid, m) and model heights(dashed, m).

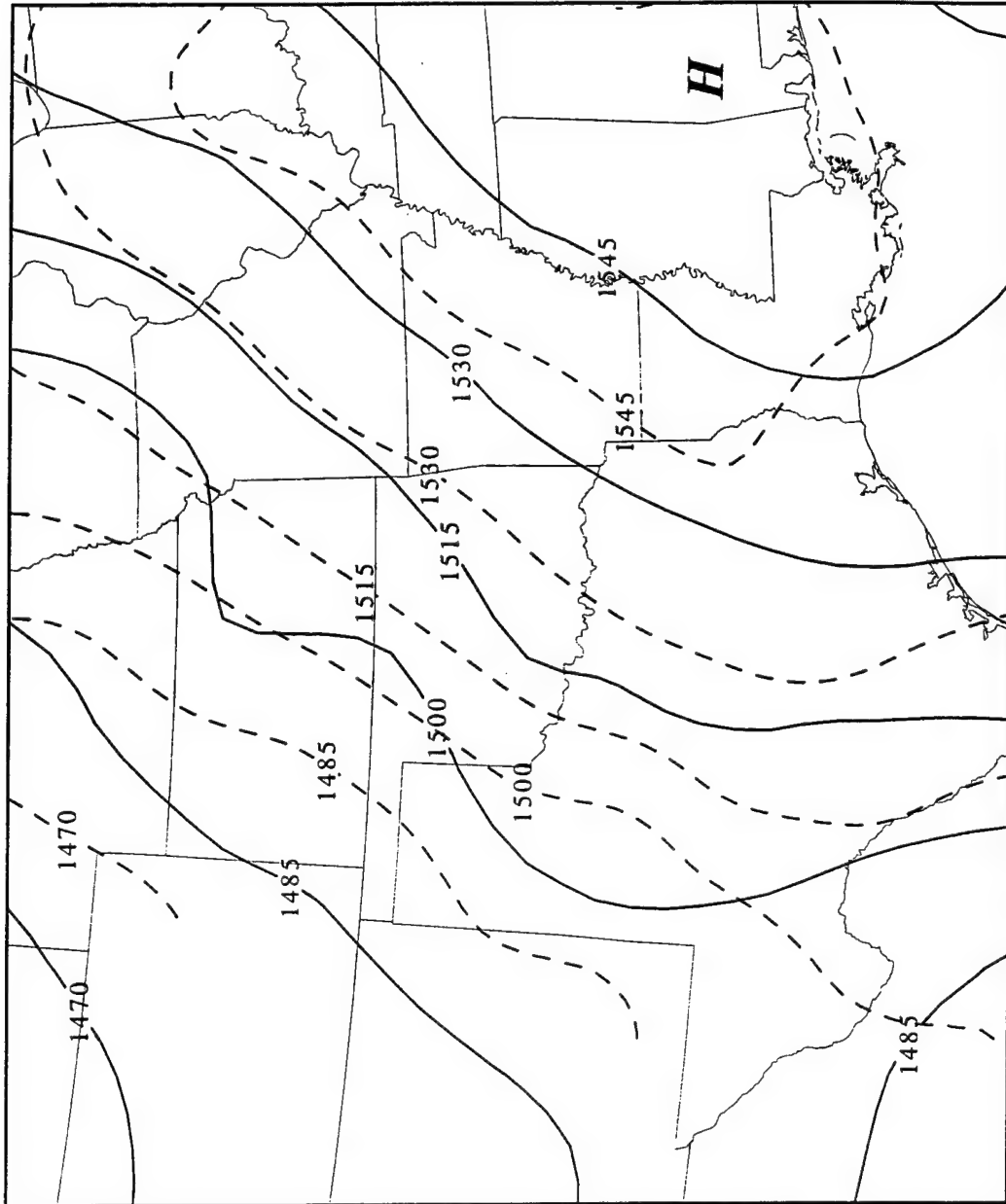


Figure 3.68. 950mb/1700 850mb Retrieved heights (solid, m) and model heights(dashed, m).



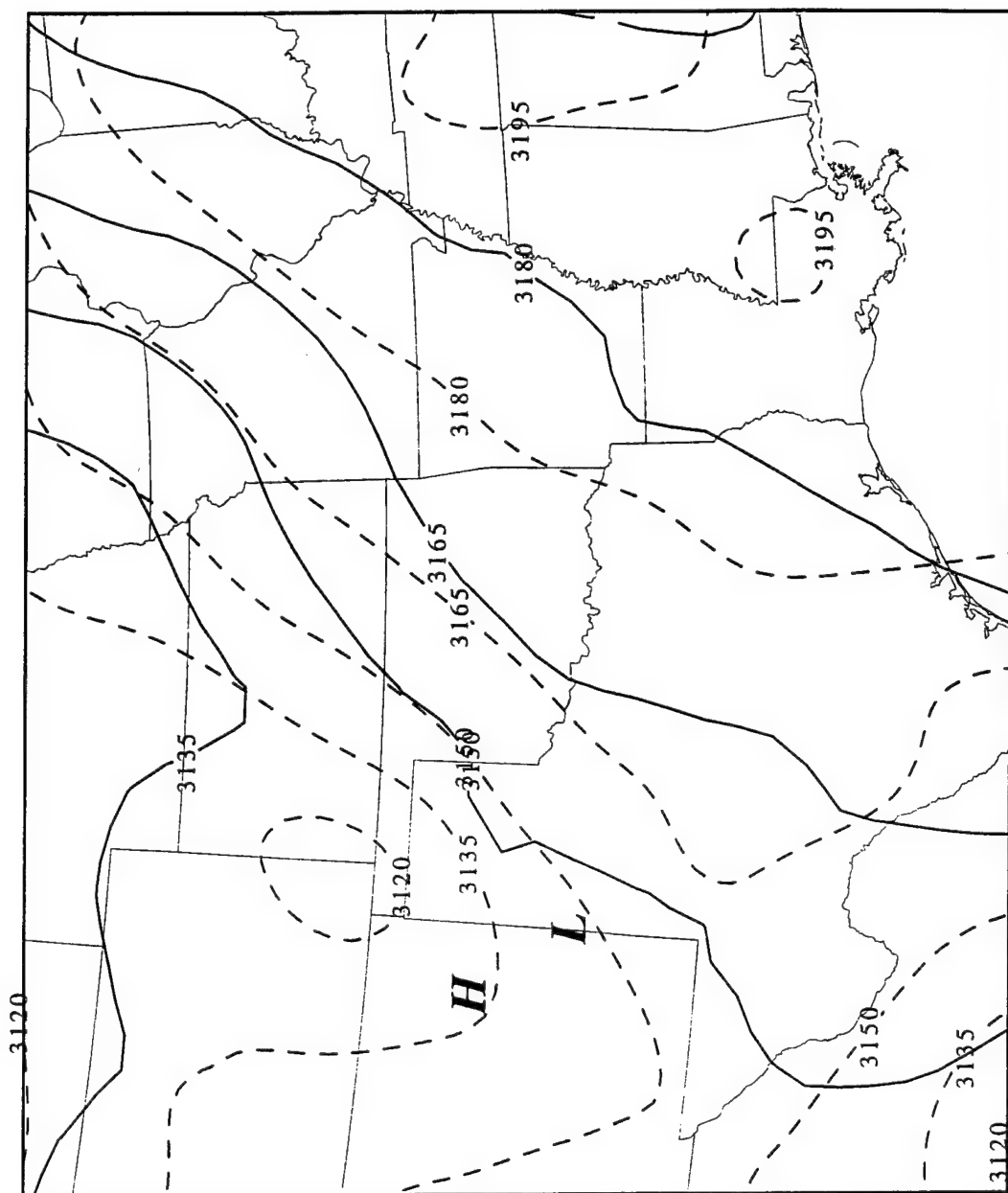


Figure 3.69. 950815/1700 700mb Retrieved heights (solid, m) and model heights(dashed, m).

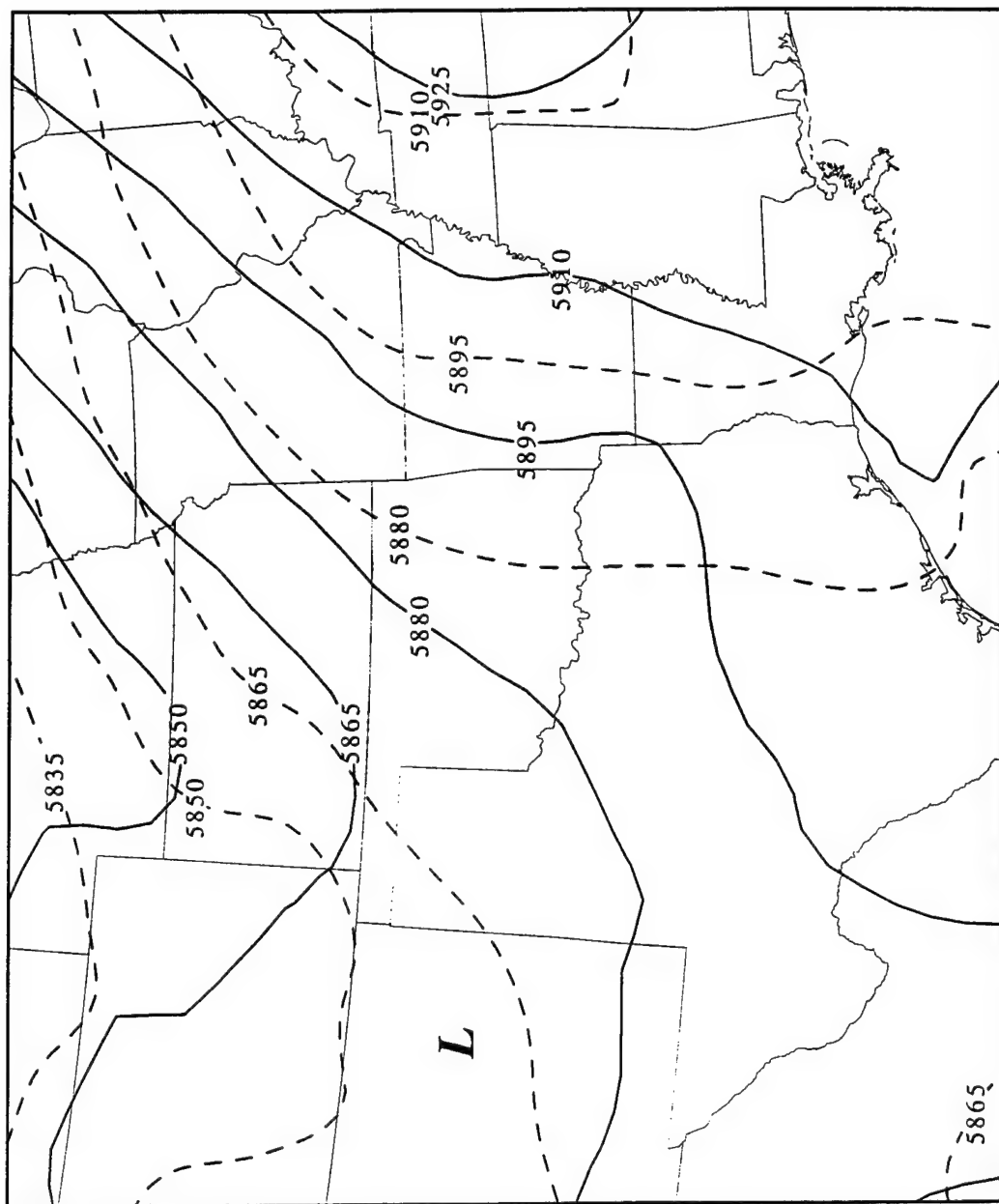


Figure 3.70. 950815/1700 500mb Retrieved heights (solid, m) and model heights(dashed, m).

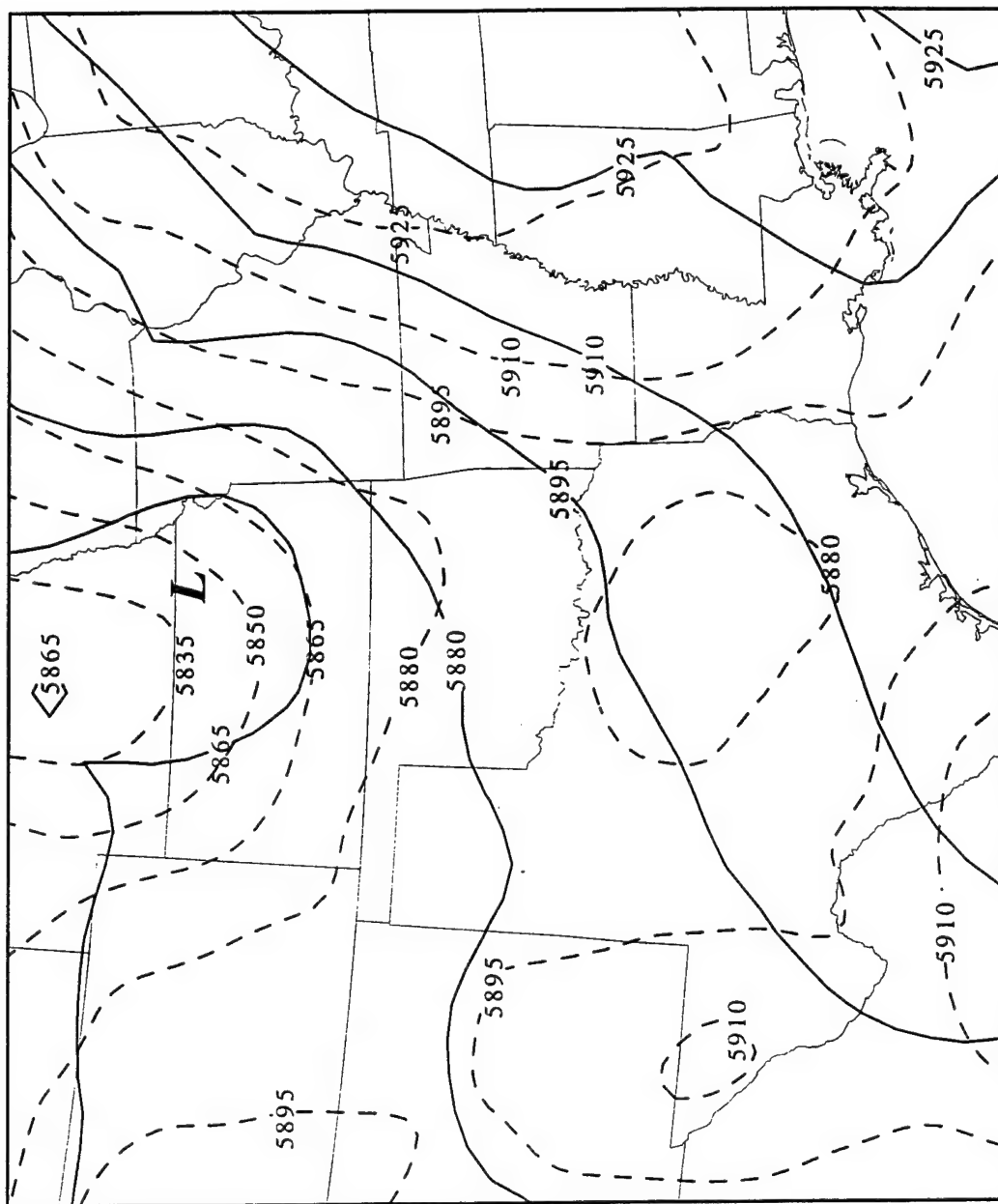


Figure 3.71. 950816/0000 500mb Retrieved heights (solid, m) and model heights(dashed, m).

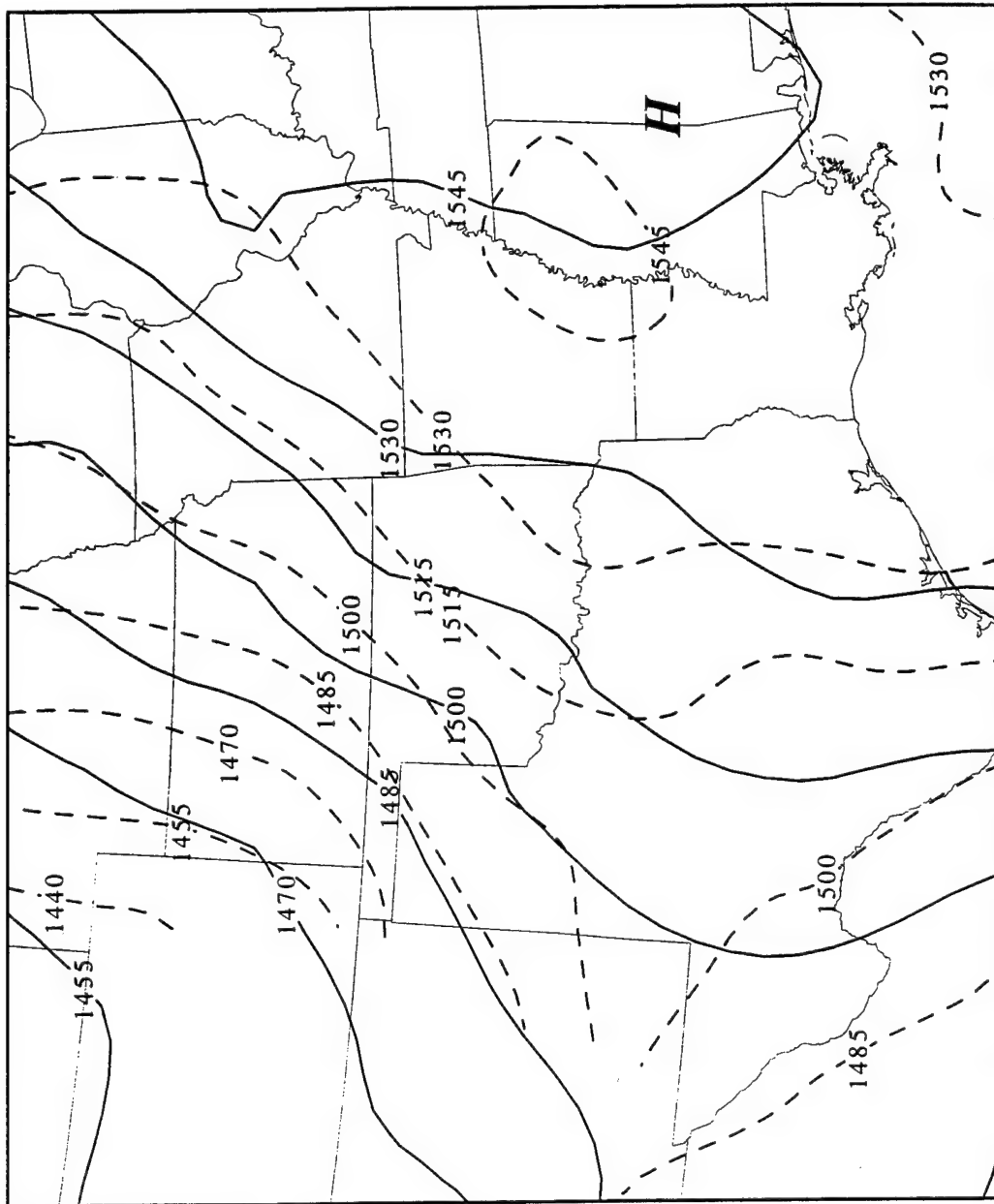


Figure 3.72. 950816/0700 850mb Retrieved heights (solid, m) and model heights(dashed, m).

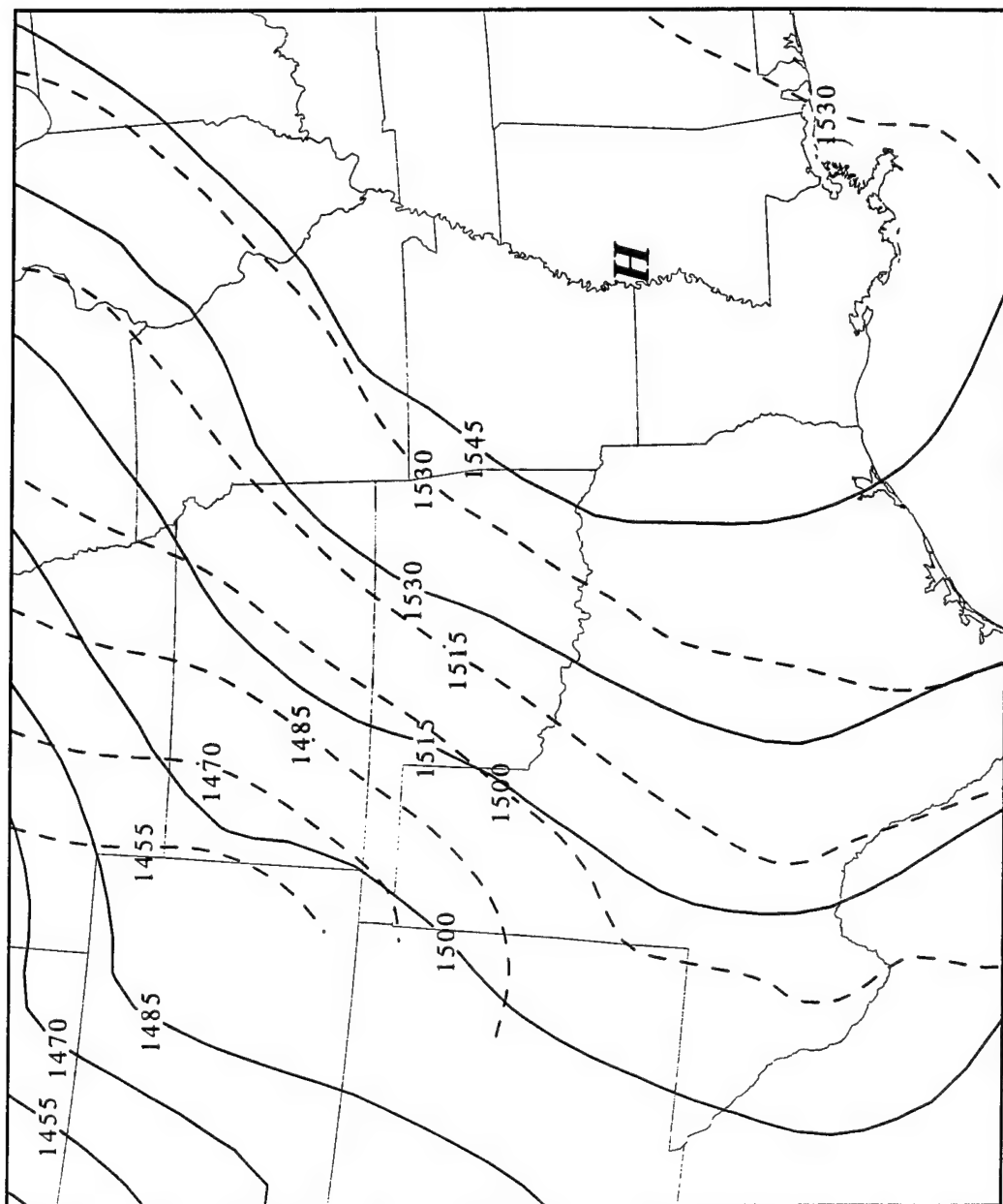


Figure 3.73. 950816/1200 850mb Retrieved heights (solid, m) and model heights(dashed, m).

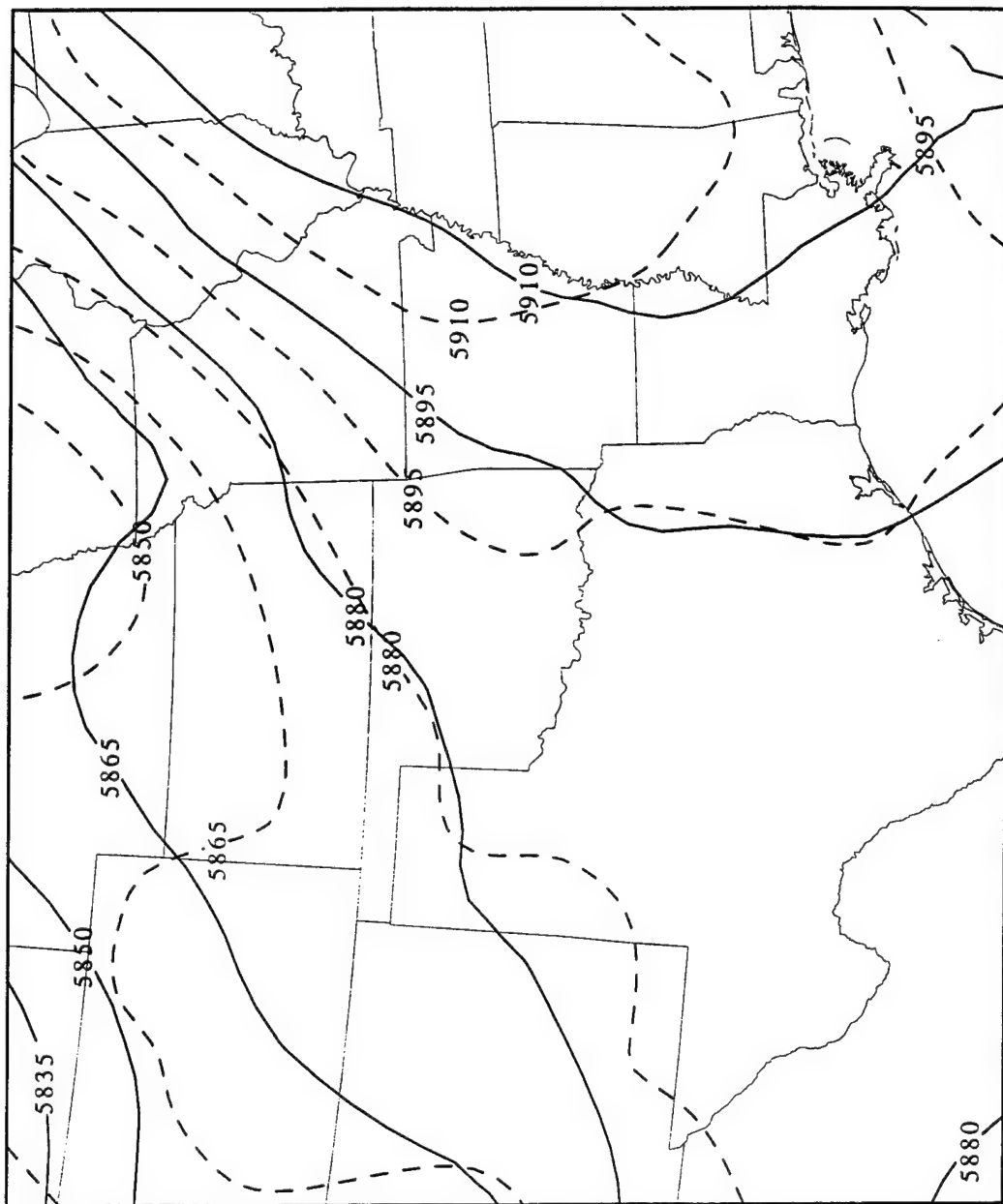


Figure 3.74. 950816/1200 500mb Retrieved heights (solid, m) and model heights(dashed, m).

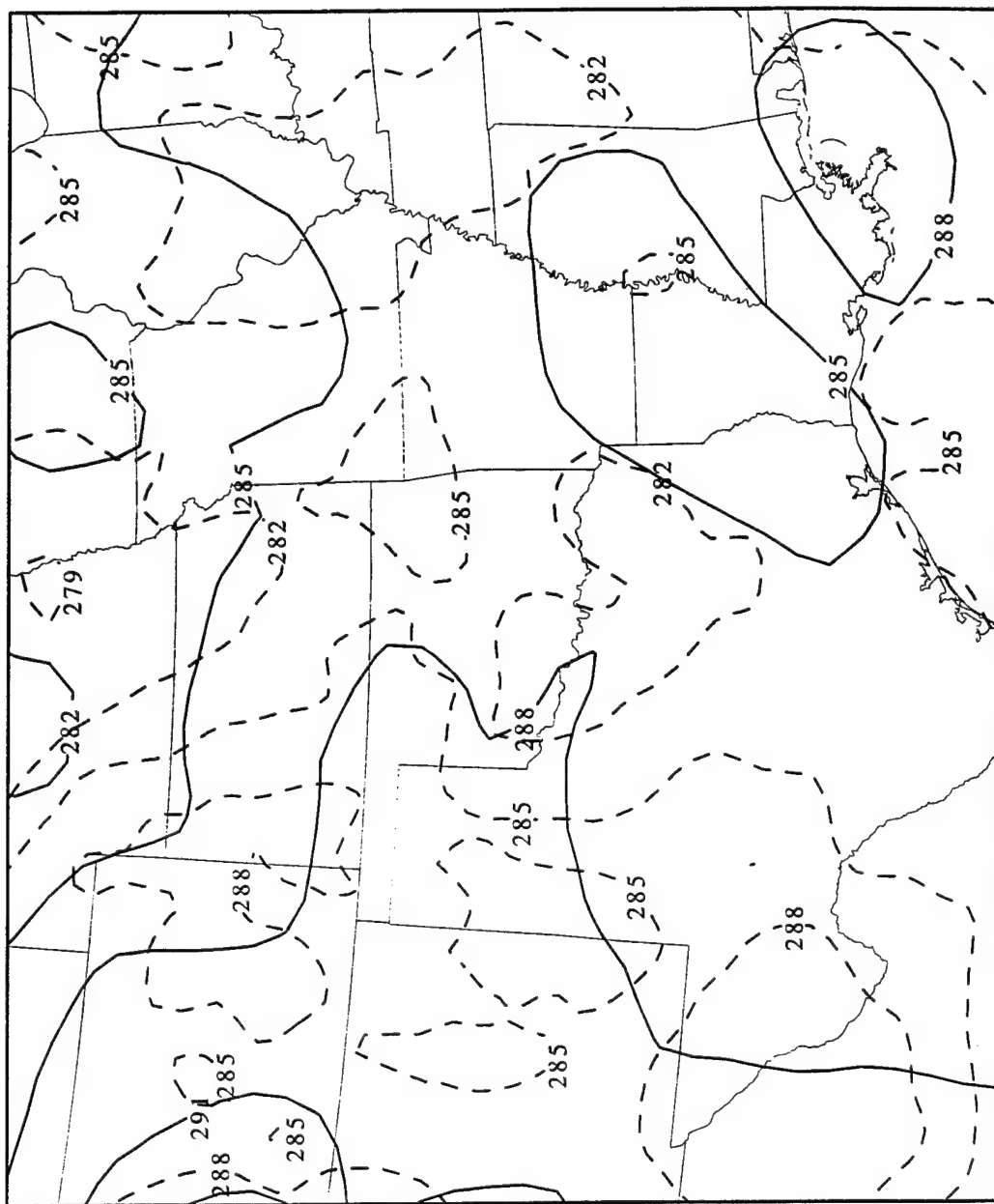


Figure 3.75. 950815/0000 700mb Retrieved temperatures (solid, K) and model temperatures(dashed, K).

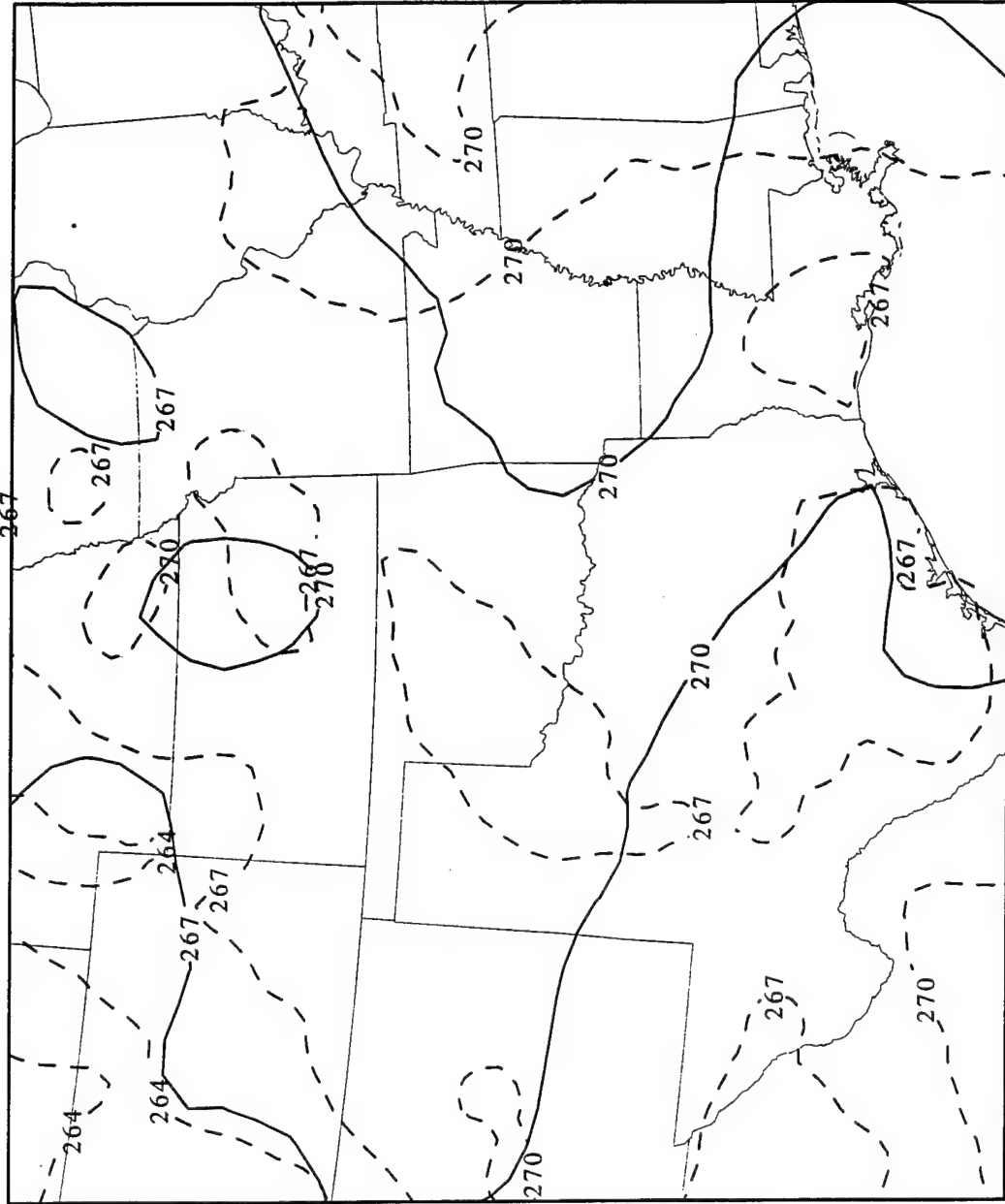


Figure 3.76. 950815/0000 500mb Retrieved temperatures (solid, K) and model temperatures(dashed, K).



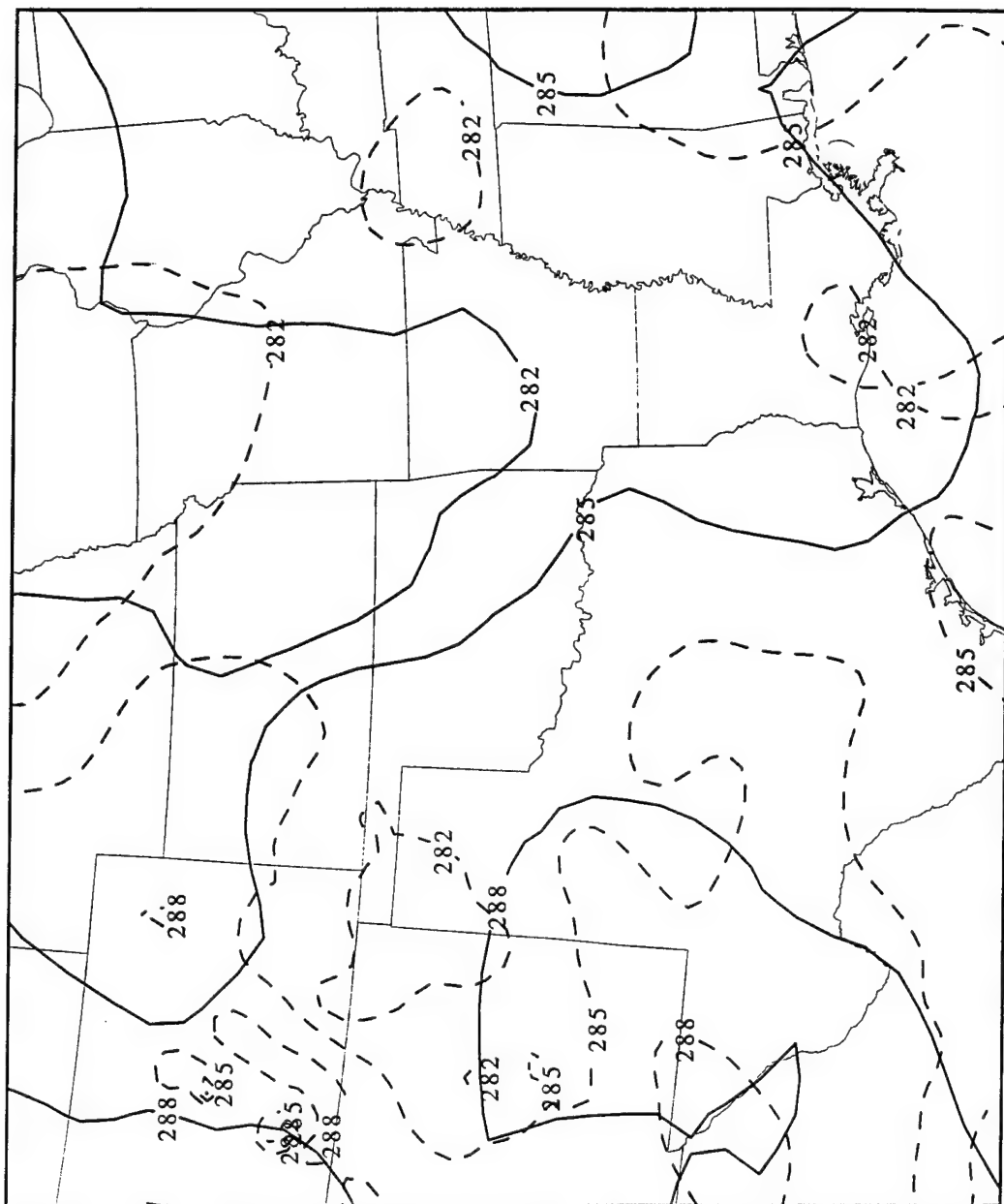


Figure 3.77. 950815/0600 700mb Retrieved temperatures (solid, K) and model temperatures(dashed, K).

level, the 500 mb chart shows favorable temperature results (Fig. 3.78). The rest of the model run has no significant temperature disparities and agrees with the retrieval technique quite well.

The wind field produced mixed results. In general, the winds were in agreement. Figure 3.79 shows the 700 mb winds at 0000Z on 15 August. This is a typical initialization comparison. At 500 mb, though, the profiler-derived winds show a small jetlet running through Wyoming, Nebraska, Kansas, and Iowa. The model, however, does not pick up on this signal (see Fig. 3.80). The winds in the Texas area are also not aligned very well. This is because there are few wind profiler stations and the winds are weak and variable in this area at the time.

By 0400Z the 850 mb chart shows the modeled winds are producing an area of stronger winds in southern Texas while the profiler winds do not show this (Fig. 3.81). Four hours later, at 0800Z on 15 August, the model winds reveal a LLJ throughout Texas (Fig. 3.82). The convection which handicapped the formation of the LLJ during this period has not hampered the model from producing a LLJ. By 1400Z the 900 mb winds are again back in general agreement with each other (Fig. 3.83).

The next initialization period shows an excellent relationship between the model and observed wind fields. The only discrepancy lies in the northern Missouri area. By observing the surrounding area and noting the surface observations at the time, the profiler winds appear to be influenced by convective activity and are, therefore, producing questionable results (Fig. 3.84). The model again produces a LLJ, this time with better accuracy than the day before. By 0500Z on 16 August, the 900 mb wind chart shows the LLJs observed by the profilers and created by the model (Fig. 3.85). By 0700Z the modeled LLJ has a larger area of extent reaching further south than the profiler's LLJ. The modeled LLJ is also a little stronger (Fig. 3.86). At the 750 mb level, both LLJs disappear and the winds are again in general agreement (Fig. 3.87). The modeled LLJ weakens just as observed, and the remainder of the model shows similar results.

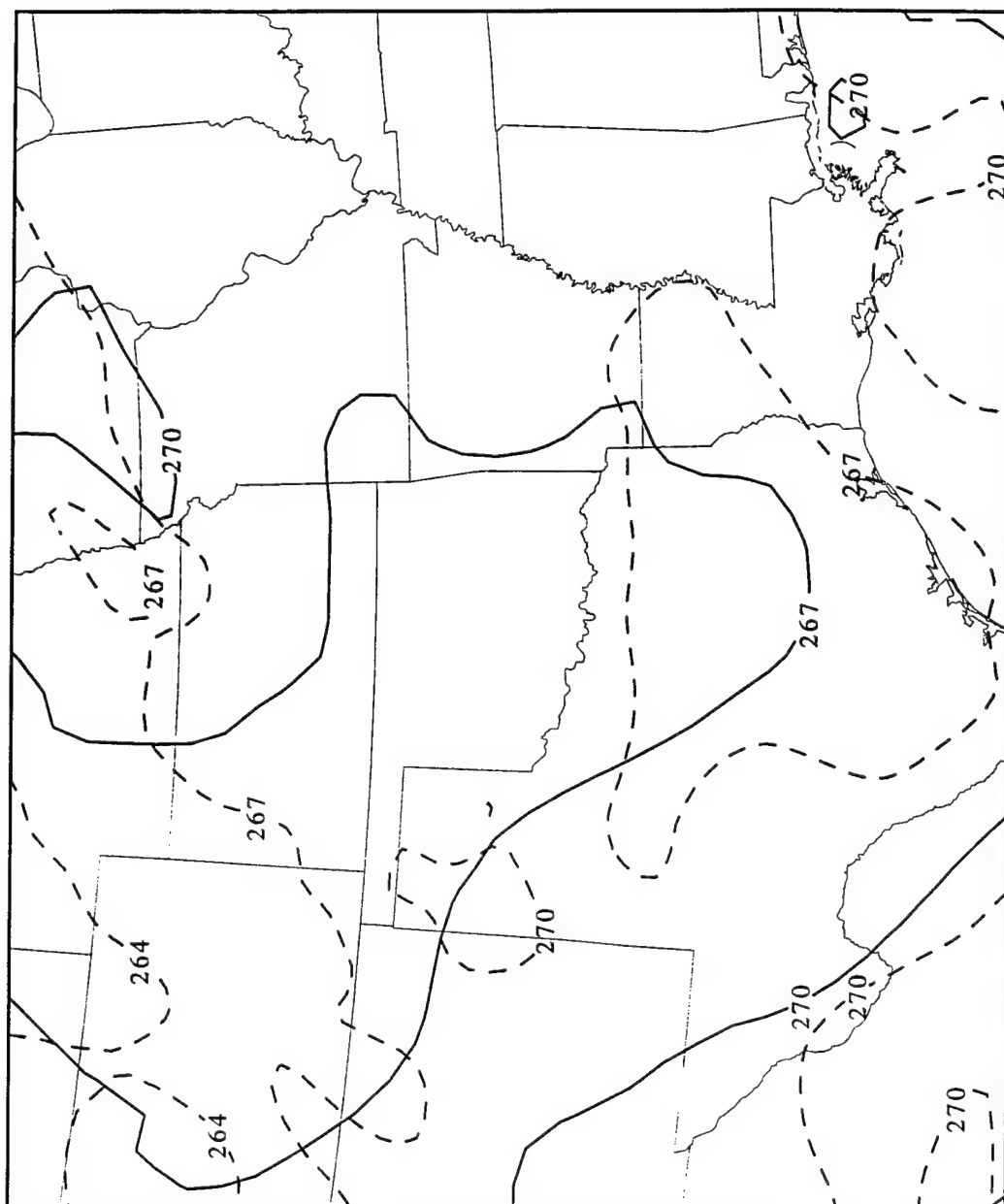


Figure 3.78. 950815/0600 500mb Retrieved temperatures (solid, K) and model temperatures(dashed, K).

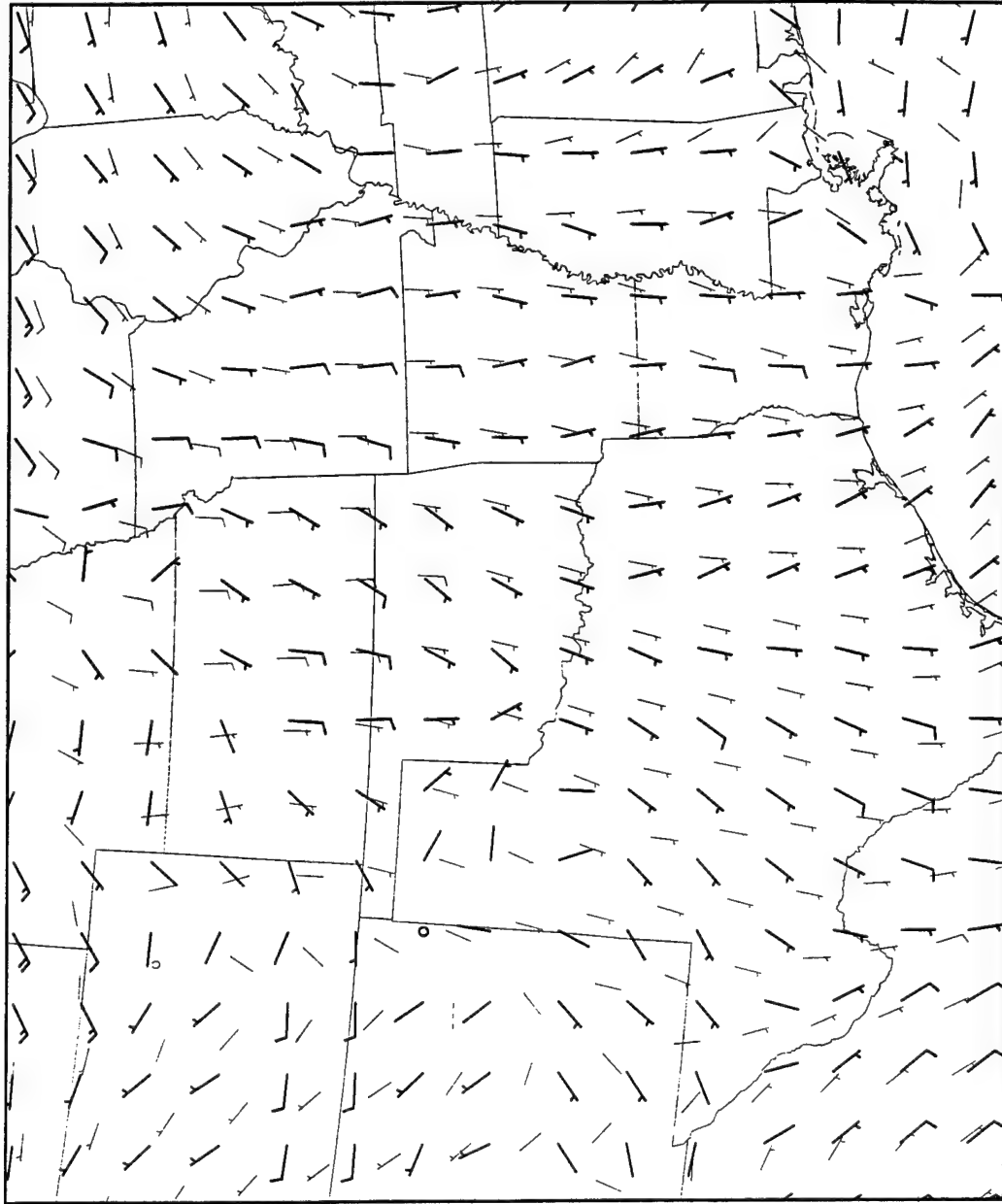


Figure 3.79. 950815/0000 700mb Profiler winds  
(thick, m/s) and model winds(thin, m/s).

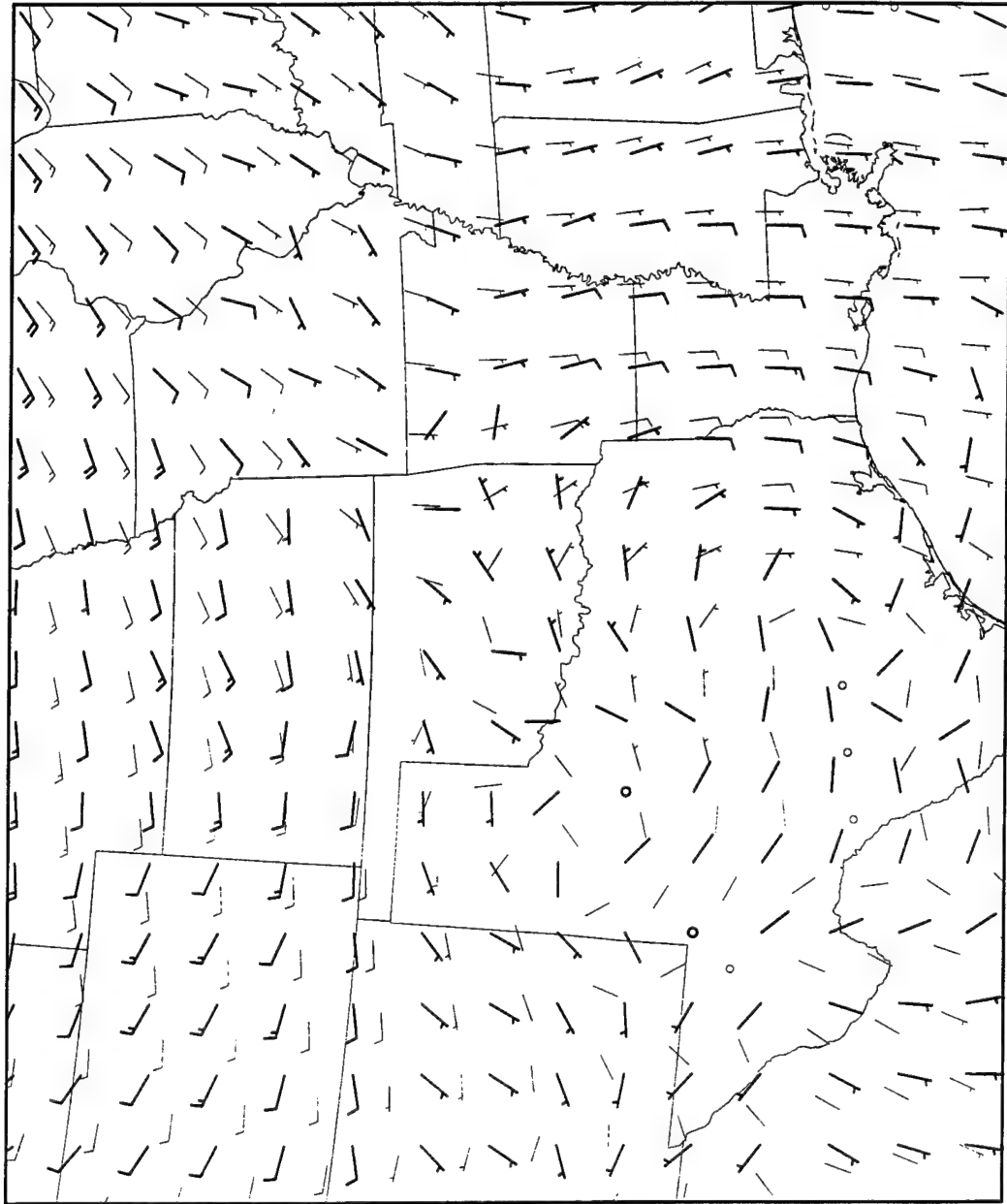


Figure 3.80. 950815/0000 500mb Profiler winds  
(thick, m/s) and model winds(thin, m/s).

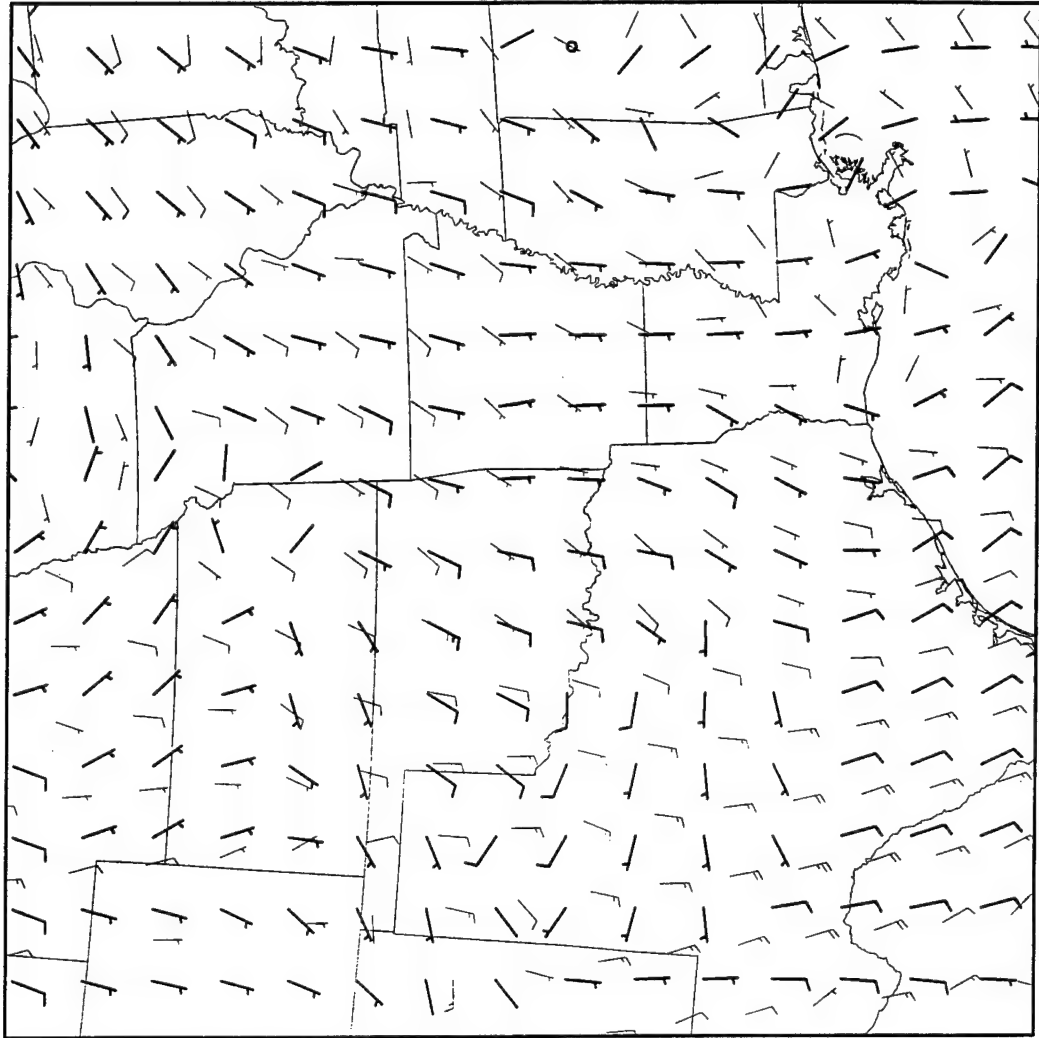


Figure 3.81. 950815/0400 850mb Profiler winds  
(thick, m/s) and model winds(thin, m/s).

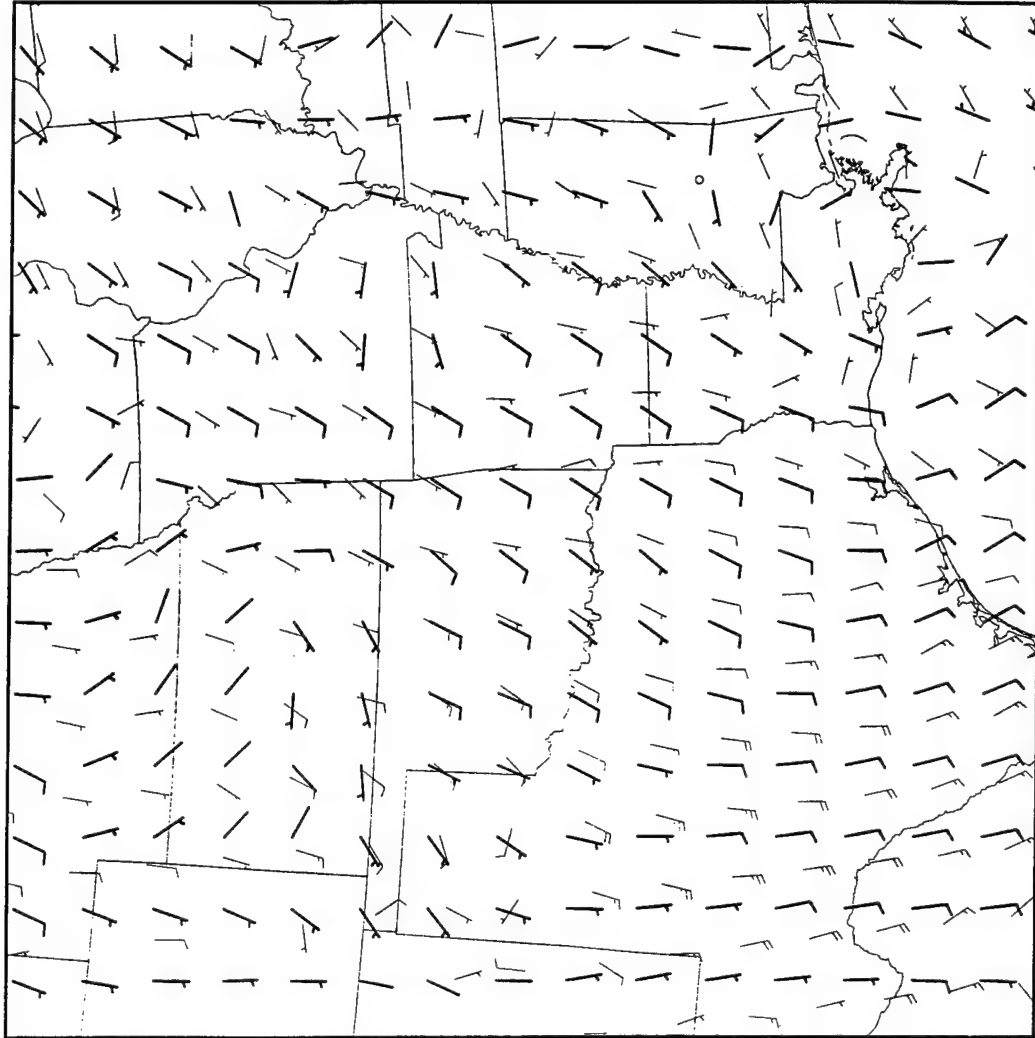


Figure 3.82. 950815/0800 850mb Profiler winds  
(thick, m/s) and model winds(thin, m/s).

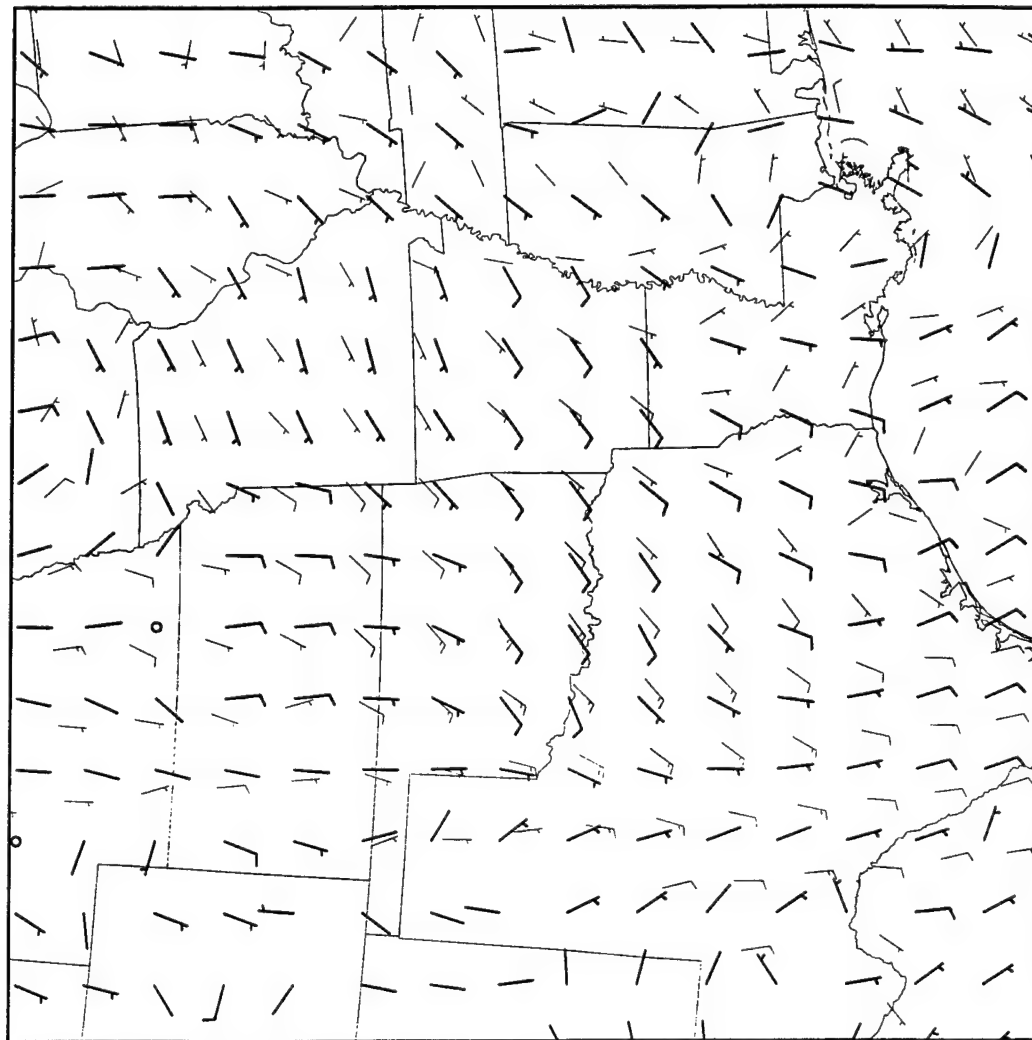


Figure 3.83. 950815/1400 900mb Profiler winds  
(thick, m/s) and model winds(thin, m/s).



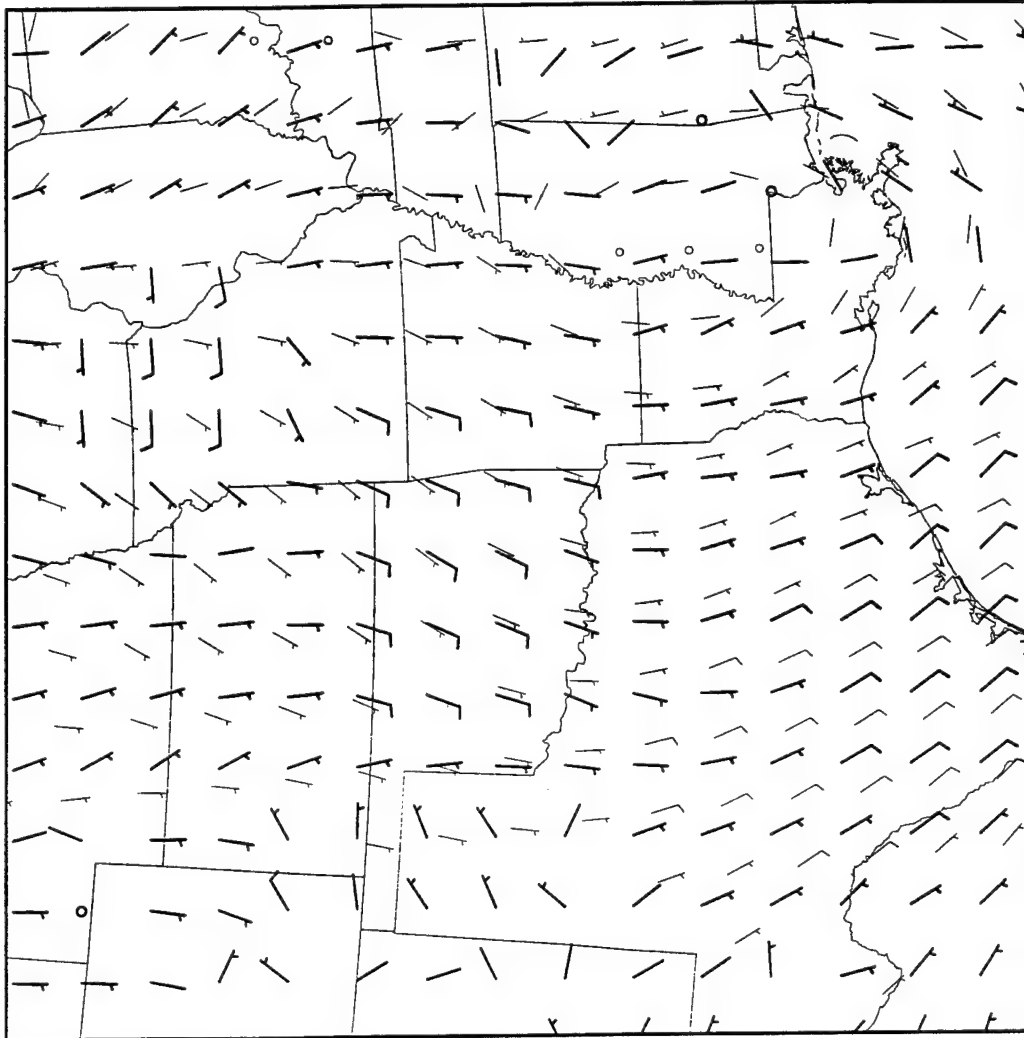


Figure 3.84. 95016/0000 900mb Profiler winds  
(thick, m/s) and model winds(thin, m/s).

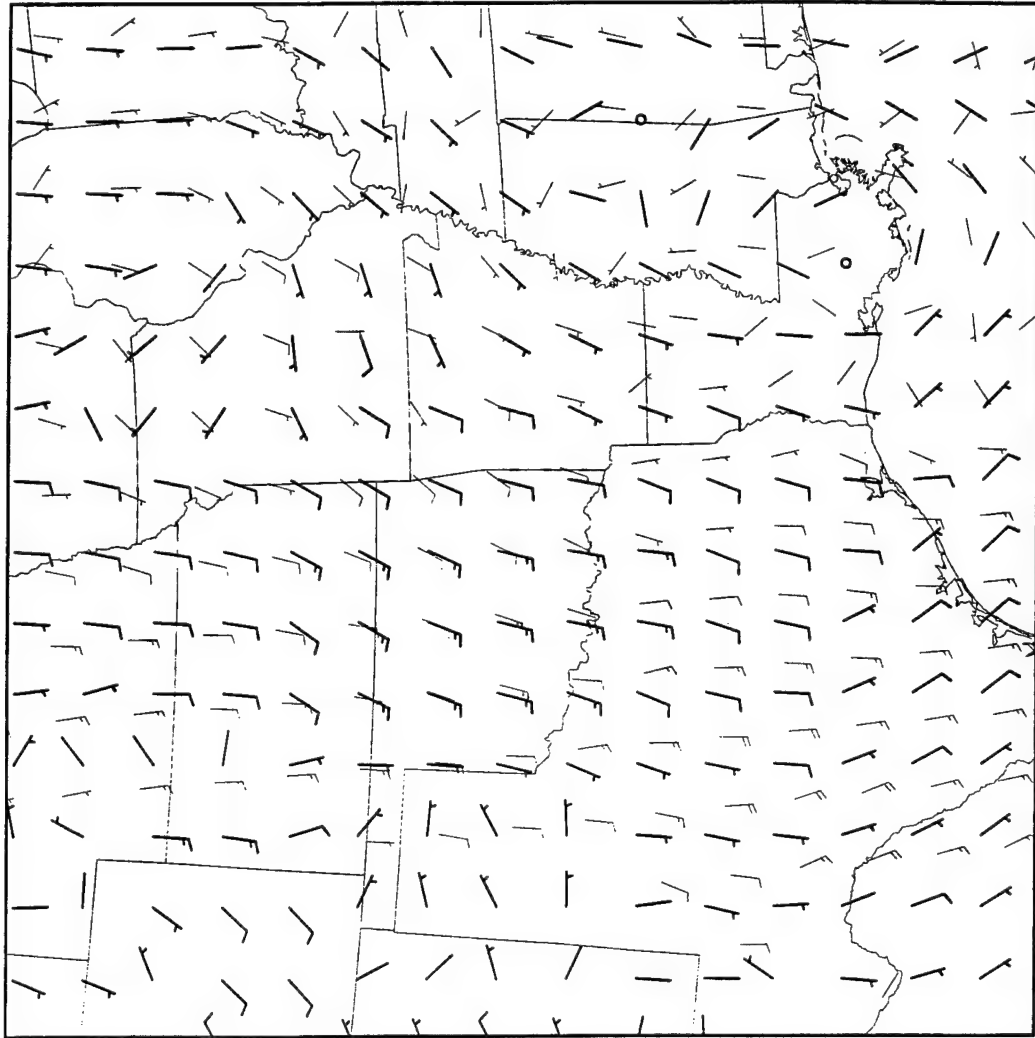


Figure 3.85. 950816/0500 900mb Profiler winds  
(thick, m/s) and model winds (thin, m/s).

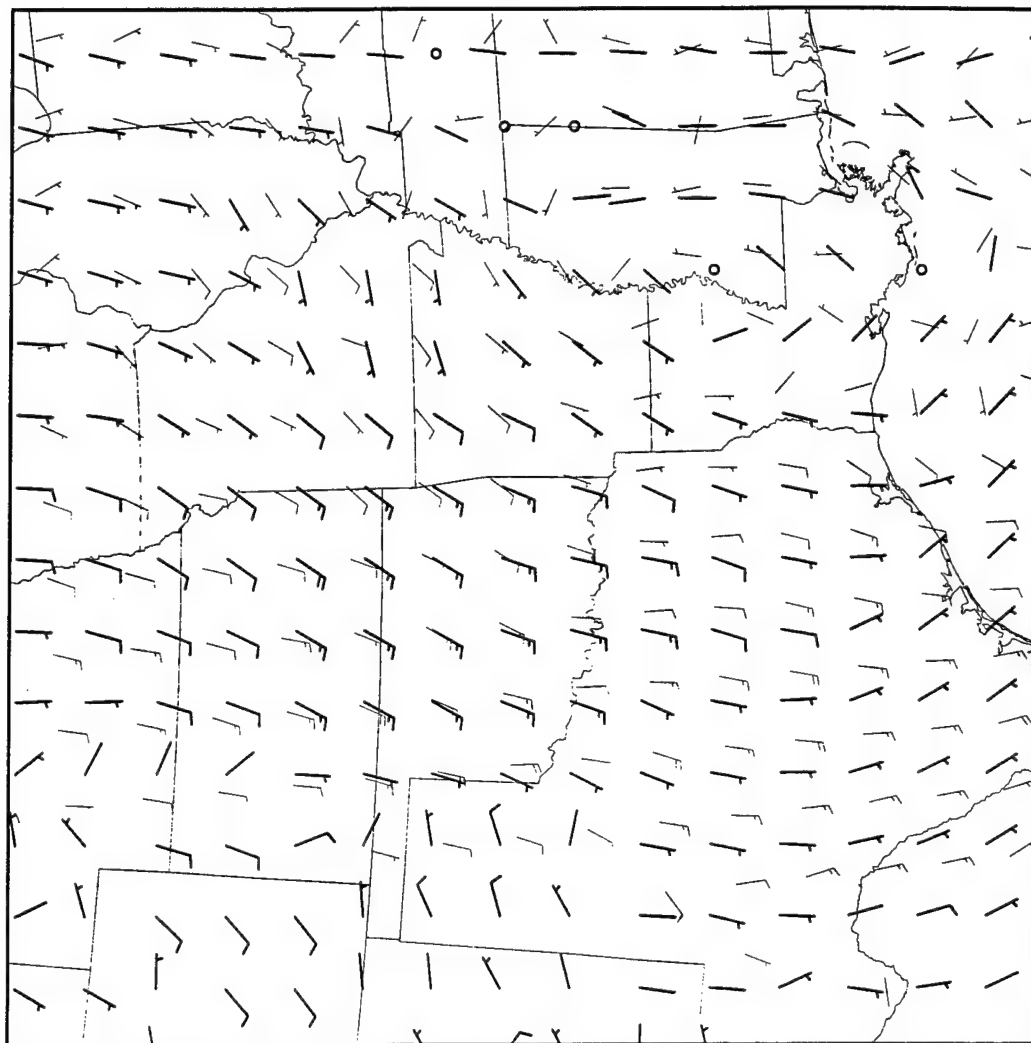


Figure 3.86. 950816/0700 900mb Profiler winds  
(thick, m/s) and model winds(thin, m/s).

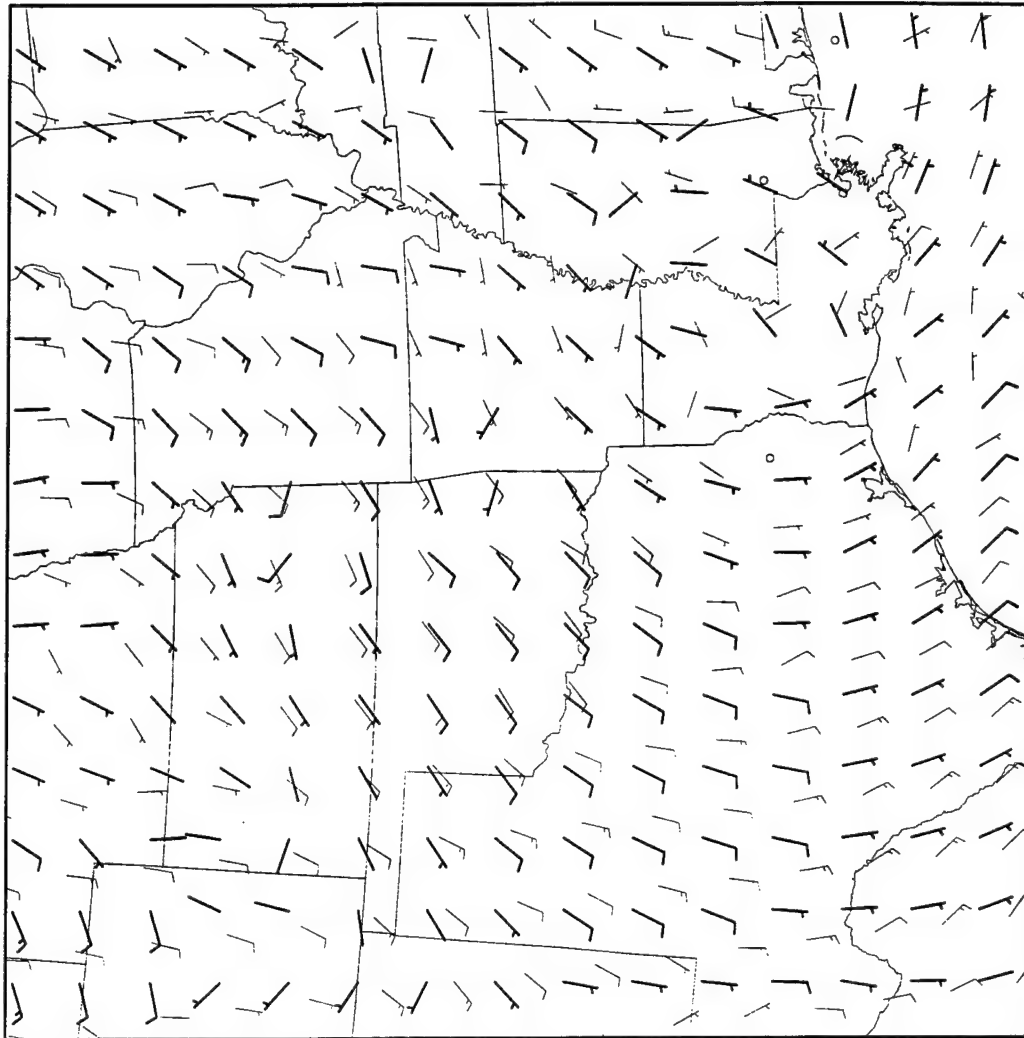


Figure 3.87. 950816/0700 750mb Profiler winds  
(thick, m/s) and model winds(thin, m/s).

## **4. Conclusion**

### **4.1 Summary of Work**

The mass retrieval technique developed above has shown some very positive results. With just the addition of wind profiler data, a higher definition mass field can be produced for many applications. This paper showed two such results. First, low-level jets (LLJs) on 15 and 16 August, 1995 in the Great Plains were analyzed. Second, the effects of friction in the divergence equation were examined for one synoptic case study.

All of the data used here was of the operational type. No special observational platform or period was employed. The combination of surface, RAOB, and wind profiler data was all that was needed. From this data, a new mass field was generated using the divergence equation. With the addition of the wind profiler data, the upper-air analysis had a smaller station separation and thus the spatial resolution was better than just the current RAOB network of observations. Also, the wind profiler data makes wind readings every 6 minutes and produces hourly averages of those winds. From this higher temporal resolution, a mass field was confidently generated every hour rather than the wide-ranging 12 hours produced by the RAOB network. Due to small errors in the profiler observations, the resulting mass field, though accurate, was a little noisy. Smoothing these fields would eliminate these concerns.

With this added resolution, mesoscale features can be seen. One such feature was the LLJ. This well-documented phenomenon is usually studied during intensive research observational periods. The retrieval technique shows the LLJ can be seen and studied by anyone with access to wind profiler information. A case study of three LLJ events were reviewed. Hourly charts produced by the wind profilers showed a new look at LLJs. Higher resolution helped at diagnosing the LLJ structure in both the vertical as well as the horizontal. The aid of better resolution made research of the LLJ events much more practical. The LLJs were produced by a combination of three forcing mechanisms. The

inertial oscillation mechanism was prevalent throughout the Criterion 2 LLJ event for the 16 August 1995 in the Oklahoma area. The rotation of the winds during the evening is consistent with results from other research. Also, baroclinicity effects can be seen during this case study. The sloped terrain, the temperature gradient, and the ageostrophic winds are all present to show signals of the baroclinic effects. All of this forcing produced a strong LLJ in the Great Plains. Transverse-ageostrophic motion could be accounted for in one of the LLJs.

The Criterion 2 LLJ was not, however, sensitive to frictional stresses in the divergence equation in terms of the retrieved mass field. The results during the daytime, while slightly more sensitive, still had similar effects. Two frictional techniques were employed in this study. Both were equally insignificant in altering the retrieved mass field to any degree. Even when the frictional parameterizations were made larger than normal for this case, the results were still rather small. This leads to the conclusion that frictional stresses near the ground in the divergence equation can be neglected for some synoptic cases especially at the scale of motion resolved by this wind profiler network.

Finally the results of the mass retrieval were compared to independently-produced model output. Overall the results compared well with each other. The geopotential heights were on average less than 15 m apart at both the initial hour and the forecasted hours. Their flow patterns were nearly identical. The few discrepancies arose when the retrieval technique would over predict the height field when the profiler winds were not consistent with the surrounding flow. Also, the modeled height field timing was slightly in error after several hours of forecast for an upper-level short-wave. Modeled winds were also in general agreement with the exception of the first LLJ event. The model tended to over predict the strength of the LLJ while the observational winds showed a much weaker LLJ. Convective parameterization failures in the model would explain this. The temperature results were in general agreement as well.

## 4.2 Future Work

The work performed here has left many avenues open for further research. The foremost question should be, does friction play such a small role in *all* synoptic cases? A generally weak high pressure case was selected in order to study the nocturnal LLJ. If vigorous convection, an intense cyclone, and/or an intense dryline was involved, would frictional stresses play a more prominent role in the retrieval of the mass field using the divergence equation? Also, how would the results have differed in the vicinity of fronts? Would the addition of more and better wind profilers aid in the understanding of the dynamics within fronts? This could be performed by acquiring different data for a different case and running the process over again. Strong frictional effects, though, might require an even finer resolution of observed data.

Also, the friction was parameterized using a simple relationship between the friction and the wind speed. Would the addition of the other components of the frictional stress have an effect on this part of the divergence equation? The Planetary boundary Layer evolution for this research used simple model data output for the two case studies. Could model data be used to see how important the other components of the frictional stress are? This way, a better picture of the friction within the layer could be utilized.

Another source of wind data could also be employed to retrieve the mass field. One other such operational wind source is the WSR-88D radar used by the National Weather Service, the Federal Aviation Administration, and the Department of Defense. The addition of the velocity azimuth display winds could provide more wind data for the retrieval technique. Not only would there be more data available, but the area of extent of these wind sources is greater than the wind profiler network. One drawback of such a methodology would be the accuracy of the WSR-88D winds. Also, the vertical range of the WSR-88D winds is less than the profilers. Another consideration involves the processing of the radar winds. Currently no such collection of just the radar winds throughout the network is kept.

As mentioned earlier, this retrieval technique could be applied on an operational basis. The time needed for data processing is relatively small and a very fast computer is not

needed. Operational forecasters could benefit tremendously with the higher resolution output needed for mesoscale forecasting. The higher resolution output can also be used for model initialization. With this in hand, better model results should ensue.



## 5. References

- Adams, M. E. 1996: Terrain-induced midtropospheric frontogenesis and jet streak development during STORM-FEST IOP-17, 8 & 9 March 1992. Ph. D. Thesis, North Carolina State University, 214pp.
- Anderson, J. R., E. E. Hardy, J. T. Roach, and R. E. Witmer, 1976: A land use and land cover classification system for use with remote sensor data. *U.S. Geological Survey Professional Paper 964*, U.S. Government Printing Office, Washington, 28pp.
- Arritt, R. W., T. D. Rink, M. Segal, D. P. Todey, and C. A. Clark, 1997: The Great Plains low-level jet during the warm season of 1993. *Mon. Wea. Rev.*, **125**, 2176-2192.
- Arya, S. P., 1988: *Introduction to Micrometeorology*. Academic Press, 303pp.
- Barnes, S. L., 1964: A technique for maximizing details in numerical weather map analysis. *J. Appl. Meteor.*, **3**, 396-409.
- Barnes, S. L., 1973: Mesoscale objective analysis using weighted time-series observations. *NOAA Tech. Memo.*, ERL NSSL-62, 60pp.
- Blackadar, A. K., 1957: Boundary layer wind maxima and their significance for the growth of nocturnal inversion. *Bull. Amer. Meteor. Soc.*, **38**, 283-290.
- Bluestein, H. B. and T. M. Crawford, 1997: Mesoscale dynamics of the near-dryline environment: analysis of data from COPS-91. *Mon. Wea. Rev.*, **125**, 2161-2175.
- Bolin, B., 1956: An improved barotropic model and some aspects of using the balance equation for three dimensional flow. *Tellus*, **8**, 67-75.
- Bonner, W. D., 1968: Climatology of the low-level jet. *Mon. Wea. Rev.*, **96**, 833-850.
- Bonner, W. D. and J. Paegle, 1970: Diurnal variations in boundary layer winds over the south-central United States in summer. *Mon. Wea. Rev.*, **98**, 735-744.
- Charney, J. G., 1955: The use of the primitive equation of motion in numerical weather prediction. *Tellus*, **7**, 22-26.
- Chen, T. C. and J. A. Kpaeyeh, 1993: The synoptic-scale environment associated with the low-level jet of the Great Plains. *Mon. Wea. Rev.*, **121**, 416-420.

- Cram, J. M., M. L. Kaplan, C. A. Mattocks, and J. W. Zack, 1991: The use and analysis of profiler winds to derive mesoscale height and temperature fields: simulation and real-data experiments. *Mon. Wea. Rev.*, **119**, 1040-1056.
- Daley, R., 1991: *Atmospheric Data Analysis*, Cambridge University Press, 457pp.
- Fast, J. D. and M. D. McCorcle, 1990: A two-dimensional numerical sensitivity study of the Great Plains low-level jet. *Mon. Wea. Rev.*, **118**, 151-163.
- Haltiner, G. J. and R. T. Williams, 1980: *Numerical Prediction and Dynamic Meteorology* John Wiley and Sons, Inc., 477pp.
- Kaplan, M. L. and P. A. Paine, 1977: The observational divergence of the horizontal velocity field and pressure gradient force at the mesoscale. Its implications for the parameterization of three dimensional momentum transport in synoptic-scale numerical models. *Beitr. Phys. Atmos.*, **50**, 321-330.
- Koch, S. E., M. DesJardins, and P. J. Kocin, 1983: An interactive Barnes objective map analysis scheme for use with satellite and conventional data. *J. Climate Appl. Meteor.*, **22**, 1487-1503.
- Kuo, Y. H. and R. A. Anthes, 1985: Calculation of geopotential and temperature fields from an array of nearly continuous wind observations. *J. Atmos. Oceanic Technol.*, **2**, 22-34.
- Kuo, Y. H., D. O. Gill, and L. Cheng, 1987: Retrieving temperature and geopotential fields from a network of wind profiler observations. *Mon. Wea. Rev.*, **115**, 3146-3165.
- Maddox, R. A., 1980: Mesoscale convective complexes. *Bull. Amer. Meteor. Soc.*, **61**, 1374-1387.
- Maddox, R. A., 1985: The relation of diurnal, low-level wind variations to summertime severe thunderstorms. Preprints, *14<sup>th</sup> Conf. On Severe Local Storms*, Indianapolis, IN, Amer. Meteor. Soc., 202-207.
- Marht, L. and H. Pan, 1984: A two-layer model of soil hydrology. *Boundary-Layer Meteorol.*, **29**, 1-20.
- McCorcle, M. D., 1988: Simulation of surface-moisture effects on the Great Plains low-level jet. *Mon. Wea. Rev.*, **116**, 1705-1720.
- McNider, R. T. and R. A. Pielke, 1981: Diurnal boundary-layer development over sloping terrain. *J. Atmos. Sci.*, **80**, 165-189.

- MESO, 1995: MASS Version 5.8 Reference Manual, MESO, Inc., Troy, NY, 119pp.
- Mitchell, M. J., R. W. Arritt, and K. Labas: A climatology of the warm season great plains low-level jet using wind profiler observations. *Wea. And For.*, **10**, 576-591.
- Mizzi, A. P. and R. A. Pielke, 1984: A numerical study of the mesoscale atmospheric circulation observed during a coastal upwelling event on 23 August 1972. I. Sensitivity studies. *Mon. Wea. Rev.*, **112**, 76-90.
- Noilhan, J. and S. Planton, 1989: A simple parameterization of land surface processes for meteorological models. *Mon. Wea. Rev.*, **117**, 536-549.
- O'Brien, J. J., 1970: Alternative solutions to the classical vertical velocity problem, *J. Appl. Meteor.*, **9**, 197-203.
- Ogura, Y., 1975: On the interaction between cumulus clouds and the larger-scale environment. *Pure Appl. Geophys.*, **113**, 869-889.
- Parish, T. R., A. R. Rodi, and R. D. Clark, 1988: A case study of the summertime great plains low-level jet. *Mon. Wea. Rev.*, **116**, 94-105.
- Pielke, R. A., R. A. Stocker, R. W. Arritt, and R. T. McNider, 1991: A procedure to estimate worst-case air quality in complex terrain. *Environ. Int.*, **17**, 559-594.
- Savijarvi, H., 1991: The United States Great Plains diurnal ABL variation and the nocturnal low-level jet. *Mon. Wea. Rev.*, **119**, 833-840.
- Stensrud, D. J., 1996: Importance of the low-level jet to climate: a review. *J. of Clim.*, **9**, 1698-1711.
- Strauch, R. G., 1981: Radar measurement of tropospheric wind profiles. Preprints, 20<sup>th</sup> Conference on Radar meteorology, Boston, MA, Amer. Meteor. Soc., 430-434.
- Stull, R. B., 1988: *An Introduction to Boundary Layer Meteorology*. Kluwer, 666pp.
- Uccellini, L. W., D. R. Johnson, 1979: The coupling of upper and lower tropospheric jet streaks and implications for the development of severe convective storms. *Mon. Wea. Rev.*, **107**, 682-703.
- Weber, B. L. and D. B. Wuertz, 1990: Comparison of rawinsonde and wind profiler radar measurements. *J. Atmos. Oceanic Technol.*, **7**, 157-174.

- Wexler, H., 1961: A boundary layer interpretation of the low-level jet. *Tellus*, **13**, 368-378.
- Whiteman, C. D., X. Bian, and S. Zhong, 1997: Low-level jet climatology from enhanced rawinsonde observations at a site in the southern great plains. *J. Appl. Meteor.*, **36**, 1363-1376.
- Wu, Y. and S. Raman, 1997: Effect of land-use pattern on the development of low-level jets. *J. Appl. Meteor.*, **36**, 573-590.
- Zack, J. W. and M. L. Kaplan, 1987: Numerical simulations of the subsynoptic features associated with the AVE-SESAME I case. Part I: the preconvective environment. *Mon. Wea. Rev.*, **115**, 2367-2382.